

Sheffield Hallam University

Development of PVD coating processes informed by plasma diagnostics.

EHIASARIAN, Arutiun Papken.

Available from the Sheffield Hallam University Research Archive (SHURA) at:

<http://shura.shu.ac.uk/19603/>

A Sheffield Hallam University thesis

This thesis is protected by copyright which belongs to the author.

The content must not be changed in any way or sold commercially in any format or medium without the formal permission of the author.

When referring to this work, full bibliographic details including the author, title, awarding institution and date of the thesis must be given.

Please visit <http://shura.shu.ac.uk/19603/> and <http://shura.shu.ac.uk/information.html> for further details about copyright and re-use permissions.

CITY CAMPUS, HOWARD STREET
SHEFFIELD S1 1WB

101 698 957 1



REFERENCE

Fines are charged at 50p per hour

22/03/03.5.00

29 MAR 2006 *9pm*

05 MAY 2006 4.20

ProQuest Number: 10694484

All rights reserved

INFORMATION TO ALL USERS

The quality of this reproduction is dependent upon the quality of the copy submitted.

In the unlikely event that the author did not send a complete manuscript and there are missing pages, these will be noted. Also, if material had to be removed, a note will indicate the deletion.



ProQuest 10694484

Published by ProQuest LLC (2017). Copyright of the Dissertation is held by the Author.

All rights reserved.

This work is protected against unauthorized copying under Title 17, United States Code
Microform Edition © ProQuest LLC.

ProQuest LLC.
789 East Eisenhower Parkway
P.O. Box 1346
Ann Arbor, MI 48106 – 1346

Development of PVD Coating Processes

Informed by Plasma Diagnostics

Arutiun Papken Ehasarian

A thesis submitted in partial fulfilment of the requirements of
Sheffield Hallam University
for the degree of
Doctor of Philosophy

June 2002



*Սիրելի
Եստերին, Սիմային և Բարգեճին*

To my family: Ester, Sima and Papken

Abstract

Physical vapour deposition technologies have been on the fast track of development for the last two decades due to their ability to meet demands for special materials and performance tools. The ever increasing complexity of the required coating microstructure and chemical composition can be achieved only by the development of PVD technology and in particular plasma sources for vapour generation that can provide the necessary tools.

This thesis describes plasma diagnostic studies of plasma discharges, developments of plasma sources and deposition of CrN coatings.

Initially the project investigated vacuum arc plasma discharges used in the Hauzer HTC1000/ABS industrially sized coater. The attention was concentrated to the plasma pretreatment by low energy (1200 - 3600 eV) Cr ion implantation into substrates, which contributed to an enhanced adhesion of subsequently deposited TiAlN coatings. Optical emission spectroscopy (OES), electrostatic probes, and time-of-flight (TOF) spectroscopy were used to study the interactions of the arc plasma with the gas atmosphere in the chamber. It was shown that increasing the pressure of Ar gas had a strong effect on the composition of the generated metal ion flux as the density of highly charged metal species reduced significantly to the benefit of gas ionisation. The mechanisms behind these observations are discussed and supported by further experiments. Based on the plasma diagnostic results, a novel two-stage pretreatment method was developed which allowed an enhanced adhesion due to faster sputter cleaning of the substrate surface and more efficient metal ion incorporation in the substrate material.

In the final stages of the project a novel high power pulsed magnetron sputtering (HIPIMS) process utilising peak power densities of 3000 Wcm^{-2} was investigated. OES studies showed the first evidence of doubly charged Cr and Ti ions generated by the HIPIMS discharge. Peak plasma densities of 10^{13} cm^{-3} were measured and, in the case of Cr, metal ions were found to constitute 30% of the total deposition flux to substrates. The influence of power on the plasma density, plasma composition and time evolution of the plasma was studied in detail using OES and electrostatic probes. The conditions for glow-to-arc transition were investigated. CrN coatings (thickness $2 \mu\text{m}$) were deposited for the first time using HIPIMS of Cr in a nitrogen atmosphere. The microstructure observed in transmission electron microscopy cross sections was highly dense and droplet free and contributed to an excellent corrosion and wear resistance superior to $20 \mu\text{m}$ thick electroplated hard Cr, and CrN coatings deposited by arc and unbalanced magnetron sputtering. The HIPIMS discharge was used also for pretreatment of substrates with metal ions analogous to the one performed previously with arc discharge. High adhesion was achieved as indicated by the scratch test critical load value $L_C = 85 \text{ N}$.

Finally, at an intermediate stage of the PhD project, an alternative source providing metal ionisation was studied. It was based on a radio frequency (RF) powered coil that was inductively coupled to a magnetron sputtering discharge. Energy resolved mass spectroscopy and OES in a laboratory-sized version of the plasma source revealed elevated metal ion densities and high ion energies of the order of 60 eV. This source was upscaled, installed, and tested successfully in the industrially sized Hauzer coater. The ion-to-neutral ratio at the substrate position could be increased 5-fold for a similar increase in RF power.

Acknowledgements

I would like to thank Dr. Roger New, my Director of Studies, for giving me invaluable guidance to conduct scientifically sound experiments and for his patience and support during my growth as a scientist. I would like to thank also Prof. W.-D. Münz, my First Supervisor, for sharing with me his invaluable experience in building industrially viable products based on state of the art fundamental scientific research.

The work constituting the present thesis benefited immensely from a number of visiting collaborations with leading laboratories in the field of plasma and materials research worldwide. In large part these visits were possible thanks to the remarkable capabilities of Prof. W.-D. Münz to network with leading scientists working in all aspects of PVD.

The start of the PhD project was boosted during a visit to the HVM Plasma Ltd., Prague, Czech Republic, company where the expertise, experience, and professionalism of the people make state of the art development of plasma sources and PVD coatings based on plasma diagnostics, magnetic field modelling and material characterisation look like a child's play. In particular, I would like to acknowledge the great help of Dr. Jan Valter and Dr. Jiri Vyskocil.

At a more mature stage of the PhD project, a visit to the Materia Nova Research Centre in Mons, Belgium, was organised in order to study the radio frequency amplified magnetron sputtering process. The high level of commitment of the scientists (of whom only two physicists!) and a good taste for carnivals are models for anyone interested in optical emission spectroscopy and particle interactions in plasmas. I would like to thank Professor Michel Hecq, the director of the centre and my collaborators Dr. Corinne Nouvelon, Ms. Laetitia Blott and Mr. Stephanos Konstantinidis.

Towards the end of the PhD thesis, I visited the Thin Film Physics group at the University of Linköping. The laboratory is famous for developing the superlattice coating structure and pioneering the studies of plasma-surface interactions in thin films. I would like to thank prof. Ulf Helmersson and prof. Lars Hultman who gave me the opportunity to test my abilities to apply and to extend my knowledge by working with the state of the art high power pulsed magnetron sputtering (HIPIMS) process. This unique technology has a great potential in the PVD field.

Finally, at the very end of the PhD project, I had the opportunity to work with Prof. Jochen Schneider of Aachen University and Dr. Andre Anders at the Lawrence Berkeley National Laboratory, Berkeley, U.S.A. This laboratory is one of the leaders worldwide in the analysis and modelling of arc discharge plasmas and plasma-surface interactions. The Plasma Applications group is famous for compiling a periodic table listing experimentally obtained and theoretically modelled charge state distributions of ion fluxes generated in arc discharges. I would like to thank Jochen for arranging the visit and for very fruitful discussions on science and scientific life. I would like to thank Andre for being a great scientific mentor and a good host.

Last but not least, I would like to acknowledge the scientific, technical and moral support of the entire Surface Engineering Research Group.

And of course thanks to all the placement semester and exchange students who made our group truly international.

Advanced Studies

The following conferences, workshops and summer schools were attended during the studies for this thesis:

1. Fifth Sheffield ABS Days, July 1999, Sheffield, UK
2. 1st Plasma Technology Training School, June 2000, Buxton, UK
3. Sixth Sheffield ABS Days, July 2000, Sheffield, UK
4. Materials Week 2000, International Congress on Advanced Materials, their Processes and Applications, September 2000, München, Germany
5. Surface Engineering for Protection of Metals and Alloys, October 2000, Aquafreda di Maratea, Italy
6. 44th Annual Technical Conference of the Society of Vacuum Coaters (SVC), April 2001, Philadelphia, U.S.A.
7. International Conference on Metallurgical Coatings and Thin Films (ICMCTF) 2001, April 2002, San Diego, U.S.A.
8. 13th International Colloquium on Plasma Processes, June 2001, Antibes - Juan-les-Pins, France
9. Seventh Sheffield ABS Days, July 2001, Sheffield, UK
10. 12th International School on Vacuum Electron Ion Technologies (VEIT), September 2001, Varna, Bulgaria
11. 48th International Symposium of the American Vacuum Society (AVS), November 2001, San Francisco, U.S.A.
12. Materials Congress 2002, April 2002, London, U.K.
13. 45th Annual Technical Conference of the Society of Vacuum Coaters, April 2002, Orlando, U.S.A.
14. 5th Pulsed Plasma Surface Technologies Workshop and Tutorials, April 2002, Indialantic, U.S.A.
15. International Conference on Metallurgical Coatings and Thin Films 2002, April 2002, San Diego, U.S.A..
16. 1st European Workshop on Pulsed Plasma Surface Technologies, June 2002, Dresden, Germany

Publications and Patents

1. C. Schönjahn; A.P. Ehiasarian; D.B. Lewis; R. New; W.-D. Münz; R.D. Twesten; I. Petrov, Optimisation of *in situ* Substrate Surface Treatment in a Cathodic Arc Plasma: A Study by TEM and Plasma Diagnostics, *J Vac Sci Technol*, A19(4), (2001),1415
2. A.P. Ehiasarian, W.-D. Munz, L. Hultman, U. Helmersson, V. Kouznetsov, Influence of High Power Densities on the Composition of Pulsed Magnetron Plasmas, *Vacuum*, 65, (2002), 147
3. K.M. Macak, A. Ehiasarian, W.D. Munz, Z. Khan, U. Helmersson, An Analysis of Breakdown Mechanisms of High Power Pulsed Magnetron Sputtering, *Proceedings of 13th International Colloquium on Plasma Processes*, Antibes - Juan-les Pins, France, 2001
4. A.P. Ehiasarian, W.-D. Munz, L. Hultman, U. Helmersson, I. Petrov, High Power Pulsed Magnetron Sputtered CrNx Films, paper presented at ICMCTF 2002, San Diego, USA, accepted for publication in *Surf. Coat. Technol.*
5. J. Alami, J.T. Gudmundsson, A.P. Ehiasarian, W.-D. Münz, U. Helmersson, Plasma Conditions in Ionized PVD by High-power Pulsed Magnetron Discharges, paper presented at ICMCTF 2002, San Diego, U.S.A.
6. W.-D. Münz, D.B. Lewis, P.E. Hovsepian, C. Schönjahn, A. Ehiasarian, I.J. Smith, Industrial Scale Manufactured Superlattice Hard PVD Coatings, *Surface Engineering*, 17(1), 15, 2001
7. G. Nayal, A.P. Ehiasarian, K.M. Macak. R. New, W.-D. Münz, Low Pressure plasma nitriding, paper presented at eMRS, Strasbourg, (2000)
8. W.-D. Münz, A.P. Ehiasarian, P.Eh. Hovsepian, Kombiniertes Beschichtungs Verfahren, magnetfeldunterstützte Hochleistungs-Impuls-Kathodenzerstäubung und unbalanziertes Magnetron, German and European patent application No. 101 24 749.4

Awards

1. **Bunshah Award**, Symposium B, International Conference on Metallurgical Coatings and Thin Films, 2002, San Diego, U.S.A.
2. **TECVAC Surface Engineering Prize**, Materials Congress 2002, London, U.K.

Table of Contents

Abstract	iii
Acknowledgements	iv
Advanced Studies	v
Publications and Patents	vi
Awards	vii
Table of Contents	x
List of Figures and Tables	xiii
1. Introduction	1-1
2. Literature Review	2-1
2.1. Plasma-Surface Interactions During Film Growth	2-1
2.1.1. <i>Thin Film Microstructure Models</i>	2-1
2.1.2. <i>Ion to Neutral Ratio and Energy of Ion Bombardment</i>	2-5
2.1.3. <i>Ions Impinging at a Substrate at High Energy (eg. > 1000 eV)</i>	2-8
2.2. PVD Plasma Sources	2-9
2.2.1. <i>Cathodic Arc Evaporation</i>	2-10
2.2.2. <i>Magnetron Sputtering</i>	2-15
2.2.3. <i>Magnetron Sputtering with Auxiliary Electron Impact Ionisation</i>	2-19
2.2.4. <i>RF Coil Enhanced Magnetron Sputtering</i>	2-20
2.2.5. <i>High Power Pulsed Magnetron Sputtering</i>	2-22
2.3. Chromium Nitride	2-25
3. Materials and Methods	3-1
3.1. Hauzer HTC 1000/ABS Coating Machine	3-2
3.2. Metal Vapour Vacuum Arc (MEVVA) with Time-of-Flight Spectrometer	3-6
3.3. High Power Pulsed Magnetron Sputtering (HIPIMS)	3-10
3.4. RF Coil Enhanced Magnetron Sputtering (Université de Mons-Hainaut, Belgium)	3-13
3.5. Plasma Diagnostic Techniques	3-16
3.5.1. <i>Optical Emission from Plasmas</i>	3-16
3.5.2. <i>Instruments Used for Optical Emission Spectroscopy</i>	3-19
3.5.3. <i>Flat and Cylindrical Electrostatic (Langmuir) Probes</i>	3-21
3.5.4. <i>Instruments Used for Electrostatic Probe Diagnostics</i>	3-26
3.5.5. <i>Energy Resolved Mass Spectroscopy</i>	3-31
3.6. Thin Film Characterisation Methods	3-34
3.6.1. <i>Sample Preparation</i>	3-34

3.6.2. Etching Rate Measurement	3-34
3.6.3. X-Ray Diffraction (XRD) Analysis	3-34
3.6.4. Transmission Electron Microscopy (TEM) for Thin Film Microstructure	3-36
3.6.5. Scanning TEM (EDX)	3-37
3.6.6. Evaluation of the Adhesion of Thin Films	3-38
3.6.7. Measurement of the Hardness of Thin Films	3-38
3.6.8. Measurements of the Friction and Wear Coefficient in Sliding Wear	3-39

4.1. Steered Cathodic Arc Discharge	4.1-1
4.1.1. Multi-fold Ionisation Observed In Cr, Ti, and Nb Metal Arc Discharges	4.1-1
4.1.2. Influence of Gas Pressure on Plasma Density, and Electron Temperature of Cr Arc Discharge	4.1-5
4.1.3. Development of a Two-Stage Cathodic Arc Etching Procedure for Enhanced Adhesion on HSS.	4.1-9
4.1.3.1. Ion Saturation Current of Cr Arc Discharge in Ar Atmosphere	4.1-9
4.1.3.2. Plasma Composition of Cr, Ti and Nb Arc Discharges in Kr, Ar, Ne, and He Atmosphere	4.1-12
4.1.3.3. Coating Sequence Incorporating a Two-Step Etching Treatment	4.1-26
4.1.3.4. Implantation Profiles of Cr Ions at Different Ar Pressures	4.1-28
Summary	4.1-33

4.2. High Power Density Pulsed Magnetron Sputtering (HIPIMS) Discharge	4.2-1
4.2.1. Influence of High Power Densities on the I-U Characteristic of Magnetrons	4.2-3
4.2.2. Multi-Fold Ionised Metal Species Found in Cr, Ti, and Ta HIPIMS and Comparison to Conventional Magnetron Discharge	4.2-6
4.2.3. Influence of Peak Power on the Plasma Composition, Ion Density and Deposition Rate	4.2-11
4.2.4. Time Evolution of the Plasma Composition and Density During a Pulse in HIPIMS of Cr, Ta and C Targets	4.2-13
4.2.5. An analysis of breakdown mechanisms of high power pulsed magnetron sputtering.	4.2-17
Summary	4.2-23

4.3. Deposition of CrN Films by Selected PVD Techniques	4.3-1
4.3.1. <i>CrN films deposited by Reactive Unbalanced Magnetron Sputtering</i>	4.3-1
4.3.2. <i>CrN films deposited by Reactive High Power Pulsed Magnetron Sputtering (HIPIMS)</i>	4.3-7
Summary	4.3-25
<hr/>	
4.4. Unbalanced Magnetron Sputtering Glow Discharge with Enhanced Ionisation by Radio Frequency (RF) Coil	4.4-1
4.4.1. <i>Typical Plasma Composition and Ion Energy in the RF Coil Amplified Magnetron Discharge</i>	4.4-2
4.4.2. <i>Influence of Power Dissipated in the RF Coil on Ion Density and Energy</i>	4.4-5
4.4.3. <i>Influence of Ar pressure on the RF Coil Discharge</i>	4.4-10
4.4.4. <i>Implementation of the RF Powered Coil in the Hauzer HTC 1000/ABS™ Coating Deposition Machine and Influence of RF Power and Pressure on the Ionisation and Plasma Composition</i>	4.4-12
<hr/>	
5. Conclusions	5-1
6. References	6-1
Annex A. Engineering Drawing of the Mirror and Collimator Assembly	A-1
Annex B. Papers published in refereed journals	A-2

List of Figures and Tables

Figure 2.1. Zone model proposed by Movchan and Demchishin. For metals $T_1 = 0.3 T_m$; $T_2 = 0.45 T_m$

Figure 2.2. Thornton zone model

Figure 2.3. Messier model of PVD film microstructure

Figure 2.4. Structure zone model relating to closed field UBM sputtering configuration after Kelly and Arnell [7].

Figure 2.5. Computer simulations of film growth under varying ion-to-neutral ratio in the deposition flux.

Figure 2.6. Refractive index versus O_2^+ ion current density of alumina films produced at $T < 150^\circ C$ after Williams et al [41]

Figure 2.7. Refractive index versus deposition rate at different target power settings taken from Shih and Dove [44].

Figure 2.8. The classification of plasma discharges according to their current density [52]

Figure 2.9. Basic arc evaporation processes and potential distribution after Martin et al [55]

Figure 2.10. Schematic of the deposition of a droplet and the structure of the film established in its vicinity after Petrov et al. [13]

Figure 2.11. Magnetic field arrangement in a steered cathodic arc discharge. 18 - evaporated cathode. 84 - magnets, 82 - magnetically conducting soft iron core. Adapted from Ramalingam [64]

Figure 2.12. Schematics of a planar magnetron illustrating the arrangement of magnets, the electric field and the plasma (shaded region)

Figure 2.13. Magnetic field lines of (a) balanced and (b) unbalanced circular magnetrons. The false colour represents the strength of the field.

Figure 2.14. RF coil enhanced magnetron sputtering set up, after Schneider et al [82]

Figure 2.15. Time evolution of the target voltage, ion saturation current density, argon neutral emission intensity, and Ti neutral emission intensity. Figure adapted from Macak et al [98]

Figure 3.1. Horizontal cross section through the middle of the ABS machine

Figure 3.2. Magnetic flux density, \mathbf{B} , at the target surface of Cathode 3 in Steered Arc (0 A coil current) and Magnetron (0 A coil current) configuration. (a) Normal component of \mathbf{B} , (b) tangential component of \mathbf{B} .

Figure 3.3. Vertical cross-section of the vacuum chamber showing the Langmuir probe position and the probe and sampling volume for OES. The inset shows detailed view of the mirror assembly.

Figure 3.4. Time evolution of arc ion current recorded by a digital oscilloscope.

Figure 3.5. MEVVA source with Time-of-Flight chamber

Figure 3.6. Oscillograms showing the arc current, the pulse driving the gates (Gate pulse), and charge/mass ratio dependent ion current trace (Time-of-Flight Spectrum), 500 ns/div.

Figure 3.7. Calculated relationship between the pressure measured in the TOF chamber and the actual pressure in the MEVVA source.

Figure 3.8. Schematic of the HIPIMS experimental setup

Figure 3.9. Top view of the laboratory sized RF coil enhanced magnetron sputtering setup.

Figure 3.10. Schematic diagram of the magnetron, RF coil, optical and energy resolved mass spectrometers

Figure 3.11. An example optical emission spectrum of Ti.

Figure 3.12. Monochromator with Czerny-Turner geometry [120]

Figure 3.13. Blazed grating. Light is incident at angle α and diffracted at several orders - β_0 , β_1 and β_{-1} .

Figure 3.14. Schematic of the optical emission spectroscopy experimental setup schematic

Figure 3.15. Sheath formation at a surface of an electrode (probe)

Figure 3.16. Ideal flat probe characteristic

Figure 3.17. Sheath (collecting area) of flat (a) and cylindrical (b) electrostatic probes. The sheath is indicated with a wireframe with sheath width d_s and the physical probe body is represented with a solid fill.

Figure 3.18. (a) Flat (plane) electrostatic probe and (b) Cylindrical probe used in the experiments

Figure 3.19. Electrical circuit used to record probe characteristics

Figure 3.20. Cylindrical probe I-V characteristic in a Cr arc discharge at background pressure (3×10^{-6} mbar), discharge current 100 A and cathode-to-probe distance of 20 cm. Oscillations in the probe current are caused by the motion of the cathode spot steered around the cathode surface.

Figure 3.21. Semilogarithmic I-V plot of a cylindrical probe obtained in a unbalanced magnetron discharge. Pure Ar atmosphere, 1.4×10^{-3} mbar, unbalancing coil current 6 A, discharge power 5 kW, cathode-to-probe distance of 20 cm.

Figure 3.22. Detail from Figure 3.21 showing the transition region of the I-V characteristic used to determine the electron temperature. Two slopes corresponding to thermalised (cold) and fast diffusing (hot) electrons are evident.

Figure 3.23. Energy resolved mass spectrometer (Balzers PPM421)

Figure 3.24. Geometry of the GA-XRD measurement.

Figure 3.25. Schematic of a TEM [138]

Figure 3.26. Loading/unloading curve of the dynamic hardness measurement

Figure 3.27. Schematic of the pin-on-disk tester

Figure 4.1.1. Optical emission spectra obtained from Cr (a), Nb (b) and Ti (c) arc discharges showing highly ionised metal ions.

Figure 4.1.2. Time of Flight spectrum for a Nb arc operated in a Kr atmosphere

Figure 4.1.3. High-speed photographs of a Cr arc discharge showing the different plasma conditions on the target due to adding background gas. (a) - Arc discharge operated at base pressure of 0.003 Pa, (b) Arc discharge operated in Ar gas atmosphere at 0.1 Pa. Exposure time 1 ms. The composition of the post plasma is an estimate based on the dominating colour of the emission (red for Ar neutrals and blue for Cr ions and neutrals and Ar ions)

Figure 4.1.4. Ion saturation current densities measured by flat Langmuir probe for positions $\theta = 0^\circ$ (circles) and $\theta = 90^\circ$ (x) and cylindrical probe (rhombi and squares)

Figure 4.1.5. Etching rate of stainless steel substrates as a function of Ar pressure.

Figure 4.1.6. Variation of the emission from Cr neutrals, and ions with pressure. In Ar atmosphere (a) the emission is altered due to collisions with Ar atoms, in He atmosphere (b) collisions are less effective.

Figure 4.1.7. Variation of the emission from Ti and Nb neutrals, and ions with pressure. In Ar atmosphere (a) the emission from Ti is altered due to collisions with Ar atoms, in He atmosphere (b) collisions with Ti ions are less effective. Nb neutral emission increases at higher Ar pressures than Ti and Cr (c).

Figure 4.1.8. Influence of gas pressure on highly charged ion densities. Legend the ions are represented by colour: Nb³⁺ - blue, Nb⁴⁺ - pink, Nb⁵⁺ - green, Cr²⁺ - orange, Cr⁴⁺ - light blue. The different gases forming the atmosphere are represented by symbols: Ne atmosphere - circles, Ar atmosphere - triangles, Kr atmosphere - squares.

Figure 4.1.9. Influence of gas pressure on low charged ion populations. Legend: the ions are represented by colour: Nb¹⁺ - blue, Nb²⁺ - red, and Cr¹⁺ - green. The different gases forming the atmosphere are represented by symbols: Ne - circles, Ar - triangles, Kr - squares.

Figure 4.1.10. Cr²⁺ ion concentration as a function of gas pressure for three types of gases. The charge transfer between Cr²⁺ and Ne needs additional 5.07 eV.

Figure 4.1.11. Influence of gas pressure on the gas ion concentration in a Cr arc discharge.

Figure 4.1.12. Average charge state determined by Time of Flight Spectrometry of Cr and Nb random arcs as a function of pressure and type of atmosphere.

Figure 4.1.13. Process sequence of one step (standard) and two-step etching procedures.

Figure 4.1.14. Plan view dark field images of TiAlN coating grown on low carbon steel after (a) 10min two step sputter cleaning procedure (b) 10 min sputter cleaning

Figure 4.1.15. STEM-EDX profiles across low carbon steel/TiAlN interfaces obtained by (a) mixed Cr/Ar ion bombardment at $p_{Ar} = 6 \times 10^{-2}$ Pa for 10 min (b) mixed Cr/Ar ion bombardment at $p_{Ar} = 8.8 \times 10^{-2}$ Pa followed by pure Cr ion bombardment.

Figure 4.2.1. Voltage and current density of plasma discharges. [52]

Figure 4.2.2. I-U characteristics of the pulsed discharge. The exponent n of the power law $I = kU^n$ is indicated. Cr sputtering in Ar atmosphere at a pressure of 0.4 Pa (3 mTorr).

Figure 4.2.3. Ion saturation current at a distance of 35 mm with the probe facing the target (circles) and with the probe perpendicular to the target surface (squares). The flat probe was biased to -150 V. Maximum plasma densities derived from the current densities are in the range 10^{13} cm^{-3} .

Figure 4.2.4. Optical Emission Spectra of HIPIMS of (a) Cr, (b) Ti, (c) Ta, and (d) C.

Figure 4.2.5. Optical emission spectra of plasmas produced by discharges in a conventional DC magnetron (bottom), a RF coil enhanced magnetron (middle) and High Power Pulsed Magnetron (top).

Figure 4.2.6. Carbon sputtering in N_2 atmosphere - HIPIMS and Continuous

Figure 4.2.7. Ion to neutral ratio vs. peak target current for Cr from optical emission line intensities $I(\text{Cr}^{2+}) / I(\text{Cr}^0)$ (triangles) and $I(\text{Cr}^{1+}) / I(\text{Cr}^0)$ (circles). Also shown is the ratio of the ion current density and deposition rate (squares).

Figure 4.2.8. Typical time evolution of the optical emission and target current at low power (peak target voltage = -500 V)

Figure 4.2.9. Typical time evolution of the plasma at high power. Time resolved optical emission spectrum of HIPIMS of Ta at peak power density = 2 kWcm^{-2}

Figure 4.2.10. Typical time evolution of the plasma at high power. HIPIMS of Cr at peak power density = 3 kWcm^{-2} . The species shown are: Cr^0 (399 nm), Cr^{1+} (232 nm), Ar^0 (811 nm), Ar^{1+} (440 nm). J_s is the ion current

Figure 4.2.11. Typical time evolution of the plasma: target voltage and current at high power (the apparent fluctuations in the current signal after 80 μs are principally caused by digitisation noise).

Figure 4.2.12. Time dependence of arcing frequency

Figure 4.2.13. Arcing frequency dependence on energy per pulse (effective pulse power).

Figure 4.3.1. Influence of nitrogen flow, Q_{N_2} , on the partial pressures of Ar, P_{Ar} , and N_2 , P_{N_2} , and the total pressure, P_{tot} . The resulting partial pressure ratios $P_{\text{Ar}}:P_{\text{N}_2}$ are shown as labels on the P_{N_2} trace. It was attempted to keep the total pressure constant.

Figure 4.3.2. (a) Electron Temperature, T_e ; and (b) Plasma density at the substrate position for different $Q_{\text{N}_2}/(Q_{\text{Ar}} + Q_{\text{N}_2})$ flow ratios.

Figure 4.3.3. XRD trace from CrN films deposited in the Hauzer ABS machine with $U_{\text{bias}} = -300 \text{ V}$ in mixed Ar+N₂ gas atmosphere with the indicated partial pressure ratios.

Figure 4.3.4. Deposition sequence

Figure 4.3.5. XTEM micrograph of the coating-substrate produced by HIPIMS. The line indicates the position and length of the area analysed by STEM-EDS

Figure 4.3.6. Chemical composition of the coating to substrate interface produced by HIPIMS. Data obtained by STEM-EDS point analysis. Ni signal is omitted.

Figure 4.3.7. Scratch test scar of CrN deposited on HSS.

Figure 4.3.8. Deposition rate produced measured in HIPIMS operated in different Ar-N₂ gas mixtures at a constant pressure $P_{\text{tot}} = 0.4 \text{ Pa}$ (3 mTorr). Measurements carried

out by QCM are marked with open circles. The full square represents a step height measurement.

Figure 4.3.9. Micrographs of CrN coating surfaces: (a) optical micrograph of CrN deposited by ABS technology (b) optical micrograph of CrN deposited by HIPIMS, (c) SEM micrograph of CrN deposited by ABS technology and (d) SEM micrograph of CrN deposited by HIPIMS

Figure 4.3.10. SEM micrograph of a CrN coating deposited by HIPIMS on 304 austenitic stainless steel.

Figure 4.3.11. The CrN coating surface viewed by (a) AFM (b) SEM. The coating conforms well to the structure of the steel grains.

Figure 4.3.12. TEM cross section of a CrN film produced by HIPIMS CrN. The films is columnar and the columns are terminated with flat tops.

Figure 4.3.13. XTEM micrograph showing the overall structure of HIPIMS CrN.

Figure 4.3.14. XTEM micrographs of a HIPIMS CrN film. (a) Void free grain boundaries (b) Grains are formed and extinguished far from the initial nucleation at the interface. (c) Strain and dislocation contrast is observed in the TEM image.

Figure 4.15. Plasma sheath near a floating substrate.

Figure 4.3.16. Glancing angle XRD scans (10° incidence) showing the phase composition of HIPIMS CrN films deposited at different Ar:N₂ partial pressure ratios. Peaks of the Cr₂N phase are marked in italics.

Figure 4.3.17. Bragg-Brentano XRD scans showing the microstructure of CrN films deposited at different Nitrogen partial pressures by Reactive HIPIMS.

Figure 4.3.18. Comparison of the sliding wear coefficient, K, of HIPIMS CrN to various coatings [170].

Figure 4.3.19. Potentiodynamic polarisation curve of monolithic CrN deposited by the HIPIMS method. The behaviour of electroplated hard Cr and arc deposited CrN is shown for comparison.

Figure 4.4.1. Typical OES spectra of an inductively coupled RF amplified magnetron discharge and conventional sputtering discharge. Ti ion lines are shaded. Conventional sputtering discharge with DC power = 200 W at Ar pressure 30 mTorr. RF coil discharge in the same conditions and RF power = 500 W.

Figure 4.4.2. Typical mass spectrum of an inductively coupled RF amplified magnetron discharge. RF power 250 W, DC power 200 W, Ar pressure 30 mTorr. The small peaks on the sides of the Ti⁺ are from naturally occurring isotopes of Ti.

Figure 4.4.3. Typical ion energy distribution function of Ar and Ti ions in an inductively coupled RF amplified magnetron discharge conditions as in Figure 4.4.2 - RF power 250 W, DC power 200 W, Ar pressure 30 mTorr.

Figure 4.4.4. Magnetron target current increases with increasing RF coil power.

Figure 4.4.5. Magnetron target voltage decreases with increasing RF coil power

Figure 4.4.6. Optical emission signals as a function of RF Coil Power. 100 W DC, 10 mTorr.

Figure 4.4.7. Dependence of Ti ion emission on Ar* metastable emission.

Figure 4.4.8. Ion Energy Distribution for Ar Ions at Varying RF Coil Power at DC power 100 W, and Ar pressure of 10 mTorr

Figure 4.4.9. Dependence of the ion energy distribution function on the Ar pressure.

Figure 4.4.10. Ion energy distribution function of Ar⁺ measured when the RF coil operated as a sole plasma generator

Figure 4.4.11. Overall appearance of the water cooled RF coil and feedthrough installed in the Hauzer HTC 1000/ABS™ coating machine

Figure 4.4.12. Water cooled 2-pin power feedthrough with coaxial connector and one half of the screening aluminium box.

Figure 4.4.13. Lower insulated support of the RF coil in the chamber.

Figure 4.4.14. Comparison of the Optical Emission of RF coil enhanced and conventional magnetron sputtering

Figure 4.4.15. Ion saturation current density as a function of applied RF power.

Figure 4.4.16. Comparison of the ion saturation current density in RF enhanced and conventional magnetron sputtering

Figure 4.4.17. Ion saturation current density as a function of Ar gas pressure. RF power = 500 W

Figure 4.4.18. Forward, reflected and effective rf power delivered to the coil as a function of Ar gas pressure

Table 4.1.1. Charge state distributions measured in the MEVVA random arc source for different cathode materials. The states marked in *italics* could be observed by the present OES setup.

Table 4.1.2 Plasma properties and ion flux at a distance of 25 cm from the source.

Table 4.1.3. Ionisation potentials and energy defect after charge exchange

Table 4.1.4. Initial kinetic energy (eV) required to compensate for the energy deficiency in a charge exchange reaction

Table 4.2.1. Properties of selected HIPIMS target materials

Table 4.3.1 Mechanical properties of a CrN film deposited by the ABS technology at a Ar:N₂ partial pressure ratio $P_{Ar}:P_{N_2} = 1:1$

Table 4.3.2. Residual stress and selected mechanical properties of HIPIMS deposited CrN films.

1. Introduction

Background

The development of coating systems based on physical vapour deposition (PVD) processes has enjoyed a boost in the last 20 years with the introduction of ceramic protective coatings such as oxides and nitrides of the transition elements. These thin films have been implemented in a broad range of applications in the machining, automotive, textile, petrochemical, decorative, etc. industries with a total turnover of billions of pounds. The success of thin coatings is due to the wide range of properties, such as high hardness, low friction coefficients, and resistance to wear, corrosion, oxidation, and a variety of colours that are possible to achieve by variations in the chemical composition and microstructure. Evolution of new coatings has been strongly related to developments in the understanding of, specifically, plasma assisted PVD processes, and the improvement of PVD technology and high vacuum technology in general.

For example, the invention of the magnetron sputtering deposition technique enabled complex metallic (TiAl, TiAlY [1]) and even ceramic (Al_2O_3) systems to be vaporised in a reactive gas (N_2 , O_2 , ...) atmosphere and the production of, e.g. the third generation nitride – TiAlCrYN [2] – with exceptional performance in metal cutting operations.

Studies of ion assisted film growth showed the dramatic influence of the ion energy and the ion-to-neutral ratio in the deposition flux on the microstructure of thin films. The control over these parameters has been enabled by further process development and the introduction of the unbalanced magnetron (UBM) [3]. UBMs use a magnetic field with a complex shape which simultaneously confines the plasma near the target surface, in order to increase the sputtering rates, and creates a magnetic path along which the dense plasma can flow out and reach long distances from the target, where the substrates are located.

Further enhancements of PVD coating deposition were brought about with the combination of several unbalanced magnetrons in a closed-loop magnetic field configuration [4, 5, 6] with a dual purpose: to enhance the plasma density near the substrates by reducing losses of plasma to the chamber walls and to allow different target materials to be sputtered simultaneously. The enhanced plasma density has been found to influence the microstructure of the coatings deposited by this method [7, 40].

The combination of different magnetron target materials enabled the commercialisation of high hardness nanoscale multilayered coatings with a ‘superlattice’ structure, consisting of different layers of ceramics in a common atomic lattice e.g. CrN/NbN, TiAlN/VN, etc. [176].

The superlattice columnar coating structure has a number of advantages in comparison to single layer columnar coatings. For example, the number of voids is decreased, healing of large scale growth defects is faster, and the wear mechanism are more favourable. The forced growth of the two different nanolayers constituting the superlattice structure into an atomic lattice, which does not match exactly either of the two, causes a high residual stress to be developed. The advantage of the high stress is that the superior properties of the superlattice coatings are combined with a high hardness [8], which can exceed the hardness of the constituent layers.

However, the adhesion to the substrate of superlattice coatings whose residual stresses can reach as much as 16 GPa is a critical issue. An elegant way of improving the adhesion to steel substrates is to promote localised epitaxial growth of the nitride films. The enhancement of the overall adhesion of the coatings to substrates influences strongly the performance in metal cutting applications for example [9], [10]. Localised epitaxy has been achieved by modifying the coating deposition process to include a pre-treatment stage during which the substrates are irradiated with a highly energetic (> 1 keV) flux of metal ions that penetrates the steel to a short range and induces lattice deformation and recrystallisation of the material. For steel grains with specific orientation the deformation helps to achieve matching between the lattice of the substrate and the nitride. Subsequently deposited nitride film can grow epitaxially on these grains thus potentially increasing the adhesion to the extremely high levels of the ionic bond.

The investigations presented in this thesis are based largely on the embodiment of this knowledge in the form of the commercially exploited Arc Bond Sputtering (ABS) technique [6]. The ABS technology combines steered cathodic arc and unbalanced magnetron deposition technology in order to produce hard, wear, oxidation and corrosion resistant coatings with an excellent adhesion. A typical ABS coating deposition process is initiated with an adhesion-enhancing pretreatment step during which substrates are immersed in an arc discharge plasma and bombarded by multiply charged metal ions (e.g. Cr, Nb, etc.) with energies acquired due to a high substrate bias voltage (-1200 V). Subsequently, nitride coatings are deposited by reactive UBM

sputtering of metallic targets, typically in N₂ atmosphere. The unique design of the ABS cathodes allows the magnetic field to be adjusted so that the same cathodes can be used during both the pretreatment and the coating deposition stages. Furthermore, operating as many as four magnetrons simultaneously and moving the substrates so that they collect a deposition flux from the different cathodes allows the deposition of nanoscale multilayer coatings.

In a successful ABS deposition process, it is crucial to produce highly charged metal ions during the pre-treatment stage and increase the ion-to-neutral ratio during the deposition stage. As outlined above the first stage contributes to an enhanced adhesion. The second stage allows a greater flexibility in the choice of deposition materials as well as the benefit of surfaces with low roughness.

A distinct drawback of the ABS technique is the deposition of macroparticles of size in the range of a few hundred nanometres created during the arc discharge phase. The size of the macroparticles (ranging from 100-5000 nm [11]) is very large compared to the typical surface roughness of the substrates, and contributes to greatly enhanced shadowing effects during subsequent film growth and the development of macroscopic defects exceeding the size of the seed by an order of magnitude [12] reaching several micrometres above the substrate [13]. These growth defects are known to compromise the wear [14], oxidation [15] and corrosion [16] resistant properties of the coatings in metal cutting applications.

The removal of macroparticles from arc discharges is typically performed by curved magnetic duct or electrostatic 'venetian blind' filters that separate neutral particles from the ion flux [67, 68]. However, the efficiency of these processes rarely exceeds 25% and new methods producing ionised metal at high rates are of strong interest to both the research and commercial community.

Present Work

A substantial part of the present thesis is dedicated to the diagnostics and development of plasma sources alternative to the arc that are capable of generating high densities of metal ions without macroparticles. When incorporated in the ABS process such a source would replace the arc discharge and therefore dramatically enhance the performance of the deposited hard coatings by improving their integrity. One of the main results of this work is the characterisation, development and utilisation of a novel

high power (im)pulsed magnetron sputtering (HIPIMS) technique as a PVD method suitable for substrate pretreatment as well as coating deposition.

The investigations presented in this thesis are based on the equipment available to the Surface Engineering Research Group at Sheffield Hallam University incorporating the ABS process on an industrial scale in a commercially available Hauzer HTC 1000/ABS coating machine. This is equipped with four rectangular cathodes (600×200 mm) that can be operated in steered arc or closed field UBM mode simply by automatic modification of the magnetic field [6].

The PhD project was initiated with studies of the arc discharge plasma, which led to the development of an improved etching stage. It is shown that the new etching procedure derived from the plasma diagnostic results improves the adhesion of coatings to the substrate by increasing the etching/cleaning rates and enhancing the metal ion implantation profile [17].

The first attempt to produce a source with a high density of ionised metal vapour was based on magnetron sputtering with additional ionisation by a radio frequency powered coil. This approach was investigated in laboratory conditions and a working scaled up model was designed, manufactured, installed and tested in the industrially sized Hauzer HTC 1000/ABS coater.

The second attempt investigated the HIPIMS technique developed in 1995 by Mozgrin et al. [27] and Kouznetsov et al [21], [22]. The plasma composition produced in HIPIMS was characterised in detail for the first time [23], [24]. The investigations in this thesis present evidence of highly charged metal ions for the first time in these discharges [23]. The potential of the HIPIMS technique to influence the interface and improve the adhesion between hard coatings and metallic substrates has been demonstrated for the first time in this thesis. Potential commercial applications of this pretreatment method have been described in a patent application [25]. Finally, the first hard CrN coatings deposited by HIPIMS were produced and analysed, showing a superb corrosion and wear resistant behaviour [26]. The plasma characterisation and the hard coating investigations have shown the potential of the HIPIMS method as a new and powerful PVD tool.

The structure of the thesis is organised in separate Chapters. Chapter 2 gives an overview of the state of the art in the field of thin film growth, plasma sources, and plasma diagnostic techniques. Chapter 3 describes the experimental apparatus used during the PhD project as well as measurement and analysis methods used to obtain and

interpret information. Chapter 4 contains the results from the relevant experiments and gives information necessary for the validation of the thesis. Finally, Chapter 5 contains the more important conclusions from the present work as well as an indication of some of the interesting problems requiring future investigations. A list of all references can be found in Chapter 6.

The experimental results and discussions are separated in four sections of Chapter 4 as follows.

Chapter 4.1 describes the development of a novel pre-treatment stage [17] whereby the incorporation of Cr metal ions into steel substrates is maximised and the adhesion of coatings improved. Plasma diagnostic studies of arc discharges in the presence of gas have indicated several important interactions that occur between metal ions and gas atoms that are characteristic of the process. High gas pressures lead to an increased scattering of metal ions. At the same time, gas atoms are ionised more readily thus increasing the ion flux to the substrates and contributing to a more efficient etching process. However, the number of highly charged metal ions can decrease significantly due to charge exchange collisions with gas atoms [18], whereby an electron is transferred from the neutral particle to the ion. Plasma diagnostic studies led to the realisation that splitting the pretreatment phase into stages with different operating conditions could make optimal use of the plasma conditions described above. The novel etching treatment combined a fast etching pre-treatment at high gas pressures followed by a pure metal ion bombardment at low gas pressure. The new etching technique is now being employed in commercial coating deposition runs.

The investigations presented in Chapters 4.2 and 4.3 describe the novel HIPIMS plasma source [21, 27].

Chapter 4.2 is dedicated to the study of plasma conditions in HIPIMS. This plasma source operates at typical peak-power-densities of 3000 Wcm^{-2} (two orders of magnitude higher than conventional UBM sputtering) dissipated in pulses with duration $100 \mu\text{s}$. Plasma diagnostic characterisation of the discharge showed a high plasma density and the presence of up to 2-fold ionised metal ions for Cr and Ti. The time evolution of different species during the pulse duration showed a separation in time between gas and metal ions [23]. The conditions of glow-to-arc transition as a function of time and target power are discussed in detail [24].

Chapter 4.3 is focused on the deposition of CrN films by UBM sputtering and HIPIMS using Ar as a sputtering gas and N_2 as the reactive gas. CrN deposited by

UBM sputtering is a widely researched material [28], which is known to have a peak Knoop hardness of approximately $HK_{0.025} = 2200$. In this thesis it was attempted to increase the hardness to values of $HK_{0.025} = 3000$ of CrN films by increasing the lattice strains induced during the growth. A high-energy ion bombardment was used and, in order to compensate for the preferential sputtering of N_2 , high nitrogen partial pressure was used [29, 30]. CrN films were deposited by HIPIMS for the first time. The microstructure observed in transmission electron microscopy cross sections was columnar and highly dense. The wear and corrosion resistance as well as the adhesion of the coatings was excellent. [26]

Chapter 4.4 of this thesis is dedicated to the diagnostics and industrial upscaling of a high ionisation density plasma source based on an inductively coupled radio frequency (RF) discharge [19]. The plasma source consisted of an unbalanced magnetron and a RF-powered concentric antenna that induced ionisation-enhancing currents in the plasma. The operation is analogous to a transformer in which the RF coil acts as the primary winding, and the plasma as the secondary winding [20]. Plasma diagnostic techniques were used to characterise the discharge parameters, plasma composition and ion energies in a laboratory-sized set up. An industrially sized RF coil was designed, constructed, and installed in the Hauzer ABS coater. Plasma diagnostic results showed that highly excited plasma with elevated density could be produced. Several applications were indicated.

2. Literature Review

2.1. Plasma-Surface Interactions During Film Growth

Since the discovery of sputtering by Sir William R. Grove in 1852 [31], physical vapour deposition (PVD) and thin films have found a remarkable range of applications. PVD methods, and in particular those enhanced by plasmas, are among the most versatile, economical and environmentally friendly. The diversity of thin film hardness, wear behaviour, electrical and thermal conductivity, colour, transparency, etc. that can be obtained by PVD methods is extraordinary. This diversity is largely possible because the microstructure, density, grain size, surface morphology, and chemical composition can be varied almost without bounds by varying the deposition temperature, the properties of the plasma and the nature of the interactions of the plasma with the growing film. Historically, the effect of substrate temperature was discovered first, revealing that, depending on the adatom mobility, PVD grown films can exhibit a range of microstructures. In further developments, extensive literature has been published establishing two properties of the deposition flux in plasma assisted (PAPVD) processes, which are crucial in determining the film microstructure:

- a) Energy of ion bombardment
- b) Ion to neutral ratio

2.1.1. Thin Film Microstructure Models

The microstructure of thin films deposited by PVD methods is usually columnar. The density and size of columns depends strongly on the energy, mass, flux and angle of incidence of the bombarding particles. Also of importance is the absorption and deposition of particles with thermal energy such as reactive gases and metal atoms on the surface.

Movchan and Demchishin [32] reported first on the correlation of the microstructure of coatings produced by thermal evaporation with the homologous temperature given as the ratio T_s/T_m (T_s - substrate temperature, T_m - melting point of the evaporated material). They found that depending on T_s/T_m the microstructure can be described by three zones (see Figure 2.1), each with its individual morphological characteristics and physical properties. Zone 1 occurring at low deposition temperatures $T_s/T_m < 0.3$ was columnar consisting of tapered units separated by voided boundaries.

The zone 2 structure ($0.3 < T_s/T_m < 0.5$) had columnar grains defined by metallurgical grain boundaries formed under conditions of surface diffusion. Finally the zone 3 microstructure consisted of equiaxed grains recrystallised grains affected strongly by bulk diffusion.

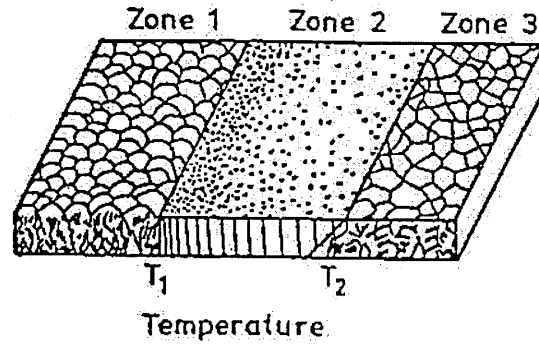


Figure 2.1. Zone model proposed by Movchan and Demchishin [32]. For metals $T_1 = 0.3 T_m$; $T_2 = 0.45 T_m$

For example in practice, in equilibrium processes such as chemical vapour deposition, a typical temperature for TiN deposition is 1000°C , while the melting point of TiN is $T_{m\text{TiN}} = 3000^\circ\text{C}$. Thus the homologous temperature is 0.3 and therefore very near the temperature T_1 marked on the diagram in Figure 2.1 signifying the transition from voided to dense columnar structures.

Thornton modified this model for the sputter deposition of coatings [33], taking into account the higher energy of sputtered atoms (5-25 eV as opposed to evaporation with 0.1 eV), and the possible loss of energy due to scattering in the gas phase. The zones defined by the model are determined not only by the temperature but also the total gas pressure which is an important parameter affecting the sputtering processes as well as the transport of particles from the sputtered target to the substrates. The same zones were observed as by Movchan and Demchishin, however a new transition zone T was found occurring between zone 1 and 2. Zone T is characterised with poorly defined densely packed fibrous grains. Figure 2.2 shows Zone 1, Zone T, Zone 2 and Zone 3 structures.

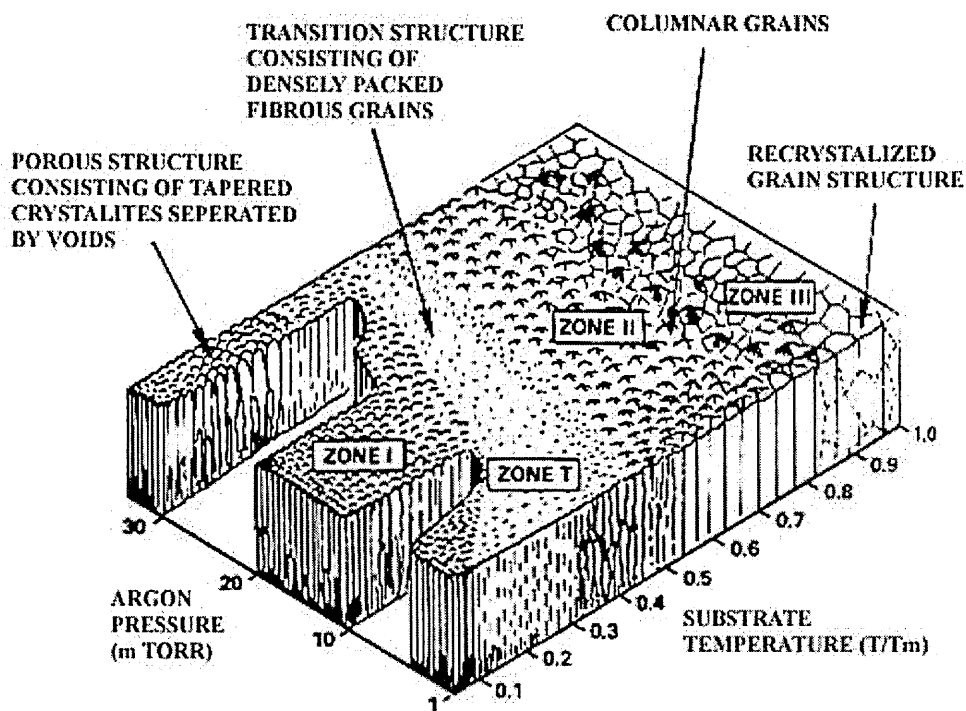


Figure 2.2. Thornton zone model

Sputtering is usually performed using a glow discharge where a dense plasma consisting of electrons and ions is produced. Mattox et al. found that the energy of interaction of the plasma ions with a sputter-deposited thin film determined the density of the film microstructure [34]. This led to a further modification of the empirical models proposed by Messier, Giri and Roy [35], who included bombardment effects in addition to the thermal mobility effects on the morphology of the coating during ion assisted deposition. The model developed by Messier et al., indicated that the dense and

smooth transition microstructure Zone T can be produced at decreased homologous temperatures when ion bombardment with suitable energy is used.

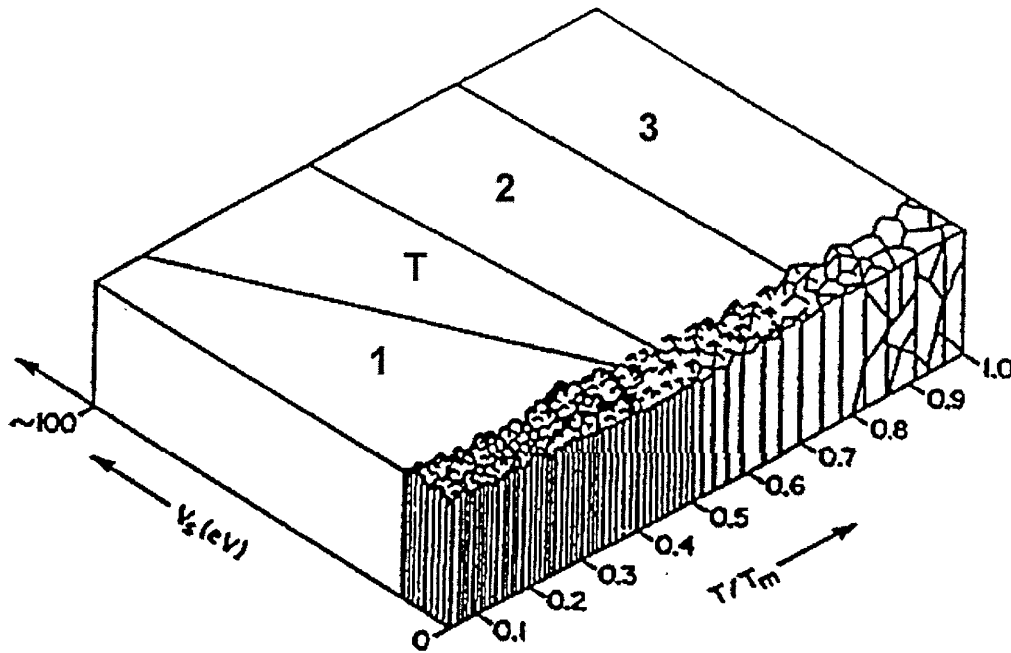


Figure 2.3. Messier model of PVD film microstructure

The increase in bombardment energy however has an additional influence on film properties. For example high bias voltages lead to generation of lattice defects in the growing film. For TiN films a critical bias of -80 V has been found where the defect density observed in TEM cross sections is considerable [39]. As a result of these interactions the residual stress in the films can increase significantly up to values of -10 GPa. High energy Ar gas ions have been found to get trapped in the growing films and form gas bubbles due to irradiation enhanced diffusion. Recoil implantation of metal adatoms due to high energy gas ion bombardment can lead to intermixing, especially important in superlattice nanometre-size layer structures.

Recently a model taking into account the influence of ion-to-neutral ratio on the microstructure has been developed by Kelly and Arnell [7] to describe unbalanced magnetron (UBM) sputtering in a closed field configuration (see Figure 3.1). In this arrangement the plasma is confined in the chamber by magnetic fields connecting the magnetrons. This contributes to substantial decrease of plasma losses to the chamber walls and subsequently to an enhanced ion-to-neutral ratio in the particle flux to the substrates. It was shown that a modified coating growth mode occurred whereby zones 2 and 3 defined by the previous models were brought to lower bias voltages and temperatures. The novel structure model included three dimensions taking into account

the homologous temperature T_s/T_m , the bias voltage on the substrates and the ion to neutral ratio J_i/J_n . Figure 2.4 shows a schematic of the closed field unbalanced magnetron sputtering model.

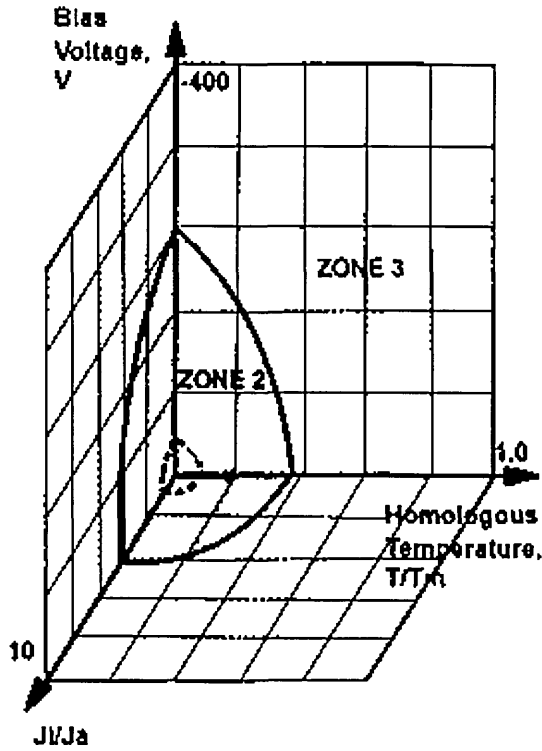


Figure 2.4. Structure zone model relating to closed field UBM sputtering configuration after Kelly and Arnell [7].

2.1.2. Ion to Neutral Ratio and Energy of Ion Bombardment

It has been demonstrated in a number of experiments on ion-assisted film growth that the number density of voids and pores decreases dramatically with increasing ion energy and/or flux. The effectiveness of ion irradiation in decreasing film porosity was demonstrated, e.g. by Hakansson et al [36] for TiAlN films grown by reactive magnetron sputtering. With no applied negative substrate bias U_b the films exhibited a columnar-type of microstructure with high void densities. The void density decreased sharply for $U_b > -100$ V upto $U_b > -120$ V, when no voids could be observed. In addition to an increase in film density at low substrate temperature (T_s), ion irradiation disrupted the columnar structure and increased the number density of defects.

Müller [37] employed molecular dynamics calculations for the simulation of the effect of ion bombardment during growth. In the model, Ni is thermally evaporated (energy on the order of 0.03 eV) (see Figure 2.5) and bombarded with 50 eV Ar ions at an angle of incidence of $\alpha = 30^\circ$. Ion to neutral flux ratios J_i/J_n of (b) $J_i/J_n = 0.04$ and (c) $J_i/J_n = 0.16$ were modelled. The computer simulation shows that the packing density of the film is strongly related to the energy per deposited atom. The packing density increased towards bulk values with increasing ion energy E_i and/or ion-to-neutral vapour flux ratio J_i/J_n . For example, in low-Ts growth simulations, the films in the Monte Carlo simulations had porous structures in the absence of ion bombardment, whereas if ion irradiation effects were taken into account, quite different growth morphologies were obtained. The film density was observed to increase almost linearly with J_i/J_n . The calculations also predicted that there should be an optimum ion energy E_i^* for densification. The optimisation resulted from the fact that for $E_i > E_i^*$ an increasing fraction of the ion energy is lost deeper in the lattice leaving vacancies which cannot be filled by arriving vapour species.

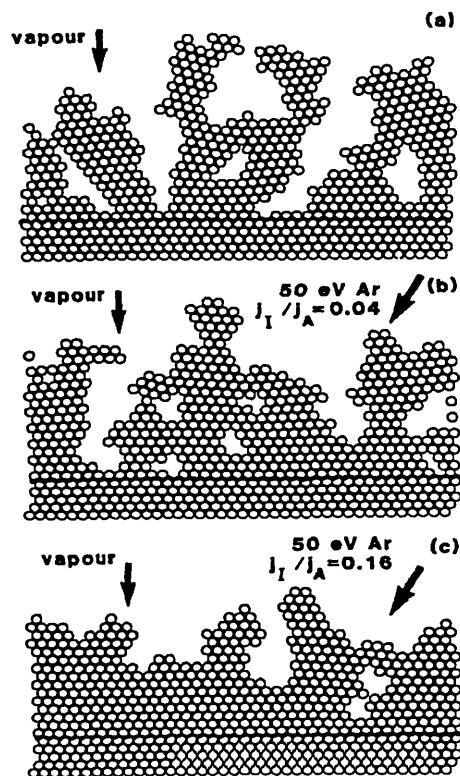


Figure 2.5. Computer simulations of film growth under varying ion-to-neutral ratio in the deposition flux after Müller [37].

At elevated T_s , low-energy ion irradiation can also reduce residual defect densities in epitaxial films [38]. Direct evidence of this is given by Petrov et al [39] and Hultman et al [40] for N_2^+ ion bombardment on growing TiN(100) films.

Experimental evidence for Müllers modelling results in general and for the densification of alumina films in particular is given by Williams et al [41]. The film packing density is related to the refractive index and was increased from 80% to 92% by increasing the flux of O_2^+ ions at 300 eV from 0 to $100 \mu A cm^{-2}$, as can be seen in Figure 2.6. The density was correlated to the measured refractive index by Maxwell-Garnett [42], based on the assumption the film density is reduced by air or oxygen inclusions.

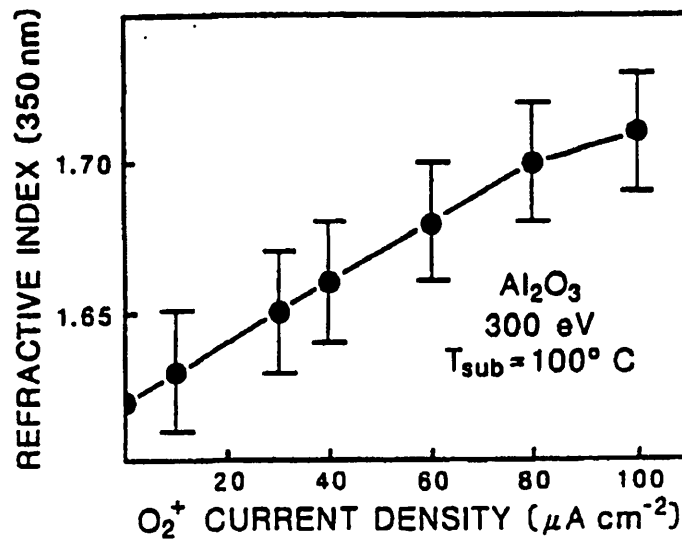


Figure 2.6. Refractive index versus O_2^+ ion current density of alumina films produced at $T < 150^\circ C$ after Williams et al [41]

Similarly, film densification can also be achieved by employing energetic neutrals. As already discussed in the Thornton diagram, the kinetic energy component of the neutral flux is a function of the total pressure. If the sputtered flux is not fully thermalised (loss of kinetic energy due to scattering collisions [43]), the kinetic energy of the neutral flux is a function of the cathode potential. The higher the cathode power the larger the kinetic energy component of the neutral flux. Shih and Dove [44] found that the refractive index of R.F. sputtered alumina films is high, if a high power is supplied to the magnetron. The results are shown in Figure 2.7, where the target power is plotted versus the refractive index.

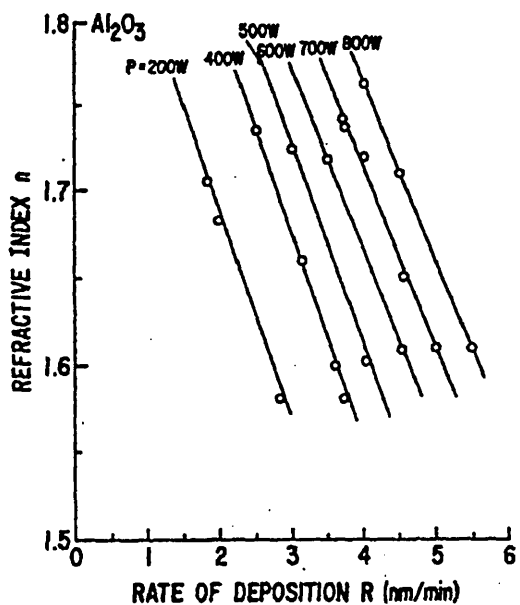


Figure 2.7. Refractive index versus deposition rate at different target power settings taken from Shih and Dove [44].

2.1.3. Ions Impinging at a Substrate at High Energy (eg. > 1000 eV)

When ions bombard a substrate with energy exceeding three times the bonding energy of the substrate material sputtering can occur. For bombardment energies of approximately 5 keV the sputtering yield of most materials reaches saturation [45], which is attributed to a balance between sputtering and implantation. The depth of implantation depends on the energy as well as the dose of ions. Hubler et al [46] have shown that the actual projected range of nitrogen ions into iron increases linearly with ion energy. The actual implantation profile however is also influenced by the ion dose. Computer simulations [46] have shown that as the ion dose is increased, the amount of eroded material is increased and the effective depth of implantation is decreased because the surface moves closer to the maximum of ion implantation.

In PVD processes, implantation of Cr and Nb ions was shown to improve the adhesion of coatings [47] to the substrates by promoting local epitaxial growth [10]. Schönjahn et al [16] found that Nb ions of intermediate energy are implanted to a shallow depth and form a high density amorphised/fine crystalline layer preventing corrosion.

Brown et al [48] have studied the composition of arc discharges systematically showing multiply ionised species for the majority of the elements in the periodic table.

The same group has used an arc discharge implantation in several applications [49], including introducing gradients in insulators, etc.

In summary, the interactions of plasma with the substrates and in particular with the growing film in PVD have a strong influence on the microstructure and mechanical behaviour of the film itself as well as on the adhesion of the film to the substrate. The main goal of the present thesis is to develop PVD process technology providing a high ion-to-neutral ratio in the deposition flux and high degree of ionisation of the sputtered metal in order to improve the control over the plasma-surface interactions.

2.2. PVD Plasma Sources

In plasma-assisted PVD processes, plasma glow- or arc-discharges are used to vaporise a target mounted on the cathode. In glow discharges, the target is sputtered due to energetic gas ion bombardment. Arc discharges are characterised by a higher current density causing heating and sublimation of the cathode material. All discharges can be classified according to their current density. Figure 2.8. shows the voltage and current, J_t , for the different types of discharges. At currents $J_t < 10^{-5} \text{ Acm}^{-2}$ the discharge is not self-sustained, i.e. requires the constant introduction of charged particles from the cathode or anode. For values $10^{-5} < J_t < 10^{-2} \text{ Acm}^{-2}$ the discharge is self sustained by electron ionisation avalanches which are maintained by the electric field on the cathode. This region is called the normal glow and is characterised by the fact that the discharge area increases as a function of J_t . When the discharge area equalises with the cathode area, J_t can be increased further by additional ionisation, e.g. by magnetic and electric field traps, and the discharge enters the abnormal glow regime, typical of magnetron sputtering devices. At currents above 10^{-1} Acm^{-2} , a transition from a distributed glow discharge to a highly localised arc discharge occurs. The transition is characterised by a considerable drop in discharge voltage and is accompanied by a strong reduction in the physical dimensions of the plasma.

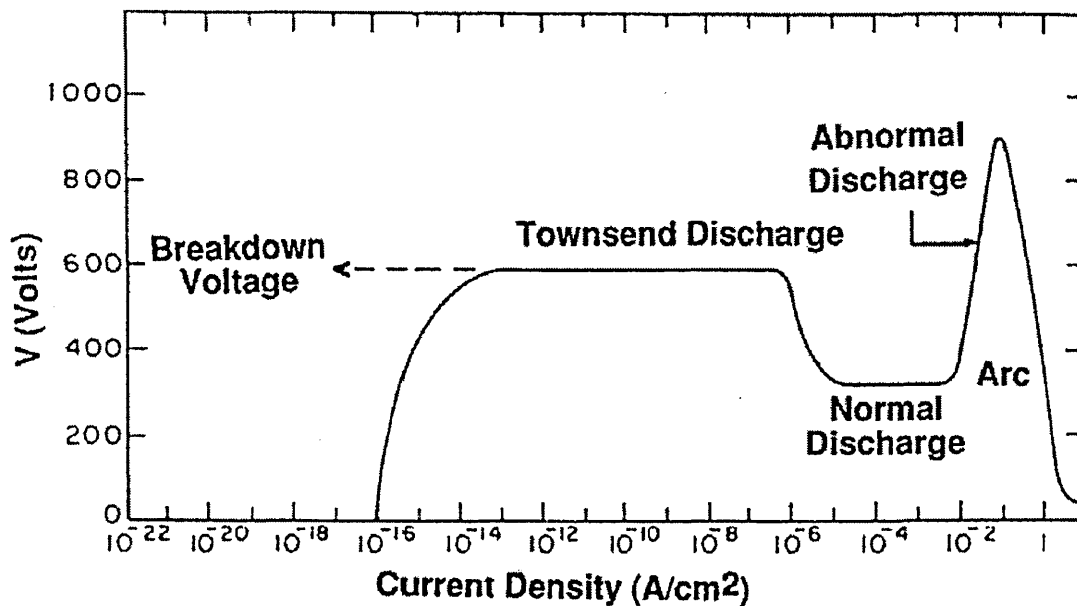


Figure 2.8. The classification of plasma discharges according to their current density. Figure adopted from Lieberman et al [52]

The remainder of this section 2.2 will give a more detailed description of selected plasma discharges used in PVD.

2.2.1. Cathodic Arc Evaporation

As mentioned in the previous paragraph, typical arc discharge current densities are in the high extreme ($> 10 \text{ Acm}^{-2}$) of the discharge diagram (see Figure 2.8). The discharge voltage varies between 20 and 60 V, depending on the cathode material [53], and the magnetic field strength [54]. Arc evaporation discharges consist of one or a few dense spots of plasma (cathode spots) with a size of a few micrometres [50] that travel in random trajectories on the cathode surface. The localised current density in arc spots is typically in the range 10^{12} Acm^{-2} and the plasma density 10^{20} cm^{-3} [50], containing highly charged metal ions [48, 51].

Cathode spots are initiated at microprotrusions (tips) on the surface of the target. The potential applied to the cathode can be enhanced by up to 5 orders of magnitude due to the sharp geometry of the tips and the electric field can reach values of 10^5 Vm^{-1} . This field is sufficient to eject electrons from the solid surface and if a high enough current is supplied the tip can "explode" (sublime) due to ohmic heating. Temperatures up to 6000 K have been measured in the cathode spot by optical emission spectroscopy [55] and infrared imaging [50]. The electron current and resulting heating are so high that the material in the tip enters a high-density plasma state, which can be approximated to a highly excited metal lattice or a highly compressed gas. The plasma

in the cathode spot is in local thermal equilibrium [117] and the frequency of ionising collisions between electrons and atoms is very high. The metal vapour flux generated in arc discharges can be ionised up to 90% [56] and contains highly charged metal ions [48, 57]. The charge state distribution (CSD) has been measured by Brown [48] for most elements of the periodic table. Anders [51] calculated the CSD functions of all elements in the periodic table based on the Saha equilibrium equation.

The high-density plasma formed in the spot causes the electric field of the cathode to be screened and a potential hump is developed across the spot [55], [58]. The potential difference between the centre of the spot and the bulk plasma was estimated to be of the order of 50 V, causing the ions to accelerate away from the cathode to the corresponding energy. Figure 2.9 shows a schematic of the potential distribution and the structure of the plasma surrounding a cathodic arc spot.

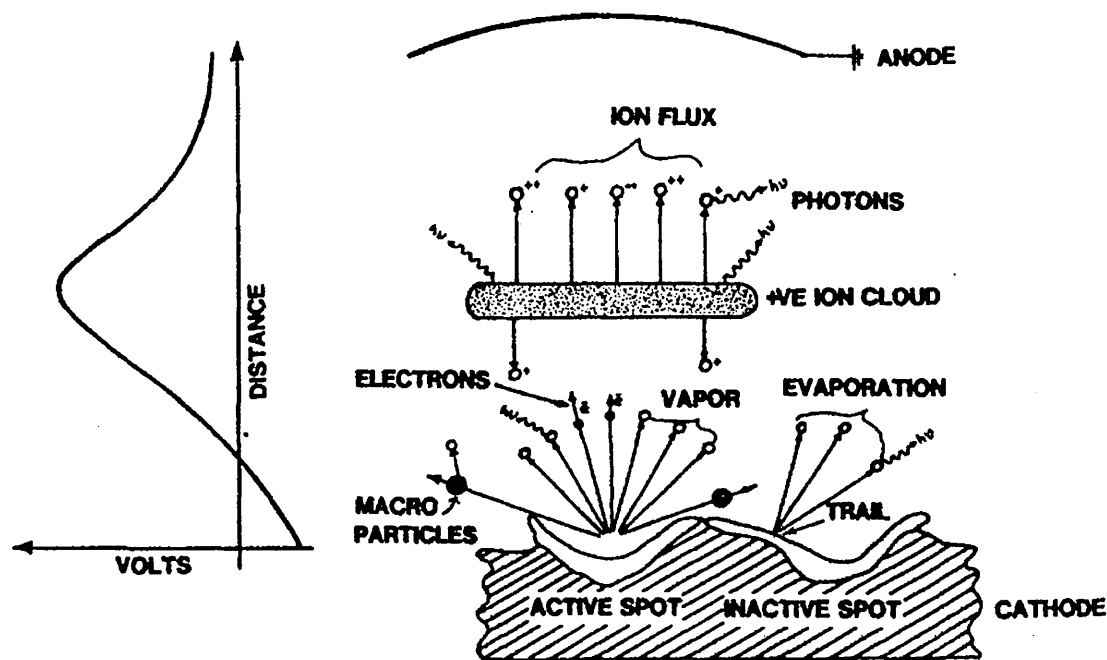


Figure 2.9. Basic arc evaporation processes and potential distribution after Martin et al [55]

In clean vacuum environments, the CSD is established in the vicinity of the spot and remains constant as the plasma expands even at relatively long distances - freezing [59]. However, in many practical systems inert and/or reactive gases are used. OES emission studies by Bergman et al [18], Martin et al [55] and Kuhn et al [157] found that an increase in N_2 gas pressure leads to a decreased optical emission from metal ions and a general shift of the CSD to lower ionisation states. This effect was attributed to

charge exchange collisions of metal ions and gas atoms. Charge exchange reactions have been studied extensively as part of the numerous fusion research programmes in the 50s [60]. A major part of the research is strongly linked to the theoretical modelling of reactions and most experiments are performed with simple atomic systems comprising proton - hydrogen, hydrogen - fully stripped ion, or inert gas - fully stripped ion [61]. In simple terms, during the collision, the atom and ion form a quasi molecule thus sharing energy levels. In cases when a suitable crossing between the levels exists, an electron can move from the vicinity of the atom to the vicinity of the ion. The cross section of this reaction is negligible if the difference in ionisation potentials of the atom and ion is negative.

The combination of high plasma density and highly charged ions deems the arc evaporation technique extremely useful as an etching step prior to coating deposition. Highly charged metal ions are accelerated to energies equal to $Z \cdot V_b$, where Z is the charge, V_b is the substrate bias. Even in treatments at relatively low bias voltages of the order of -1200 V, on steel substrates, Cr ions have been found to penetrate to depths up to 30 nm [17, 25]. The implantation of ions into a substrate gives an opportunity of producing metallic alloys unlimited by thermodynamic criteria. Petrov et al [13] found that the lattice of stainless steel substrates can also be modified by bombardment at 1200 eV of Cr ions generated by an arc discharge. In some grains, the implantation defects induced in the steel lattice increased the lattice parameter to match the lattice of subsequently deposited nitride coatings promoting localised epitaxial growth and enhancing the adhesion of the coatings to the substrate.

Chapter 4.1 of this thesis describes investigations into the interaction of the ion flux generated in arc plasmas with different gas atmospheres and shows its effect on the average charge state and density of the overall ion flux to the substrates. These interactions were shown to be important in influencing the etching and implantation of metal near the substrate surface and therefore the adhesion of films to the substrates. Using the information from plasma diagnostics a new etching method with improved efficiency of etching and implantation was designed and tested.

As mentioned above the temperatures developed in the cathode spot are very high leading to sublimation of the material. However, a substantial portion of the material in the vicinity of the arc spot reaches only a melted state. During the explosive evaporation of the tip, part of the melted material is ejected into the plasma in the chamber in the form of liquid metal droplets. Depending on the initial size and mass of

the droplets they solidify or start to evaporate. Effectively, materials with lower melting points produce smaller droplets due to their faster evaporation [12], but sizes in the range of 50nm - 500 nm have been commonly observed [62]. When arc discharges are used in coating deposition applications, a substantial number of droplets are incorporated in the growing thin films. The size of the droplets is sufficient to cause severe shadowing of the deposition flux and induce large-scale growth defects extending over micrometres [13]. Figure 2.10 shows a schematic of the structure and growth of thin film in the vicinity of a droplet.

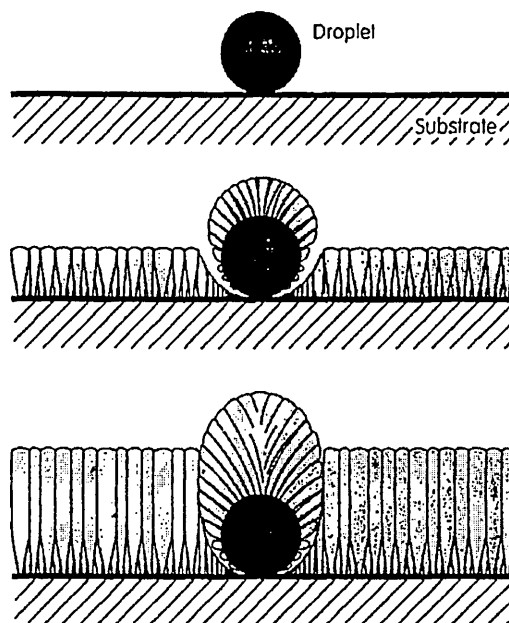


Figure 2.10. Schematic of the deposition of a droplet and the structure of the film established in its vicinity after Petrov et al. [13]

An obvious effect of droplets is the increased porosity of the coating, which can compromise its protection properties. For example, it has been shown that corrosive substances can reach coated substrates through cracks around droplets [63]. Droplet containing coatings are subjected to harsher wear conditions as droplets and the associated growth defects are easily detached from the coating and play a role of third body abrasive particles [106].

In order to minimise the number and size of droplets, steered cathodic arc evaporation has been proposed by Ramalingam [64]. Magnetic fields are used to steer the spot along a known trajectory on the target surface. Figure 2.11 shows the magnet arrangement proposed by Ramalingam.

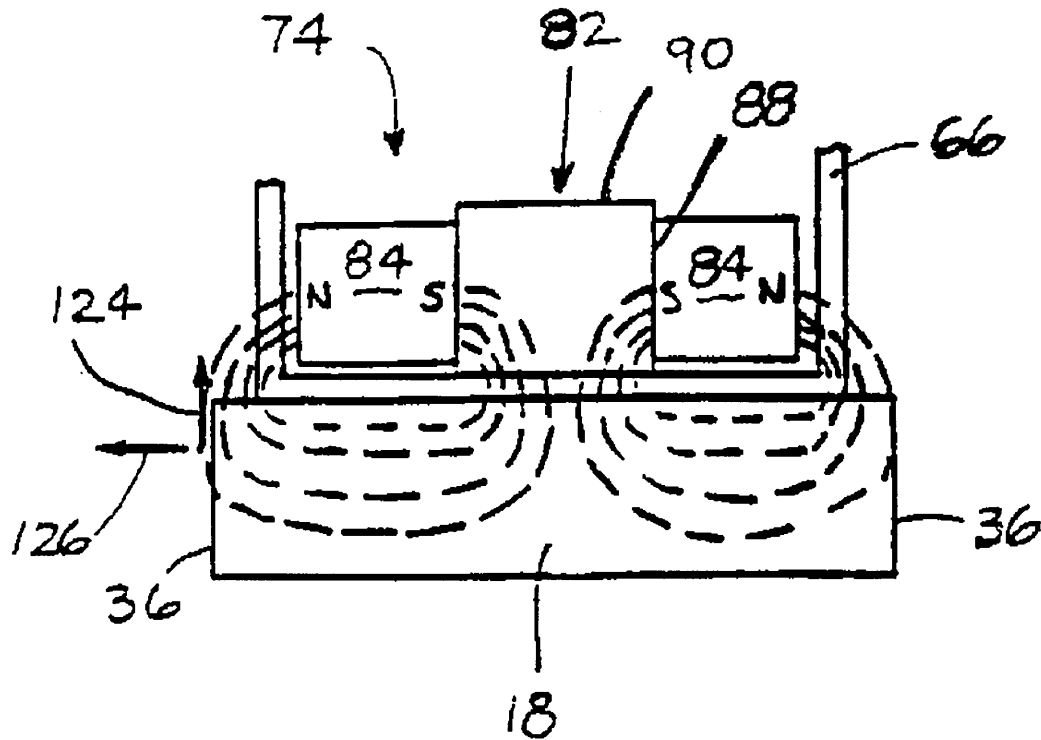


Figure 2.11. Magnetic field arrangement in a steered cathodic arc discharge. 18 - evaporated cathode. 84 - magnets, 82 - magnetically conducting soft iron core. Adapted from Ramalingam [64]

The arc spot motion is opposite to that predicted by Ampere's law and in the direction of the acute angle between the magnetic field lines and the target surface [65]. The gradient in the normal component of the magnetic field ∇B_n determines the degree of confinement of the plasma in the spot [66]. Compared to random arcs where the spot moves randomly on the surface of the target, the steered cathode spot moves at elevated velocities (10 m/s), which contributes to a decreased size of droplets. 90 degree magnetic duct [67] and 'venetian blind' [68] filtering has also been used to physically separate droplets from the deposition flux, however at the cost of severely reducing the latter.

Chapters 4.2 - 4.4 are dedicated to the development of high ionisation PVD plasma sources avoiding droplet generation.

2.2.2. Magnetron Sputtering

Magnetron sputtering is a widely used method for coating deposition suited particularly well to nitrides with complex composition. Sputtering is a collision process whereby ions bombard a solid, causing its atoms to be expelled into free space. The energy of the impinging ions is transferred to atoms from the solid lattice causing collision cascades and displacements. In PVD, glow discharges are used as ion sources. The productivity of the process is determined by the intensity of the ion bombardment flux that can be extracted from the discharge and the sputtering yield of the material, i.e. the number of sputtered atoms per incident ion. The typical cathode voltages used for sputtering are between 300 and 800 V for magnetron sputtering and 1.5-5 kV for diode sputtering. Conventional (diode) glow discharges achieve rather low sputtering rates due to the low current densities - of the order of μAcm^{-2} . In magnetron sputtering, the target current density can be two orders of magnitude higher. The additional ionisation is achieved by a crossed electric and magnetic field, which forms a plasma trap as shown in the schematic in Figure 2.12. Maximum cathode voltages in magnetron sputtering discharges are approximately 750 V limited by the efficiency of the magnetic field trap [69].

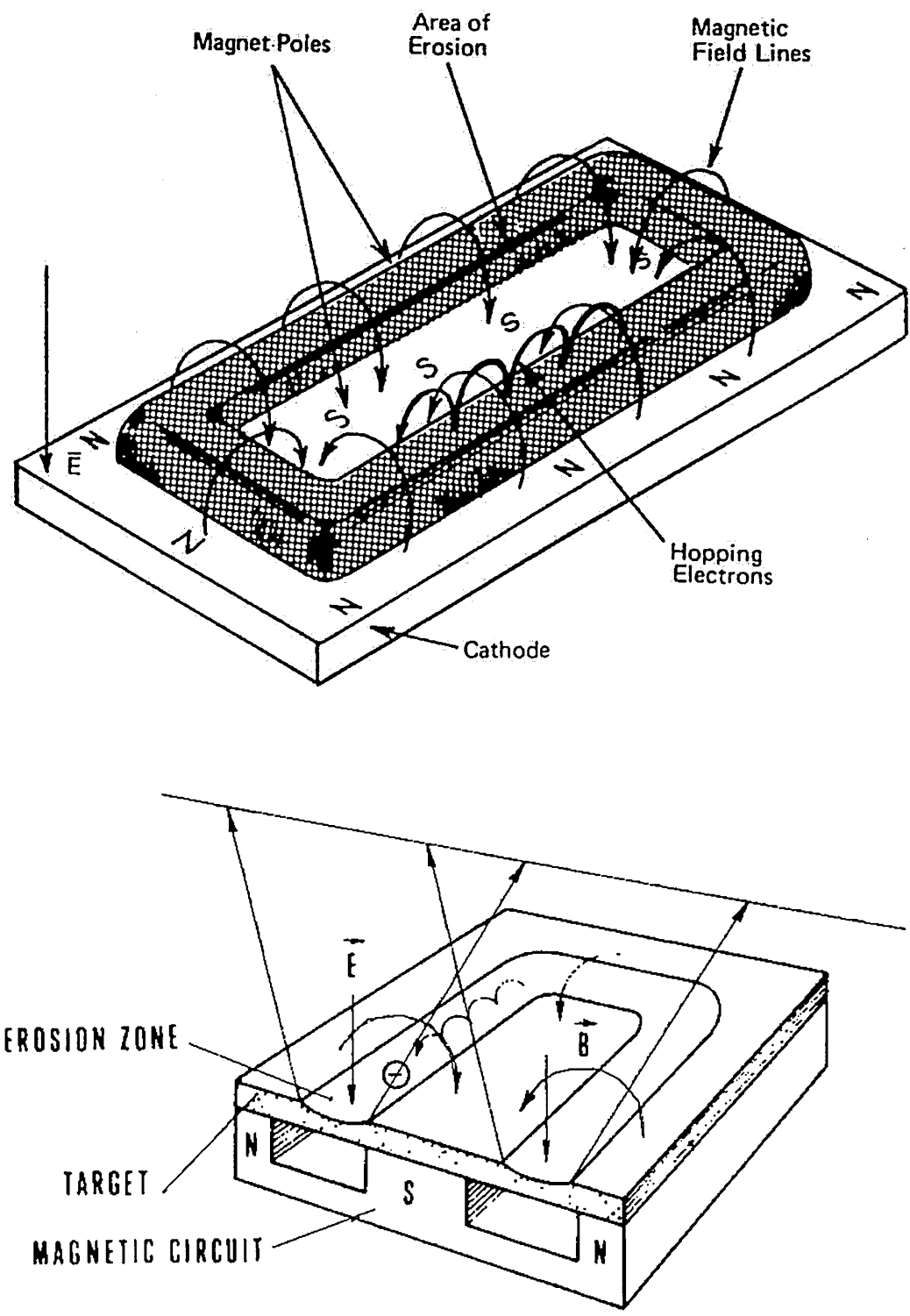


Figure 2.12. Schematics of a planar magnetron illustrating the arrangement of magnets, the electric field and the plasma (shaded region)

Chapter 2 Literature Review

Due to the crossed magnetic and electric field, electrons in the discharge plasma are guided into helical trajectories where the radius of the helix (Larmour radius) is given by the equation: [121]

$$r_L = \frac{m_e V}{B}$$

where r_L is the Larmour radius, m_e is the electron mass, V is the velocity of the electron (due to electric fields), B is the magnetic field strength. The helical shape of the electron trajectories contributes to a high collision probability with gas atoms in the chamber. Residual gas ions are the dominating ion species in magnetron plasmas. In experiments sputtering Ti in Ar/N₂ atmosphere, Petrov et al [70] reported that 94% of the total ionisation is attributed to Ar ions (even when the target becomes completely covered with dielectric TiN layer at high nitrogen pressures - target poisoning regime). Rossnagel et al [71] published a model explaining the dominating collisions and creation paths of all atomic and ionic species produced in a magnetron plasma. The main ionisation and excitation mechanism in magnetron discharges is assumed to be by electron impact. The density of sputtered metal n_m as a function of discharge current Jt is given by the relation $n = Y*Jt$, where Y is the sputtering yield of the target material. The density of the residual gas is strongly depleted (gas rarefaction) when high power levels are used due to gas heating [72]. The model has been verified by measurements of the optical emission from the plasma using a Corona model (described in Section 3.5.1) for the plasma and an electron-ion collision integral to estimate the relationship between the emission intensity and actual density of species [71], [73], [74].

In conventional magnetrons, the magnetic field is equal in the centre and periphery of the target (balanced magnetrons) and while a high plasma density is achieved in the vicinity of the target, at long target-substrate (throw) distances the ion flux is very low. This drawback was tackled by Window et al [3] with the invention of the "unbalanced magnetron". The magnetic field of the unbalanced magnetron is stronger e.g. in the periphery than in the centre. Figure 2.13 shows a finite element calculation of the magnetic field shape of a balanced (a) and unbalanced (b) magnetrons. In the balanced case, the lines far from the target are mainly tangential to the target surface. In contrast, in the unbalanced case the lines are pointed in a direction normal to the target. Electron motion is confined in helical trajectories around the field lines and a crossing from one line to another occurs only due to collisions with atoms or ions. It is clear that in the balanced case an electron has to cross several lines in order to

reach long distances from the target. The unbalanced arrangement breaks some of the loops of magnetic field lines and allows the plasma electrons to follow trajectories normal to the target surface leading to substrates at long distances [75]. The Larmour radius of ions in the typical magnetic and electric fields used in magnetrons are some tens of centimetres [75] i.e. they are practically not affected. However, ions follow the long-range motion of the electrons due to an ambipolar diffusion process [76]. The ion to neutral flux can be increased by a factor of 6 with this arrangement [77]. In the work of Petrov et al [78], the ion to Ti ratio J_i/J_{Ti} was found to be in the range of 4.

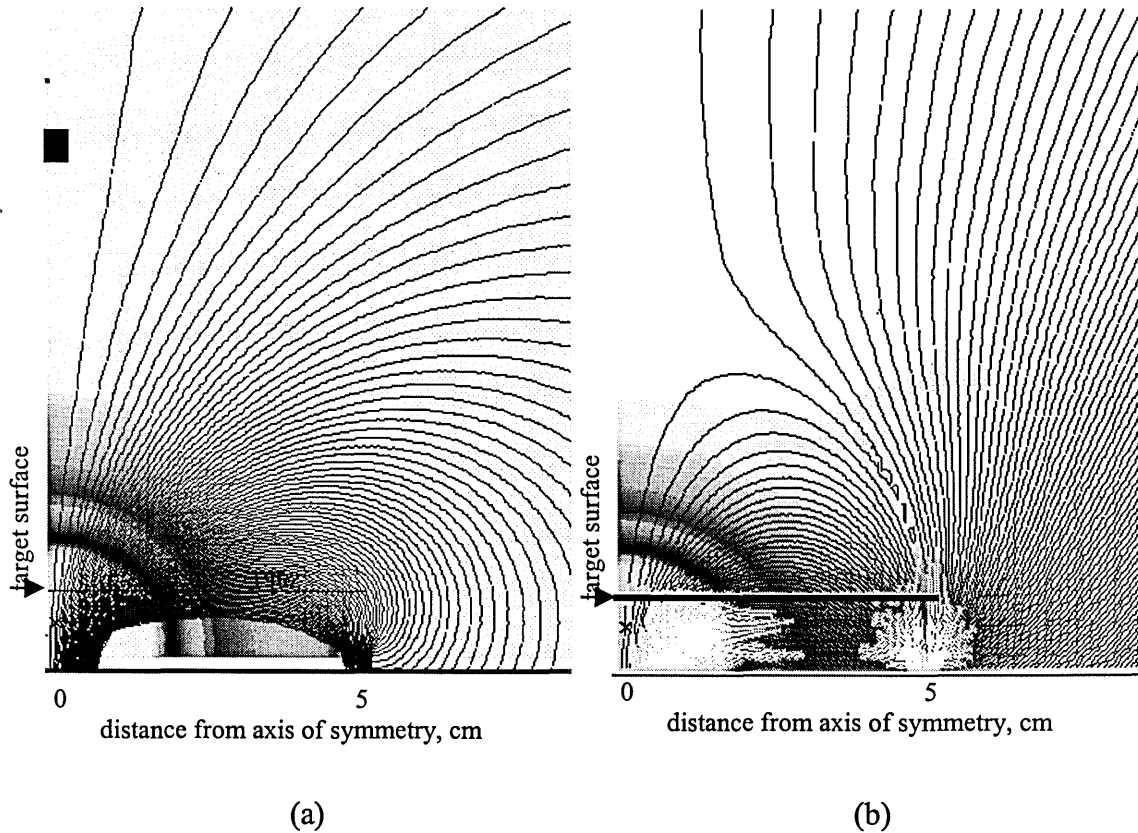


Figure 2.13. Magnetic field lines of (a) balanced and (b) unbalanced circular magnetrons. The false colour represents the strength of the field. Courtesy of HVM Plasma Ltd.

Further increase of ionisation near the substrates is achieved in the ABS machine by an array of four unbalanced magnetrons arranged in a closed field assembly. Magnets of neighbouring magnetrons are installed in an alternating fashion so that the magnetic fields form a connecting loop [4], [5], [6]. As shown in the machine schematic in Figure 3.1 of Chapter 3, the four magnetrons of the ABS machine form a complete loop of magnetic lines encircling the chamber volume. The plasma surrounded by the loop can only drift upwards or downwards but not in the direction of the chamber walls [79]. Shields are placed above and below the substrate table in order

to protect the top and bottom chamber walls from exposure to the plasma. The advantage of the closed loop arrangement is that the plasma is confined in the centre of the chamber significantly enhancing the ion flux to the substrates that are placed there. The introduction and exploitation of this technique even on an industrial scale [6] has enabled the production of thin films with extraordinary chemical composition, microstructure and properties due to the specific plasma environment and cathode arrangement. As mentioned in section 2.1.1, this has triggered the modification also of the microstructure zone model [7].

2.2.3. Magnetron Sputtering with Auxiliary Electron Impact Ionisation

The obvious advantage of preventing plasma losses to the chamber walls by a confining magnetic field has raised considerable interest in the PVD scientific community and has led to the development of alternative methods. In the majority of sputtering systems the chamber walls play the role of the anode of the discharge. This anode is usually large in size and electrons in the plasma diffuse naturally towards the chamber walls where they are recombined. Plasma losses can be reduced substantially in closed magnetic field systems where the diffusion of plasma to the chamber walls is hampered by the geometry of the field lines, however electrons still have a propensity to move towards the chamber walls. An alternative method of reducing plasma losses to the chamber is to practically exclude the chamber walls from the discharge circuit. The Highly Ionized Sputtering (H.I.S.TM) patent by Leyendecker et al. [80] describes a system comprising a magnetron cathode and a defined anode, which are both floated to a positive potential with respect to the chamber walls. In this arrangement, discharge electrons flow predominantly from the cathode to the anode and are repelled by the chamber walls, which are effectively at a negative potential with respect to the plasma. The degree of ionisation of the sputtered metal is claimed to be 50 % while the ion flux at the substrates is claimed to increase by 2 to 8 times compared to normal circuit connection.

2.2.4. RF Coil Enhanced Magnetron Sputtering

As emphasised in section 2.1 the energy of adatoms is a crucial factor in determining the properties of thin films. In practical systems, it is almost impossible to control the energy of neutral atoms, while the ion energy is easily controlled by the bias voltage. Increasing the ionisation of plasma discharges has been a driving force in many a development in PVD plasma sources. An efficient way of energising of plasma electrons and hence enhancing collisional ionisation is to transmit radio frequency (RF) power to the plasma through inductive coupling. Hopwood et al [81] were the first to use an RF antenna coil in conjunction with a magnetron sputtering discharge in order to produce a high degree of sputtered metal ionisation. Figure 2.14 shows a typical setup used by Schneider et al [82] utilising an RF powered coil and a magnetron.

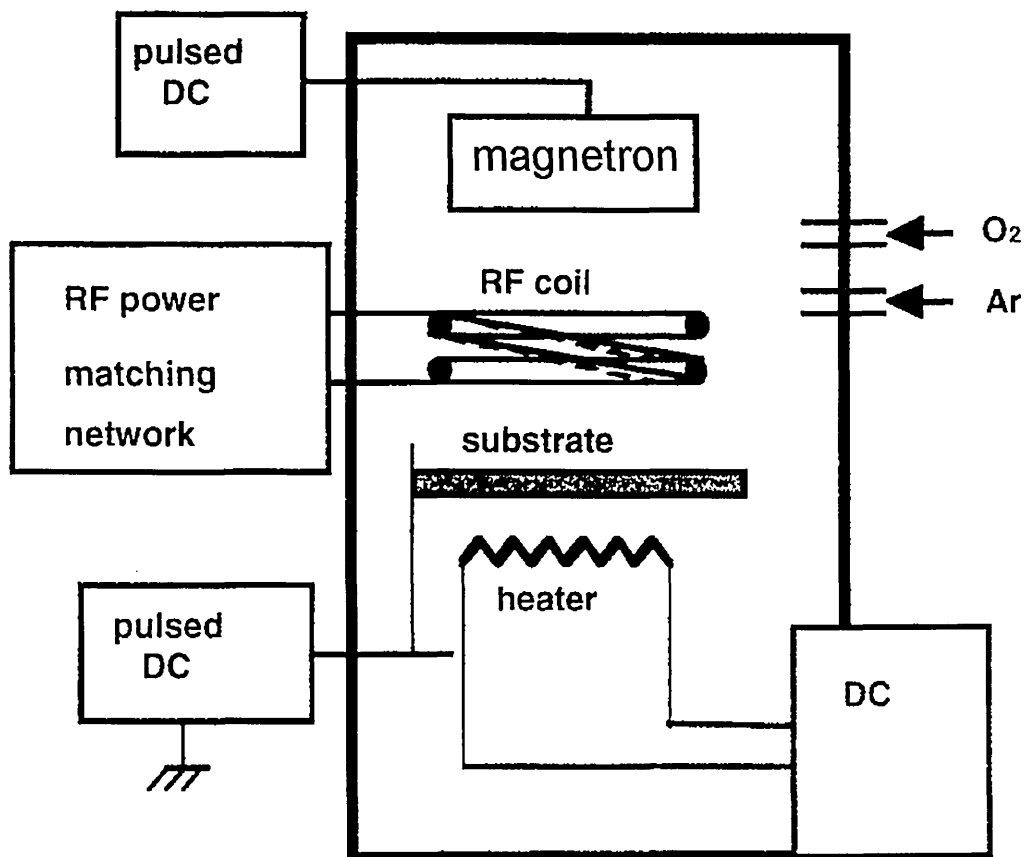


Figure 2.14. RF coil enhanced magnetron sputtering set up, after Schneider et al [82]

The ionisation efficiency in the RF coil enhanced magnetron sputtering discharge is strongly dependent on the gas pressure. The maximum metal (Cu) ionisation of 70% was reported at an Ar gas pressure of 30 mTorr (4 Pa). The magnetron was operated in

ordinary conditions, and the influence of the coil was to increase the plasma conductivity. Mostly singly ionised Ar and metal were found in the discharge. Due to the RF power applied at 13.56 MHz, the plasma sheath around the coil oscillates at a similar frequency. This frequency is specific in that it affects the high mobility electrons while the far heavier ions are only influenced by fields oscillating slower than 100 kHz. As a result, electric fields build up whose net effect is to accelerate both electrons and ions to high energies. The electron energy distribution function shifts to higher energies increasing the ionisation as well as excitation probability in collisions. Emission from the plasma is excited in the overall chamber volume and atoms are pumped to higher states. Hopwood et al [81] investigated the ionisation mechanisms in the RF coil enhanced magnetron plasma. A particularly important path for the ionisation of metal atoms was found to be the Penning ionisation process:



where Me is a metal neutral atom, Ar* is an excited Ar neutral atom, Me+ is a metal ion, e⁻ is the resulting electron and dE is an energy defect.

The Penning process occurs when a gas atom in an excited state collides with a metal atom. Upon interaction, the gas metastable state can decay to a ground state, releasing the excess energy to produce a metal ion. Most excited states have lifetimes that are too short for this process to be significant. However, metastable excited states that are not allowed to decay to a lower atomic state by the selection rules are characterised with a practically infinite lifetime. At the same time in the case of Ar, for example, metastable states are found with energies of 11 eV, which are higher than the ionisation potential of metal ions (about 5 eV for most metals). Penning ionisation is particularly important at high pressures (30 mTorr / 4 Pa) because the collision cross sections for atom-atom collisions are higher than those for electron impact ionisation. In the pressure range when the RF coil ionisation is most efficient, the deposition rates are very low due to the short mean free path of sputtered metal atoms and slower diffusion [19].

RF coil plasmas are widely used in gas etching applications.

Chapter 4.4 of this thesis describes investigations of the RF-coil discharge on a laboratory scale and the upscaling and implementation of an RF coil in the industrially sized Hauzer HTC1000/ABS coater. It was envisaged that this method could be used instead of the arc discharge to influence the coating-substrate interface and avoid the deposition of droplets thus eliminating micrometre size growth defects in the coatings.

2.2.5. High Power Pulsed Magnetron Sputtering

Pulsed magnetron sputtering has enjoyed a rapid development in the last decade. The application of power in pulses is safer than radio frequency and at the same time allows high powers to be applied without arcing. Jäger et al showed that alumina films grown with pulsed magnetron sputtering exhibit smoother surfaces and better mechanical properties [87] than those deposited using DC or RF sputtering. The constant striking and extinguishing of the glow discharge creates highly energetic ions [83, 84] and increases the electron temperature [85, 86] of the plasma.

High power pulsed magnetron sputtering is a newly developing technique. It is based on a high current form of glow discharge where the current density is in or above the arc discharge region shown in Figure 2.8. High current glow discharges based on hydrogen are incorporated extensively into switches used in the energy supply industry, fusion devices, particle accelerators and missile launching equipment. Diffuse glow discharges with extremely high current densities, sometimes called superdense glows, have been observed since 1979 [88] and applied to back-of-the-cathode (or simply back-) lighted thyatron switches [89]. These devices operate with hydrogen or deuterium and are used for commutation of high currents. The plasma densities observed in the superdense glow discharge of back lighted thyatrons reach an order of 10^{15} - 10^{16} cm^{-3} for discharge current densities of 10^4 Acm^{-2} . The models of formation of the superdense glows assume a transformation from hollow cathode to superdense glow due to a macroscopic homogeneous electron emission from the cathode [90]. The current balance on the cathode was suggested to consist of the sum of ion current, thermionic electron emission, secondary electron emission, photoelectron emission, and self-sputtering [91]. There is no agreement as to the mechanism of this superemissivity. The existing models are based on homogeneous field-enhanced thermionic emission [92], localised emission from Schottky emission sites [93], or non-stationary explosive emission [94]. A model proposing the formation of high plasma densities by beam heating has also been published [95].

In 1997 superdense glow discharges were used for sputtering of a cylindrical cathode in a ExB field by Volosov and Churkin [96] to generate particles with energies in the range 0.5-10 keV for low energy implantation.

In 1995, Mozgrin et al. [27] published the first results on high power pulsed magnetron sputtering (HIPIMS) utilising high power glow discharges produced by planar magnetrons cathodes. The power was applied in pulses of approximately 100 μs

and high magnetic fields of the order of 0.1 T (1000 G) were used. The investigations by Mozgrin et al. differentiated at least two types of discharge according to the discharge current density J_t . When $J_t \leq 2 \text{ Acm}^{-2}$, the discharge voltage was in the range up to 2000 V, the plasma density was in the range 10^{13} cm^{-3} . This regime of operation has been termed high current magnetron discharge and is characterised with high rates of sputtering of the cathode. As the current increased the discharge entered the so-called high current diffuse regime with J_t in the range $2 \text{ Acm}^{-2} < J_t < 16 \text{ Acm}^{-2}$ the discharge voltage dropping to 70-170 V. In this mode a high density gas plasma was observed ($n_e = 10^{14} - 10^{15} \text{ cm}^{-3}$), however the sputtering rates of the cathode were negligible. In conclusion Mozgrin et al. described HIPIMS as 'sufficiently effective for technological applications' and suggested its use as a technique for deposition of films and for plasma etching. Investigations of the high current magnetron discharge in 1999 by Kouznetsov et al [21] showed that the degree of ionisation of the Cu deposition flux reached values as high as 70%. These investigations also showed evidence of the potential of this technique for Cu metalisation and trench filling applications for the electronic and semiconductor industry. In parallel, Fetisov et al. [97] reported on the production of various thin films using the same regime of operation as Kouznetsov et al. to sputter Cu, Mo, Ti, Al and stainless steel.

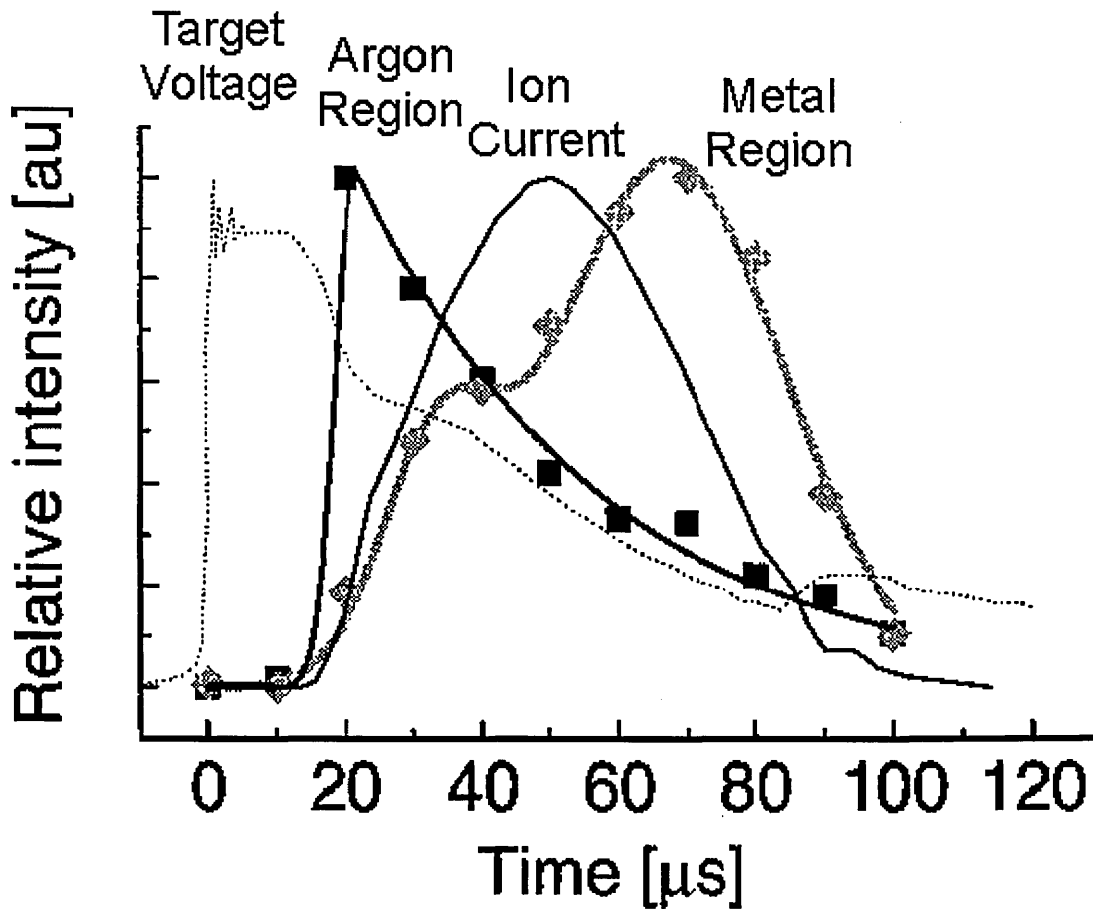


Figure 2.15. Time evolution of the target voltage, ion saturation current density, argon neutral emission intensity, and Ti neutral emission intensity. Figure adapted from Macak et al [98]

Using a set-up similar to Kouznetsov et al [21], Macak et al [98] investigated the time evolution of plasma parameters by optical emission spectroscopy and electrostatic probes. The comparison of gas and metal neutral optical emission and ion saturation current showed that the HIPIMS plasma develops from gas-dominated to metal-dominated within the pulse (see Figure 2.15). This has been attributed to gas rarefaction due to high powers [72]. Self-sputtering during the metal dominated part of the pulse has also been predicted.

Several issues of HIPIMS have been addressed in Chapters 4.2 and 4.3 of this thesis - the discharge operation current and voltage, the discharge chemistry produced and its time evolution, the maximum plasma density, deposition rates, and probability of glow-to-arc transition. Evidence of highly charged metal ions in the HIPIMS was

produced for the first time [23] (see Chapter 4.2). The potential of the metal ionisation and the high density plasma were realised for the first time in coating deposition of hard metal nitride coatings. It was shown that the interface and the adhesion between the coating and the substrate can be influenced by high energy bombardment with metal ions produced by HIPIMS [25]. Reactive mode HIPIMS was utilised to produce chromium nitride (CrN) films for the first time. The microstructure and mechanical properties of these films were investigated [26] (see Chapter 4.3).

2.3. Chromium Nitride

Chromium nitride (CrN) is the second most investigated nitride coating after Titanium Nitride (TiN). It has raised interest of the research community for several years [99-112], [29] because of its corrosion-, wear-, and oxidation-resistance and the advantage that it may be deposited at extremely low temperatures, namely at 200°C with excellent adhesion. Components with galvanically deposited Cr (hard chrome) are produced in their millions and are used in a great variety of industries. Environmental issues with the galvanising process have instigated a considerable interest in the development of an equivalent coating based on PVD. Extensive research on CrN thin films (with typical thickness of 3 µm) has proved largely unsuccessful in providing improved corrosion and wear protection compared to hard Cr. This can be attributed primarily to the higher thickness of hard Cr (typically 20 µm) and the inherently porous PVD film microstructure (see Thornton model, section 2.1). However, CrN is attractive because it can be deposited with sufficient adhesion to steel substrates even on electroplated or electroless Ni plated brass moulds for the plastic industry.

A disadvantage of CrN is its relatively low hardness in the range $HK_{0.025} = 1500-2000$. There are two stable chemical compounds of Cr and N namely Cr_2N and CrN. It is well documented that Cr_2N films have a greater hardness than CrN [103]. They can be produced by deposition with low N_2 partial pressure in metallic mode of sputtering. Recently experiments have shown that the hardness can be increased by operating in the heavily poisoned target mode using extremely high N_2 flows and bias voltages as high as -300 V. Knoop hardness values of $HK_{0.025} = 3000$ have been reported [29, 112].

In Chapter 4.3 of this thesis, an attempt has been made to produce the special high hardness CrN films by using high bias voltage and elevated Nitrogen partial pressure as reported previously [29], [112].

3. Materials and Methods

The experiments described in this thesis are based on four different equipment installations:

- Hauzer 1000/ABS™ industrially sized coater combining Unbalanced Magnetron Sputtering (UBM) and Arc Evaporation in a closed field magnetic configuration available at Sheffield Hallam University [6]
- Metal Vapour Vacuum Arc (MEVVA) Ion Source available at the Lawrence Berkeley National Laboratory, U.S.A. [114]
- High Power Pulsed Magnetron Sputtering (HIPIMS) Rig available at Linköping University, Sweden [21]
- RF Coil Enhanced Magnetron Sputtering Rig available at Université de Mons Hainaut, Belgium [113]

The emission from the plasma was measured *in vacuo* by an in-house developed optical cable and mirror assembly. Further plasma diagnostics were performed using in-house produced cylindrical and flat electrostatic (Langmuir) probes. Ions in plasma were characterised by energy using energy resolved mass spectroscopy in the RF coil rig and by ionisation states by time-of-flight spectroscopy in the MEVVA facility. Coatings were deposited in the Hauzer coating machine and the HIPIMS setup. The coating microstructure was investigated using X-Ray diffraction analysis, and transmission electron microscopy. Mechanical properties were evaluated by adhesion scratch testing, static and dynamic hardness measurements and sliding wear tests.

3.1. Hauzer HTC 1000/ABS Coating Machine

The industrially sized HTC 1000 ABS coater (Hauzer Techno Coating Europe B.V., Venlo, NL) [6] was used to perform plasma measurements of the arc discharge (Chapter 4.1) and to make CrN coating depositions (Chapter 4.3.1).

The unit was evacuated to a base pressure better than 10^{-3} Pa by two turbomolecular pumps with total capacity 4000 l/s. The total pressure was measured to within $\pm 10^{-5}$ Pa using a viscosity pressure gauge (Leybold Viscovac VM212). The machine is equipped with four ABS cathodes (see Figure 3.1) which are able to operate in either unbalanced magnetron or steered arc mode.

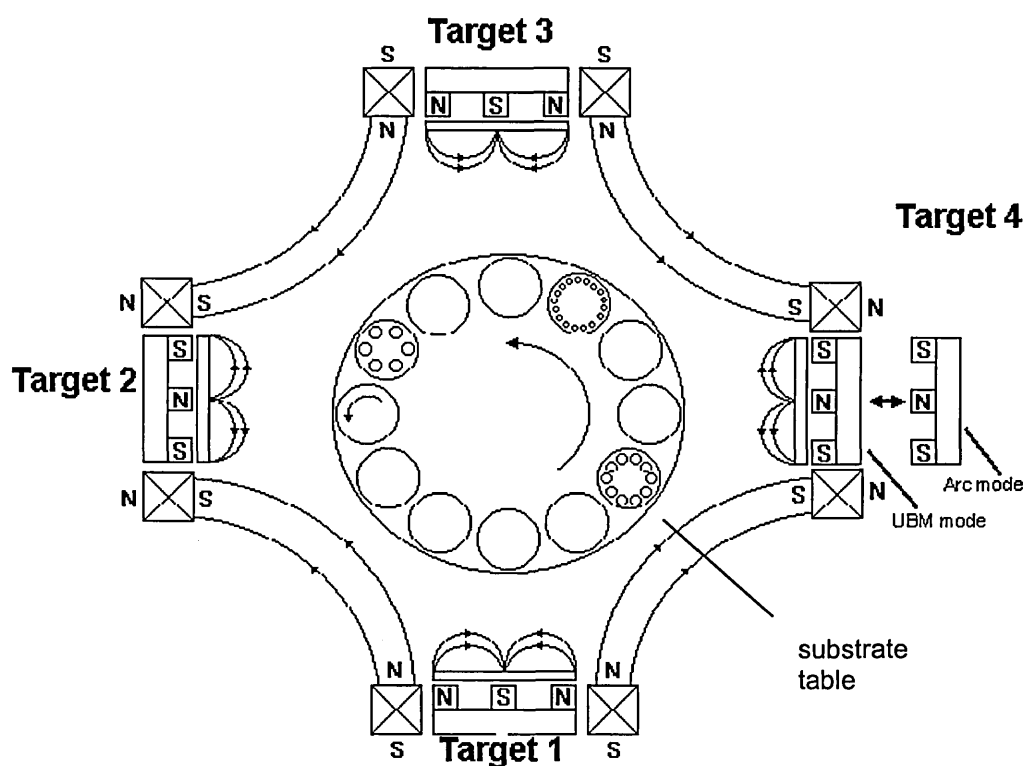


Figure 3.1. Horizontal cross section through the middle of the ABS machine

Each cathode has a movable magnetic confinement array, capable of producing a range of magnetic field strengths - from 40 mT for magnetron sputtering to 10 mT for steered arc operation. Figure 3.2 illustrates the magnetic flux density B on the target surface of an ABS cathode in arc and magnetron mode.

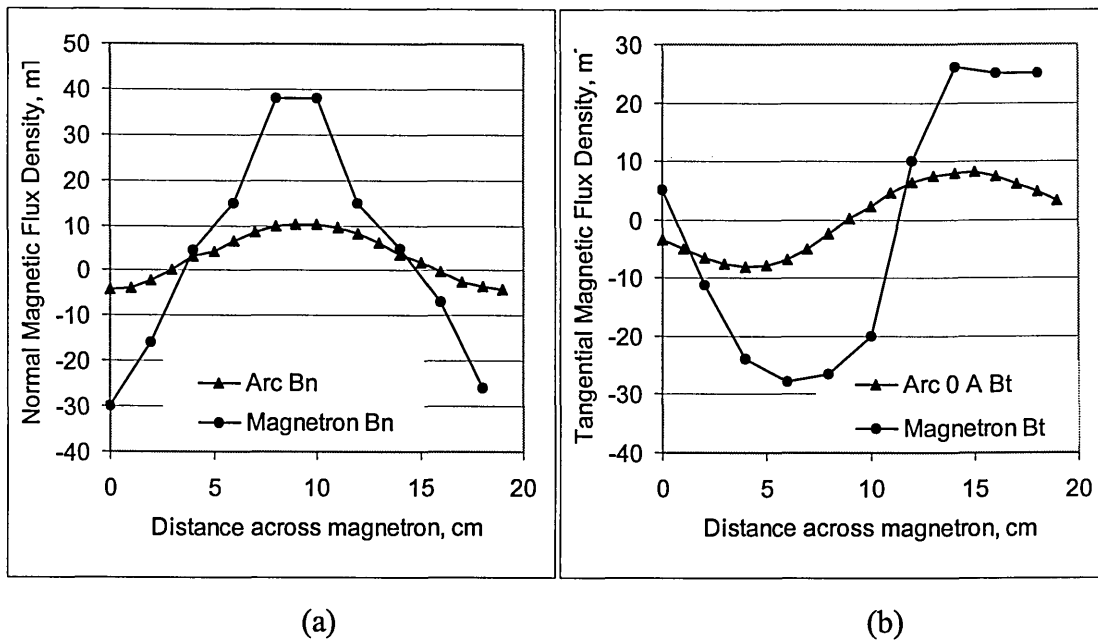


Figure 3.2. Magnetic flux density, B , at the target surface of Cathode 3 in Steered Arc (0 A coil current) and Magnetron (0 A coil current) configuration. (a) Normal component of B , (b) tangential component of B .

During the etching stage, the arc spot was steered on a 106 cm long path by a combination of permanent magnets and electromagnetic coils disposed concentrically around the cathode [6]. At the position on the cathode surface where the normal component of the magnetic field was zero the transverse field was ~ 7.5 mT, and the gradient of the normal component at the same position was ~ 0.6 mT/cm.

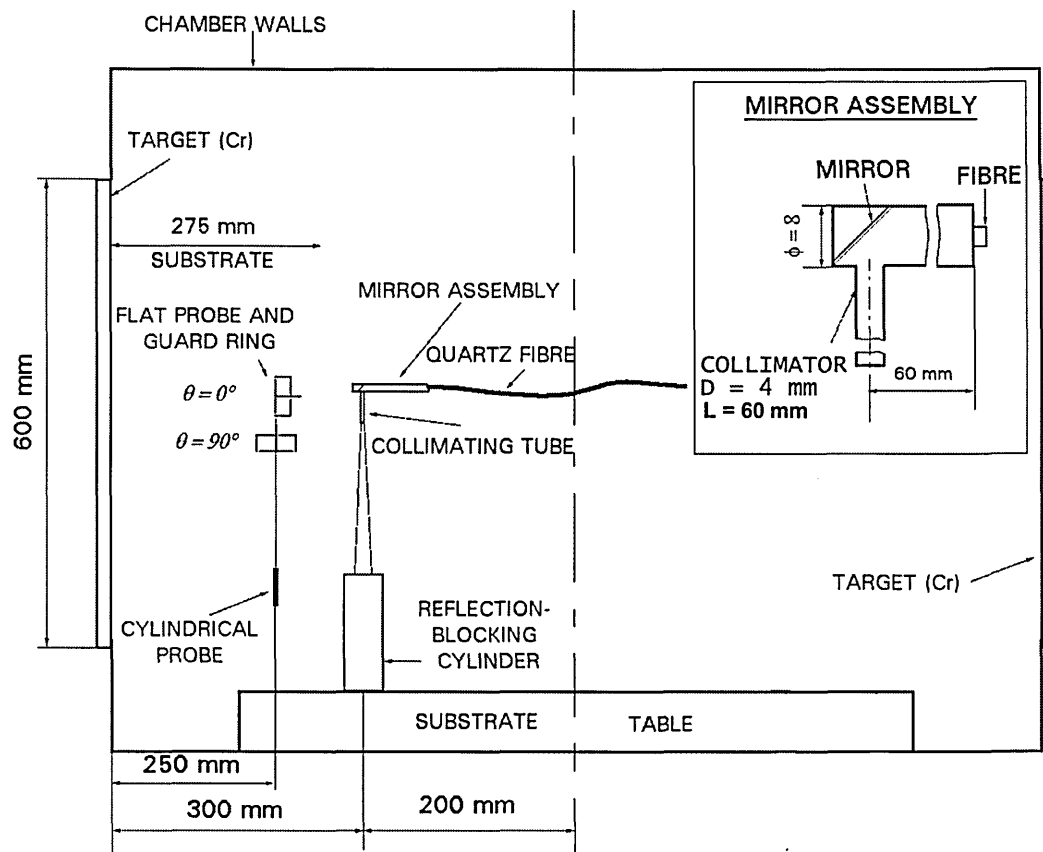


Figure 3.3. Vertical cross-section of the vacuum chamber showing the Langmuir probe position and the probe and sampling volume for OES. The inset shows detailed view of the mirror assembly.

Figure 3.3 shows a vertical cross section of the machine and the typical layout of the experimental arrangement. The flat and cylindrical Langmuir probes described in section 3.5.4 were situated at a distance of 25 cm from the arc cathode. The flat probe was halfway and the cylindrical probe was one-quarter-way up the cathode height. Whilst keeping the same distance from the cathode, the flat probe could be attached in two orientations of the collecting plane - parallel to the cathode plane (angle between planes $\theta = 0^\circ$) and perpendicular to the cathode plane, facing downwards ($\theta = 90^\circ$). Comparison of the probe currents observed in the two orientations enabled estimates of the directionality of the ion flux from the arc or magnetron to be made.

Orbital motion of the steered cathode spot resulted in oscillations of the ionic saturation current measured by the Langmuir probes. The temporal evolution of the ion current recorded by a digital oscilloscope (see Figure 3.4) allowed the estimation of the velocity of the arc spot.

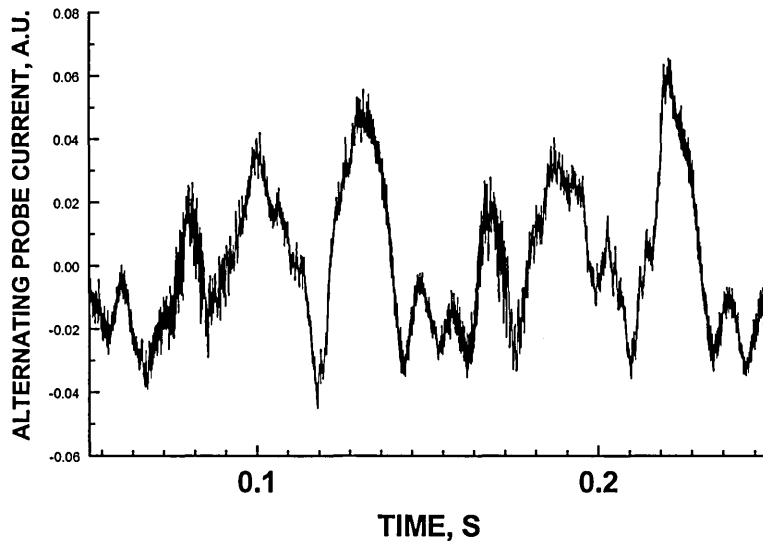


Figure 3.4. Time evolution of arc ion current recorded by a digital oscilloscope.

A quartz fibre bundle was positioned inside the chamber and used to collect optical emission from the plasma *in vacuo*. A mirror assembly (see inset of Figure 3.3) was used in order to avoid coating of the fibre. A collimator tube, 4 mm ϕ x 60 mm, was attached to the mirror assembly reducing the sampled volume to a defined cone. The collimating tube was directed towards a larger tube with diameter 20 mm and length 200 mm which was blocked at one end and attached to the base of the chamber. This ensured that no light emitted from the plasma outside the sampled volume could enter the fibre through reflection from the chamber walls. The sampled volume was 200 mm long and was situated 300 mm from the cathode with a symmetry axis parallel to the target surface.

3.2. Metal Vapour Vacuum Arc (MEVVA) with Time-of-Flight Spectrometer

The MEVVA source was used to study the interaction of cathodic arc discharge plasmas with gas atmospheres. The MEVVA source generates ions by a pulsed random arc discharge. Quantitative compositional analysis of the various charge states of the ions can be performed using a time-of-flight spectrometer attached to the arc source. The influence of gas pressure on the density of the various charge states was studied quantitatively as a complementary analysis to similar studies with OES in the ABS coater. Results from both investigations are given in Chapter 4.1.3.

The cathodes in the MEVVA source were cylindrical with diameter ϕ 8 mm. The source has been successfully tested with most elements in the periodic table [48, 51]. The power is applied in pulses with length 250 μ s and repetition frequency of 1 Hz. In the experiments the current was set to 100 A. The MEVVA source was usually attached to the Time-of-Flight spectrometer as shown in Figure 3.5. This complete setup was designed by Ian Brown in 1985 and has been used in ground breaking research in the field of vacuum arcs [49].

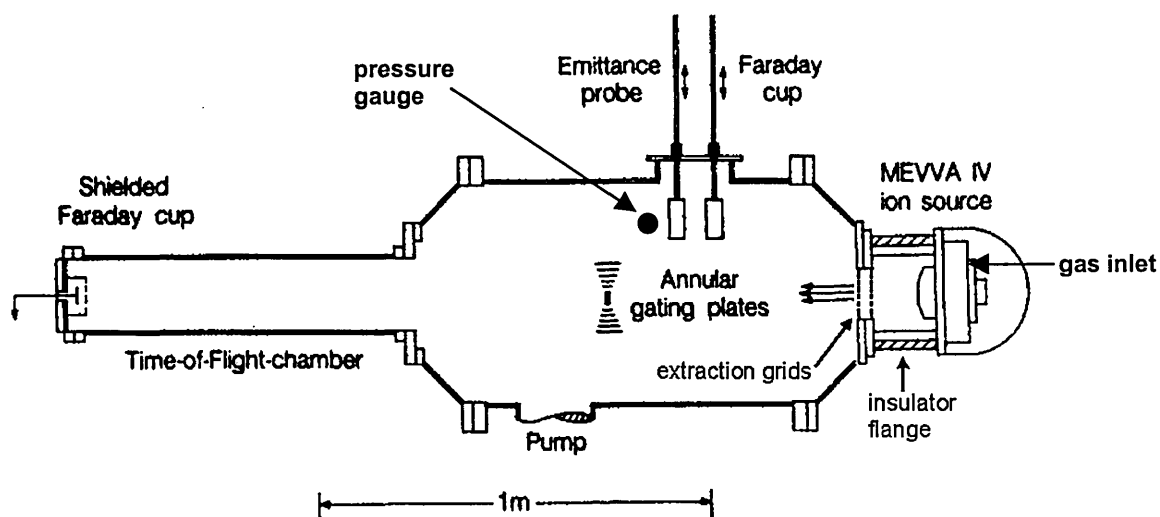


Figure 3.5. MEVVA source with Time-of-Flight chamber

A Time-Of-Flight (TOF) spectrometer was used to measure the charge state distribution of the ions produced in the MEVVA source. Figure 3.5 shows the MEVVA

source and TOF spectrometer. The ions from the arc plasma were sampled by a grid, which was located at a distance of ~ 100 mm from the cathode and was connected to the anode, i.e. had the same potential as the plasma. The MEVVA source and the first grid were floated up to a potential of 30 kV relative to ground. A second grid attached to the grounded TOF chamber was placed near the first grid. The potential difference of 30 kV between the two grids accelerated the ions to a velocity depending on their charge-to-mass ratio. The accelerated ion flux was directed to a magnetically suppressed Faraday cup that was used to measure the ion current. An array of gating plates was placed between the ion collector and the extraction grids. These plates could be biased in two ways either allowing all ion flux through or repelling all ions thus acting as a gate. In order to obtain a charge state distribution the ions were accelerated between the extraction grids by the 30 kV potential difference, the ion flux gate was opened for 200 ns and the current at the Faraday cup was recorded by a digital oscilloscope. Figure 3.6 shows typical oscilloscope traces of the arc current, the pulse used to drive the gating plates and the time of flight spectrum comprising ion current pulses at different times. Due to the different charge-to-mass ratios of the different charge states the ions were accelerated to a corresponding velocity by the grid potential and arrived after a different delay thus generating peaks in ion current at different times.

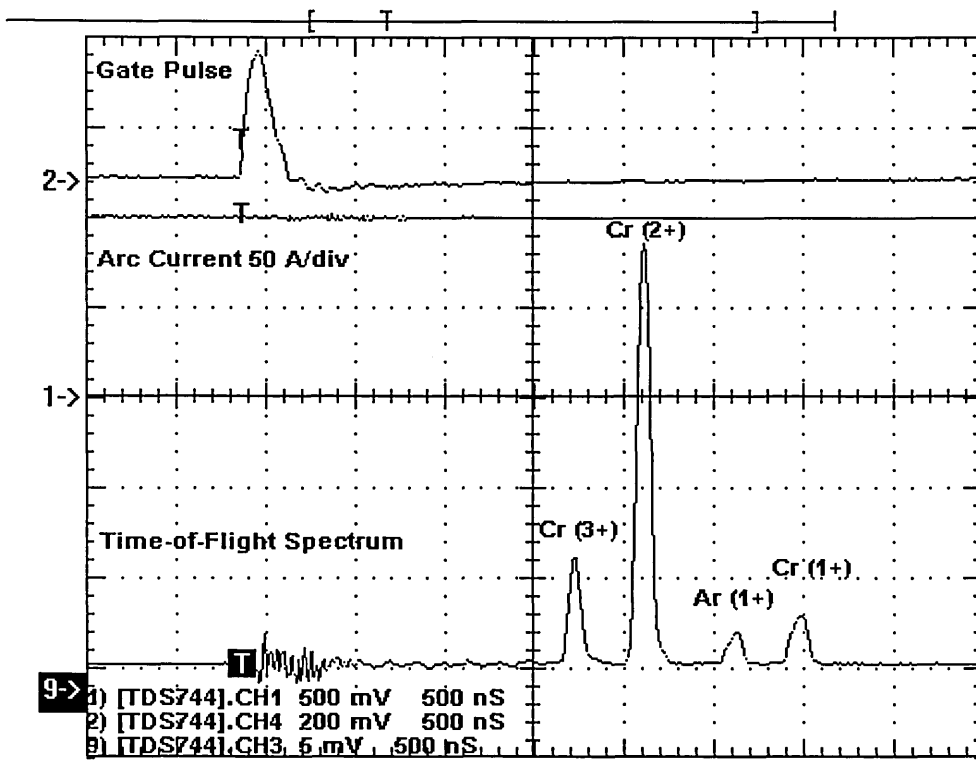


Figure 3.6. Oscilloscope traces showing the arc current, the pulse driving the gates (Gate pulse), and charge/mass ratio dependent ion current trace (Time-of-Flight Spectrum), 500 ns/div.

The experiments performed in the MEVVA source investigated the arc plasma properties as a function of gas partial pressure. Both the TOF and MEVVA chambers were pumped with a single cryopump located in the TOF chamber. The total pressure was monitored via an ionisation gauge located near the pump, as shown in Figure 3.5. Various gases could be introduced through a leak valve located near the cathode in the MEVVA chamber. Separating the two chambers were the extraction grids with different orifice sizes. The smaller grid consisted of a circular stainless steel plate (diameter ϕ 111 mm) with 91 holes with diameter ϕ 2 mm distributed homogeneously within a circular area of diameter ϕ 52.5 mm. The small size of the grid created a pressure difference between the two chambers, which was calculated assuming molecular flow [115]. It was assumed that the two chambers could be approximated by two pipes with equal diameter separated by a single aperture (the extraction grids). The pressure difference, dP , between two pipes of equal diameter separated by an aperture is given by:

$$dP = S * P / C,$$

where S - pumping speed, P - pressure, C - conductance of the aperture.

The conductance C of a thin circular aperture with diameter much smaller than the diameter of the pipes is given by:

$$C = \frac{d^2 \pi}{4} \sqrt{\frac{RT}{2\pi M_{molar}}}$$

where d - diameter of aperture, R - universal gas constant, T - temperature, M_{molar} molar mass of the flowing gas.

The total area of 91 holes with 2 mm diameter is 285.88 mm². A single hole with the same area has a diameter $d = 19.1$ mm. Therefore the conductance of the grid for air at 20 °C is

$$C = 9.1 * d^2 = 9.1 * 3.64 = 33.12 \text{ ls}^{-1}$$

Finally, the pressure difference between the two chambers can be calculated by:

$$dP = P_{TOF} * S / C = P_{TOF} * 1200 \text{ ls}^{-1} / 33.12 \text{ ls}^{-1} = 36.2 * P_{TOF} [\text{Torr}],$$

where P_{TOF} is the pressure in the TOF chamber. For a $P_{TOF} = 1 \times 10^{-7}$ Torr the pressure in the MEVVA source is $P_{MEVVA} = 3.7 \times 10^{-6}$ Torr and for $P_{TOF} = 1 \times 10^{-4}$ Torr, $P_{MEVVA} = 3.7 \times 10^{-3}$ Torr.

Figure 3.7 illustrates the relationship between the pressure measured in the TOF chamber and the pressure calculated in the MEVVA chamber.

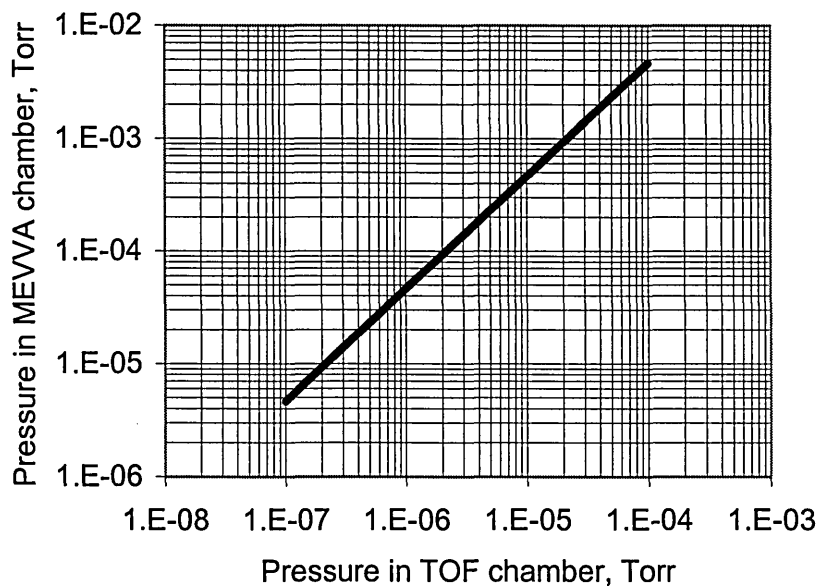


Figure 3.7. Calculated relationship between the pressure measured in the TOF chamber and the actual pressure in the MEVVA source.

3.3. High Power Pulsed Magnetron Sputtering (HIPIMS)

High power pulsed sputtering (HIPIMS) is a newly developed technique utilising pulses with very high power density and short duration of 100 μ s. HIPIMS is envisaged as a PVD technique with great potential for metal ion generation and coating deposition under highly ionised conditions. The experiments with HIPIMS concentrated on characterising the pulsed magnetron plasma by measuring current-voltage characteristics (Section 4.2.1), carrying out optical emission and probe diagnostics (Section 4.2.2) and determining the metal ion to neutral ratio in the deposition flux using a biasing/deposition technique [21] (Sections 4.2.1 and 4.2.3).

The experiments were performed using a turbomolecular pumped vacuum chamber with a diameter of 600 mm and a height of 750 mm. The chamber was evacuated prior to the measurements to a base pressure of 10^{-4} Pa (10^{-6} Torr). Ar gas of \sim 99.998% purity was introduced through a leak valve so that the desired pressure of the sputtering gas was achieved. N_2 was introduced through an electronically controlled flow meter. The depositions were made using a standard balanced planar magnetron source with a circular target, 50 mm in diameter and thickness of 8 mm. A 150 mm diameter magnetron with modified magnetic field [21] was used in ion plasma diagnostic experiments.

The magnetron cathode was driven by a pulsed power supply (Chemfilt R&D AB, Stockholm, Sweden). The power supply was able to deliver pulses with peak power up to 2.4 MW (\sim 2000 V and 1200 A) at a repetition frequency of 50 Hz and a pulse width in the range of 50–100 μ s. During the experiments, the power supply was operated in constant power mode, i.e. the total energy per pulse dissipated on the target remained constant.

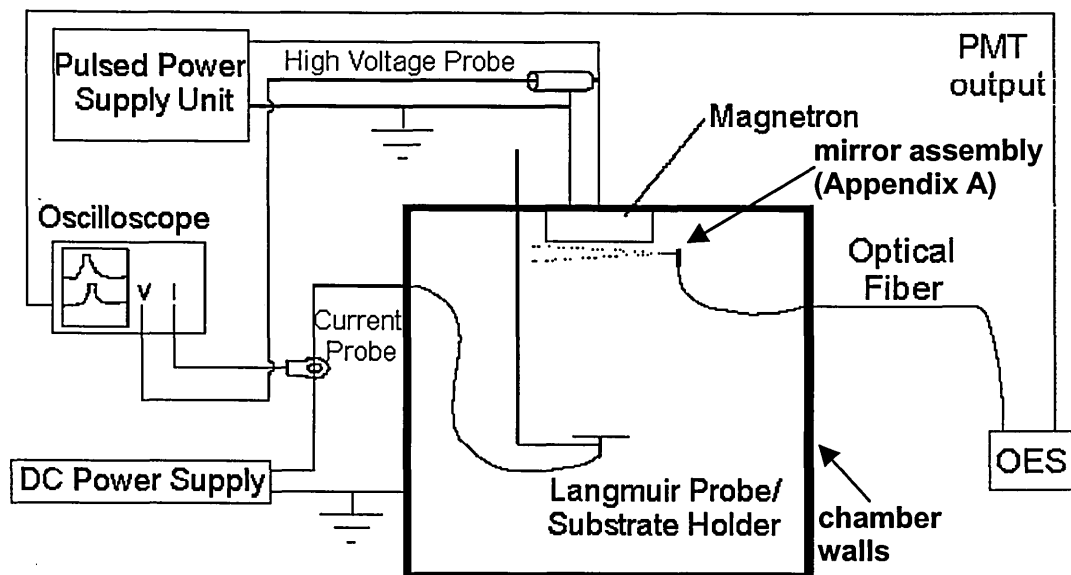


Figure 3.8. Schematic of the HIPIMS experimental setup

A schematic drawing of the experimental setup used for plasma probe measurements is shown in Figure 3.8. Target current, target voltage, and probe current were monitored by a Tektronix TDS 520C (500 MHz, 1 gigasamples/s) oscilloscope. The target voltage lead was connected to the oscilloscope through a Tektronix P6015 high voltage probe (1000x attenuation) with a 75 MHz bandwidth. For the measurements of the target current a Tektronix TCP202 probe (15 A ac/dc current probe with bandwidth 50 MHz) was used in combination with a high current transformer Tektronix CT-4 (20 kA peak current and 20 MHz bandwidth).

The probe measurements were done with a flat Langmuir probe with a collecting area of 3.14 cm^2 (see Figure 3.18a). A cylindrical screen, spaced 1 mm from the probe and kept at the probe potential, limited the collection surface to the top surface of the probe. The collecting area was positioned along the central axis of the magnetron and the distance between probe and magnetron could be adjusted between 10 and 500 mm without breaking the vacuum. The negative probe bias remained constant at -150 V during the pulse by using a power supply with sufficiently high output capacitance.

The plasma emission was collected *in vacuo* by a quartz fibre optic cable with a collimator and mirror assembly described in sections 3.5.2 and 3.1. The volume of the plasma monitored included the high-density plasma region approximately 10 mm in front of the source. The analysis of the light spectrum was performed with a Jobin Yvonne Triax 320 scanning monochromator described in section 3.5.2. The results

from the plasma compositional analysis are given in Section 4.2.1. The time evolution of the OES signals was studied using the same monochromator. Due to the slow response time of the commercial pre-amplifier of the photomultiplier tube (PMT), an alternative monitoring set up was used. The output of the PMT was connected to ground via a 100 k Ω resistor. The current produced in the PMT passed through the resistor and induced a voltage drop that was monitored with a 10 M Ω probe connected to a Tektronix 520 digitising oscilloscope, triggering on the target voltage signal. The temporal evolution of HIPIMS is shown in Section 4.2.4.

Ion saturation current measurements in Section 4.2.3 were performed with a flat probe with diameter of 20 mm equipped with a guard ring and positioned 35 mm from the target surface.

The deposition rate was measured using a quartz crystal microbalance situated at a distance of 65 mm from the target surface.

The metal ion to neutral ratio in the deposition flux was calculated by depositing for a known time on one positively biased (+75 V) - and one floating metal-plate located 500 mm from the target. The difference in mass gain between the plates was measured and the metal ion and neutral flux were determined.

The film thickness determination in Section 4.3.2 was carried out by masking an area of the substrates with TiO₂ powder prior to deposition. The step height was measured using a DEKTAK 3030 profilometer.

3.4. RF Coil Enhanced Magnetron Sputtering (Université de Mons-Hainaut, Belgium)



Figure 3.9. Top view of the laboratory sized RF coil enhanced magnetron sputtering setup.

The RF coil enhanced magnetron sputtering rig at the Université de Mons Hainaut was equipped with state of the art plasma diagnostic equipment and was used to investigate the plasma properties of the discharge. Various plasma diagnostic techniques such as energy resolved mass spectrometry, mass spectrometry and optical emission spectrometry were used to study the ion energy distribution functions and the plasma composition. The results from these investigations are presented in Sections 4.4.1-4.4.3. The knowledge and experience of this laboratory sized rig was utilised in

upscaling the technology and implementing it into the industrially sized commercially available Hauzer HTC 1000/ABS coater described in Section 3.1. The results from these investigations are presented in Chapter 4.4.4.

The details of the experimental set-up are shown in Figure 3.10.

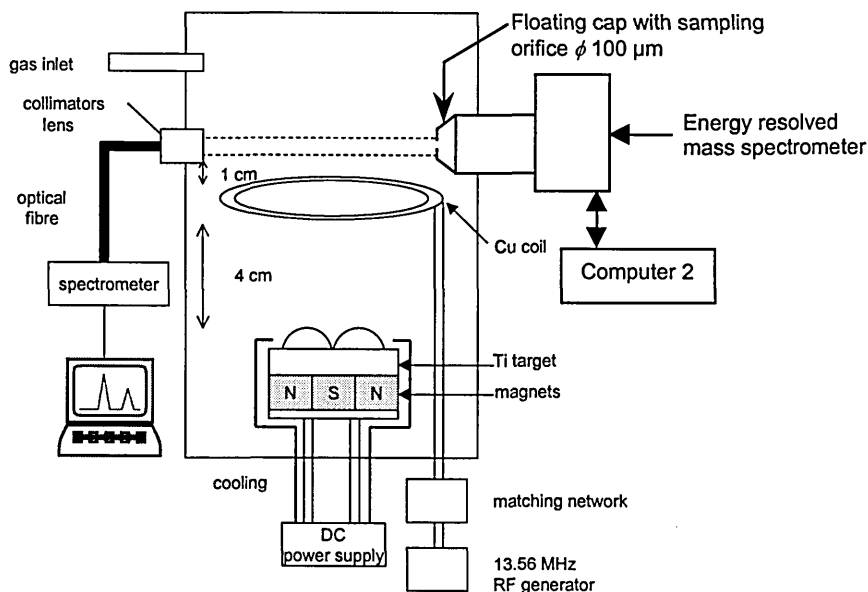


Figure 3.10. Schematic diagram of the magnetron, RF coil, optical and energy resolved mass spectrometers

The cathode was located inside a 250 mm diameter stainless steel chamber. After attaining an ultimate vacuum of about 10^{-7} Torr, the argon gas was introduced into the vacuum chamber at a constant flow rate. The total pressure was regulated via a throttle valve. The magnetron cathode was a 100 mm diameter and 6 mm thick titanium target (Target Materials, Inc). It was powered by a DC generator (ENI - RPG 50) with power available up to 5 kW. The induction coil was a grounded copper ring (inside diameter 120 mm, 6 mm thick) placed 40 mm above the cathode. It was powered by a 13.56 MHz RF generator (HFS 1001 S - Plasma Product). In order to minimise the reflected power, a matching netbox (AMN 1000 - Plasma Product) was connected between the coil and the RF generator. The power delivered in the coil varied between 0 to 500 W.

The plasma was analysed by optical emission spectrometry (OES) and energy resolved mass spectrometry (ERMS). The OES analysis was performed via a quartz optical fibre protected from sputtered metal deposition by collimators and placed 10 mm above the RF coil. A lens was placed between the collimator and the entrance slit of the fibre. The system was mounted on a horizontally and vertically movable bellows. The

spectral line intensities were recorded by means of a Jobin-Yvon HR 460 grating monochromator (focal length 46 cm, 1200 grooves/mm). Intensity acquisition was achieved by means of the Jobin-Yvon software for analytical applications (Spectramax for Windows).

ERMS analysis was performed with a Balzers Plasma Process Monitor PPM421 described in Section 3.5.5. The plasma was sampled through a floating cap with an orifice with diameter of $\varnothing 100 \mu\text{m}$. The sampled ions passed through three chambers of the ERMS spectrometer. The first chamber was an energy filter consisting of three electrostatic lenses. By choosing suitable voltages on the lenses only ions within a certain energy interval can exit the filter. The voltages on the lenses were set using a Keithley Instruments power supply. An ionisation chamber where neutral atoms could be ionised was situated after the energy analyser. This chamber was not activated during the measurements. Finally, the ions entered the quadrupole mass analyser where they were filtered according to their mass.

3.5. Plasma Diagnostic Techniques

Optical Emission Spectroscopy, Electrostatic (Langmuir) Probes and Energy Resolved Mass Spectroscopy were used to study the properties of the various plasmas used in the present thesis.

3.5.1. Optical Emission From Plasmas

Optical Emission Spectroscopy (OES) allows the measurement of the intensity and wavelength of light emitted from a plasma. Although completely quantitative plasma analysis is difficult to obtain, the technique does not disturb the plasma and is successful in determining the type, charge state and excitation temperature of the species in the plasma as well as the electron temperature.

Light is emitted from plasma when atoms or ions relax from an excited energy state to a lower (or ground) state. The excitation of atoms or ions in the plasma environments discussed in this thesis is primarily due to low energy collisions, whereby energy is transmitted from free electrons in the plasma to bound electrons belonging to the atom. The energy acquired by a bound electron causes it to change its wavefunction and move to a higher energy "orbit" around the nucleus.

The high energetic state is usually not stable and, after a lifetime ranging from 1 ns for resonant transitions to 1 s for metastable atoms, the electron decays to a lower energy state, releasing the energy dE in the form of a photon with wavelength λ , where $dE = hc\lambda^{-1}$ ($h = 6.626 \times 10^{-34}$ - Planck's constant, $c = 3 \times 10^8$ ms⁻¹ - speed of light). The probability of decay is highest when the electron transition is to the ground level (resonant transitions). According to the dipole selection rules [116], the electron can decay only between levels where the changes in total angular momentum, ΔJ , orbital angular momentum, ΔL , and the intrinsic electron spin angular momentum, ΔS , are given by $\Delta J = 0; \pm 1$; $\Delta L = 0; \pm 1$; (but not $L=0 \rightarrow L=0$); and $\Delta S = 0$. In certain cases, an electron can occupy an excited orbital with quantum numbers such that it is not allowed to decay to a lower state. These excited states are called metastable and can have very high energies (11.5 eV in the case of Ar).

Because the energy levels in an atom are discrete, the emission from a certain element consists of a unique series of discrete lines with wavelengths corresponding to the energy differences between the levels. Figure 3.11 illustrates an example spectrum

of a Ti HIPIMS plasma. Transitions between different energy states of the neutral Ti^0 are seen together with emission from Ti^{1+} and Ti^{2+} ions present in the plasma.

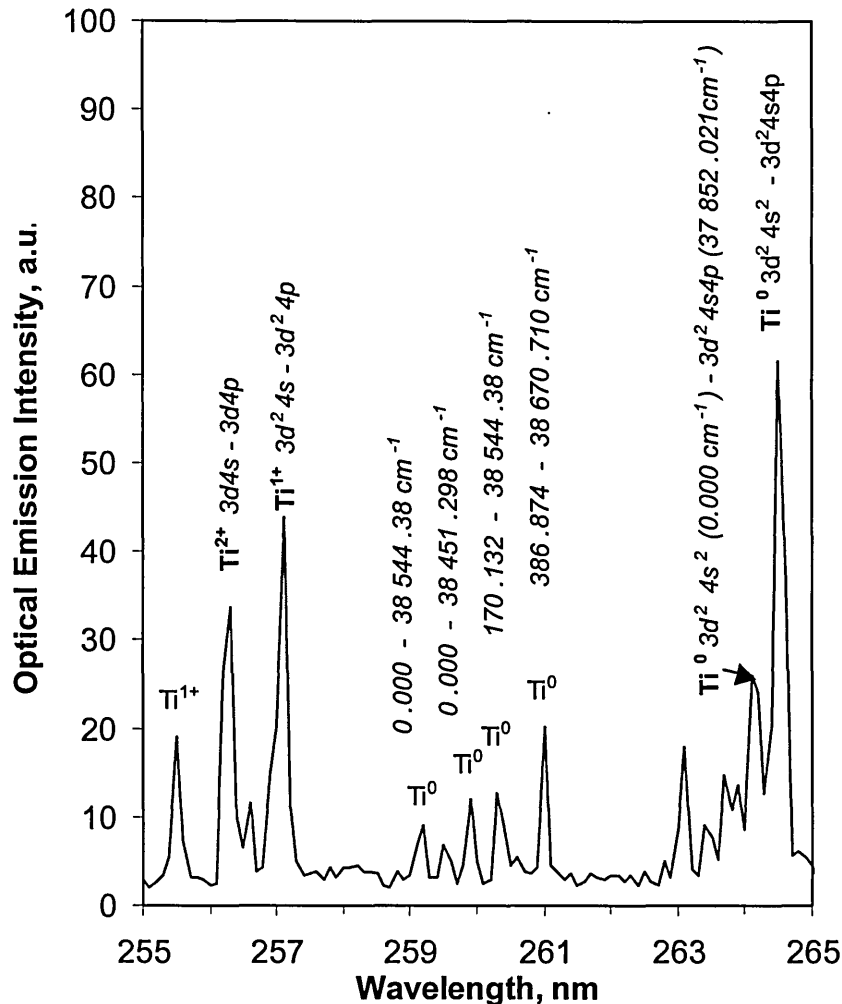


Figure 3.11. An example optical emission spectrum of Ti.

Several emission lines from the spectrum have been identified using atomic energy level tables [118] and the NIST standard wavelength tables [119]. Investigation of collected spectra showed that peak intensities with subtracted background and peak areas had the same dependencies on external parameters within the experimental errors. Since measurements of the peak intensity were faster, they were employed in the analysis of experimental results.

There are two basic models describing the effect of plasma conditions on the intensity of emission lines [117].

The Local Thermal Equilibrium model is valid in high density plasmas, such as the cathodic arc spot, where the frequency of particle collisions is high and the electron energy distribution can respond instantaneously to any change in the plasma condition.

Plasma densities of the order of 10^{17} cm^{-3} are a necessary (but not sufficient) condition for the applicability of the LTE model. In these circumstances, all processes of excitation (or ionisation) are accompanied by the inverse process of emission (or recombination). The intensity $I(p,q)$ of a line arising from a transition between bound levels p and q can be given by

$$I(p,q) = \frac{1}{4\pi} \int n(p) A(p,q) h\nu(p,q) ds = Cn(p)A(p,q),$$

where $A(p,q)$ is the atomic transition probability, $h\nu(p,q)$ is the photon energy and C is a constant. The integration is taken over the depth of the plasma that is viewed by the detector. $n(p)$ is the number density of the population of state p . In a local equilibrium plasma a given energy level, p , is populated according to a Boltzmann distribution:

$$n(p) = n_0 \frac{g_m}{Z} \exp\left(-\frac{E(p)}{kT_{exc}}\right),$$

where $n(p)$ is the population density of level p , $E(p)$ is the energy of level p , T_{exc} is the excitation temperature, k is Boltzmann's constant, n_0 is the number density of particles, g_m is the statistical weight of level p , and Z is the partition function. Combining the two equations, the intensity can then be expressed by:

$$I(p,q) = C_1 n_0 A(p,q) \exp\left(-\frac{E(p)}{kT_{exc}}\right).$$

This equation can be used to determine excitation temperature of species in the plasma from emission spectra [74].

Plasmas with lower densities, such as in a magnetron glow discharge, are described better by the Corona model, so named because it was first developed to explain the spectrum of the solar corona. Because of the lower density, the plasma is not in thermal equilibrium. In contrast to LTE, the collision processes in the Corona model are not accompanied by their opposite, rather the balance is established between collisional ionisation (or excitation) and radiative recombination (or spontaneous decay). The excitation energy distribution of ions is independent of electron density and is strongly affected by electron temperature.

According to the Corona model the intensity of a line is given by the following collision integral:

$$I(p, q) = \frac{1}{4\pi} \int n_e n(z, g) \sigma(T_e, g, p) \frac{A(p, q)}{\sum_{r < p} A(p, r)} ds \sim n_e n(z, g) A(p, q) f(T_e, \sigma_s)$$

where n_e - electron density, $n(z, g)$ - number density of species in state z , $\sigma(T_e, g, p)$ - collision cross section, $A(p, q)$ - probability of spontaneous emission from levels p and q , $f(T_e, \sigma)$ - function describing the collisional excitation probability

For plasmas in general the variation of external discharge parameters such as power, pressure, gas composition, etc... could alter the excitation paths for all emission lines. In order to factor out an overall change in emission the relative intensities were plotted - the emission intensity for each line was divided by the sum of intensities of all lines.

3.5.2. Instruments Used for Optical Emission Spectroscopy

The light collected from the plasma was analysed using a Czerny-Turner type monochromator - a schematic diagram is shown in Figure 3.12.

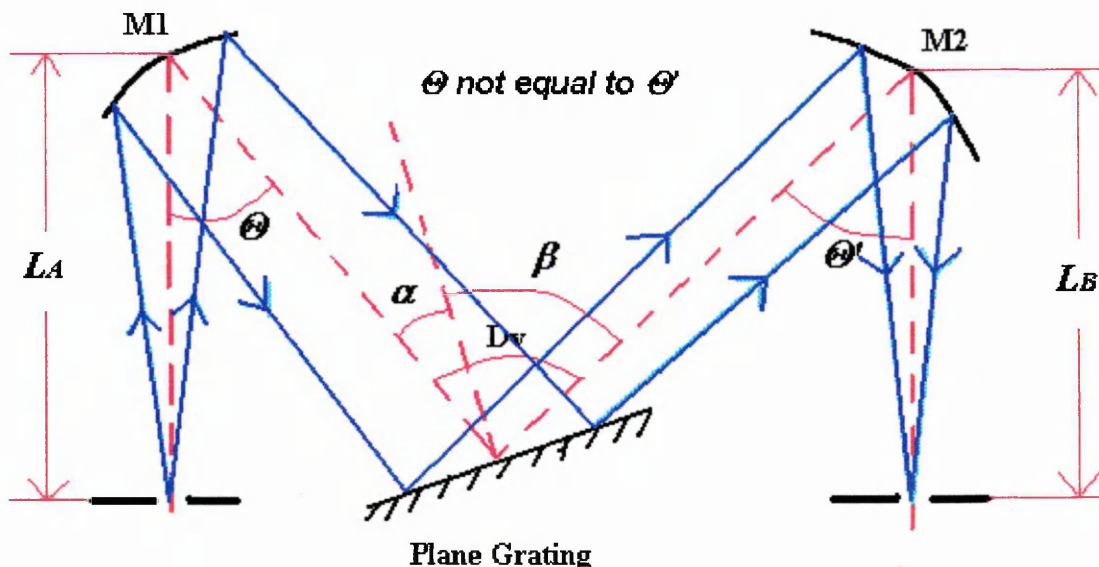


Figure 3.12. Monochromator with Czerny-Turner geometry [120]

The light enters the monochromator through a slit and, after reflection from a concave mirror M1, is collimated onto a diffraction (Echelle/holographic) grating.

Figure 3.13 shows an Echelle grating - it is a *blazed grating*, i.e. the grooves are shaped as steps and the front sides of these steps have a reflecting coating.

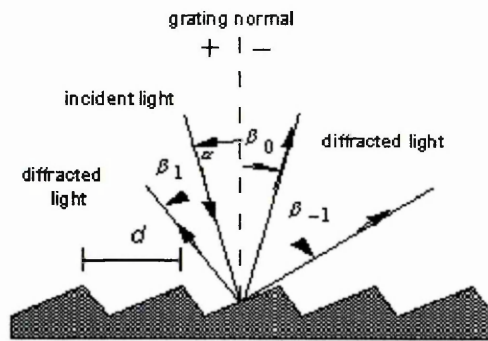


Figure 3.13. Blazed grating. Light is incident at angle α and diffracted at several orders - β_0 , β_1 and β_{-1} .

Light incident on the blazed surface of the grating is diffracted and each groove becomes a new light source. Depending on the wavelength and distance between grooves there is a set of discrete angles for which the light sources are in constructive interference. Effectively, light incident on the grating at an angle α is diffracted at an angle β depending on its wavelength λ , according to the following formula.

$$m\lambda = d (\sin\alpha + \sin\beta_m),$$

where m is the diffraction order and the other variables are described in Figure 3.13.

After diffraction, the light is collected by the second mirror M2 and focused onto an exit slit where the intensity is measured by a photomultiplier tube (PMT) or another detector. By rotating the grating, different wavelengths of light are focused onto the exit slit and a spectrum of wavelength vs. intensity can be collected.

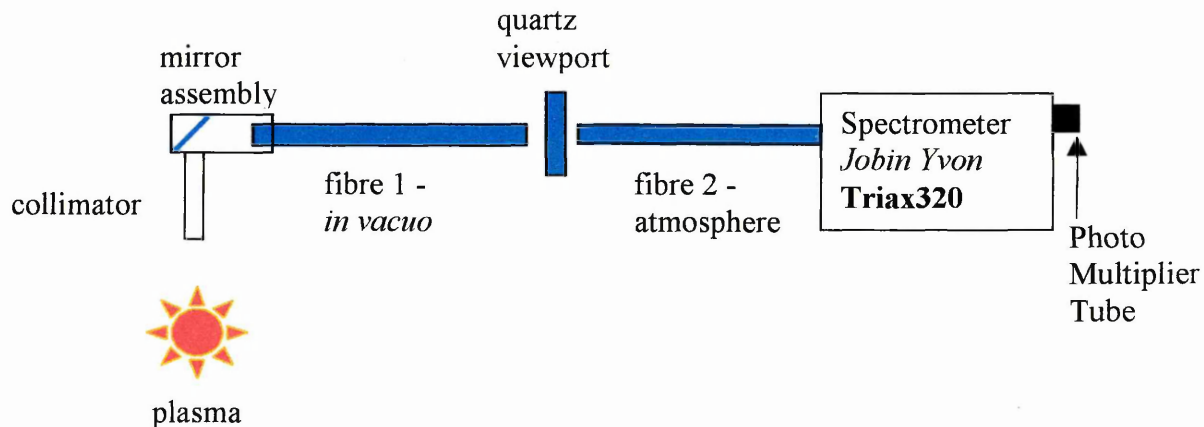


Figure 3.14. Schematic of the optical emission spectroscopy experimental setup schematic

A schematic of the typical experimental setup used to analyse the optical emission from plasmas is shown in Figure 3.14. The emission was collected *in vacuo* by an optical fibre bundle. A mirror assembly shown in the inset of Figure 3.3 was attached at the end of the fibre in order to protect it from coating. The observation volume was defined by a collimating tube ($\varnothing = 4$ mm, $l = 50$ mm) attached to the mirror assembly. The emission signal collected by this fibre was transmitted through a quartz viewport attached to the chamber to a second optical fibre, which was used to guide the light to a Jobin Yvon Triax320 spectrometer with a photomultiplier tube. The complete optical set-up was sensitive to emission in the wavelength range 200-950 nm.

The Jobin Yvon Triax 320 scanning monochromator had a Czerny-Turner type geometry and a 300 nm blaze holographic grating (1200 grooves/mm, resolution 0.12 nm). The monochromator was equipped with a Hamamatsu R928 photo-multiplier tube (PMT) with radiant sensitivity of 7.4×10^5 A/W and rise time of 2.2 ± 1.2 ns. The output of the PMT was measured and recorded digitally with an ISA instruments preamplifier and LabView computer control.

Time evolution of the OES signals was studied using the same monochromator, with the output of its photo-multiplier tube (PMT) connected to ground via a 100 k Ω resistor. The voltage across the resistor was proportional to the current signal in the PMT and was monitored using an oscilloscope with a 10 M Ω probe. In order to obtain the temporal evolution of a certain emission line the monochromator was set to transmit the wavelength of interest and the voltage across the resistor was recorded with time.

The spectrometer used to characterise (results presented in Chapter 4.4) the RF coil enhanced magnetron sputtering rig at the Université de Mons-Hainaut (described in Chapter 3.4) was also a Jobin-Yvon Czerny-Turner type with a resolution of 0.02 nm.

At Linköping University, a spectrometer with a single grating and a CCD array was used [98] to carry out HIPIMS plasma analysis (see Chapter 4.2 for results and Chapter 3.2 for experimental details).

3.5.3. Flat and Cylindrical Electrostatic (Langmuir) Probes

One of the most useful tools in plasma diagnostics is the electrostatic (Langmuir) probe (LP). When correctly analysed, the measurements obtained with a LP can be used to estimate the plasma density, electron temperature and electron energy distribution functions at a specified location in the plasma. In essence, LPs are electrodes placed in direct contact with the plasma. Different particles from the plasma

are collected by the biased (at potential V_b) electrodes depending on their potential with respect to the potential of the plasma (V_{pl}).

When an insulated electrode is introduced into a plasma it absorbs electrons and ions arriving at its surface and assumes a self bias called the floating potential (V_f), which is negative with respect to V_{pl} [121]. Figure 3.15 shows the charge and potential distribution adjacent to the electrode surface. The self biasing is caused by the different mobility of ions and electrons in the plasma. The ions have a low mobility and when the electrode is inserted in the plasma, it absorbs ions only within a short distance and the spatial distribution of ions is not perturbed significantly. On the other hand, electrons have a mobility that is two orders of magnitude higher than the ions and they are absorbed over much greater distances. The maximum distance from which electrons can be absorbed in the electrode is termed the sheath. The sheath thickness at a floating electrode depends on the mobility and therefore the temperature of the electrons. The difference in size of the regions where ion and electron densities are depleted results initially in a larger electron flux thus establishing the sheath and biasing the electrode negatively, to V_f . After the sheath has been established, the negative bias V_f repels electrons so a net positive charge is accumulated in the sheath and equal electron and ion currents are established.

The transition between the strongly charged sheath and the quasi-neutral plasma occurs in a region of a few Debye lengths, called the presheath. The potential in the presheath drops much more slowly than in the sheath, however its electrical field accelerates the ions to a critical (Bohm) velocity given by $u = (kT_e m_i^{-1})^{1/2}$ [122].

In cases when the electrode is biased to a potential V_b , the sheath changes width according to the difference ($V_{pl} - V_b$). However, practically all the potential drop occurs within the sheath and the bulk plasma is essentially screened from V_b .

In operation the LPs are biased to potentials, V_b , ranging from negative to positive with respect to the anode of the discharge. The current, I_b , is measured and an I_b - V_b curve is plotted.

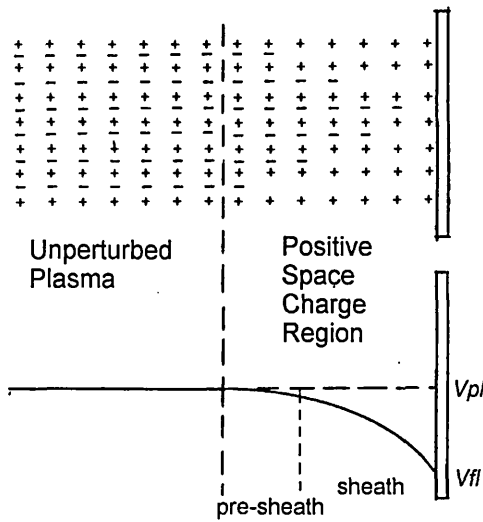


Figure 3.15. Sheath formation at a surface of an electrode (probe)

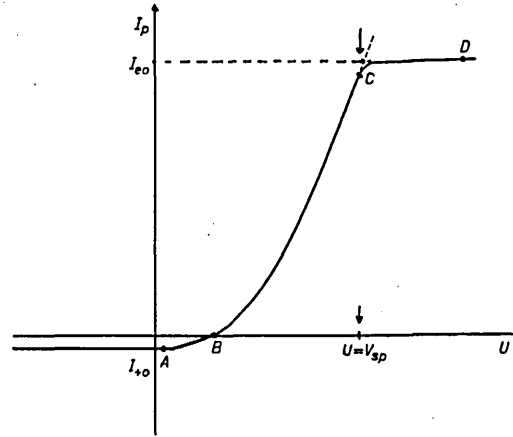


Figure 3.16. Ideal flat probe characteristic

An idealised flat probe characteristic is shown in Figure 3.16. In the region to the left of point A, the probe voltage is so negative that all electrons are repelled and only ions are collected. Since the electric field of the probe is practically confined only within the sheath, the ion current is due to plasma ions that enter the sheath by random motion. The current depends then on the ionisation density and the area of the sheath. Both these quantities are constant to a good approximation so the ion current saturates at point A. The probe current is equal to the ion saturation current j_i , which is a function of the plasma density and electron temperature [123]:

$$j_i = 1/4 n_+ e V_+ S = 1/4 n_+ e V_+ A,$$

where n_+ is the ion density in the undisturbed plasma outside the sheath and A and S areas of the probe and the sheath respectively. In the case of a plane probe, A is assumed to be equal to S . The ion velocity, V_+ , is acquired in the pre-sheath where an accelerating potential of the order of kT_e exists.

Therefore, V_+ is calculated from kinetic theory by:

$$\frac{m\overline{V_+^2}}{2} = \frac{1}{2}kT_e + \frac{3}{2}kT_i = \xrightarrow{T_i \ll T_e} \frac{1}{2}kT_e$$

where T_i - temperature of ions (~ 300 K), T_e - electron temperature, V_+ - ion velocity, m - ion mass.

For a Maxwellian distribution, it can be shown that

$$\overline{V_+} = \sqrt{\frac{8kT_e}{\pi m}}$$

Finally, for a large probe the following is valid [124]:

$$j_i = n_+ e A \sqrt{\frac{kT_e}{2\pi m}} = 0.4 n_+ e A \sqrt{\frac{kT_e}{m}}$$

Practical considerations of the probe theory demand that corrections of the order of 10% in the measured current be made for secondary electron emission from the probe [124].

As the probe voltage is set to the right of point A, plasma electrons with high energy start arriving at the electrode. At point B the probe collects an equal flux of electrons and ions and is effectively at floating potential. When the probe potential is higher than the floating potential, the ionic current immediately diminishes because of the low temperature of the ions. As more and more electrons can overcome the negative potential of the probe, the current increases as a function of voltage (point B – point C). The velocity distribution $n(V)$ of electrons is assumed to be Maxwellian, i.e. $n(V) \sim \exp(-eV/kT_e)$. That is why the variation of probe current with probe voltage (slope) is also exponentially dependent on the electron temperature T_e :

$$\frac{\Delta \ln(Ib)}{\Delta Vb} \sim \frac{1}{kT_e}$$

In plasmas with discontinuous energy distribution of electrons, variations in the slope itself have been reported [125], [126]. The exact Electron Energy Distribution Function (EEDF) can be obtained from probe characteristics by the method of Druyvesteyn. It can be shown that the second derivative of the electron current with respect to the voltage is proportional to the EEDF [127].

As the probe voltage becomes more positive, it approaches the plasma potential and the sheath disappears. At voltages more positive than V_{pb} , the sheath width starts increasing again.

In the case of a flat probe, the electron current reaches saturation because as the width changes the area of the sheath, which is also the effective collecting area of the probe, remains constant (see Figure 3.17a). In contrast, cylindrical probes do not reach saturation but rather a region where, according to the orbital motion limited theory [130], I_b is proportional to $Vb^{1/2}$.

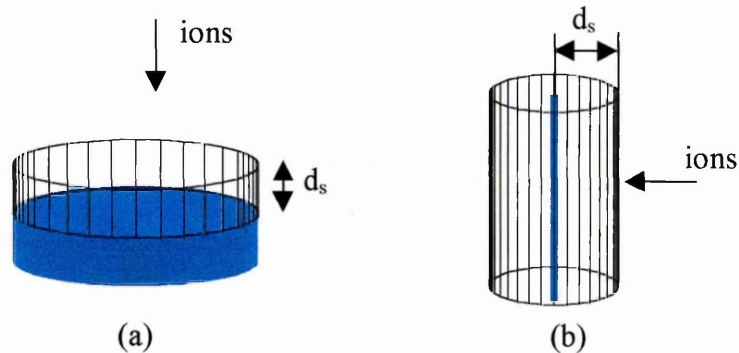


Figure 3.17. Sheath (collecting area) of flat (a) and cylindrical (b) electrostatic probes. The sheath is indicated with a wireframe with sheath width d_s and the physical probe body is represented with a solid fill.

In practice, electrostatic probes can provide quantitative information about plasma parameters in sputtering [33], [128], [124], [129], and arc [127] discharges. There are five types of probe: cylindrical, plane, spherical, hot and double probes. There are separate theories about all types [127] and because of the complex interactions with the plasma, the theories are not exact. The main drawback is the uncertainty in the form of the space charge sheath around the probe. A further issue is the influence of the probe on the plasma and on the measurement. The sheath, considered as the actual collecting surface of the probe, can be well defined, however the electric field could increase the density of ions or electrons near the probe artificially [130].

One of the main assumptions of all probe theories is that of a collisionless plasma sheath. In magnetron sputtering with an ionisation density of $\sim 10^{11} \text{ cm}^{-3}$ at 0.1 Pa the mean free path for Ar ions in Ar is of the order 10^{-2} m . For electrons, the mean free path is of the order of 1 m. The Debye length is of the order 10^{-4} m - significantly smaller than the collisional mean free paths, which means that any changes in the

plasma due to collisions would be screened. Thus, the magnetron sputtering plasma is effectively a collisionless plasma [128].

Another important assumption of probe theory is that ions are singly charged. This is true in general for dc magnetron discharges. However, in the literature on arc discharges, there are several reports describing the charge state distribution of metal ions performed for example by time of flight [131], [114] and Thomson mass spectrometer (method of the parabolas) [132]. The mean charge state ranges from 1 to 3.07 for different materials [51]. Therefore in arc discharge plasmas the ion current collected by the probe must be corrected by a factor of e.g. 3 depending on the material and pressure used. There is no published literature on exact methodology incorporating multiply charged ions into electrostatic probe theory.

The magnitude of the magnetic field in the plasma should also be considered since it determines the gyration radius (Larmor radius) r_L of the electrons. If r_L is comparable to the radius of the probe, the collected electron current can be significantly diminished. In unbalanced magnetrons, the magnetic field strength is sufficient to influence electron collection by the probe [133].

3.5.4. Instruments Used for Electrostatic Probe Diagnostics

Cylindrical and flat probes were used in the present work (Figure 3.18).

The flat Langmuir probe consisted of a stainless steel disc with diameter of 20 mm and a concentric guard ring as shown in Figure 3.18a. The area of the probe is quite significant and the bias voltages used were always chosen more negative than V_{fl} in order to avoid disturbance of the plasma or attracting the total anode current to the probe. The probe was used for measuring the ion saturation current and estimations of the plasma density and V_{fl} . In operation, the disc and the guard ring were kept at the same potential and the current to the disc was measured. The design of the probe was obtained from HVM Plasma, Prague through personal communications [134]. The probe was slightly redesigned and was constructed at the School of Engineering at Sheffield Hallam University.

A schematic of the cylindrical Langmuir probe is shown in Figure 3.18b. It consists of a tungsten wire with diameter 100 μm and a length of 10 mm. Because of its small area ($3.14 \times 10^{-4} \text{ cm}^2$) this probe could be biased negatively (up to -150 V) as well as positively (up to +20 V) without a significant drain of particles from the plasma. This probe was used to estimate the V_{fb} , V_{pl} , plasma density and electron temperature.

The probe was also manufactured in-house from design ideas obtained also from HVM Plasma, Prague.

New cables and insulated mounts were introduced in the vacuum chamber of the Hauzer HTC 1000/ABS coater to connect to both probes.

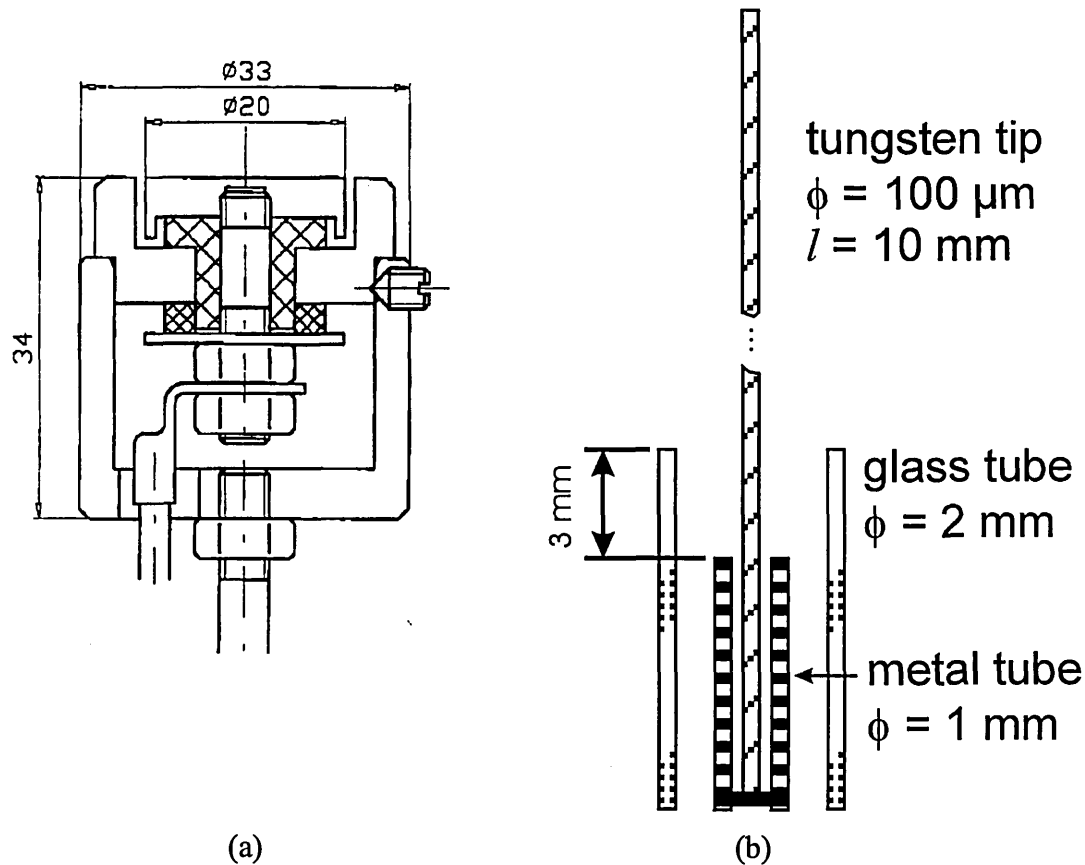


Figure 3.18 (a) Flat (plane) electrostatic probe and (b) Cylindrical probe used in the experiments

Both probes were biased using the electrical circuit on Figure 3.19. The circuit was designed and built in house. The voltage of the probe was provided by a variable and constant power supply connected in series. This complicated setup was necessary in order to achieve a stable voltage output near 0 V. The voltage-current characteristic of the probe was recorded by an X-Y plotter on paper and was digitised semi-automatically using a scanner and self developed Matlab image processing software. Calculations of the parameters were performed according to the procedure outlined in the literature [124], [129]. Ion flux densities, ionisation densities, the electron temperature, the floating and plasma potentials were measured.

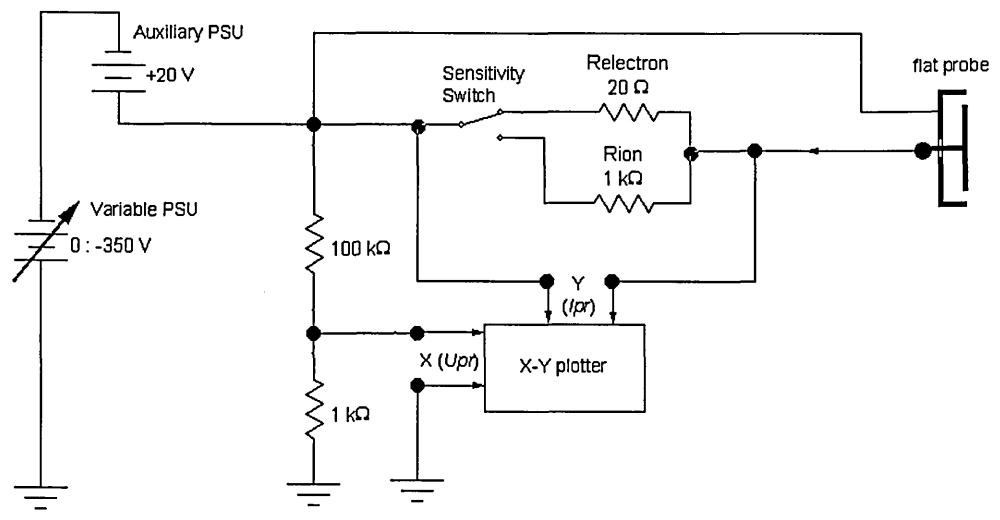


Figure 3.19. Electrical circuit used to record probe characteristics

Some typical I-V characteristics obtained with cylindrical probes are shown for arc discharge plasma (Figure 3.20) and unbalanced magnetron glow discharge plasmas (Figure 3.21). The plasma potential was determined from the intercept of the tangents in the transition area and electron saturation region as shown in Figure 3.21. The electron temperature was determined from the slope of the transition region of the characteristic as shown in Figure 3.22 and following the procedure in the previous section 3.5.3.

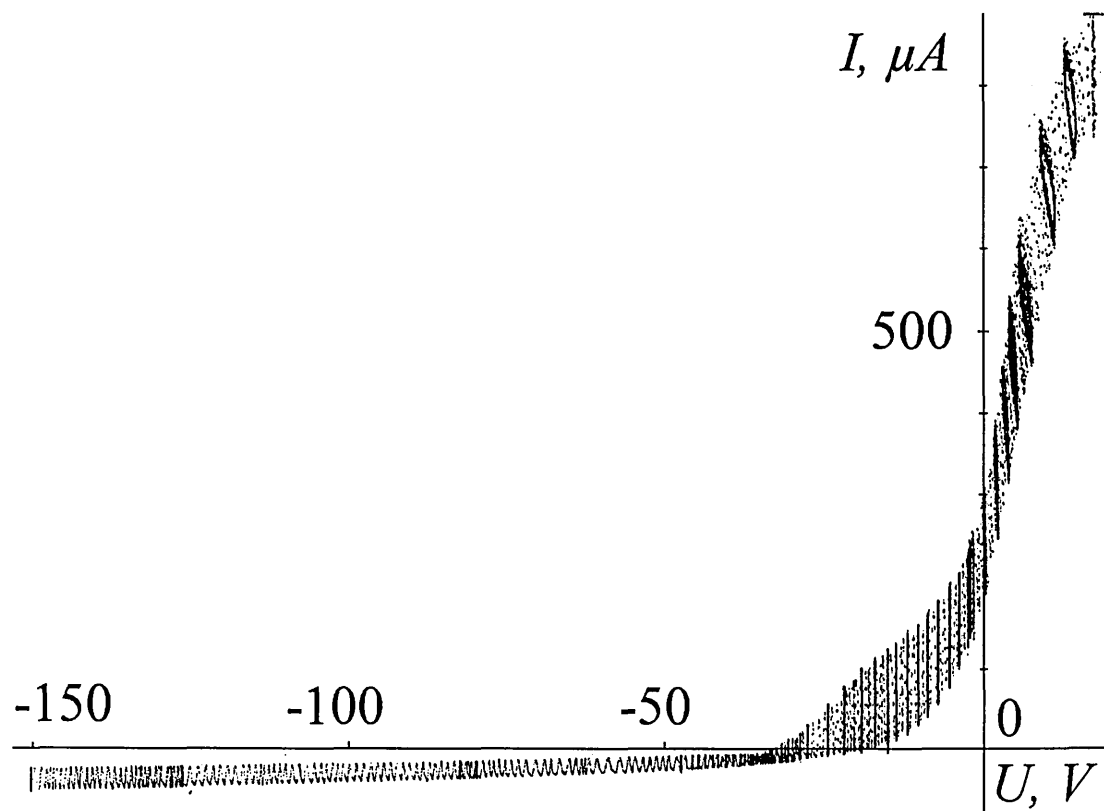


Figure 3.20. Cylindrical probe I-V characteristic in a Cr arc discharge at background pressure (3×10^{-6} mbar), discharge current 100 A and cathode-to-probe distance of 200 mm. Oscillations in the probe current are caused by the motion of the cathode spot steered around the cathode surface.

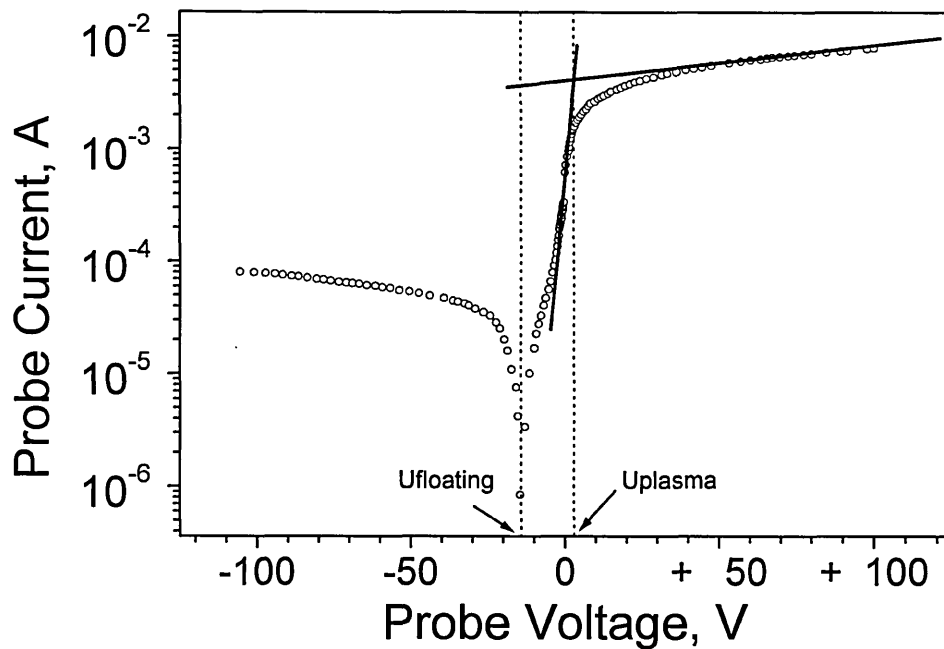


Figure 3.21. Semilogarithmic I-V plot of a cylindrical probe obtained in a unbalanced magnetron discharge. Pure Ar atmosphere, 1.4×10^{-3} mbar, unbalancing coil current 6 A, discharge power 5 kW, cathode-to-probe distance of 200 mm.

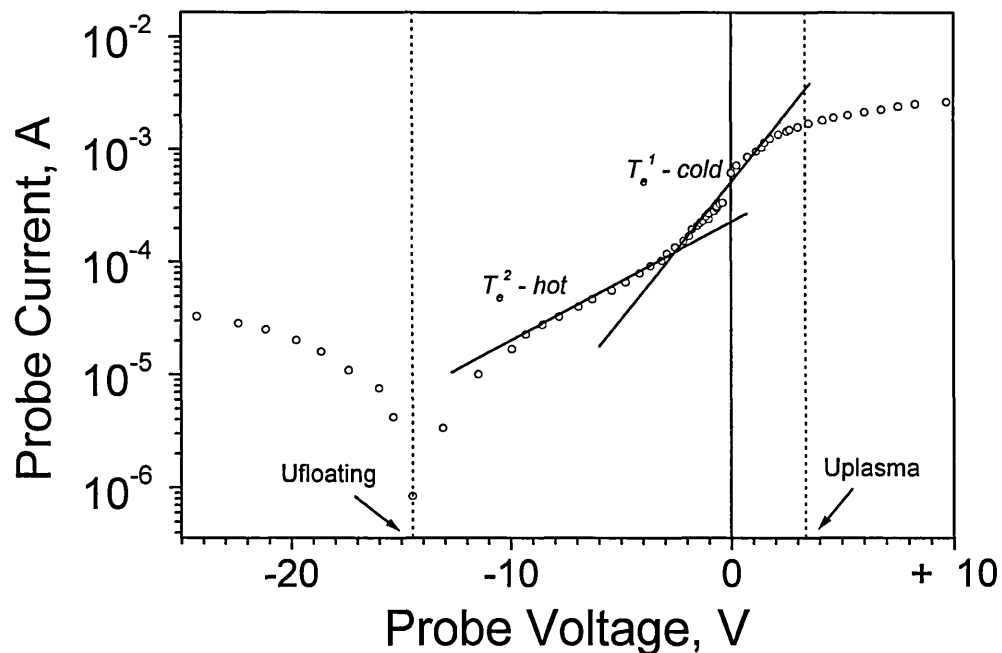


Figure 3.22. Detail from Figure 3.21 showing the transition region of the I-V characteristic used to determine the electron temperature. Two slopes corresponding to thermalised (cold) and fast diffusing (hot) electrons are evident.

The ion flux was determined with the flat probe using negative biasing. Although saturation in the ion current occurred at about -30 V, the typical probe bias used was -150 V. The plasma density was also evaluated using the following formula [124]:

$$n_i = \frac{4 Is}{e A} \sqrt{\frac{\pi m}{8kT_e}}$$

n_i - ion density, e - elementary charge, Is - ion saturation current of the flat probe, A - area of the flat probe, m - ion mass, T_e - electron temperature, k - Boltzmann's constant.

3.5.5. Energy Resolved Mass Spectroscopy

Mass spectrometry is widely used in plasma diagnostics. Although it is an intrusive technique the required number of extracted ions can be low and disturbance of the plasma can be minimal [123]. The selectivity of the mass analysis is very high and signal to background ratios of 10^8 can be achieved allowing species with large differences in number density to be studied. Analysis of neutrals is also possible by secondary ionisation inside the mass spectrometer itself. The energy of a species with a specific mass can also be studied if an energy analyser is combined with mass filter.

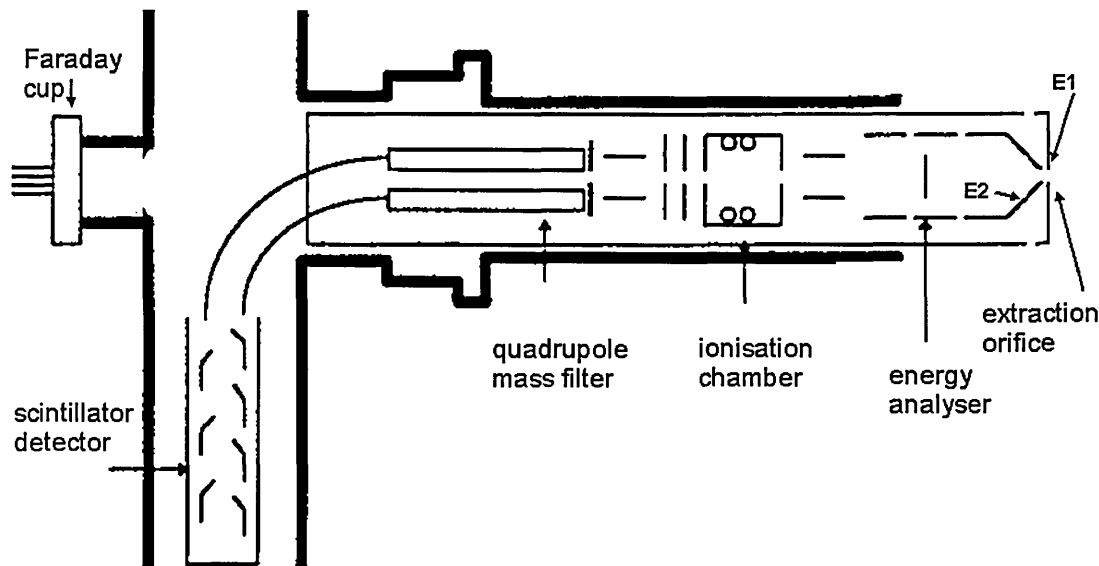


Figure 3.23. Energy resolved mass spectrometer (Balzers PPM421)

The energy resolved mass spectrometer used in the RF coil experiments (see results presented in Chapter 4.4) is shown in Figure 3.23. Particles from the plasma are sampled by the extraction system and flow through the energy resolved mass

spectrometer (ERMS) (from right to left in Figure 3.23) passing the energy analyser, ionisation chamber, quadrupole mass filter and arriving finally at the detector - Faraday cup or scintillator detector.

The extraction system consists of a plate with an orifice E1 which is in direct contact with the plasma. Behind the orifice sits a biased electrode E2. The potential applied to E1 determines the composition and number of the sampled species. In the case when E1 is floating, the plasma is sampled by ambipolar effusion and both ions and electrons enter the analyser. The current I_e through the orifice of E1 is given by [123]

$$I_e = -eS \frac{D_i \mu_e + D_e \mu_i}{\mu_e + \mu} (\nabla n)_{E1} \stackrel{\mu_i \ll \mu_e}{=} -eSD_i (\nabla n)_{E1} = -eS\mu_i \frac{kT_e}{e} (\nabla n)_{E1}$$

where μ is the electron or ion mobility, D is the electron or ion diffusion coefficients, n is the plasma density, e is the elementary charge, S is the extraction orifice diameter, T_e is the electron temperature, k is Boltzman's constant.

For plasma consisting of two ionic species with mass M , the ratio of detected currents I is related to the ratio of densities n by:

$$\frac{n_i}{n_k} = \frac{I_i}{I_k} \sqrt{\frac{M_i}{M_k}}$$

The sampled flux passes through two electrostatic lenses that focus ions with an energy $E = E_0 \pm dE$ at the exit. E_0 depends on the lens focal radius, which is controlled by the electric potential.

Following the energy analyser is the ionisation chamber where an electron beam with energy 50-150 eV can be used to ionise neutrals thus enabling their mass filtering and detection.

The selection by mass is performed in the quadrupole mass filter. It consists of two pairs of parallel poles arranged in a square. The poles are biased by an RF potential causing the particles entering their field to acquire an oscillatory trajectory. The amplitude of oscillation of the RF field determines the mass-to-charge ratio of particles that are able to pass through and reach the detector, while all others are absorbed by the poles.

Finally, the particles are detected by a Faraday cup [135] or another particle detector. The Faraday cup consists of an electrode biased to a negative potential. When

ions arrive at the electrode they are absorbed and generate an electrical current signal. In some cases, the ions can cause ejection of electrons from the electrode surface, which can cause additional current to flow. Magnetic fields parallel to the electrode surface are used to confine the electrons to helical trajectories, so that even if they are ejected they would return to the electrode thus bringing the net contribution to the current to zero.

3.6. Thin Film Characterisation Methods

The microstructure and chemical composition of the coatings and interfaces with the substrate and mechanical properties of the coatings (see Chapters 4.1 and 4.3), were evaluated using X-Ray diffraction (XRD) analysis, transmission electron microscopy (TEM), scanning TEM-energy dispersive spectroscopy (STEM-EDS), scratch tests, nanoindentation and microhardness measurements, and pin-on-disk sliding wear tests.

3.6.1. Sample Preparation

The substrates used in the etching and coating experiments in Chapter 4.1 were manufactured from A7 low carbon steel and M2 high speed steel. They were polished using 1 μ m diamond paste in the final step. The substrates used for X-Ray Diffraction analysis were 304 stainless steel.

3.6.2. Etching Rate Measurement

Etching rates were measured (Section 4.3.1.1) on steps on polished 304 austenitic stainless steel substrates. A part of the specimen was covered by a wedge shaped washer in order to minimise an influence of sample geometry. The step height was measured with both a UBM Laserprofilometer and a Talysurf. A profile line over a distance of 1 mm was recorded and then levelled in order to measure the profile line.

3.6.3. X-Ray Diffraction (XRD) Analysis

Phase analysis was carried out using a Philips PW1710 automated diffractometer using CuK_α radiation and the Bragg-Brentano geometry [136]. The X-Ray generator settings were 40 kV and 40 mA. The step size was 0.05°, and scans were acquired from 30 - 120 2 θ .

XRD was used also to determine the residual stress. The technique is based on the change in crystal lattice interplanar spacing due to the action of a residual stress [137]. The glancing angle method is particularly useful for thin film evaluation, because of the constant penetration depth and excitation volume in the samples. Figure 3.24 shows a diagram of the geometry of the GA-XRD measurement. A constant low incidence angle γ is used while only the detector is driven across the 2 θ range. The Bragg diffraction condition is satisfied by only those planes inclined at an angle of

$\alpha(\theta) = (\theta - \gamma/2)$ with respect to the surface, i.e., for small γ , the diffracting planes are parallel to the surface when θ is small and normal when θ is large.

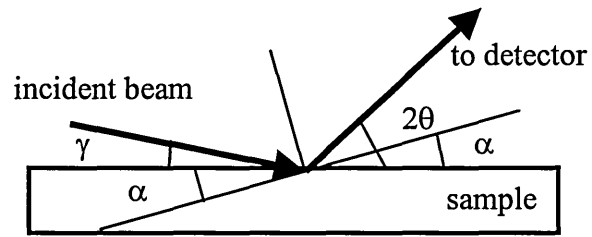


Figure 3.24. Geometry of the GA-XRD measurement. $\gamma = \text{const}$

In the experiments in section 4.3, a set of four incidence angles γ of 1, 2, 5, and 10 degrees were used.

The residual stress is calculated by the shift of the diffraction peaks with respect to a reference sample. In order to improve the accuracy of the measurement the shifts for all orientations are averaged together.

3.6.4. Transmission Electron Microscopy (TEM) for Thin Film Microstructure

The microstructure of thin films was investigated by transmission electron microscopy (TEM) (for results see Section 4.3) using a Philips CM20 microscope. The principle of TEM is similar to a diaprojector where a beam of light passes through a transparency and is focused onto a screen to form a magnified image. The resolution of the TEM is enhanced by using monochromatic illumination in the form of an electron beam with energy from 100 keV up to 1 MeV (small de Broglie wavelength = 0.0025 nm for 200 keV). Figure 3.25 shows a schematic of a transmission electron microscope.

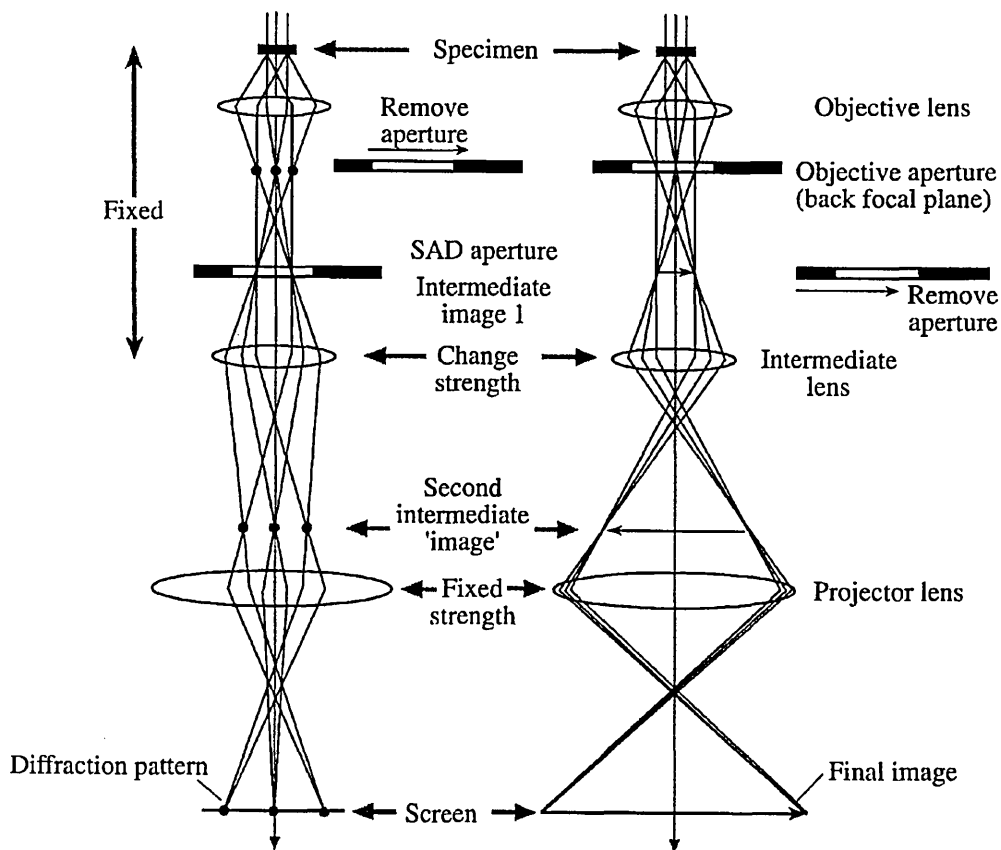


Figure 3.25. Schematic of a TEM [138]

A condenser lens guides the electrons into parallel trajectories onto the electron transparent sample. The electrons are diffracted from the crystallographic planes in the sample and a diffraction pattern and an image containing phase contrast is formed by the objective lens at different distances (the focal length and the image distance respectively). An intermediate lens with variable focal length is used to further magnify either the diffraction pattern or the image. The final pattern is projected onto a

fluorescent screen, photographic film or a CCD camera by the projector lens. By selecting the position of the objective lens aperture, the image can be formed by the direct beam (bright field imaging) or one of the diffraction maxima (dark field imaging).

Electron transparent cross sections of the thin films of interest were produced in several steps. Saw blade cutting, mechanical grinding, mechanical polishing were used to reduce the sample thickness to 30 μm . Subsequently Ar ion beam milling (GATAN PIPS 691) was used to produce a small hole in the coating region of the sample. The electron transparent areas were found on either side of the hole.

3.6.5. Scanning TEM (EDX)

Scanning TEM (STEM) is a microscopy technique, which enhances the analytical capabilities of conventional TEMs by allowing compositional and structural information to be obtained with a spatial resolution of the order of a few Ångstroms [138]. The STEM method relies on focussing the electron beam onto a small area of the sample surface and rastering it across an area of interest. One of the big advantages of this method is that no image forming lenses are used and therefore problems such as astigmatism and chromatic aberration are eliminated. Additionally, the limited area of illumination of the specimen (sometimes as low as 3 nm with a field emission gun source) allows spatially resolved analysis of the interaction of the electron beam with the specimen to be performed. Of particular interest are the inelastic interactions whereby incident electrons transfer a defined energy to excite atoms of the specimen which later decay by emitting X-Ray radiation. Electron energy loss spectroscopy (EELS) can be used to measure the amount of lost energy and determine the composition of the specimen. In this thesis, an alternative method was used whereby measurements of the wavelength (energy) of emitted X-Rays were used to calculate the energy levels of atoms contained in the illuminated area of the specimen and identify its chemical composition. This technique is called energy dispersive x-ray spectroscopy (EDS or EDX).

The chemical composition of the interface was analyzed by STEM-EDS of TEM cross sections. The results are presented in Chapter 4.1 describing the arc etching stage and Chapter 4.3 describing the interface obtained by HIPIMS pretreatment. For the observations in section 4.1.2.3, a TiAlN coating was deposited by unbalanced magnetron sputtering using two TiAl targets with 8 kW power each and a bias voltage of -75V during growth. Deposition time was 10 minutes giving a coating thickness of

~100 nm. These samples were analyzed in a Vacuum Generators HB.501 STEM, equipped with a field emission gun with a probe size of approximately 1 nm.

3.6.6. Evaluation of the Adhesion of Thin Films

A scratch test was used to evaluate the adhesion of the coatings. The test is performed with a Rockwell C indenter diamond sliding linearly on the sample with increasing load. As the load increases, the stresses induced in the coating overcome the forces binding it to the substrate, and a spallation occurs. The force at which a spallation reveals the substrate is called the critical value L_C .

The coating adhesion was assessed by scratch tests performed with a CSEM REVETEST scratch tester with indenter radius of 200 μ m and a load rate of 10N/mm. Two types of coatings were characterised by these tests:

a) ~3.2 μ m thick $Ti_{0.44}Al_{0.53}Cr_{0.03}Y_{0.02}N$ coating deposited by unbalanced magnetron sputtering on an approximately 300 nm thick $Ti_{1-x}Al_xN$ base layer on HSS steel. (see Chapter 4.1)

b) ~2-3 μ m thick CrN films deposited by the ABS and HIPIMS methods on HSS (see Chapter 4.3)

3.6.7. Measurement of the Hardness of Thin Films

The hardness of thin films is defined as the resistance to penetration by another body under load. The hardness was evaluated by two methods - static, using a Knoop indenter and dynamic loading-unloading nanoindentation, using a Vickers indenter.

The Knoop indenter used in the static hardness determination is especially designed for small penetration depth and so is particularly suited to measurements in thin films. The diamond is a rhombic pyramid with ratio of the diagonals 7:1. A constant load of 250 mN (25 g) was applied for 20 s and the size of the indentation was measured. The hardness was calculated from the expression [139]

$$HK = C * P d^{-2},$$

where C - constant, P [kg] - load, d [mm] - length of the longest diagonal of the indenter footprint. All measurements were performed with a Mitutoyo MVK-G1 tester equipped with an optical microscope for measuring the size of the indenter footprint.

Although static hardness measurements give a good estimate of the plastic hardness dynamic hardness measurements provide more insight into the elastic and plastic properties of materials [140]. In dynamic measurements, the load is increased in

steps and the penetration depth is measured for each step. Figure 3.26 shows a plot of the load [mN] versus the penetration depth. The curves showing the loading and unloading can be used to estimate the universal hardness, plastic hardness and the Young's modulus of the material. The technique does not require measurements of the size of the indent footprint and therefore small loads and penetration depths can be afforded thus avoiding substrate effects.

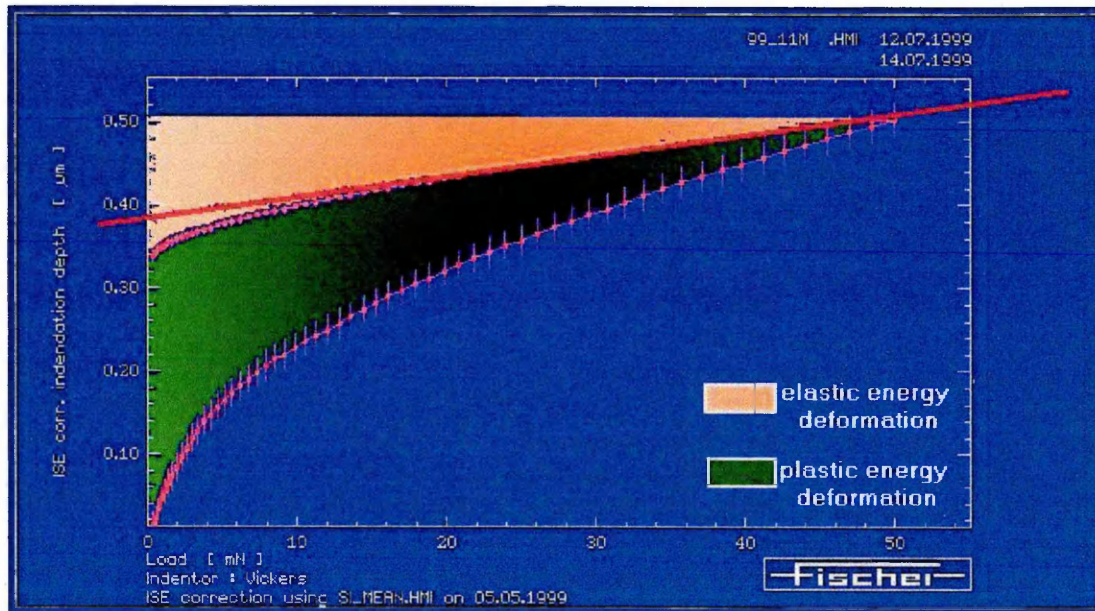


Figure 3.26. Loading/unloading curve of the dynamic hardness measurement

The dynamic hardness measurements in this thesis were performed with a Fischerscope H100 with a Vickers type diamond indenter. The maximum load was 50 mN and the loading time was 60 s. The typical indentation depths were of the order of 500 nm.

3.6.8. Measurements of the Friction and Wear Coefficient in Sliding Wear

The friction and sliding wear coefficients are amongst the most important mechanical properties determining the suitability of a coating for a specific application. In the present thesis these properties were investigated for CrN coatings deposited by the ABS technique (Section 4.3.1) and CrN deposited by reactive HIPIMS (Section 4.3.2)

Friction occurs when two bodies in contact move relative to each other. The force resisting the movement is the friction force and its magnitude is equal to the force normal to the direction of motion multiplied by the coefficient of friction. The coefficient of friction is characteristic of the two counterparts in contact and depends mainly on their tendency to react, inter-solubility, and mechanical properties such as hardness, toughness, and internal stress.

By definition, wear is the removal of material from a solid surface as a result of mechanical action. Sliding wear is described by the Archard model [141]:

$$\frac{V_r}{l_s} = K \frac{F_N}{HV}$$

where K - sliding wear coefficient, F_N - load, HV - hardness, V_r - volume of material removed, l_s - sliding distance. If l_s is brought to the right side of the equation, the Archard model states that the volume removed due to the wear is proportional to the work of the friction force $A \sim F_N l_s$.

In the experiments, a CSEM pin-on-disk wear tester was used. A schematic of the tester is shown in Figure 3.27.

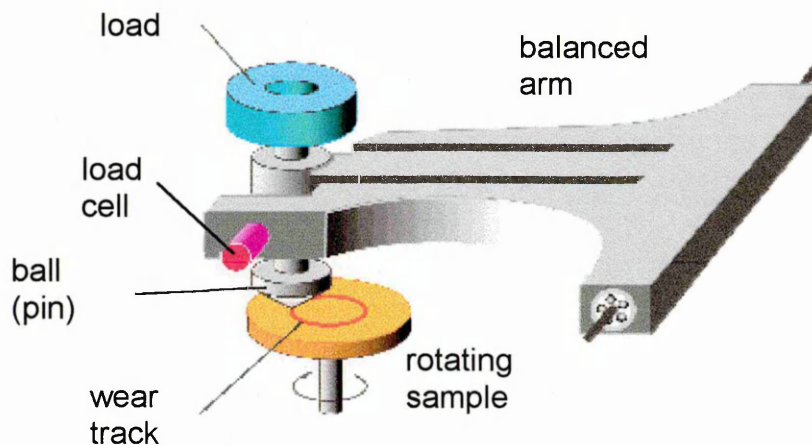


Figure 3.27. Schematic of the pin-on-disk tester

The sample is clamped onto a rotating holder. The counterpart (usually a 6 mm diameter Al_2O_3 ball) is supported by an arm. The load is applied by a weight placed on the arm above the pin. The friction force was measured with a load cell, which was calibrated with 0 and 5 N loads prior to each test. The tester was computer controlled and the number of laps as well as the calculated friction coefficient were recorded at a frequency of 1 Hz. The load was 5 N, the radius of the track was 12 mm and the linear speed of the sample relative to the counterpart was 10 cm/s.

For the calculation of the dimension coefficient of wear, the worn off volume can be expressed as [141]:

$$V_r = 2 \pi R A_t$$

Where V_r - volume removed, R - radius of wear track, A_t - cross sectional area of the wear track. Therefore, the coefficient of wear can be determined according to the formula:

$$k = A_t F_N^{-1} N^{-1} v$$

where N - number of laps, v - linear speed.

A_t was measured with a *Talysurf* profilometer available in the School of Engineering.

4.1. Steered Cathodic Arc Discharge

The primary application of the arc discharge plasma in this work is to treat the substrates prior to coating deposition. Gas ions created in the vicinity of the arc spot are accelerated by a high bias (typically -1200 V) and bombard the metal substrates with energy sufficient to clean their surface from residual oxides. Metal ions created in the arc discharge are accelerated to energies equivalent to two or more times the applied bias voltage depending on their charge state. These ions, with energy in the low keV range, can be implanted up to a few tens of nanometres under the substrate surface. The implantation generates local lattice defects and improves the lattice matching between the substrate material and subsequently deposited nitride films. It has been shown that more implanted material and higher implantation depth are beneficial for improving the adhesion of nitride films on high speed steel and WC substrates.

4.1.1. Multi-fold Ionisation Observed in Cr, Ti, and Nb Metal Arc Discharges

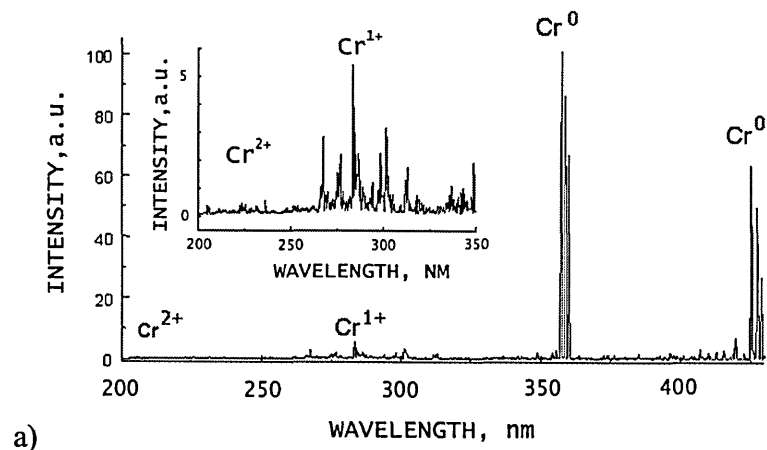
The arc discharge plasma is characterised by two main regions. The first region is called the cathodic arc spot. It exists in a volume of a few cubic micrometres close to the target surface [50, 66]. Plasma densities in this region are very high, reaching 10^{20} cm^{-3} [56, 50]. The ions and electrons exist in Local Thermodynamic Equilibrium [117, 55], i.e. have similar temperatures, and evaporated target atoms are easily ionised to a range of charge states - from 1+ to 5+ depending on the material [51]. The highly charged ions are expelled from the cathode spot with average energies of tens of eV (70 eV for Cr^{1+}) [57, 55, 141] and form the second region of the plasma which exists in non-equilibrium [51, 59]. The electrons in the second region of the plasma have energies typically 2 eV and the ions can have a much lower, even thermal, energy especially if the arc operates at high gas pressures. The charge state distribution of ions does not change further unless they collide with other atoms in the atmosphere. In the publications of Brown and Anders [48, 51] the charge state distribution has been measured precisely in high vacuum for most materials in the periodic table. Table 4.1.1 quotes the published values for some metals.

In this work the charge states of Cr, Ti, and Nb were studied qualitatively by Optical Emission Spectroscopy. The OES investigations performed in the ABS coating machine (see Section 3.1 for experimental details) indicated that charge exchange reactions could occur between the metal ions and gas atmosphere in the chamber.

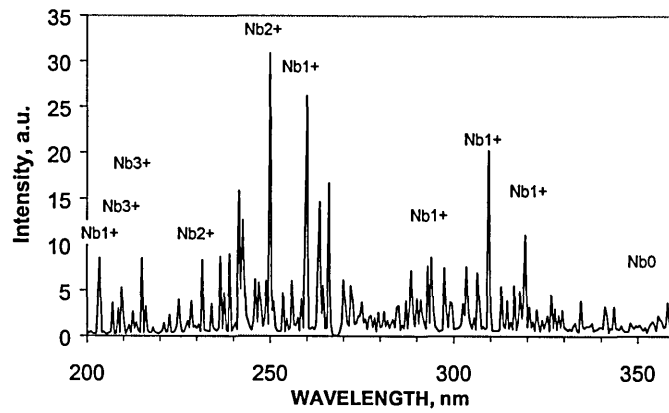
These interesting observations were investigated further by quantitative measurements to a greater depth and precision using Time of Flight Spectrometry in the MEVVA source operating with Cr and Nb cathodes (see Section 3.2 for experimental details). OES did not allow the detection of all charge states present in the plasma because of the limited wavelength range - 200 nm to 950 nm. The charge states observed by OES and used in this work are marked in *italics* in Table 4.1.1. Examples of spectra for Cr, Nb, and Ti showing several ion species are shown in Figure 4.1.1. A sample time of flight spectrum is shown in Figure 4.1.2.

Table 4.1.1. Charge state distributions measured in the MEVVA random arc source for different cathode materials. The states marked in *italics* could be observed by the present OES setup.

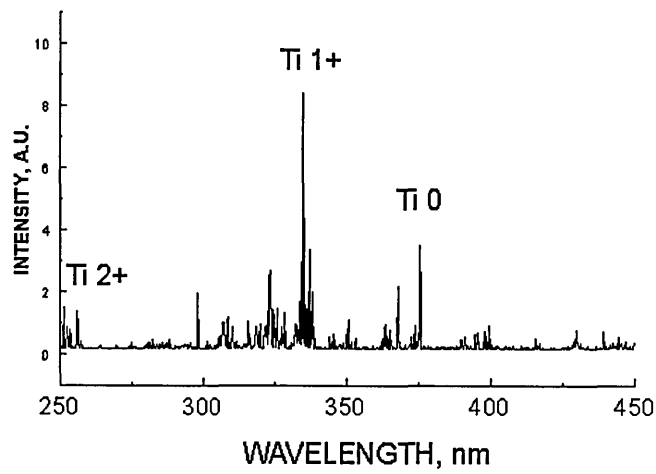
Charge State:	\bar{Q} (mean)	1+	2+	3+	4+	5+
Spectroscopic notation		II	III	IV	V	VI
Ti	2.03	<i>11</i>	<i>75</i>	14		
V	2.14	<i>8</i>	<i>71</i>	<i>20</i>	1	
Cr	2.09	<i>10</i>	<i>68</i>	21	1	
Nb	3.00	<i>1</i>	<i>24</i>	<i>51</i>	22	2



a)



b)



c)

Figure 4.1.1 Optical emission spectra obtained from Cr (a), Nb (b) and Ti (c) arc discharges showing highly ionised metal ions.

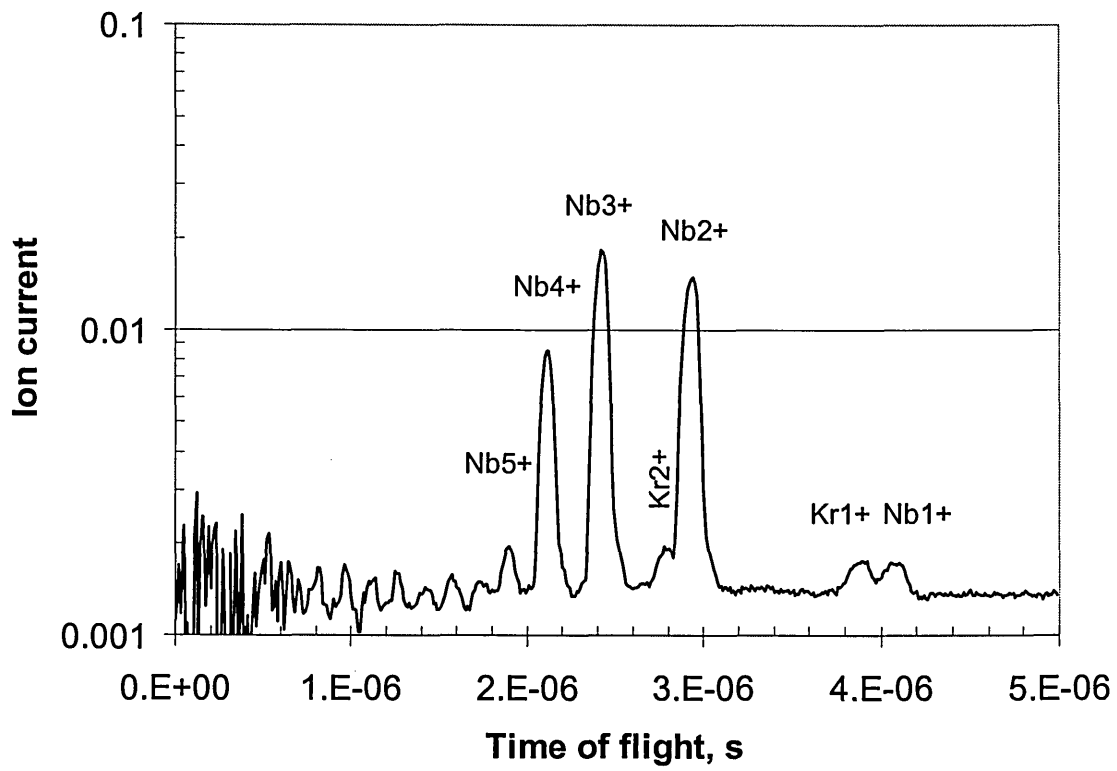


Figure 4.1.2. Time of Flight spectrum for a Nb arc operated in a Kr atmosphere

4.1.2. Influence of Gas Pressure on Plasma Density, and Electron Temperature of Cr Arc Discharge

As mentioned in the introduction, arc discharges are useful for treatment of substrates prior to coating deposition. In practice however, substrates are often treated in a simple Ar glow discharge, usually ignited between the substrates and the chamber walls. In both pretreatment methods, the substrates are biased to a high potential in order to cause sputtering of the uppermost layer. It is obvious that discharges with higher plasma density are more efficient in this process. The plasma parameters of an Ar glow and an arc discharge at typical parameters used for pretreatment in the Hauzer ABS machine were compared.

The Ar glow discharge was ignited between the substrate table serving as a cathode and the chamber walls serving as an anode. The cathode voltage was -1200 V and the gas pressure was 0.636 Pa (6.36×10^{-3} mbar).

The arc discharge was operated on one of the ABS cathodes. The discharge current was 100 A and the Ar gas pressure was varied from 0.115 Pa (1.15×10^{-3} mbar) down to base pressure of 0.0007 Pa (7×10^{-5} mbar).

Cylindrical and flat electrostatic probes (described in Section 3.5.4) were installed at a distance of 25 cm from the arc cathode near the usual substrate position as shown in Figure 3.3 in Section 3.1. U-I curves were recorded from -150 V to +20 V. The curves were analysed using Langmuir probe theory, as described in Chapter 3.5.3, assuming singly ionised species. The cylindrical probe was used to evaluate the electron temperature, plasma and floating potential and density. The flat probe was used to make an accurate estimate of the ion saturation current and plasma density.

The plasma parameters during an Ar glow discharge and an arc discharge are summarised in Table 4.1.2. The electron temperature was evaluated by taking the integral over the transition region of the probe I-V curve [127] or from the difference in plasma and floating potentials and assuming a Maxwellian distribution [124].

Table 4.1.2 Plasma properties and ion flux at a distance of 250 mm from the source.

Discharge	Ar glow	Cr arc	Cr arc	Cr arc	Cr arc
Total pressure, Pa	0.636	0.0007	0.06	0.083	0.115
Ar flow, sccm	400	0	43	70	100
Ion Density, cm ⁻³	2.02E+8	4.57E+8	1.60E+10	1.21E+10	2.55E+10
Ion flux, ions.m ⁻² .s	2.01E+16	4.54E+16	1.59E+18	1.20E+18	2.53E+18
Ion saturation current, A	5.08E-06	2.00E-05	7.20E-05	9.20E-05	1.23E-04
Ion saturation current density, mA.cm ⁻²	0.16	0.64	2.29	2.93	3.92
U _{plasma} , V	-11	15.8	8	8.2	7.2
U _{floating} , V	-22.2	-46	-3.5	-0.63	-0.68
Te from integral, eV	4.3	14	1.9	2.02	1.77
Te assuming Maxwell, eV	2.07	11.4	2.129	1.6	1.45

For the Ar glow discharge, the measured plasma density reached a value of 2×10^8 cm⁻³ and the ion flux was 2.01×10^{16} ions.m⁻².s⁻¹, as evaluated from the ion saturation region of the flat probe. The plasma potential measured for the Ar glow discharge plasma was highly negative: U_{pl} = -11 V and the electron temperature was relatively high: Te = 4 eV. The high plasma potential could be explained by the position of the probe with respect to the substrate table, which in this case is also the cathode of the discharge. Due to the high cathode potential, a plasma sheath extending over several centimetres can be formed [121]. The plasma potential inside the cathode sheath is more negative than the real plasma potential, additionally electrons are accelerated due to the inhomogeneous electrical fields created in the sheath. It could be argued that the probe was inside the sheath during the measurements. However, during Ar glow discharge etching the substrates act as cathodes and are also situated within the sheath, therefore ion flux values measured by probes inside the sheath give a reasonable approximation of the flux reaching the substrates.

In comparison in arc discharge plasmas the charge carrier densities reached $2.55 \times 10^{10} \text{ cm}^{-3}$ with ion flux of $2.53 \times 10^{18} \text{ ions.m}^{-2}\text{s}^{-1}$ at a pressure of 0.115 Pa (1.15×10^{-3} mbar). At a background pressure, 0.0007 Pa (7×10^{-5} mbar), without intentionally introducing gas, the ion density and ion flux were lower by almost two orders of magnitude. At high pressures, the electron temperature was in the range 1.5 - 3 eV. At background pressure, the electron temperature was much higher, $T_e = 14 \text{ eV}$, due to an easier electron diffusion from the source to the substrates as a result of the decreased plasma density and gas density.

The measured plasma properties show that the ion flux received by the substrates during pretreatment is comparable in the cases of arc discharges operated in vacuum and Ar glow discharges. However, in pretreatments by arc discharge, the ion flux can be increased by two orders of magnitude if a relatively high Ar pressure is used.

The presence of gas is not essential for the operation of an arc discharge, however, in many practical applications, inert and reactive gases are used to help sustain the arc discharge or to form metal nitrides on substrates in the chamber. The presence of gas in the chamber during arc discharge has a strong influence on the plasma density and composition.

Figure 4.1.3 shows two high speed photographs of the cathode surface during the operation of a magnetically steered Cr arc discharge at different gas pressures. It is clearly seen that when no gas is present (a), the plasma is concentrated only in the cathode spot, typically a few micrometres in size. When Ar gas is introduced (b), the plasma of the cathode spot is complemented by a post-plasma that is maintained over a large area around the target. Due to the trapping of electrons by the magnetic field and slower metal ion diffusion through the residual gas, the post plasma is characterised by a longer life time.

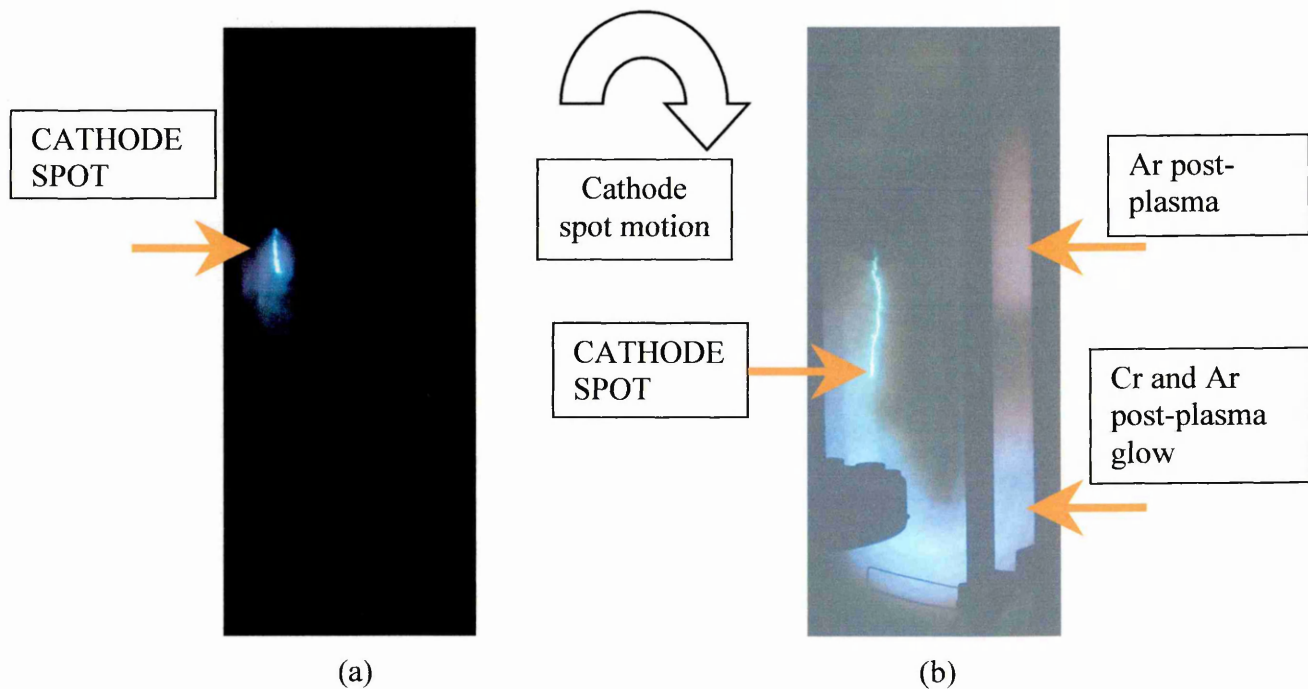


Figure 4.1.3. High-speed photographs of a Cr arc discharge showing the different plasma conditions on the target due to adding background gas. (a) - Arc discharge operated at base pressure of 0.003 Pa, (b) Arc discharge operated in Ar gas atmosphere at 0.1 Pa. Exposure time 1 ms. The composition of the post plasma is an estimate based on the dominating colour of the emission (red for Ar neutrals and blue for Cr ions and neutrals and Ar ions)

An important effect of adding gas in the vacuum chamber is that it promotes charge exchange reactions through collisions of metal ions with gas atoms [142, 55, 18]. The average charge state of the metal ions can be significantly reduced and gas atoms can be ionised.

4.1.3. Development of a Two-Stage Cathodic Arc Etching Procedure for Enhanced Adhesion on HSS.

The adhesion of hard films (TiAlYN) to substrates has been found a limiting factor in the performance of coated tools in the harsh conditions of dry high speed milling [143]. Extensive research on the substrate coating interface showed that adhesion can be improved dramatically by the introduction of an arc etching step prior to coating deposition [9, 143, 17]. The main factors improving the adhesion are considered to be a deep metal ion penetration and high metal ion concentration in the substrate.

The preceding section 4.1.2 showed that variations in gas pressure could be used to produce arc plasmas with a wide range of densities, structure and composition that can influence the effect of plasma treatment of substrates. In particular, such variations in plasma parameters can have a strong effect on the interfaces produced by arc etching as used in ABS processes. The controlled use of these plasma conditions required an in-depth investigation of the plasma composition and density as well as a more detailed understanding of the types of collisional processes occurring as a function of gas pressure (Section 4.1.3.1 and 4.1.3.2). Based on the plasma diagnostic results, a new two-step pretreatment stage incorporating operation of an arc discharge at high and low gas pressures was designed and applied on real components (Section 4.1.3.3). Finally, the chemical composition of the coating-substrate interface produced by the double-step pretreatment was investigated in TEM cross-sections (Section 4.1.3.4).

4.1.3.1. Ion Saturation Current of Cr Arc Discharge in Ar Atmosphere

The ion saturation current density received by substrates during cathodic arc pretreatment in the Hauzer ABS coater was investigated using planar and cylindrical electrostatic probes described in Chapter 3.5.4. The probes were positioned at a distance of 25 cm from the arc cathode as shown in Figure 3.1 in Chapter 3. The collecting plane of the flat probe could be rotated either to be parallel or perpendicular to the cathode plane.

Figure 4.1.4 shows the ion saturation currents measured at a probe voltage of -150 V with the flat and cylindrical probe in the two probe orientations given in Figure 3.1. The flat probe values in both orientations increase by $< 50\%$ as the pressure is

increased from 0.006 to 1 Pa and remain nearly constant at higher pressures. In a pure metal discharge (at 0.006 Pa with no intentional gas introduced in the chamber) the metal vapour flux is highly directional and a fraction of the electrons are lost from the ionisation process when scattered away from the metal plume. As the Ar pressure is increased the gas uniformly fills the chamber volume thus reducing these losses which results in more effective utilisation of the thermal electrons in the ionisation processes.[144, 145] This effect of increased plasma density around the substrate saturates for pressures above 1 Pa for the conditions of our experiment.

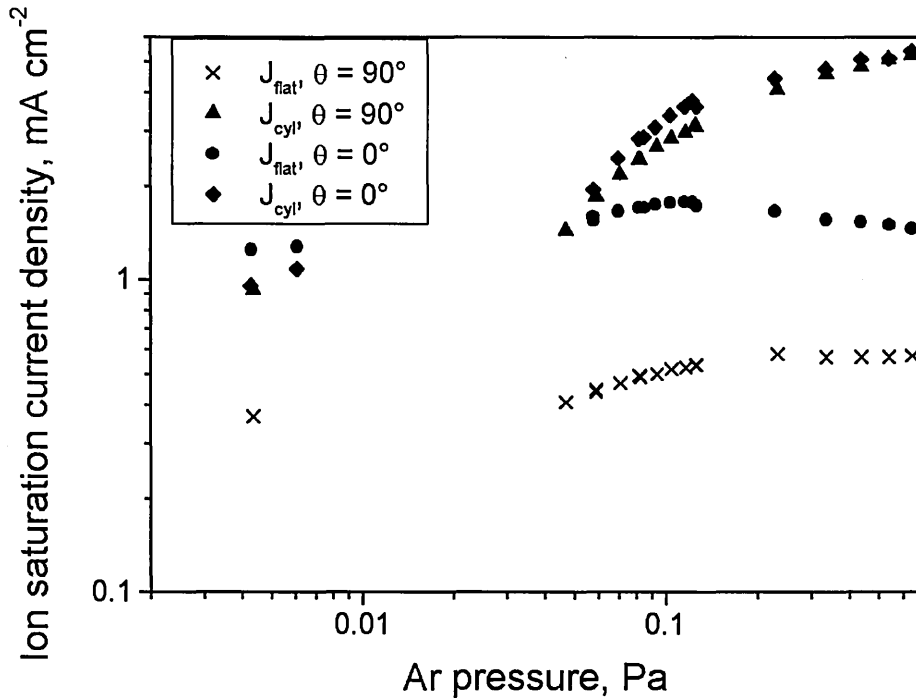


Figure 4.1.4. Ion saturation current densities measured by flat Langmuir probe for positions $\theta = 0^\circ$ (circles) and $\theta = 90^\circ$ (x) and cylindrical probe (rhombi and squares)

The data in Figure 4.1.4 show that the currents with the flat probe facing the cathode, $\theta = 0^\circ$, are larger than the currents with $\theta = 90^\circ$ by a factor of > 3 . When the probe plane is parallel to the cathode plane, it collects both ions arriving directly from the cathode spot (line of sight effect) and randomised ions that have undergone a number of collisions. In case of the perpendicular probe plane ($\theta = 90^\circ$), only randomised ions are collected [146]. Particularly at low pressures substantial differences in the current densities collected in the two different orientations were observed (Figure 4.1.4) indicating a highly anisotropic ion velocity distribution in the plasma. However, the dependencies tend to converge for both orientations with increasing $p_{Ar} > 1$ Pa due to gas scattering. This effect is more pronounced for the

cylindrical probe where the measured ion current densities increased rapidly with pressure and had overall higher values. When considering the practical applications, the latter means that samples with complex geometry, sharper edges and protruding parts will be etched at higher rates. To minimise distortions in the sample shape it is desirable to keep the gas pressure < 1 Pa and to reduce the overall etching time.

In order to estimate the effect of the variations in ion flux measured by the probes, substrate etching rate, R_{etch} , measurements at different Ar pressures, p_{Ar} , during the arc discharge were performed using the method outlined in Section 3.6.2. Figure 4.1.5 shows the variation of the R_{etch} as a function of p_{Ar} at a constant arc current on the Cr target of 100 A. The etch rate increased from 4.2 to 9.1 nm/min (by $\sim 115\%$) as the pressure is increased from 6×10^{-3} to 0.09 Pa.

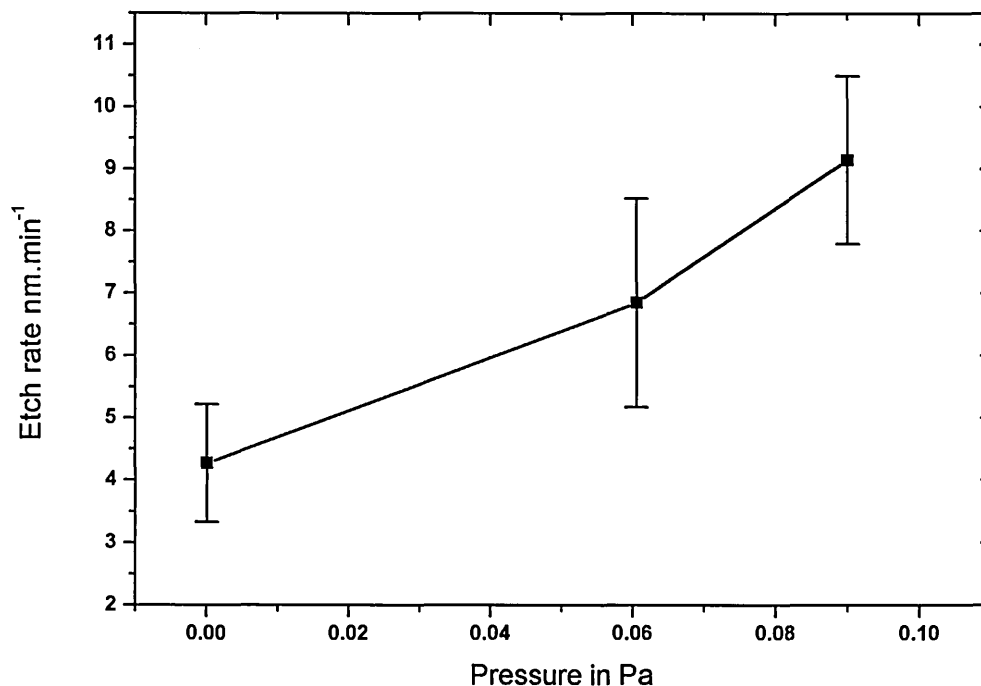


Figure 4.1.5 Etching rate of stainless steel substrates as a function of Ar pressure.

The increase in etching rates at higher gas pressures correlates with the increase in the ion saturation currents at the substrates indicating higher plasma density values (Figure 4.1.4). The measured increase in the ion current values (by $< 50\%$) in the pressure range < 1 Pa, however, accounts for less than half of the increase in the etch rate over the same pressure interval. The further enhancement of R_{etch} with p_{Ar} can be ascribed to an additional glow discharge, maintained at the substrate surface by the bias voltage of -1200 V, accelerating the electrons ejected during a secondary ion-electron emission by ions impinging on the substrate surface. The current density associated with

this discharge would be an increasing function of the gas pressure [121]. Such a discharge can be observed visually as a uniform glow around the biased substrates with an intensity which increases with p_{Ar} .

4.1.3.2. Plasma Composition of Cr, Ti and Nb Arc Discharges in Kr, Ar, Ne, and He Atmosphere

As shown by OES investigations in Chapter 4.1.1, the ion flux originating from the cathode spot is highly ionised and contains multiply charged metal ions - in the Cr arc, an average charge of up to 2.09 with up to 3-fold multiply charged ions have been reported [48]. We were able to detect optical emission signals from Cr neutrals and Cr ions with charges 1+ and 2+ within the spectral range of 200-950 nm of the spectrometer used. An example of a spectrum collected at an Ar pressure of 0.06 Pa is presented in Figure 4.1.1a.

The effect of gas type and pressure on the charge state distribution of metal ions in the arc discharge was studied in detail. Optical emission spectroscopy (OES) (Sections 3.5.1 and 3.5.2) studies of steered arc discharges in the Hauzer ABS coater (Section 3.1) was used to gain a qualitative understanding of the behaviour of metal neutrals and ions at different gas pressures ranging from 0.006 Pa to 0.6 Pa. Time of Flight spectroscopy measurements in the MEVVA random arc source (Section 3.2) were used to analyse the behaviour of the metal and gas ions and to determine quantitatively the charge state distribution of the metal ions. The range of pressures investigated was measured to be from 10^{-5} Pa to 10^{-2} Pa. Due to a differential pumping arrangement, the actual pressure in the arc chamber was calculated to be two orders of magnitude higher.

Figure 4.1.6 shows the relative optical emission measurements of Cr^0 , Cr^{1+} , and Cr^{2+} received from a Cr arc discharge as a function of p_{Ar} . As the Ar pressure is increased the concentration of Cr^{1+} and Cr^{2+} ions decreases continuously. Particularly in the case of two-fold charged Cr the intensity drops to half of its value when the Ar pressure is raised from 0.01 to 0.1 Pa. The overall ion current densities increase, however, which indicate that this increase is largely due to Ar ions. The trends for Cr are observed also in Ti and Nb arc discharges. Figure 4.1.7 (a) and (b) shows the normalised emission intensity of Ti neutrals and ions. In an Ar atmosphere, the Ti^0 neutral emission starts increasing as soon as some Ar is introduced in the chamber. In a

Helium atmosphere, the increase in Ti neutral emission occurs at much higher pressures. The case of Niobium shown in Figure 4.1.7c is different from both Cr and Ti in that the increase in neutral emission occurs at a higher pressure of about 0.1 Pa

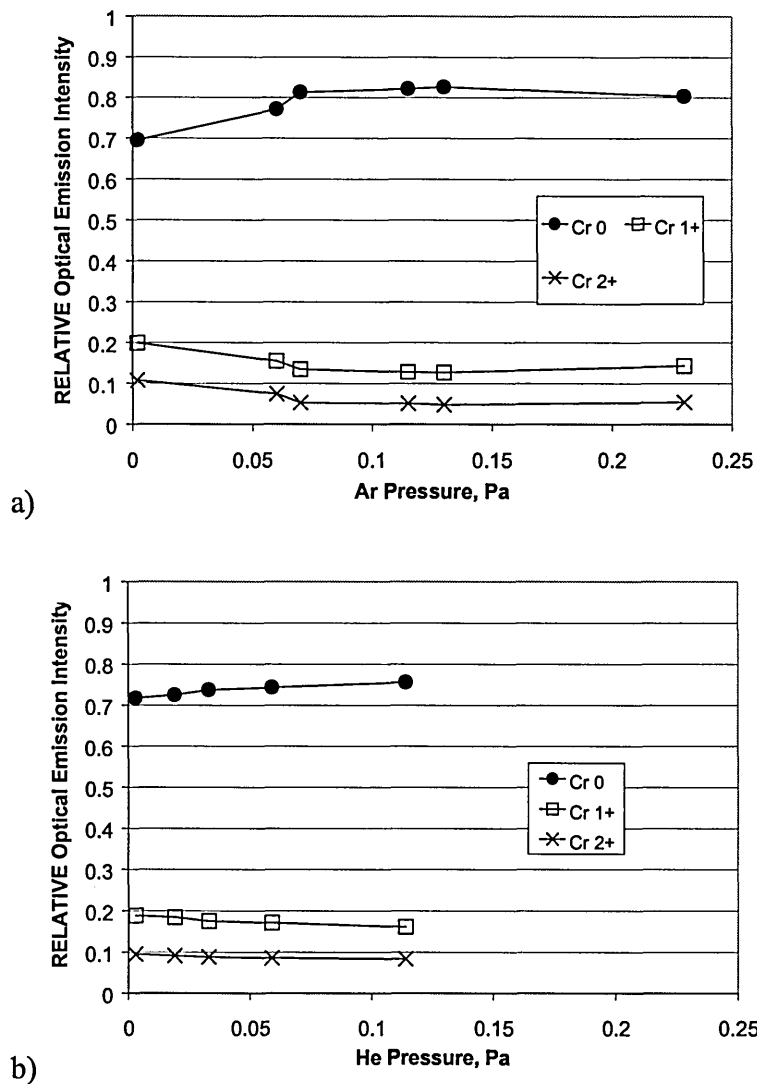


Figure 4.1.6. Variation of the emission from Cr neutrals, and ions with pressure. In Ar atmosphere (a) the emission is altered due to collisions with Ar atoms, in He atmosphere (b) collisions are less effective.

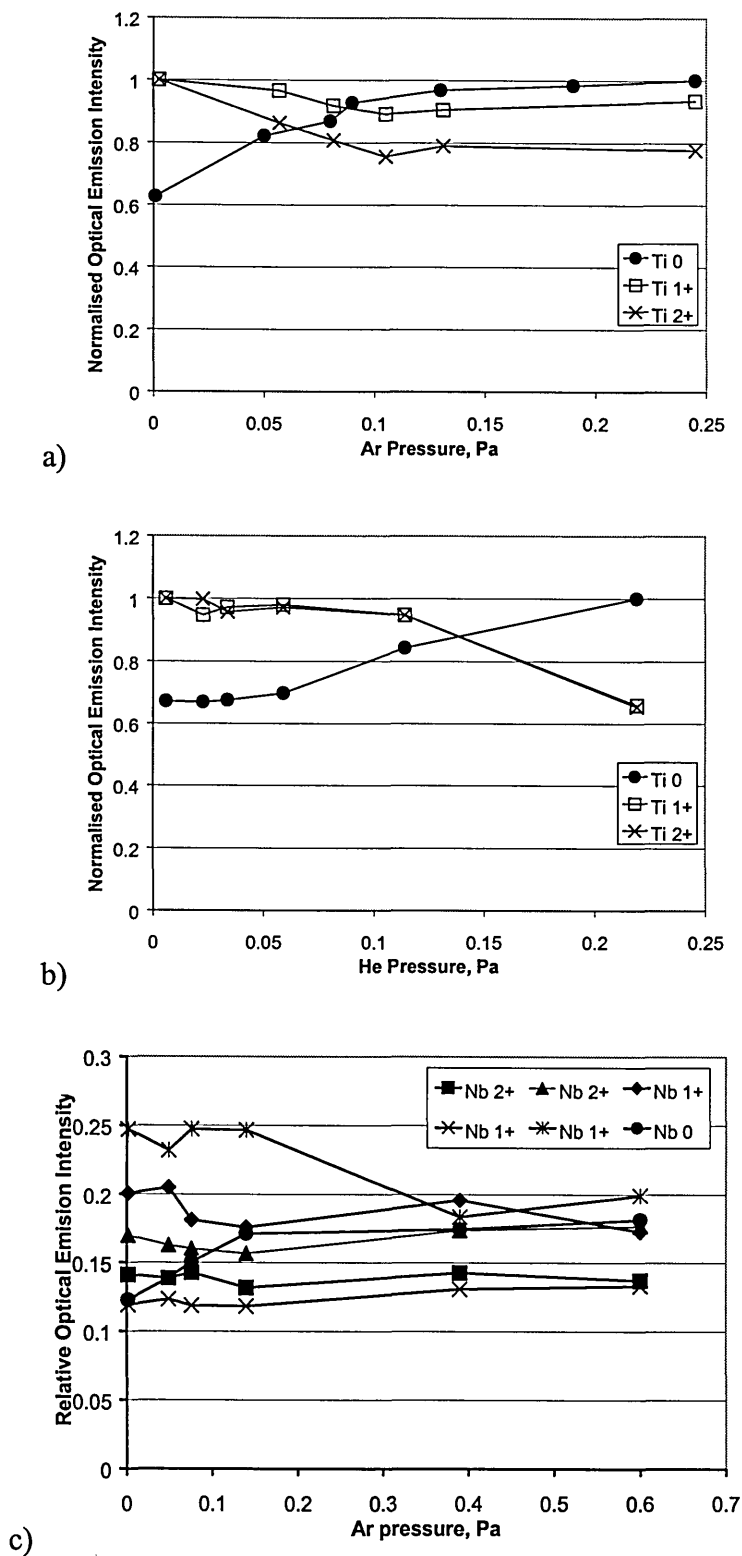


Figure 4.1.7 Variation of the emission from Ti and Nb neutrals, and ions with pressure. In Ar atmosphere (a) the emission from Ti is altered due to collisions with Ar atoms, in He atmosphere (b) collisions with Ti ions are less effective. Nb neutral emission increases at higher Ar pressures than Ti and Cr (c).

The results obtained from OES show that increasing the gas pressure in general causes the intensity of higher charged ions to decrease and the intensity of neutral species to increase. In order to quantify the observed effect, time of flight spectroscopy in the MEVVA source as described in Section 3.2 was used. Although the experimental conditions such as gas pressure and discharge current were similar in the Hauzer ABS machine and the MEVVA arc source, there was a major discrepancy between the two sources in that the first one employs a magnetic field with a strength of a few hundred Gauss to steer the arc while the latter is a random arc. Arc discharge characteristics are influenced strongly by the presence of magnetic field [54], mainly due to ionisation of the gas or effects due to the confinement of the spot. However the results obtained in both set ups agreed reasonably well, indicating that the dominating processes observed were independent of magnetic field.

A typical TOF spectrum is shown in Figure 4.1.2. The y-axis represents the current measured at the collector. The charge state distribution was derived by dividing the current by the charge. The TOF spectra were recorded after averaging over 100 pulses. The trends showing the influence of external parameters such as gas pressure on the TOF spectra were reproducible to within 5% as verified by repeating the same measurement 4 times using different cathodes of the same material.

The MEVVA discharge was operated with a current of 100 A. Cr and Nb were used as cathode materials. Ne, Ar and Kr were used as atmosphere forming gases. The effect of increasing gas pressure on the charge state distribution was studied. After compiling all measurements of the influence of gas pressure on individual charge states, a clear differentiation could be made between the behaviour of high and low charge states.

Figure 4.1.8 summarises the behaviour of the metal charge states 3+ and higher for Nb and Cr in Ne, Ar, and Kr atmospheres. A marked decrease in density of all highly charged ions is clearly identifiable.

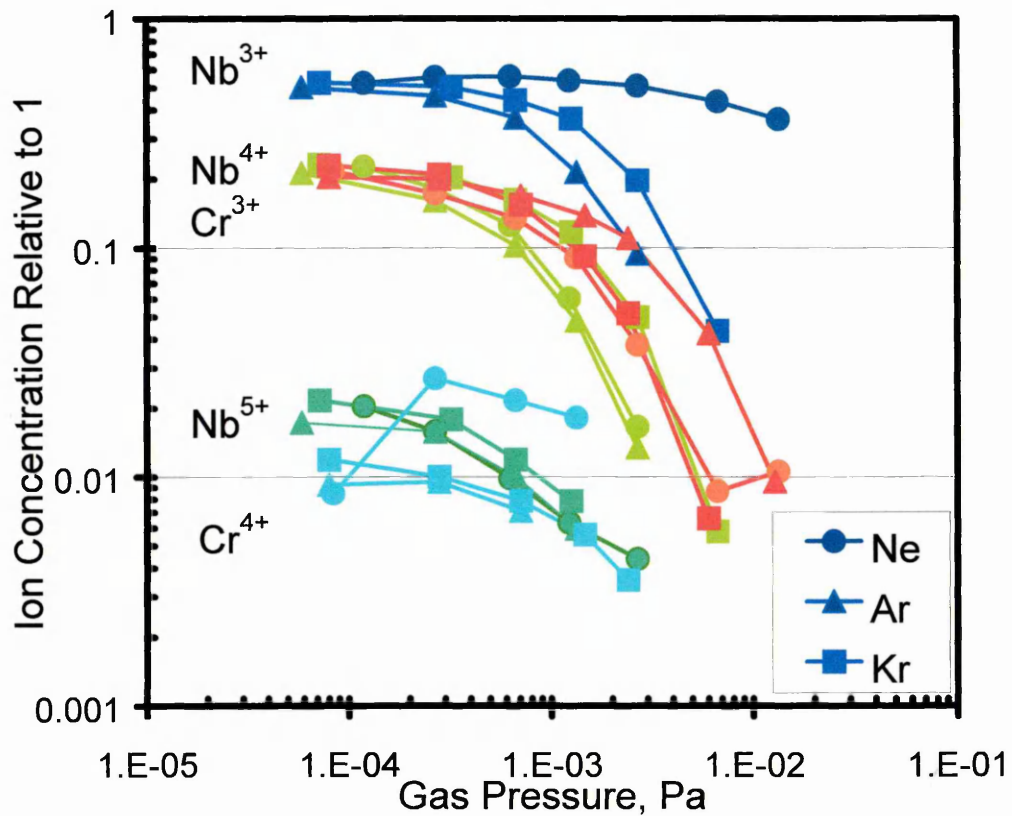


Figure 4.1.8. Influence of gas pressure on highly charged ion densities. Legend the ions are represented by colour: Nb^{3+} - blue, Nb^{4+} - pink, Nb^{5+} - green, Cr^{2+} - orange, Cr^{4+} - light blue. The different gases forming the atmosphere are represented by symbols: Ne atmosphere - circles, Ar atmosphere - triangles, Kr atmosphere - squares.

In contrast, the population of lower ionisation states such as Cr^{1+} , Nb^{2+} and Nb^{1+} increase monotonically with pressure, as summarised in Figure 4.1.9. Additionally, the increase of density of lower charged states is influenced by the gas type, with heavier gases (Kr) causing larger increase. An obvious exception is the Nb + Kr interaction. The increase in Nb^{1+} density is considerably faster in Kr than in the other gases. The increase in Nb^{2+} metal ion density is weaker in Kr than in Ar atmosphere.

Finally, it can be seen that the Nb^{2+} density reaches a saturation point at a certain pressure level. The saturation pressure is lowest in Kr and highest in Ne atmosphere

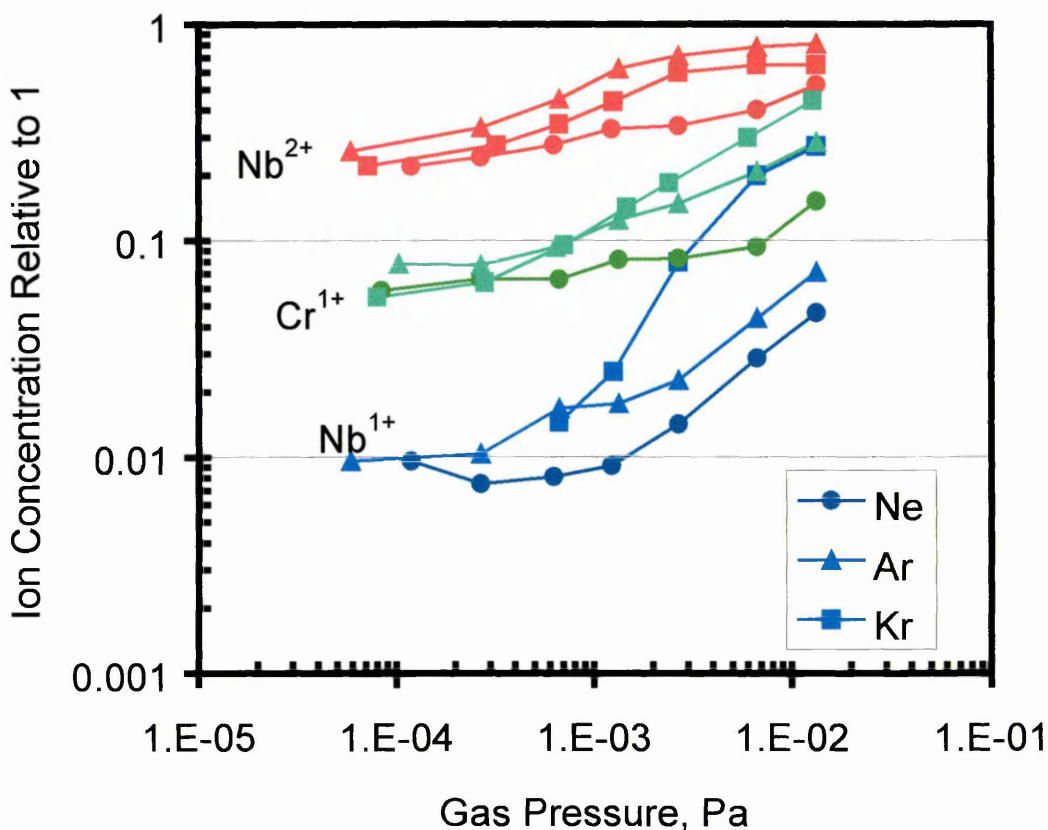


Figure 4.1.9. Influence of gas pressure on low charged ion populations. Legend: the ions are represented by colour: Nb^{1+} - blue, Nb^{2+} - red, and Cr^{1+} - green. The different gases forming the atmosphere are represented by symbols: Ne - circles, Ar - triangles, Kr - squares.

A qualitative difference in behaviour of Cr^{2+} in different atmospheres is illustrated in Figure 4.1.10. The population of Cr^{2+} is depleted due to collisions in Ar and Kr atmosphere. However, in Ne atmosphere, the Cr^{2+} density does not decrease at high pressures, on the contrary a slight increase can be observed.

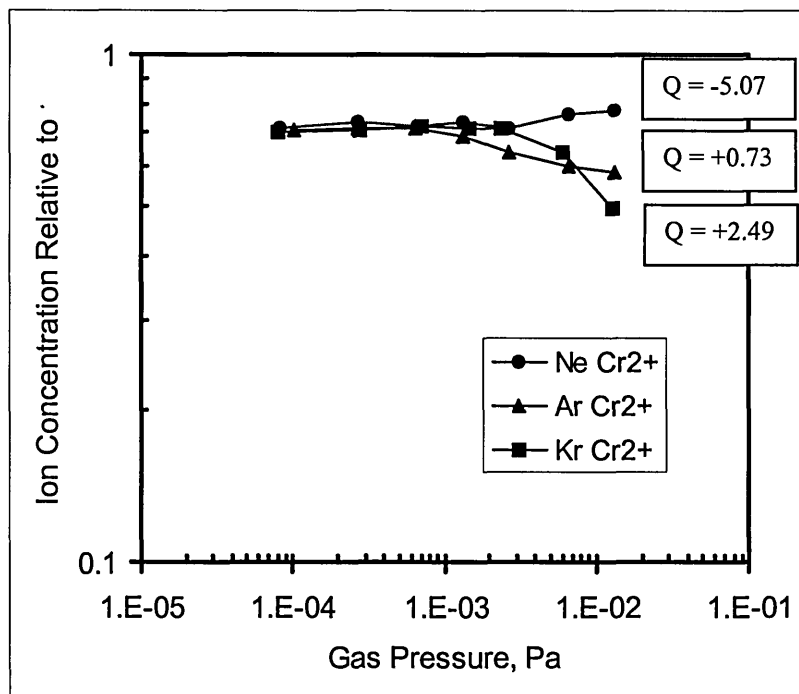
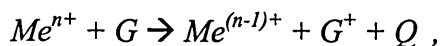


Figure 4.1.10. Cr^{2+} ion concentration as a function of gas pressure for three types of gases. The charge transfer between Cr^{2+} and Ne needs additional 5.07 eV.

The results from TOF spectroscopy agree well with the OES results, showing that higher charged states are strongly depleted at high gas pressures, while the density of neutrals and ions with lower charge is increased. These findings can be attributed to intensive charge exchange collisions occurring between metal ions and gas atoms. [60, 52, 142, 55, 18]

When the metal vapour produced in the cathode spot enters the anodic region of the arc discharge, the metal ions collide with gas atoms. These collisions are the main reason for metal neutralisation since the process of direct recombination of electrons with metal ions in two-body collisions does not conserve energy and momentum, and a three-body recombination is unlikely at the pressures discussed. The ion-atom collisions lead to a charge exchange process [60, 142, 18] of the type:



where Me^{n+} is a metal ion with charge n , G is a gas atom, and Q is the energy defect determined from the difference in ionisation potentials of the ion and the atom, viz. $Q = IP(Me^{n+}) - IP(G)$. It is important to note that the conservation of momentum and energy impose some restrictions on the initial kinetic energy E_0 of the impacting particles, especially in the cases when $Q < 0$. In particular, $E_0 \geq Q (m_{Me} + m_G)/m_G$.

In the cases when $Q > 0$, the charge exchange reaction is exothermic and the excess potential energy is dissipated as kinetic energy of the resulting particles. Charge exchange can occur even when the atoms have initial kinetic energies near zero eV [147]. In this case the mass ratio of the colliding species (e.g. m_{Me} / m_G) does not influence the charge transfer reaction and its cross section is limited mainly by the probability of collision. The situation $Q > 0$ is typically observed in collisions of highly charged metal ions with inert gas neutrals.

Charge exchange collisions of singly and, in special cases, doubly ionised metal ions with inert gas atoms usually have $Q < 0$ eV. The probability of charge exchange is much lower compared to highly charged ions but the reaction could take place if the energy deficiency is supplied from excitation states or kinetic energy of the impinging metal ion [148, 149, 61]. The charge exchange process is also more likely for ions from the high-energy tail of the ion energy distribution function (IEDF) and atoms with large radii and, therefore, large collision cross section.

Table 4.1.3 shows the ionisation potentials and the energy defect Q for the particular metals and gases used in this work.

Table 4.1.3. Ionisation potentials and energy defect, Q , eV, after charge exchange

Charge State	Ionisation potential, eV	Ne	Ar	Kr	Kr ¹⁺
		21.56	15.76	14.00	24.36
Cr					
1+	6.76	-14.80	-9.00	-7.24	-17.60
2+	16.49	-5.08	0.73	2.49	-7.88
3+	30.96	9.40	15.20	16.96	6.60
4+	49.16	27.60	33.40	35.16	24.80
Nb					
1+	6.76	-14.80	-9.00	-7.24	-17.60
2+	14.32	-7.24	-1.44	0.32	-10.04
3+	25.04	3.48	9.28	11.04	0.68
4+	38.03	16.47	22.27	24.03	13.67
5+	50.55	28.99	34.79	36.55	26.19

Table 4.1.4 lists the initial kinetic energies required to compensate for the reactions from Table 4.1.4 as calculated from momentum and energy conservation equations.

Table 4.1.4. Initial kinetic energy E_0 , eV required to compensate for the energy deficiency in a charge exchange reaction

Charge State		²⁰ Ne	⁴⁰ Ar	⁸⁴ Kr	
⁵² Cr	$(m_g+m_{Cr})/m_g:$		3.60	2.30	1.62
	1+		53.28	20.70	11.72
	2+		18.27	-1.67	-4.02
	3+		-33.84	-34.96	-27.46
	4+		-99.36	-76.82	-56.93
⁹³ Nb	$(m_g+m_{Nb})/m_g:$		5.65	3.33	2.11
	1+		83.63	29.93	15.26
	2+		40.91	4.79	-0.67
	3+		-19.66	-30.86	-23.26
	4+		-93.06	-74.05	-50.63
	5+		-163.79	-115.68	-77.02

The tables can be used as follows: for a reaction between Cr and Ar:

$Cr^{1+} + Ar \rightarrow Cr^{0+} + Ar^+ - 9.00 \text{ eV}$ ($Q = -9.00 \text{ eV}$). The initial kinetic energy required to compensate for the negative Q is 20.7 eV.

The decrease in population of highly charged states is consistent with a domination charge exchange reaction. Comparison of the reactions shown in Figure 4.1.8 (TOF) with the data listed in Table 4.1.3 shows that the reactions leading to a decrease all have positive Q values. As indicated above, reactions with $Q > 0$ have a large cross section and are independent of the mass ratio of the colliding species. Therefore, Cr and Nb charge states above $3+$ undergo charge exchange reactions at high rates regardless of the type of gas in the atmosphere.

The results from lower charge states are also consistent with a charge exchange theory. All reactions shown in Figure 4.1.9, except $\text{Kr}^{2+} + \text{Ar}$, have a $Q \ll 0$ and the density of all species increases as a function of pressure. The increase is due to the additional ions produced in intensive charge reducing exchange reactions involving highly ionised species. Table 4.1.4 shows that in order to undergo a charge transfer collision the ions are required to have energies between 4.79 eV and 83 eV. The IEDF of ions produced in the cathode spot peaks at energy in the range 30 - 50 eV, while the high energy tail can extend to 80 eV [57]. These energies are sufficient to enable the charge transfer reaction and promote the production even of metal neutral species, as was shown by OES results presented in Figures 4.1.6 (a) and 4.1.7(a) and (c).

The charge transfer probability depends also on the geometrical size of the atoms. Gases with larger atomic radii have larger collision cross sections. As shown in Figure 4.1.9, lower charge states are populated fastest in Kr with atomic radius 88 pm and slower in Ar - 71 pm and Ne - 38 pm.

An interesting behaviour is manifested in the Cr^{2+} density. In Ar and Kr, the Q value in charge transfer reactions is positive and the metal ion density is depleted. However in Ne atmosphere, the Q value is negative and the metal ion density is increased due to population from higher charge states.

A similar behaviour to that of Cr^{2+} is manifested by the Nb^{2+} interaction. The Q value for $\text{Nb}^{2+} + \text{Kr}$ is slightly positive but the reaction rate is not fast enough to cause an overall decrease. Instead, Figure 4.1.9 shows that the charge exchange rates in Kr atmosphere drop below those in Ar atmosphere (c.f. other reactions in the same figure). Additionally an intensified population of the Nb^{1+} state is observed.

The behaviour of the gas ion density reveals further details of the interactions in the arc discharge. Figure 4.1.11 shows the influence of gas pressure on the gas ion density in a Cr arc discharge measured by TOF spectroscopy. As the pressure increases, the gas ion density increases to a saturation point after which it decreases

rapidly. Moreover, the concentration of the lighter gas ions saturates at lower pressures than heavier ones.

The saturation and decrease of the signal indicate that there is a competition between two opposing processes. On one hand, the increase in pressure leads to a decrease in the mean free path for collisions. Consequently, the charge transfer process of gas neutrals with Cr^{3+} ions resulting in the creation of ionised gas is intensified. On the other hand, the increase of pressure also increases the frequency of elastic scattering collisions whereby fast ions lose energy and are confined to a smaller space near the source. A decrease in the signal from all species was routinely observed during the experiments at the high pressure end.

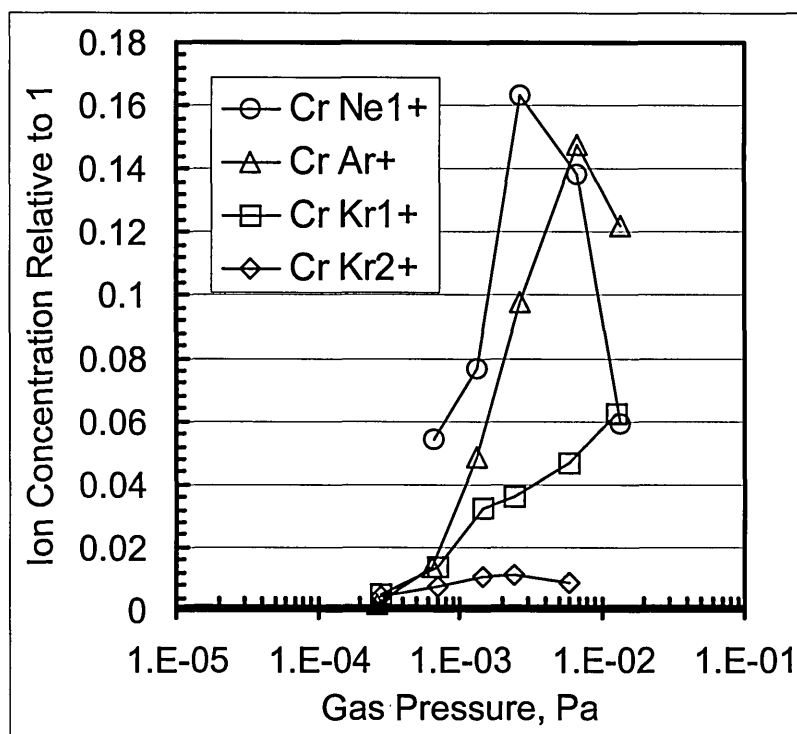


Figure 4.1.11. Influence of gas pressure on the gas ion concentration in a Cr arc discharge.

Scattering is also observed for the metal ions. It is especially clear in the Nb^{2+} case shown in Figure 4.1.9. The metal ion density saturates at low pressures when the atmosphere comprises heavy and large atoms like Kr. However, no saturation is observed in Ne atmosphere comprising lighter and smaller atoms.

Finally, the overall effect of the charge exchange collisions is demonstrated clearly in the influence of gas pressure on the average charge state. Figure 4.1.12 shows the behaviour of the average charge state of Cr and Nb in Ne, Ar, and Kr atmosphere at

different pressure. In the case of Cr the average charge state drops most strongly in Kr atmosphere from 2.1 at 8×10^{-5} Pa (8×10^{-7} mbar) to 1.5 at 0.01 Pa (1×10^{-4} mbar). The Nb charge state drops most strongly in Kr atmosphere from 3 at 8×10^{-5} Pa (8×10^{-7} mbar) to 1.7 at 0.01 Pa (1×10^{-4} mbar). Changing the type of gas in the atmosphere leads to differences of the order of 20 % in the Cr case and 35 % in the Nb case.

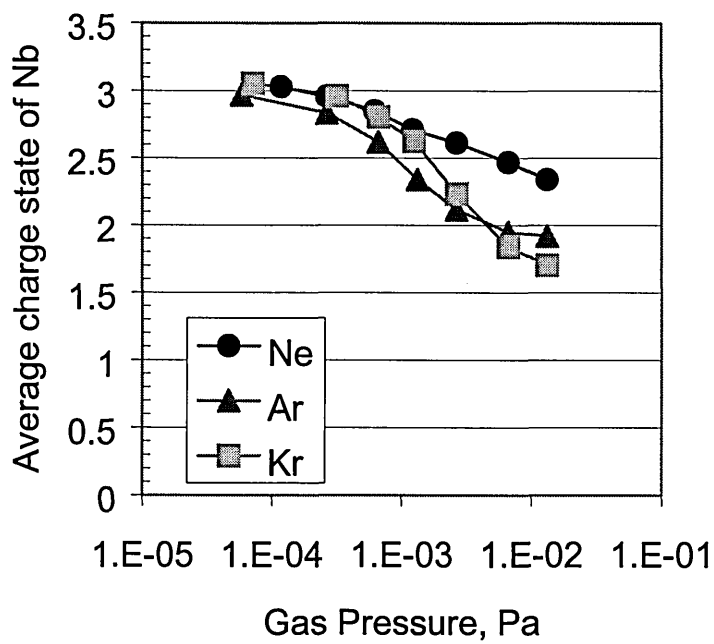
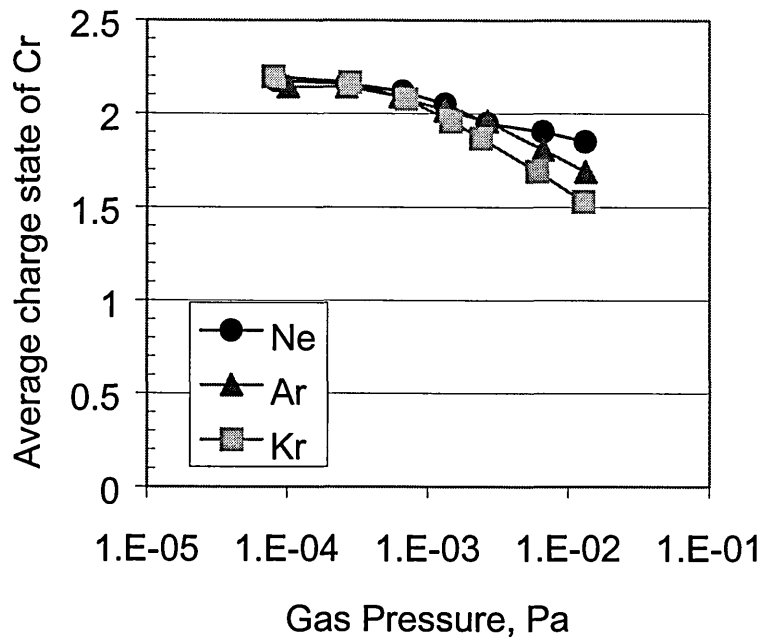


Figure 4.1.12. Average charge state determined by Time of Flight Spectrometry of Cr and Nb random arcs as a function of pressure and type of atmosphere.

Investigations by Nikolaev et al [150] and Spädtke et al [151] have revealed the behaviour of the CSD of a plurality of cathode materials and in a variety of gas atmospheres. The data presented in these studies is consistent with the explanation proposed here that charge exchange processes are an important part of particle interactions between arc plasmas and gas.

The plasma investigation results can be summarised as follows.

1. Increasing the gas pressure decreases strongly the average charge state of metal ions in an arc discharge depleting strongly the highly charged states.
2. Lighter and smaller gas atoms contribute less to the charge transfer process.
3. Increasing the gas pressure increases the ion flux to the substrates due to ionisation of the gas atoms
4. Increasing the gas pressures leads to randomisation of the ion flux.
5. Elastic scattering ultimately causes a decrease in ion flux to substrates at high gas pressures (> 0.1 Pa)

4.1.3.3. Coating Sequence Incorporating a Two-Step Etching Treatment

In summary the investigations from sections 4.1.3.1 and 4.1.3.2 showed that increasing the gas pressure during an arc discharge leads to enhanced etching rates as a result of an increase in the plasma density around the substrate, randomisation of the ion fluxes generated in the cathode spot and ignition of an additional glow discharge on the negatively biased substrates. The concentration of highly charged metal ion species, as revealed by optical and TOF spectroscopy, falls; thus the increase in the ion densities is primarily due to ionisation of argon atoms.

Using this information we designed a coating process presented in Figure 4.1.13. The process starts with heating and outgassing of the substrates. This is followed by sputter cleaning of the targets using a magnetron glow discharge and closed shutters. Before coating deposition, a modified etching step was introduced and investigated. The etching process was based on a Cr arc discharge operating in Ar atmosphere and consisted of two steps. During the high-pressure (0.09 Pa) etching step, which is with longer duration (8 min), we use ion irradiation with a significant component of Ar ions to clean the substrate at a high rate and effectively remove surface oxides and carbides. During the shorter (2 min) second step we use Cr arc with no intentionally introduced gases (only residual gases) seeking to maximise the transport of highly charged metal ions and achieve an enhanced metal ion implantation while preserving the crystallographic order of the substrate grains and, hence, allowing localised epitaxial growth during subsequent film deposition. The total time is reduced by half compared to the standard procedure developed in ref. [143] and [10] in which Cr-arc etch at $p_{Ar} = 0.06$ Pa for 20 min was used. As presented in Figure 4.1.13 we also investigated the latter process with the etching time reduced to 10 min. In the specific case of the ABS technology, it is extremely beneficial to minimise the etching (pretreatment) duration because it is directly related to the number of droplets and growth defects incorporated in the coating.

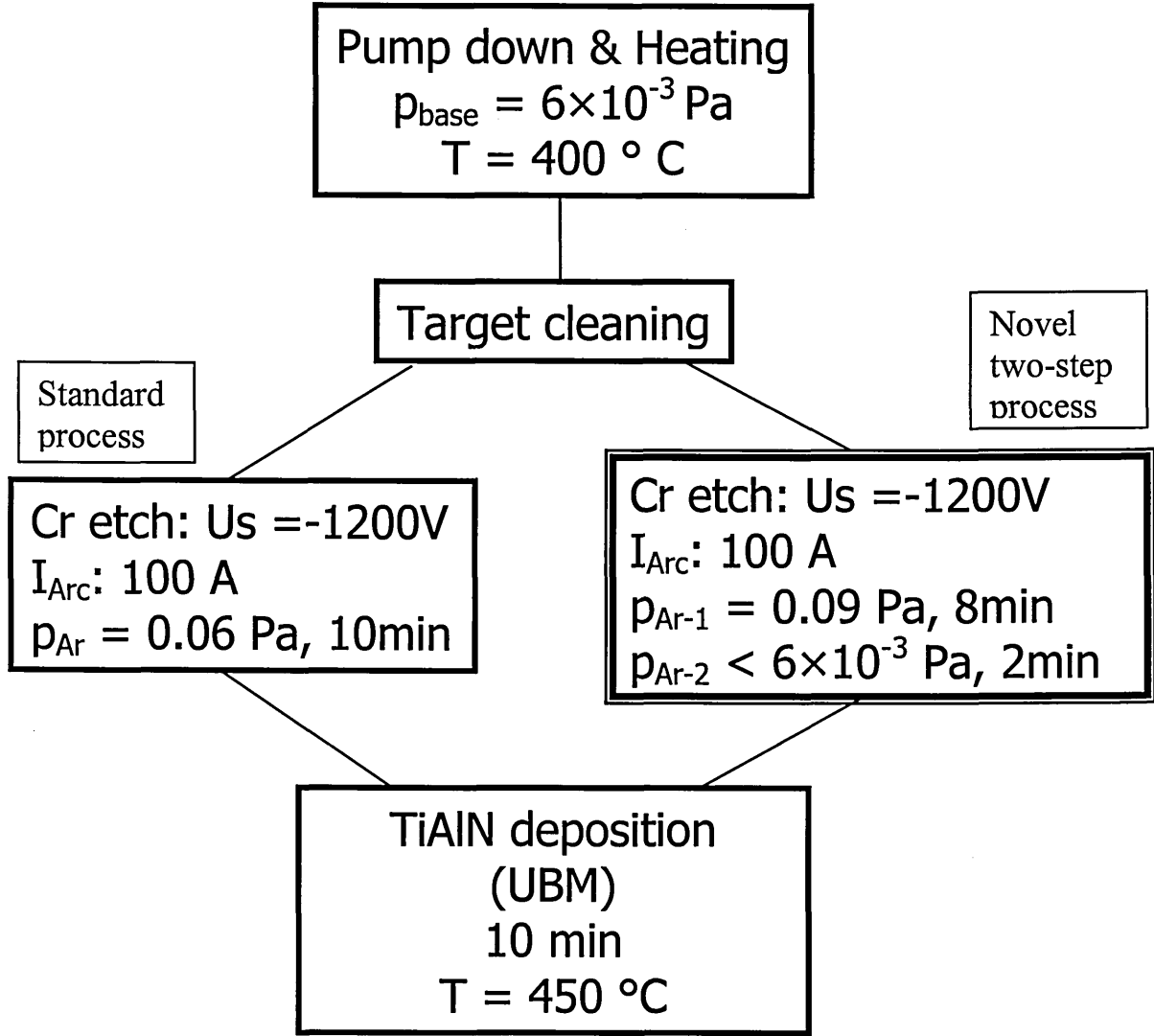


Figure 4.1.13. Process sequence of one step (standard) and two-step etching procedures.

4.1.3.4. Implantation Profiles of Cr Ions at Different Ar Pressures

Reports in the literature have shown that a clean substrate surface together with a well-preserved crystal structure at the substrate surface is crucial to promote local epitaxial growth and to achieve beneficial preconditions for excellent adhesion [143, 10]. A combined / mixed Cr^+ and Ar^+ ion bombardment of the substrate surface lasting over a period of 20 minutes has been shown to be sufficient to satisfy both demands mentioned above. In those experiments the substrate material removal rate was estimated to be ~ 7 nm/min leading to a total etching depth of ~ 140 nm ($p_{\text{Ar}} = 6 \times 10^{-2}$ Pa). In both procedures studied here, the etching period has been recommended to be reduced to only 10 min. The total etch depth in the present experiments was determined to be approximately 70 and 80 nm for the one-step and two-step etch procedures respectively. Although the total removal of substrate material is reduced to ~ 80 nm the substrate surface is obviously clean enough to provide conditions for local epitaxial growth of $\text{Ti}_x\text{Al}_{(1-x)}\text{N}$ on Cr implanted α -Fe. A definite indication of local epitaxial growth of the $\text{Ti}_x\text{Al}_{(1-x)}\text{N}$ coating on the ferritic low carbon steel substrate is observed from plan view TEM imaging. This can be concluded from dark field (DF) images as given in Figure 4.1.14a. Regions of identical crystallographic orientation extend over several micrometres, exhibiting sharp grain boundaries between adjacent grains. These boundaries are correlated with grain boundaries of the underlying steel substrate as was previously shown by cross sectional TEM for the case of 20 min Cr ion bombardment at $p_{\text{Ar}} = 6 \times 10^{-2}$ Pa, [10] indicating typical grain sizes of several micrometres. In the absence of local epitaxial growth on substrate grains typical column sizes, revealed by TEM, are two to three orders of magnitude smaller (see e.g. Ref. [10]).

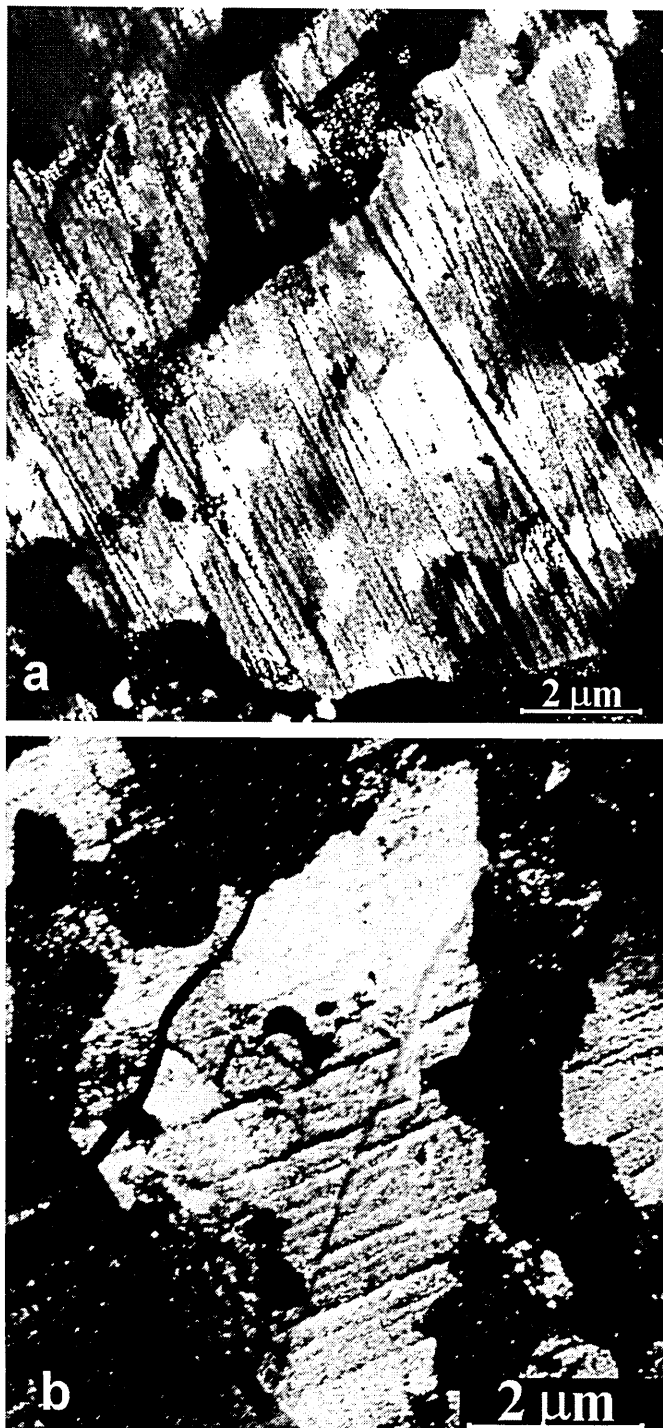


Figure 4.1.14. Plan view dark field images of TiAlN coating grown on low carbon steel after (a) 10 min two step sputter cleaning procedure (b) 10 min sputter cleaning

These results are confirmed, as exemplified by the plan view TEM dark field image in Figure 4.1.14b, in the present experiments of sample treatment with mixed Cr + Ar ion bombardment at $p_{Ar} = 6 \times 10^{-2}$ Pa, despite the fact that the etching time has been reduced to 10 min.

Despite the similarities in the microstructure of the $Ti_xAl_{(1-x)}N$ coatings grown subsequently after etching, significant differences in the interface chemistry are observed when the one step etching process ($p_{Ar} = 6 \times 10^{-2}$ Pa) is compared to the modified two step etching case starting with a mixed $Cr^+ + Ar^+$ ion bombardment at $p_{Ar} = 9 \times 10^{-2}$ Pa followed by “pure” Cr ion bombardment at residual gas pressure. STEM-EDX profiles of the resulting two interfaces are shown in Figure 4.1.15. An apparently identical maximum concentration of Cr of about 37at% is observed for both the one step and the modified two step etching cases (Figure 4.1.15). (These values of maximum concentration at the interface involve the uncertainty caused by the limited lateral resolution of ± 2.7 nm). However, the shapes of the implantation profiles exhibit significant differences. A comparatively sharp interface profile for the 10 min. process with mixed $Cr^+ + Ar^+$ bombardment (Figure 4.1.15a) is observed. In contrast, the corresponding profile of Cr in the two stage process, which is completed with the “pure” Cr bombardment exhibits a narrow plateau close to the interface extending 4.5 nm into the steel (Figure 4.1.15b). In addition, a deeper Cr penetration is observed in the latter case. Here a significant Cr peak (not shown) was detected in the EDX spectrum even as deep as 20 nm whereas in the case of the one step etching procedure significant levels of Cr could be found only to a depth of 13 nm (Figure 4.1.15a). These results indicate clearly a more efficient implantation when a “pure” Cr ion bombardment of only 2 minutes duration completes the etching process. This conclusion is further confirmed by the determination of the integrated peak areas of 368 ± 27 at%nm representing Cr incorporated in the two step etching procedure compared to 216 ± 34 at%nm for Cr incorporation in the one step etching mode.

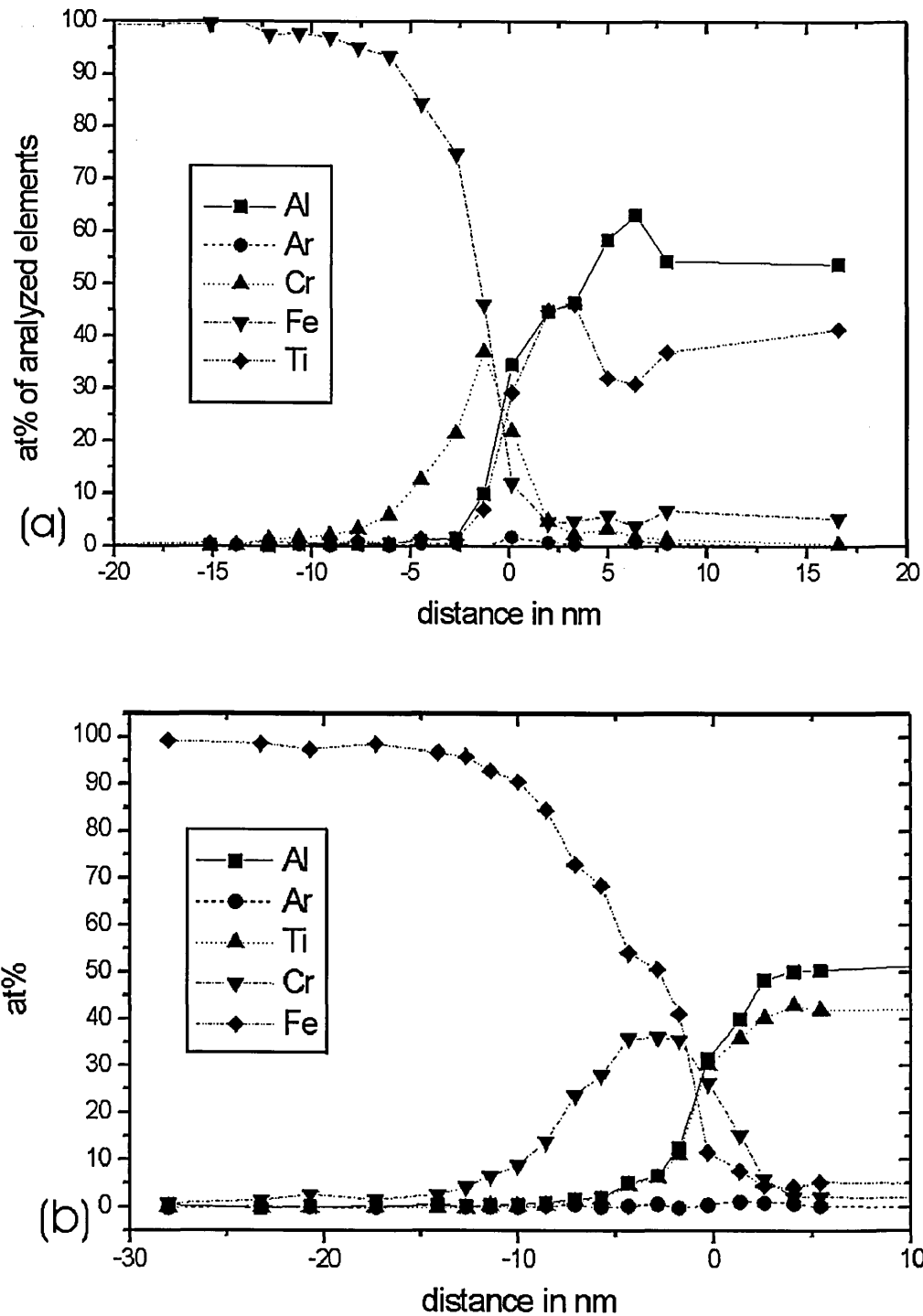


Figure 4.1.15. STEM-EDX profiles across low carbon steel/TiAlN interfaces obtained by (a) mixed Cr/Ar ion bombardment at $p_{Ar} = 6 \times 10^{-2}$ Pa for 10 min (b) mixed Cr/Ar ion bombardment at $p_{Ar} = 8.8 \times 10^{-2}$ Pa followed by pure Cr ion bombardment.

Further differences between the two etching processes were found with respect to the stress distribution across the interfaces as measured by glancing angle XRD. The stress levels measured directly at the interface of the etched, but uncoated austenitic

stainless steel substrates are too low to be quantified. However, high compressive stresses were found in the 100 nm thin coatings grown after both sputter-cleaning processes. The interface with the lower Cr incorporation exhibited a higher compressive residual stress in the coating (-8.3 GPa) in comparison to the case when pure Cr ion bombardment was involved (-6.8 GPa). It is interesting to note that the average residual stress in a 3.5 μm thick $\text{Ti}_x\text{Al}_{(1-x)}\text{N}$ coating was 3 GPa, independent of the two etching procedures applied.

The lower stress gradient found in the two stage etching process might explain the significant differences in the critical load values L_C obtained for both interfaces. Indeed the mean critical load value for samples processed in the two step etching mode showing the enhanced Cr incorporation was $L_C = 85 \pm 5\text{N}$ as compared to samples prepared after the one step etching procedure ($L_C = 63 \pm 3\text{N}$). Although the high stress values found in the 100 nm thin $\text{Ti}_x\text{Al}_{(1-x)}\text{N}$ coating adjacent to the interface could be attributed to grain size effects when competitive growth is involved (Hall-Petch), it is believed that epitaxial stresses are more likely to explain the observed effects. The higher Cr content found at the steel surface resulting from the two stage sputter cleaning procedure could therefore be responsible for an increase of the lattice parameter of the substrate which should reduce the mismatch between steel and $\text{Ti}_x\text{Al}_{(1-x)}\text{N}$ coating therefore leading to a lower epitaxial stress component and a flatter stress gradient at the interface. Similar observations were made for plasma nitriding the surfaces [152, 153].

The two-step process has now been adopted for routine use in research and production coating deposition runs by the surface engineering group at Bodycote/SHU Coatings Ltd.

Summary

It was found that the etching rates of negatively biased (-1200 V) steel substrates more than doubled with the introduction of argon gas to pressures ~ 0.1 Pa at constant arc current during a steered arc on a Cr target. Plasma probe measurements indicate that the ion current density on negatively biased substrates increases significantly with the increase of the argon pressure which is attributed to more efficient volume ionization processes in the presence of a gas atmosphere and to the ignition of an auxiliary glow discharge at the substrate surface. Optical emission and time-of-flight spectroscopy revealed a decrease in the concentration of metal ions with p_{Ar} , as a result of charge exchange processes, thus the increase in the ion current densities, and correspondingly in the etching rates, is due to argon ions. Based on these results we designed a two-stage sputter-cleaning procedure with reduced overall duration that involves a high-rate etch in the presence of Ar and an ion implantation step in pure Cr discharge. The modified sputter cleaning procedure provides substantial improvement of the adhesion conditions of the $Ti_xAl_{(1-x)}N$ coatings thus making the PVD process more robust. This improvement may be attributed mainly to the microchemistry in the interface transition zone controlled by the incorporation of Cr into the steel matrix. Critical load measurements confirm an increase of L_C from typically 63 ± 3 N to 85 ± 5 N. Stress measurements in the interface region suggest a flatter stress gradient in case of enhanced Cr content.

4.2. High Power Density Pulsed Magnetron Sputtering (HIPIMS) Discharge

This Chapter presents investigations of the plasma and discharge parameters of a novel PVD technique based on high power density pulsed magnetron sputtering (HIPIMS). Compared to conventional magnetron glow discharges, the power densities used in HIPIMS are two orders of magnitude higher, reaching 3000 Wcm^{-2} at a discharge current of 2 Acm^{-2} . As shown in Chapter 2, all plasma discharges can be classified according to their current. Figure 4.2.1 shows a plot of the discharge voltage vs. the discharge current for the different discharge types. The curve shows that at current densities above 100 mAcm^{-2} a transition from abnormal glow to arc discharge occurs.

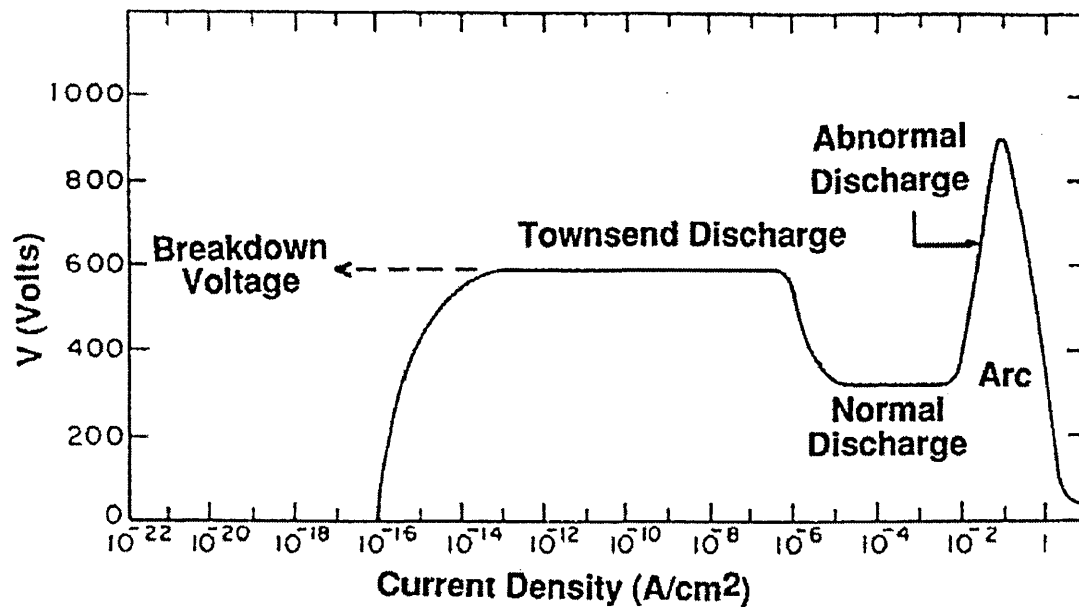


Figure 4.2.1. Voltage and current density of plasma discharges. [52]

The benefits of high plasma densities and metal ionisation and the corresponding high ion-to-neutral ratio in the particle flux generated in arc discharges are numerous (see Chapter 2 for details). For example, in plasma-immersion surface treatments faster etching rates can be achieved without deposition, as well as a deep ion implantation profile [17]. In thin film deposition, the increased ion-to-neutral ratio contributes to a densification of the microstructure [78], [37].

Despite these advantages, arc spots are detrimental in thin film deposition, because along with the vapour of the target material, they produce metal liquid 'droplets'. When embedded in a thin film, droplets induce large-scale (micrometer size)

growth defects that compromise severely the structure and density of the films (see Chapter 2 and discussion in Chapter 4.3).

The generation of arc spots and droplets is avoided in HIPIMS technology. Due to the pulsed nature of HIPIMS the discharge current densities reach values up to 2000 mAcm⁻² while the discharge remains distributed over practically the entire area of the cathode, similar to conventional magnetron sputtering. The plasma densities in HIPIMS reach extraordinarily high values, as much as 10¹³ cm⁻³ [21, 23] at a distance of 35 mm from the target. The ionisation probability of atoms in such a plasma is high.

This study shows that sputtered metal atoms, can be, e.g. for Cr and Ti, as much as two-fold ionised [23]. The results presented in this and the following Chapter 4.3 show the strong potential of HIPIMS as a PVD technique providing high ion-to-neutral ratios and multiply charged metal ions. Hard nitride films deposited by HIPIMS for the first time exhibited an extraordinarily dense microstructure while the mechanical properties rivalled those of superlattice multilayer thin films [26]. Additionally HIPIMS was used successfully for adhesion enhancing treatment of substrates prior to coating deposition [25].

The results presented in this chapter describe the influence of power on the HIPIMS discharge and its plasma parameters and discuss the conditions that may cause a glow-to-arc transition.

Cr, Ti, Ta, and C cathodes were used as model systems. The discharge I-V characteristic and confinement by crossed electric and magnetic (E×B) fields were evaluated. The plasma density was measured by electrostatic probes and the plasma composition was investigated by optical emission spectroscopy (OES). The metal ion to neutral ratio in the deposition flux was evaluated using the biasing/deposition technique described in Chapter 3.3. The effect of power on the time evolution of the plasma composition is discussed. Finally, the influence of operation time and pulse power on the frequency of glow-to-arc transitions is also discussed.

The chamber, power supply characteristics and discharge current and voltage measurements were as described in Section 3.3 and by Macak et al [98]. A target with a diameter of 50 mm was used for plasma investigations (Sections 4.2.1-4.2.4). Experiments with counting the number of arcing events (Section 4.2.5) were performed using a ø150 mm Cu target.

Macak *et al.* [98] were first to report a study of the plasma composition and temporal evolution of the HIPIMS using OES. Similar measurements presented in this chapter go beyond previous investigations in terms of an enhanced spectral range, covering the ultraviolet region, an improved resolution reducing the signal to noise ratio and a vastly superior sensitivity of photo-multiplier tubes (PMT) over charge coupled device detectors.

4.2.1. Influence of High Power Densities on the I-U Characteristic of Magnetrons

The current-voltage (I-U) characteristics of magnetron discharges carry a wealth of information about the mechanism of the discharge. The characteristic is found to be determined mainly by the pressure and the strength of the confinement magnetic field. It is well documented that conventional magnetron I-U characteristics follow a power law $I = kU^n$. The exponent n is typically in the range 5 to 15 [154] reaching low values when the discharge operates at low pressures or is confined by a weak magnetic field. Figure 4.2.2 shows the I-U characteristics of a magnetron discharge operated on a typical industrially sized rectangular (600×200 mm) cathode (Hauzer ABS machine, Chapter 3.1) and the high power density pulsed magnetron discharge of the present work operated on a cylindrical cathode, 50 mm in diameter.

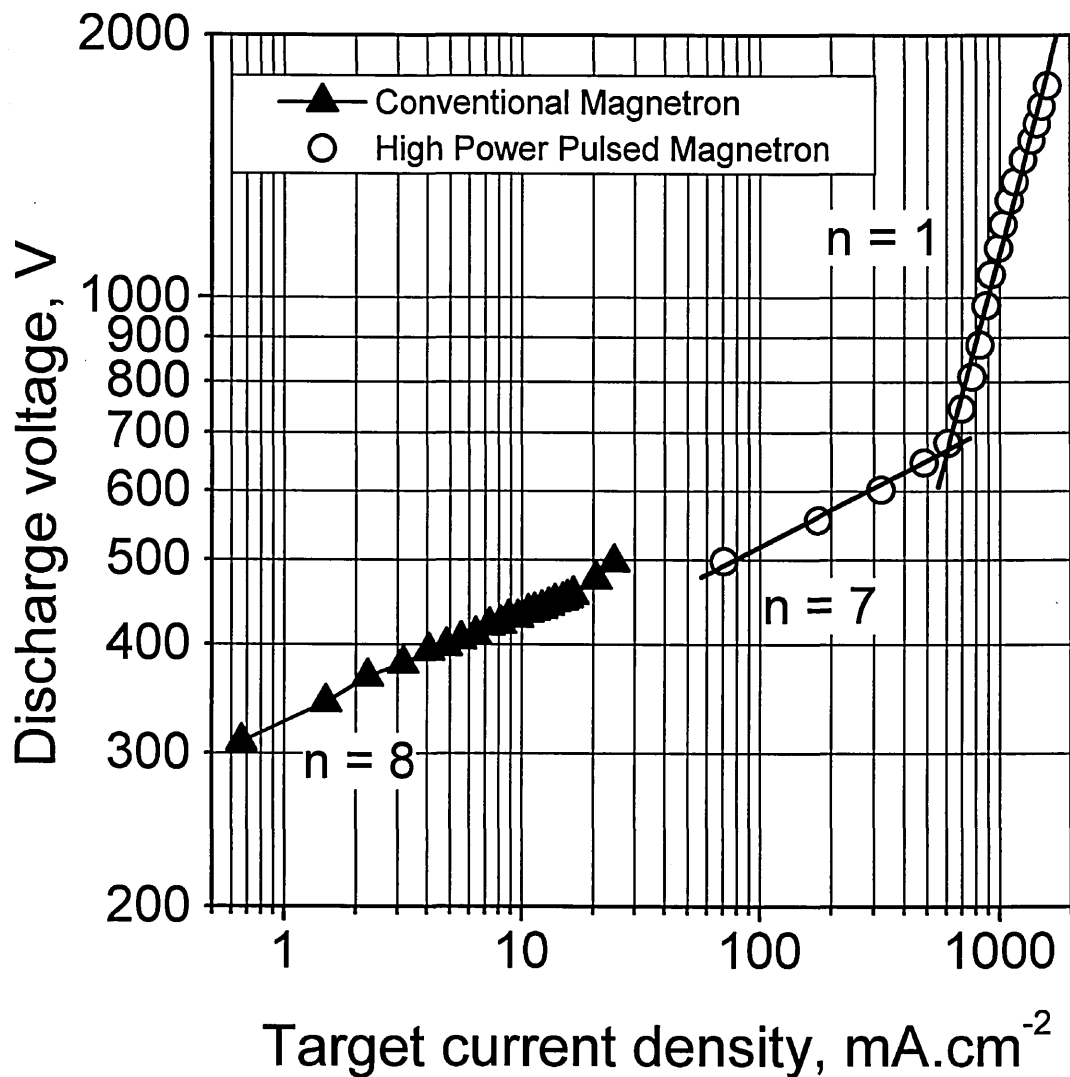


Figure 4.2.2. *I-U characteristics of the pulsed discharge. The exponent n of the power law $I = kU^n$ is indicated. Cr sputtering in Ar atmosphere at a pressure of 0.4 Pa (3 mTorr).*

Both discharges were operated at a pressure of 0.4 Pa (3 mTorr). The exponent calculated from the slope of the relation for the conventional magnetron is 8, which is well within the range defined above. The pulsed discharge exhibits two slopes depending on the target current. At low currents ($<600 \text{ mAcm}^{-2}$), the exponent is approximately 7 indicating normal magnetron operation. At higher currents, the exponent changes to 1, in a mode of operation in which the increase of discharge voltage to very high values of 1.6 kV is not accompanied by a correspondingly large increase in the discharge current.

The influence of power on the ion saturation current at a distance of 35 mm from the target is shown in Figure 4.2.3. The current was measured for two orientation of the flat probe - facing the target (upper data points) and perpendicular to the target (lower

data points). Large differences in currents in the two orientations of the probe are obvious. It can also be seen that at the higher powers the plasma density increases faster than at low powers. The peak density calculated from the ion saturation current and assuming low ion energy was estimated to be 10^{13} cm^{-3} at a target power density of 3 kWcm^{-2} and Ar gas pressure of 3 mTorr (0.4 Pa).

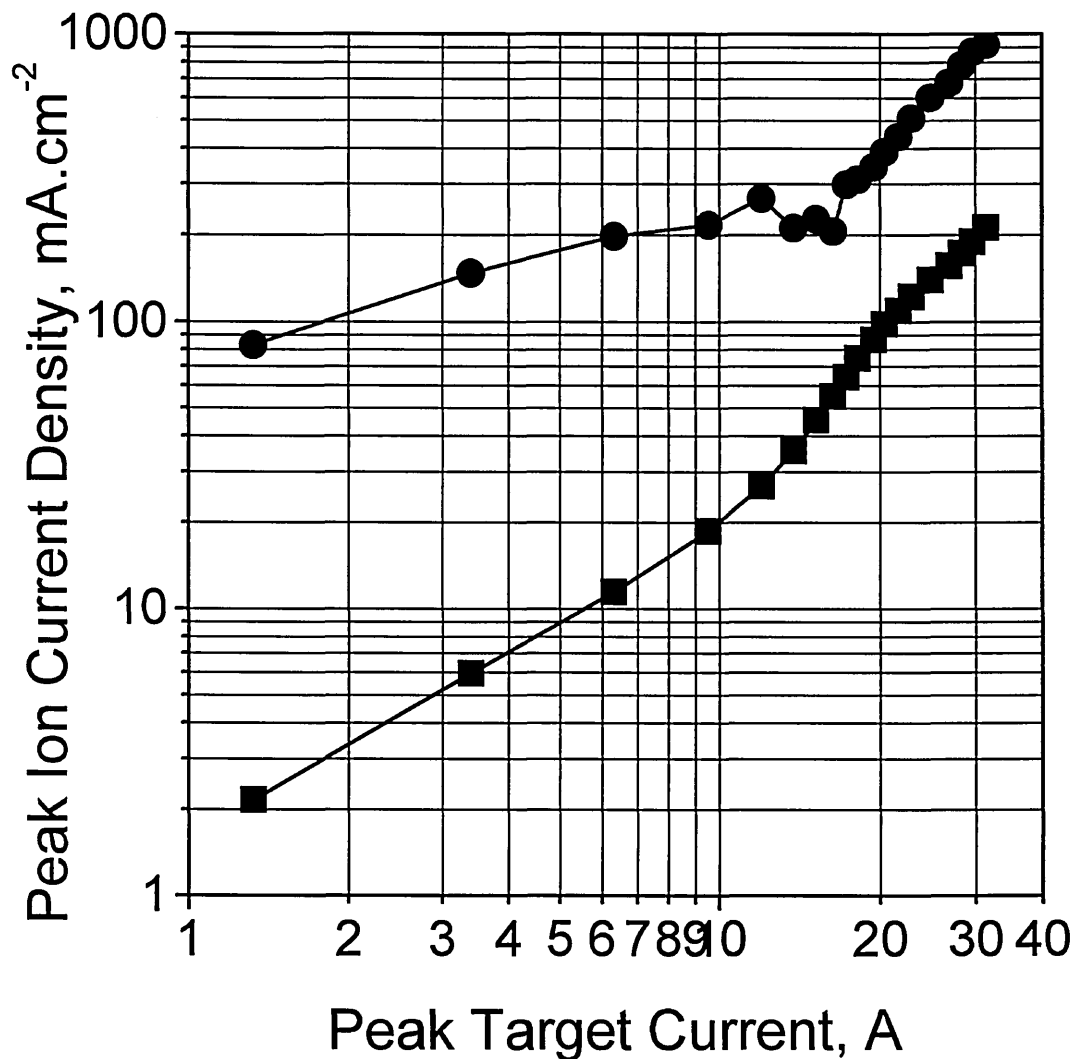


Figure 4.2.3. Ion saturation current at a distance of 35 mm with the probe facing the target (circles) and with the probe perpendicular to the target surface (squares). The flat probe was biased to -150 V. Maximum plasma densities derived from the current densities are in the range 10^{13} cm^{-3} .

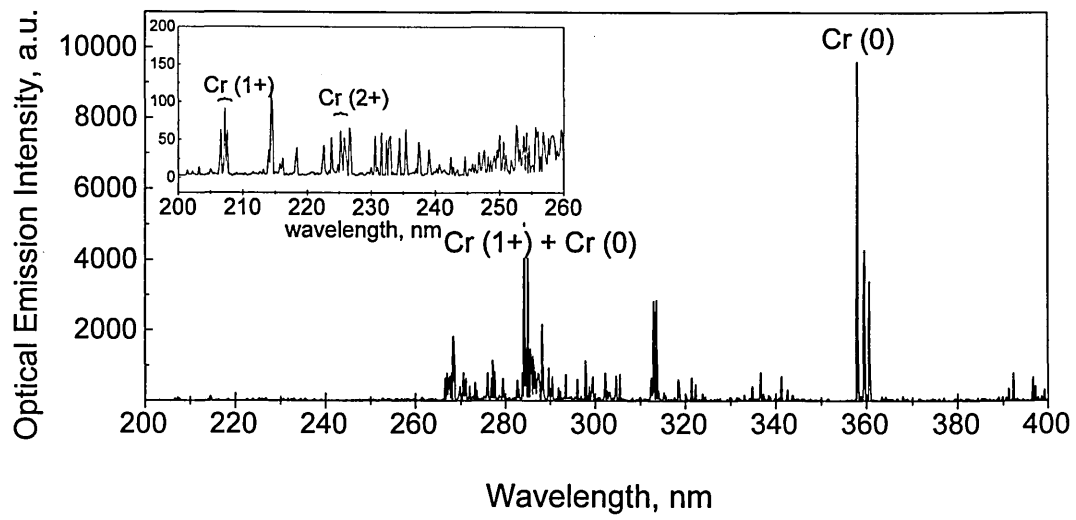
An important quantitative result describing the ion-to-neutral ratio has been found in the present work. The deposition flux at a distance of 500 mm from a $\varnothing 150 \text{ mm}$ Cr target surface was found to contain 30 % metal ions for peak target power of 1.5 kWcm^{-2} . As suggested from figure 4.2.3 the ionisation degree may increase at higher powers.

Discussion

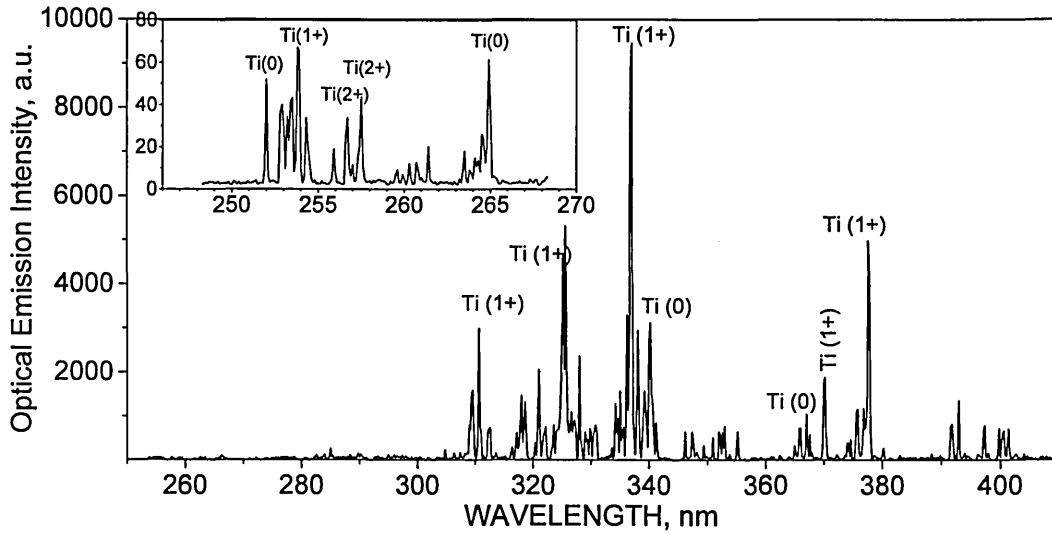
The change in the exponent n at high powers shown in Figure 4.2.1 may be attributed to an insufficient magnetic field strength. The energy acquired by the secondary electrons in the sheath (up to 1.6 keV) cannot be trapped by the magnetic field and the probability of ionising collisions per electron is decreased. Additionally the high discharge current can induce its own magnetic field opposing the one of the magnetron itself. This would weaken the confinement and the plasma would be able to escape from the target increasing the ion flux at far distances, as confirmed by the steeper increase of ion saturation current at higher powers.

4.2.2. Multi-Fold Ionised Metal Species Found in Cr, Ti, and Ta HIPIMS and Comparison to Conventional Magnetron Discharge

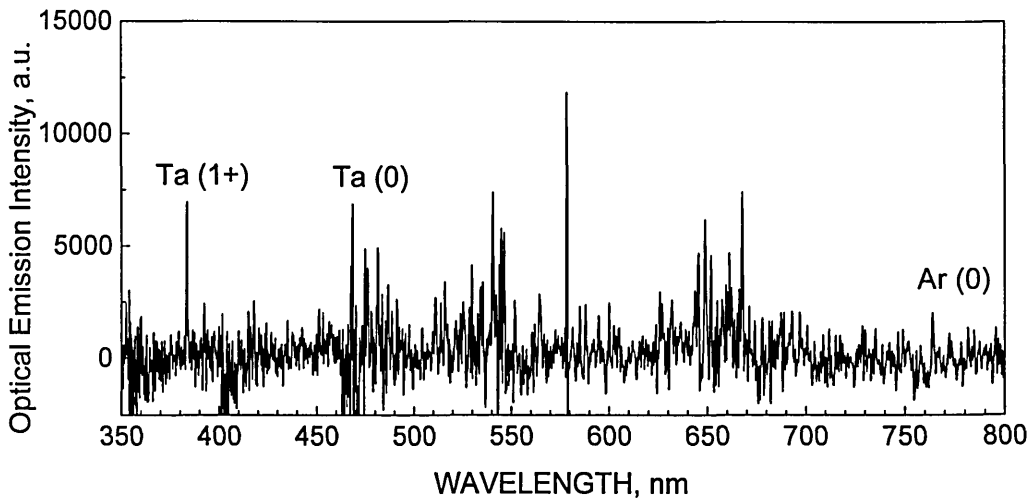
The composition of the dense plasma region during sputtering of several target materials was investigated by OES. Figure 4.2.4 shows the emission spectra of HIPIMS of a) Ta (1 kWcm^{-2}), b) Cr (3 kWcm^{-2}), and c) Ti (1 kWcm^{-2}). In the case of Ta sputtering, singly ionised metal ions are detected. One-fold and two-fold ionised metal species are present in the Cr spectrum. Up to two-fold ionised metal ions can be found also in a Ti pulsed discharge.



a) Optical Emission Spectrum of HIPIMS of Cr.



b) Optical Emission Spectrum of HIPIMS of Ti.



c) Optical Emission Spectrum of HIPIMS of Ta (the light detector was a CCD).

Figure 4.2.4. Optical Emission Spectra of HIPIMS of (a) Cr, (b) Ti, (c) Ta

Figure 4.2.5 shows a comparison between the optical emission spectra of three kinds of magnetron sputtering plasmas: a HIPIMS with peak power 1.5 kWcm^{-2} and average power 300 W; a conventional magnetron operated at average power of 300 W; and a magnetron with enhanced ionisation by RF coil¹ ($P_{\text{DC}} = 300 \text{ W}$ and $P_{\text{RF}} = 450 \text{ W}$) [113]. The spectra were taken using spectrometers with different resolution (Sections 3.4 and 3.5.2) which contributes to the different widths of the peaks in the RF coil spectrum.

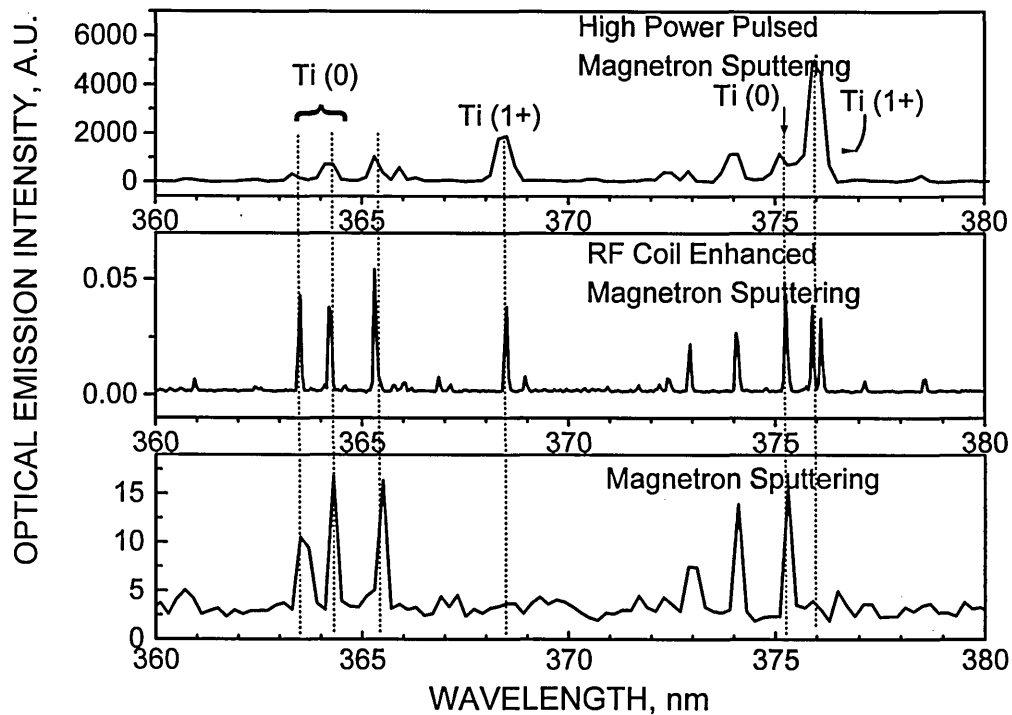


Figure 4.2.5. Optical emission spectra of plasmas produced by discharges in a conventional DC magnetron (bottom), a RF coil enhanced magnetron (middle) and High Power Pulsed Magnetron (top).

In particular, the ratio of two spectral line intensities of the Ti^{1+} ion (375.93 nm) and Ti^0 neutral (375.29 nm) was studied. These particular emission lines were chosen because they are formed by transitions for which the upper level energies are similar: 3.8 eV and 3.4 eV for Ti^{1+} , and Ti^0 respectively. Assuming a Corona model for the plasma, the line emission intensity ratio can be used as a qualitative measure of the density ratio of the species [117, 74] because of the similarity in their excitation energies. The line intensity ratio $I(\text{Ti}^{1+}) / I(\text{Ti}^0)$ is negligible in the conventional magnetron sputtering and increases from 0.9 in the RF coil enhanced discharge to 5 in

¹ The discharge was operated with DC magnetron power of 300 W, RF coil power of 450 W, and $P_{\text{Ar}} = 4 \text{ Pa}$ (30 mTorr). The experimental details are described in [113]

the pulsed discharge. These ratios are regarded only as a qualitative comparison of the degree of ionisation in the three methods of sputtering.

The above evidence for significant metal ionisation is further supported by the dense, smooth films generated in subsequent coating runs, which are described in detail in Chapter 4.3 of this thesis. The films had an excellent adhesion due to the pre-treatment of the substrates by metal ion containing HIPIMS plasma bombardment under a bias of -1200 V.

The ionisation of the sputtering gas in HIPIMS is significantly increased compared to continuous magnetron discharges. Emission from Argon ions was found in Ti and Cr sputtering (the time evolution of Ar^{1+} emission is shown in Chapter 4.2.3). The ionisation of the sputtering gas can be observed especially in the case of low sputtering yield materials, such as Carbon, where the optical emission spectrum is dominated by lines of the background gas.

Figure 4.2.6 shows a typical spectrum of HIPIMS of carbon in N_2 atmosphere (3mTorr (0.4 Pa)) exhibiting excited but also single ionised $\text{N}_2(1+)$ (391.4 nm), the intensity of the latter peak being double that of $\text{N}_2(0)$ (337.1 nm). In the case of continuous magnetron discharge the $\text{N}_2(1+)$ and $\text{N}_2(0)$ peaks reach similar intensities.

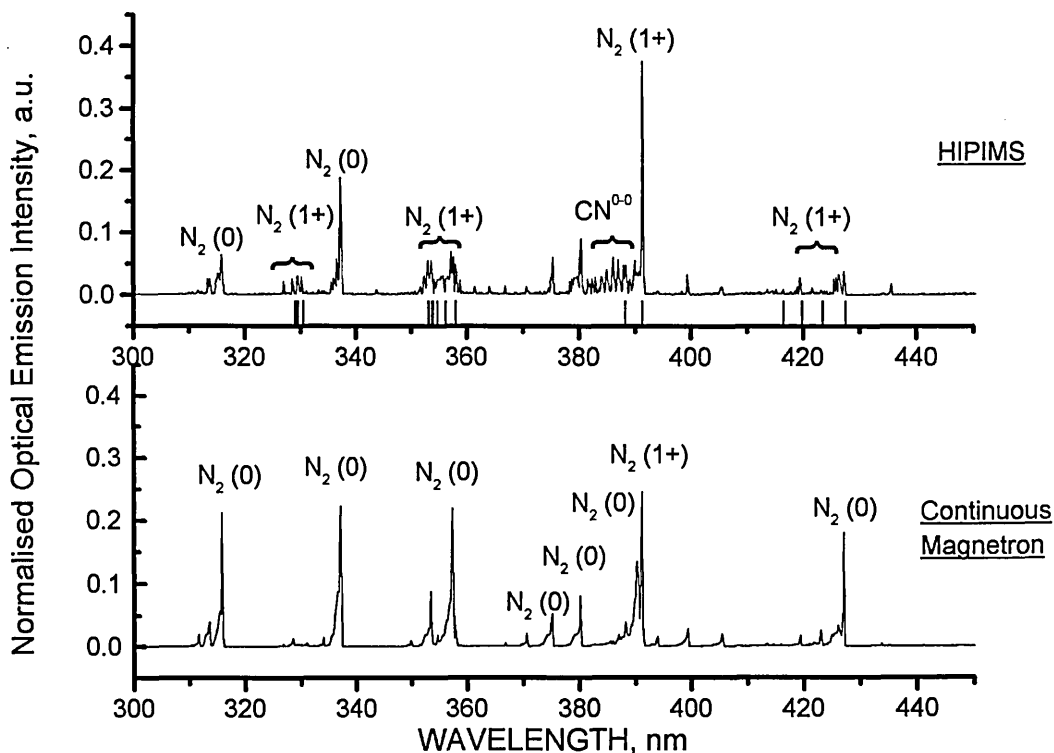


Figure 4.2.6. Carbon sputtering in N_2 atmosphere - HIPIMS and Continuous

Emission from N(1+) was also detected at higher wavelengths in the HIPIMS and conventional magnetron discharges (not shown).

The vibrational temperature of the N₂ molecule was evaluated according to the procedure outlined in Ref. [74]. The resulting value of 7000 K, as calculated in this study, is higher than the typically observed in r.f. magnetron sputtering discharges (6000 K) [74], arc discharges (4000 - 6000 K) [155] and dc magnetron sputtering discharges (3000 K) [74]. This suggests that the nitrogen molecules in the HIPIMS plasma are strongly activated and reactive which could lead to target poisoning at a relatively low N₂ partial pressure and an enhanced N incorporation at the substrate side, altogether one would need less N₂. An interesting effect, which has also been observed in laser ablation [156] of C in N₂ atmosphere, is the detection of CN molecule emission in the HIPIMS plasma.

Discussion

It is well known that the probability of ionisation of species depends on their dwell time in the plasma and the energy of ionising species. In typical magnetrons, the plasma comprises mainly residual gas ions [70], which have energies in the meV range. Electrons confined in an ExB drift loop in the magnetron collide with the almost stationary gas atoms and the ionisation probability per electron is quite high. On the other hand, sputtered metal atoms leave the target surface with relatively high energies, typically a few eV, traversing the dense plasma region in a few microseconds. In typical magnetron discharges, the plasma density is such that the traverse time is too short for ionising collisions to occur and only a negligible proportion of metal ions is created. In the high power pulsed discharge, although the sputtering voltage can be at least two times higher, the sputtered atoms leave the target with the same energy of a few eV. However, they can not penetrate the dense highly energetic electron cloud formed in the sheath due to the high discharge power without collisions and the probability of ionisation of the pulse-sputtered flux is high. The maximum tangential magnetic field of the magnetron (~500 G) is not sufficient to magnetise the ionised metal and it readily escapes from the dense plasma region and reaches long distances where deposition samples can be placed. On the other hand, a portion of the metal ions is accelerated back to the target surface, giving rise to self-sputtering and decreasing the sputtering rate due to the low self-sputtering yield. Preliminary results show a clear trend between self-sputtering yield and deposition rate [157].

4.2.3. Influence of Peak Power on the Plasma Composition, Ion Density and Deposition Rate

OES measurements of the Cr^{2+} line at 232.03 nm, Cr^{1+} line at 205.55 nm and the Cr^0 line at 399.11 nm were carried out in order to investigate the degree of ionisation of the sputtered metal flux. These particular emission lines have been chosen because they are formed by transitions for which the upper level energies are similar: 5.4 eV, 6.0 eV and 5.66 eV for Cr^{2+} , Cr^{1+} , and Cr^0 respectively (see discussion relating to Figure 4.2.5). It should be noted that since only Cr neutrals are sputtered from the target all Cr ions are created in the discharge by a process of electron impact ionisation, which depends strongly on the electron temperature. The intensity ratio of such optical emission lines depends directly on the density of the species and is influenced indirectly by changes in electron temperature. The ratio of the spectral line intensities of Cr^{2+} and Cr^0 indicated in Figure 4.2.7 with triangles shows an increasing ionisation with target current. Two other diagnostic results that indicate an increased ion to neutral ratio are also shown on Figure 4.2.7, namely the spectral line intensity ratio $I(\text{Cr}^{1+}) / I(\text{Cr}^0)$ recorded during early conditioning runs. The ratio of saturation current to deposition rate is also given as a qualitative measure of the ion-to-neutral arrival rate.

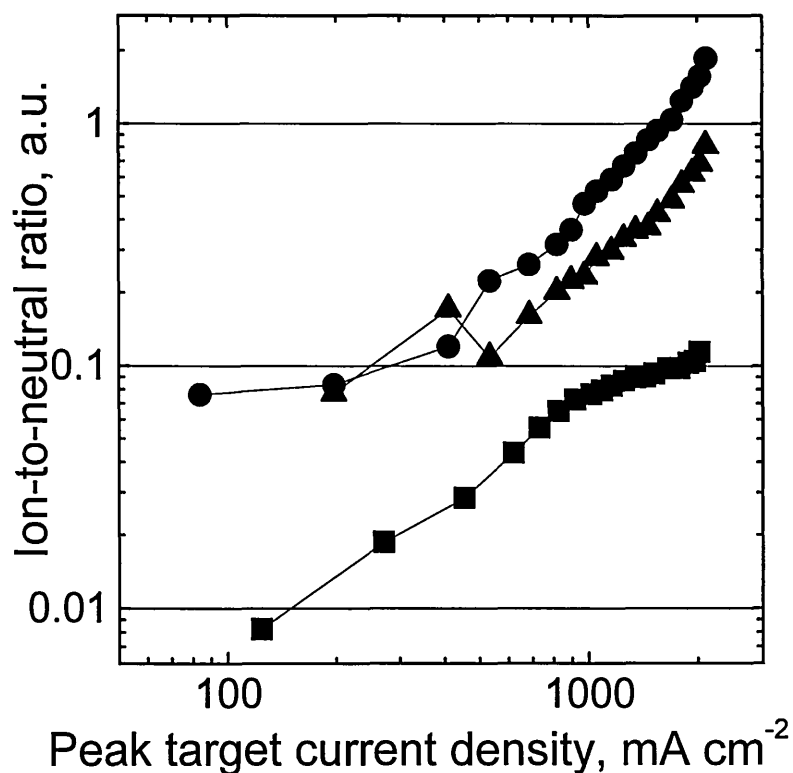


Figure 4.2.7. Ion to neutral ratio vs. peak target current for Cr from optical emission line intensities $I(\text{Cr}^{2+}) / I(\text{Cr}^0)$ (triangles) and $I(\text{Cr}^{1+}) / I(\text{Cr}^0)$ (circles). Also shown is the ratio of the ion current density and deposition rate (squares).

Discussion

As can be seen from Figure 4.2.3, the peak density of the magnetron plasma increased monotonically by approximately two orders of magnitude as the peak target current increased by a factor of 30. It is interesting to note that when high powers are dissipated in the discharge, the discharge voltage increases simultaneously with the current with an exponent close to 1 (see Figure 4.2.2). The increased discharge voltage is probably responsible for increasing, for example, the hot electron temperature, which, combined with the increased plasma density, is a prerequisite for an improved ionisation efficiency of the sputtered Cr atoms.

4.2.4. Time Evolution of the Plasma Composition and Density During a Pulse in HIPIMS of Cr, Ta and C Targets

The time evolution of the plasma was found to be strongly influenced by the power of the discharge pulse. Figure 4.2.8 shows a typical time evolution of a pulsed magnetron discharge at relatively low power of 0.3 kWcm^{-2} . The target current and the optical emission from Ar and Cr neutrals occur almost simultaneously. This kind of relationship is routinely observed in pulsed magnetron discharges operating at lower powers than presented here [158].

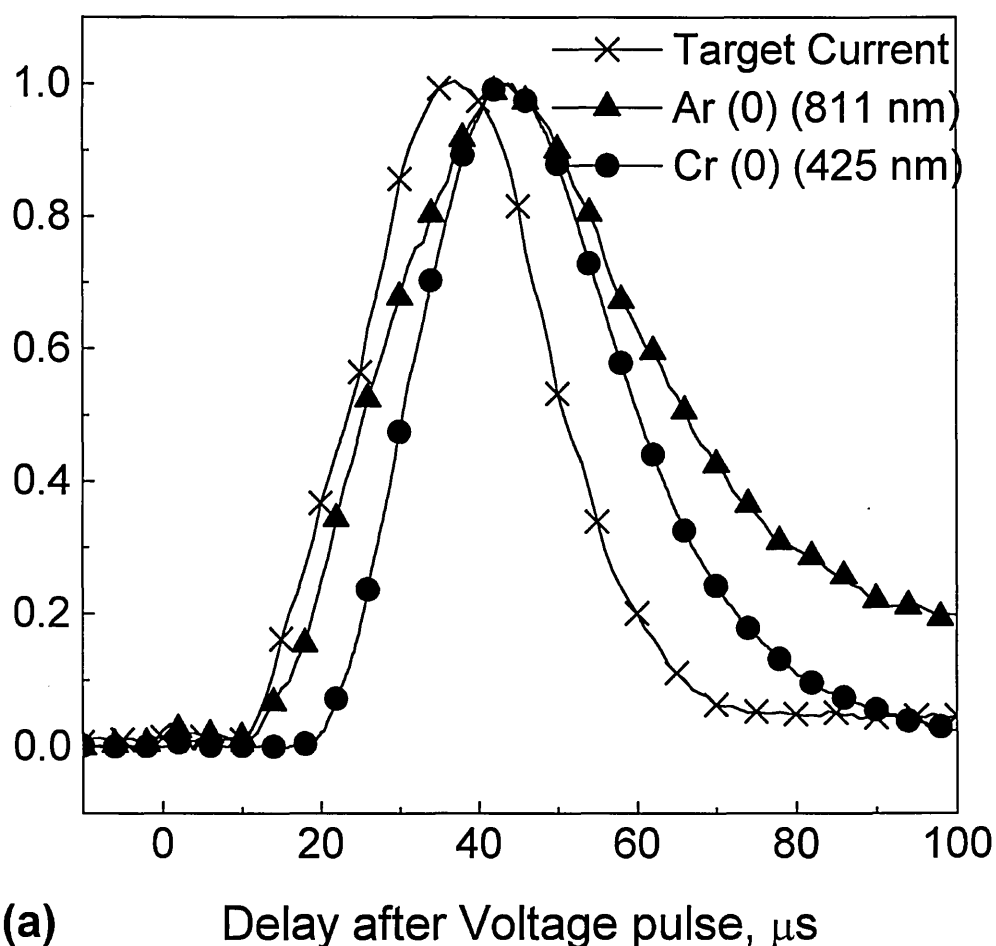


Figure 4.2.8. Typical time evolution of the optical emission and target current at low power (peak target voltage = -500 V)

However, when the peak power density is increased to a few kWcm^{-2} the time evolution of the discharge plasma is quite different. Time resolved OES traces for the HIPIMS discharge in an Ar atmosphere at high powers are shown in Figure 4.2.9 for a

Ta target and Figure 4.2.10 for Cr target. In both figures, the OES time maxima appear in a clearly differentiated sequence beginning with Ar neutral and ending in Cr or Ta neutral. A similar separation in time at high powers was first reported by Macak *et al.* [98] for the case of HIPIMS of Ti in an Ar atmosphere. The plasma model proposed by them assumed that the plasma developed from being Ar dominated to metal ion dominated due to the gas rarefaction effects discussed by Rosnagel *et al.* [72]. The separation for high powers is confirmed in the present work also for Cr and Ta.

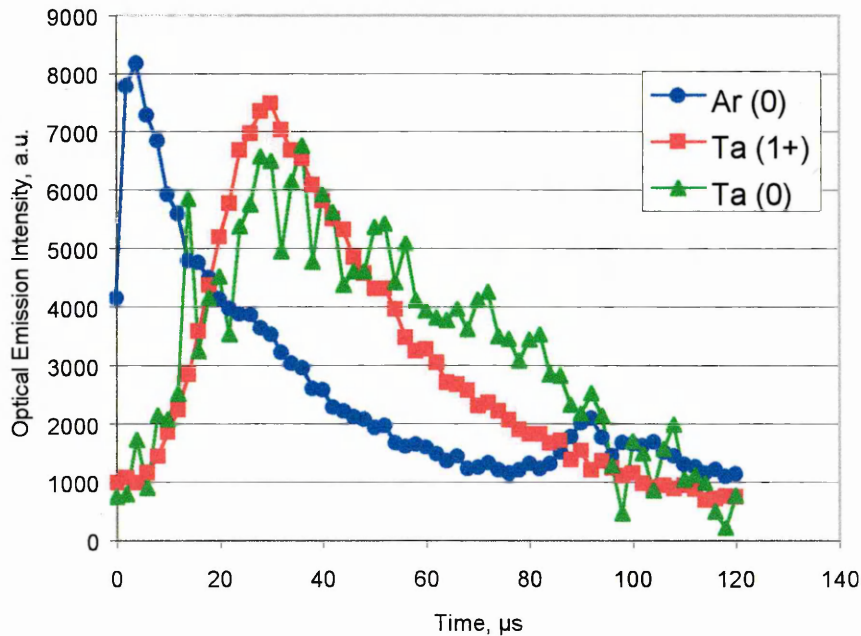


Figure 4.2.9. Typical time evolution of the plasma at high power. Time resolved optical emission spectrum of HIPIMS of Ta at peak power density = 2 kWcm^{-2}

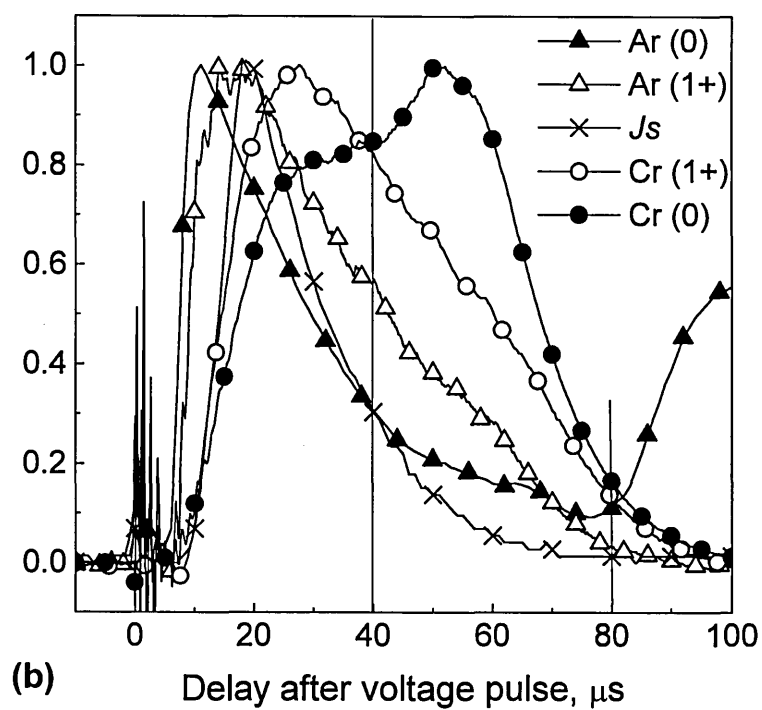


Figure 4.2.10. Typical time evolution of the plasma at high power. HIPIMS of Cr at peak power density = 3 kWcm^{-2} . The species shown are: Cr^0 (399 nm), Cr^{1+} (232 nm), Ar^0 (811 nm), Ar^{1+} (440 nm). J_s is the ion current

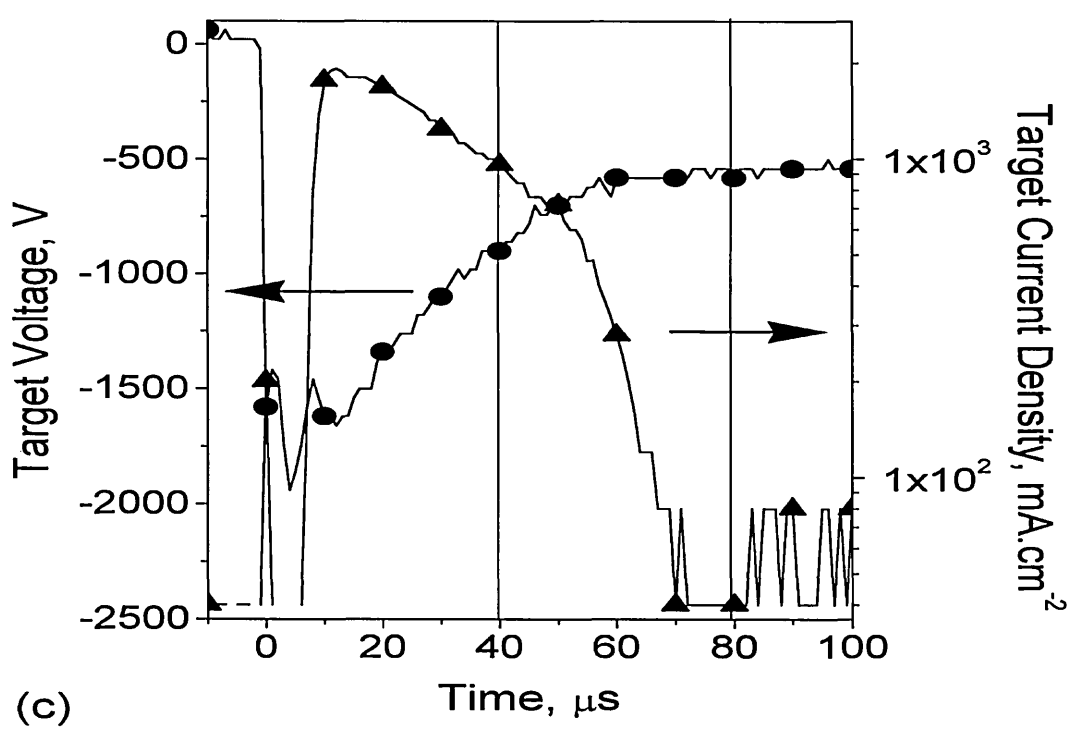


Figure 4.2.11. Typical time evolution of the plasma: target voltage and current at high power (the apparent fluctuations in the current signal after $80 \mu\text{s}$ are principally caused by digitisation noise).

Discussion

In detail, the evolution of the optical emission signals of HIPIMS of Cr shown in Figure 4.2.10 can be separated into three stages as follows. A high power and high plasma density discharge is produced during the first stage, from 0 μs to 40 μs . The first emission is observed from Ar atoms, present in the background gas when vacuum breakdown occurs. As Ar is ionised the plasma density and target current increase, and Ar^{1+} emission is developed. With a delay of a few microseconds after the Ar lines, the Cr^0 emission lines are detected. After further 3 μs emission from Cr ion lines is detected, indicating that the sputtered Cr flux is being ionised in the high density plasma. The Cr^{1+} lines peak at approximately 30 μs , approximately 10 μs after the ion saturation current J_s has reached its maximum value. The rapid fall in Ar emission at this time may indicate that the Ar pressure is being locally reduced by the momentum transfer from sputtered Cr atoms [72, 154]. The Cr ion emissions fall over the next 40 μs .

At 40 μs the discharge voltage and current have fallen to levels which indicate the start of a second stage. At this time the voltage is approximately -750 V and the discharge is leaving the high power regime as shown in Figure 4.2.2. and entering a regime of normal magnetron operation with a high target current. During this phase the Cr^0 emission is stronger and the Cr^{1+} emission is weaker than in the high power stage, and the target current shown in Figure 4.2.11 starts to drop quickly for a small decrease in voltage as is typical of a normal magnetron discharge. The magnetic confinement field in these circumstances is very efficient and works in favour of decreasing the rate of decay of the plasma density peak at 20 μs .

The final stage of the discharge occurs at about 80 μs when a typical magnetron glow discharge is initiated with voltage of -500 V and current density some tens of mAcm^{-2} . The subsequent emission from Ar neutral probably indicates the return of the discharge voltage and current to typical magnetron levels and the restoration of the Ar pressure respectively.

4.2.5. An analysis of breakdown mechanisms of high power pulsed magnetron sputtering.

The extraordinarily high glow discharge current densities discussed in Section 4.2.1 are in the region where a transition from abnormal glow to arc discharge should be observed (see Figure 4.2.1). The probability of arcing is known to depend on the cathode material [92]. In this work, several elements such as Cr, Ti, Ta, Cu, and C were tested as targets for HIPIMS. Arcing was not observed for Cr, Ti, or Ta in Ar atmosphere even after tens of hours of operation at peak power levels of 3 kWcm^{-2} . However when C was sputtered arcing was avoided only by using peak power densities below 0.5 kW.cm^{-2} . Cu cathodes showed no arcing in the beginning but in long term runs the frequency of arcing increased with time. This section presents an analysis of the factors influencing the glow to arc transition.

The experiments were carried out in the vacuum equipment described in Chapter 3.3 using a 150 mm diameter Cu target. Prior to each test run the target surface was polished by mechanical grinding and cleaned with isopropanol. For measurement of arc frequency, the trigger signal from the oscilloscope was set to current level $\sim 20 \%$ higher than the peak current of the glow discharge, and the number of pulses was recorded over 60 s time periods.

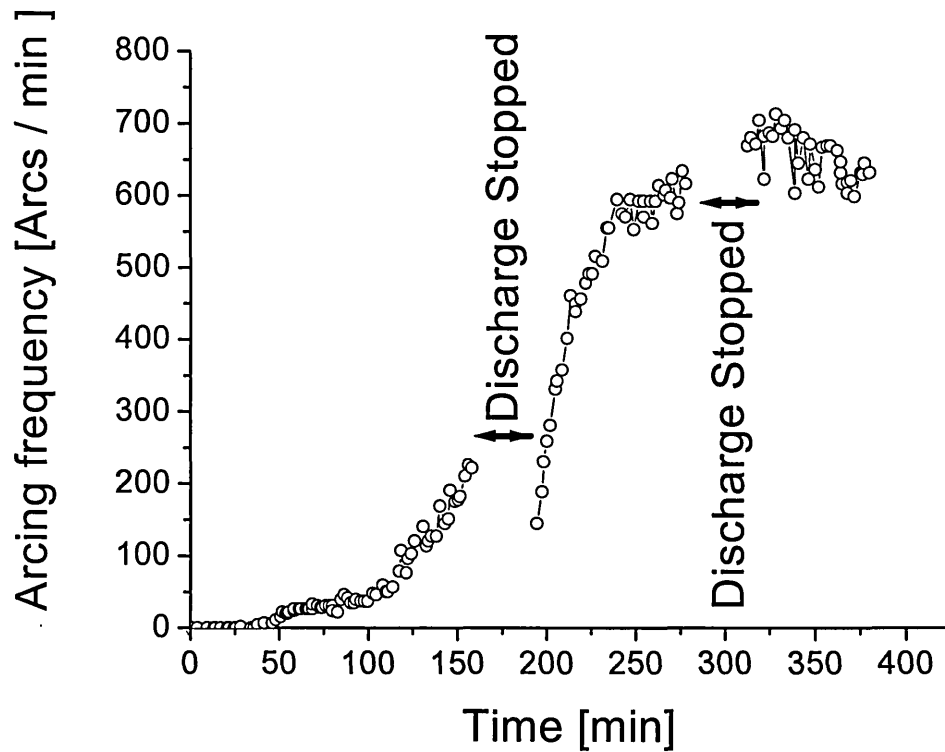


Figure 4.2.12. Time dependence of arcing frequency

Figure 4.2.12 shows a typical evolution of arcing frequency as a function of time measured on a $\varnothing 150\text{mm}$ Cu cathode with an average energy of 11 J per pulse. After the initial burst of arcs resulting from the sputter cleaning of oxides [159], there is a period of ~ 50 min when the pulsed glow discharge operation is stable without transition to the arc mode. The period of stable glow discharge conditions is then followed by a continuous increase in arcing frequency up to the upper detection limit of the oscilloscope trigger circuitry ~ 700 arcs/min. This means that for longer deposition times film quality might be seriously impaired by emission of macro-particles.

Further experiments were conducted measuring the arcing frequency as a function of the applied power per pulse shown. Figure 4.2.13 shows a rapid increase in arcing frequency with increasing power.

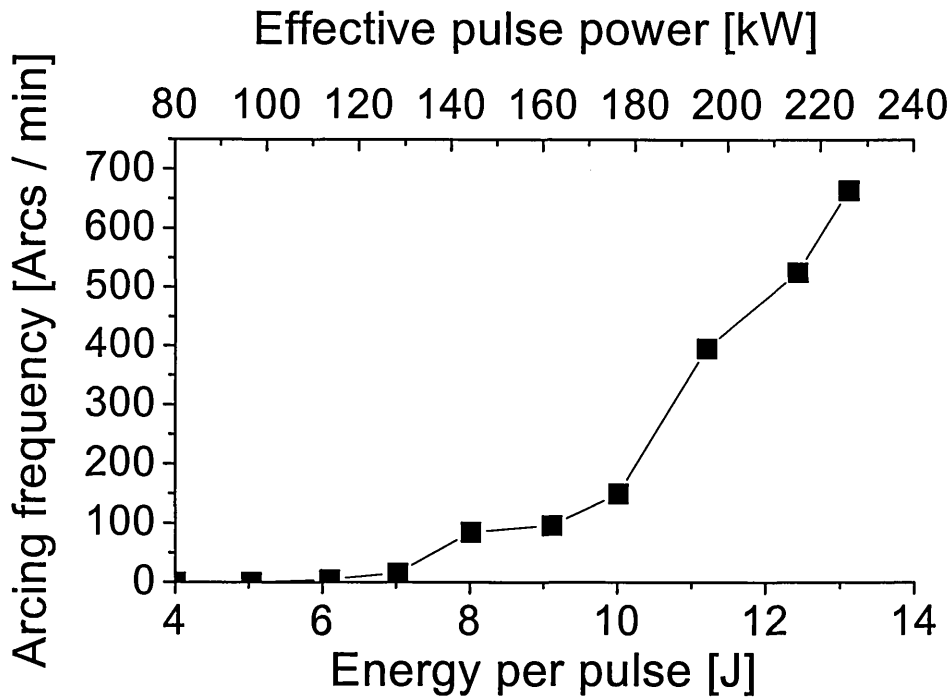


Figure 4.2.13. Arcing frequency dependence on energy per pulse (effective pulse power).

Discussion

The mechanism of glow to arc transition has been studied by Mesyats and Proskurovskii [92]. They found that the arc spots are initiated due to field enhanced thermo emission of electrons from sharp microprotrusions (asperities) on the surface where the electrostatic field and the temperature is enhanced locally. This thermofield emission current leads to a breakdown and arc spot generation.

In order to understand the physical phenomena governing the behaviour observed in the experiments it is necessary to evaluate the surface temperature, which is crucial in inducing sufficient electron emission and triggering the glow to arc transition. Assuming an ideally flat target surface the increase of surface temperature can be calculated by balancing the power load and thermal properties of the target and cathode materials.

For a homogeneous target heated by ion bombardment the following approximate formula for the temperature change can be used [91]:

$$\Delta T(x,t) = \left(\frac{\sqrt{\xi}}{K\sqrt{\pi}} \right)^t \int_0^t f(t-\tau) \exp\left(\frac{-x^2}{4\xi\tau} \right) \frac{1}{\sqrt{\tau}} d\tau$$

where K is thermal conductivity, ξ is defined as $\xi = K/(\rho C_s)$, ρ is the mass density, C_s is the specific heat, $f(t)$ is the time dependent power flux (power density) at the surface, and x is the depth below the cathode surface. For typical target power densities of 1 kW.cm^{-2} (target current densities of 1 A.cm^{-2} with target voltage of $\sim 1 \text{ kV}$) and pulse lengths of $100 \text{ }\mu\text{s}$ the amplitude of the surface temperature oscillations is well below $100 \text{ }^\circ\text{C}$. This is well below the temperature rise needed to create substantial thermo-emission current. For Cu used as cathode material and plasma densities ($\sim 10^{15} \text{ cm}^{-3}$) the resulting electric field E across the sheath can be estimated from the voltage drop across the sheath, $U_{cathode}$, and the sheath width, d : $E = U_{cathode} / d \sim 10^6 - 10^8 \text{ V m}^{-1}$.

The Child-Langmuir equation [160] was used to evaluate the order of magnitude of the effective sheath width. In the first order approximation of electric field strength of the pulsed magnetron discharge, the effect of magnetic field is neglected and it is assumed that breakdown occurs after a time sufficient to establish the cathode sheath. For the low-pressure discharge model, it is also possible to neglect the influence of pressure, which plays an important role for the transition of streamers to arcs in high pressure discharges.

The combined thermo- and field- emission electron current can be estimated using the formula given by Hantzsche [161]. For a typical field strength of 10^8 Vm^{-1} and temperatures below the melting point, it represents only a very small fraction of the total target current ($< 10^{-5} \text{ Am}^{-2}$). We can therefore conclude that even for HIPIMS, where the peak target power densities are in the range of 1000 W cm^{-2} , the average variation of surface temperature is negligible (due to the short duration of the pulses and the long off-times) and therefore the conditions for homogeneous thermo and field emission from the surface cannot be met.

At high powers, the stronger electron emission from the surface produces a denser plasma, where the cathode sheath width is reduced and the electric field strength is increased. The electric field is further affected by irregularities on the surface. The

electric field strength can be increased locally on a protrusion by the so-called field concentration factor, β , which can reach values in the range $\{50 - 5000\}$, depending on the surface state and geometry of the tip. The electric field strength readily reaches values of $>10^9 \text{ V m}^{-1}$ while inducing a substantial localised electron emission current (10^8 Am^{-2}), much higher than the calculations for an ideally flat surface. The increase of arcing with time (Figure 4.2.12) can be attributed, most probably, to the increased roughness, i.e. number and sharpness of microprotrusions on the target surface. Surface roughening leading to arcing has been reported to occur in magnetron sputtering of Cu targets [162] after similar values of average total ion dose.

This effect is believed to be responsible also for the localised heating of microtips leading to an increased thermofield emission and eventually to explosion of the asperity. The thermofield emission current can flow for a limited time t_d before overheating and explosion of the asperity occurs and an arc spot is initiated on the cathode surface. The critical electron emission current, j_{cr} , passing through an asperity is related to the explosive time delay t_d by the equation [92]

$$j_{cr}^2 t_d = (\rho C_s / \kappa_0) \ln(T_c / T_0)$$

where ρ - density, C_s - specific heat, κ_0 - resistivity, T_c - critical temperature, T_0 - temperature at time $t = 0$. For a specific material the equation can be transformed to $j_{cr}^2 t_d = const$ meaning that high currents can be drawn from the target for a limited time t_d without initiating an arc spot. However, for a constant duration of the power pulse, the probability of arcing would increase with discharge power, as is confirmed by the graph in Figure 4.2.13.

The quantity ($j_{cr}^2 t_d$) and other properties of selected materials are given in Table 4.2.1.

Table 4.2.1. Properties of selected HIPIMS target materials

Element	Specific Heat Capacity, $C_s, \text{Jg}^{-1}\text{K}^{-1}$	Density, ρ, gcm^{-3}	Resistivity $\kappa_0, 10^{-8} \Omega\text{m}$	Electrical Conductivity, $\mu\Omega^{-1}\text{m}^{-1}$	Thermal conductivity, $\text{Wm}^{-1}\text{K}^{-1}$	Critical Temperature, $T_c, ^\circ\text{C}$	Self Sputtering Yield	$j_{cr}^2 t_d \times 10^6, \text{A}^2 \text{s cm}^{-4}$
C	0.71	2.267	1639	0.06	129	6470	0.59	0.396
Ti	0.52	4.500	42	2.6	22	5577	0.67	20.539
V	0.49	6.100	20	5.1	31	5657	0.84	51.479
Nb	0.27	8.570	15	6.6	54	8427	0.81	56.550
Ta	0.14	16.650	13	8.1	57	9977	1.20	74.330
Cr	0.45	7.140	12.5	7.9	94	4427	1.62	79.955
W	0.13	19.250	5	18.2	170	11727	1.25	186.479
Cu	0.39	8.920	1.7	60.7	400	5148	2.79	687.846

In practical terms, the explosive time delay t_d can be used as an indicator for the maximum pulse on-time for which glow-to-arc transition within a pulse is avoided. As shown in Table 4.2.1, for a constant current j_{cr} , the time t_d is short for materials with high electron emission such as Carbon, Tungsten and various nitrides and oxides, in bulk form or as thin films formed on metallic targets during reactive sputtering. The on-time is influenced also by the degree of the ExB plasma confinement, the background gas pressure, etc.

Summary

High power pulsed magnetron sputtering with peak powers of 3 kWcm^{-2} were used to produce magnetron glow discharges with very high plasma densities. By optical emission, doubly and singly charged metal ions were detected in the dense plasma region for both Cr and Ti targets. The degree of ionisation of the sputtered flux that was measured for Cr reached a value of 30 %. The plasma conditions were strongly influenced by the peak power applied to the target as seen from I-U characteristic and time evolution of the composition of the discharge. A threshold current when the discharge switched from typical magnetron sputtering to ionised sputtering was observed.

The state of the surface roughness of Cu targets plays a crucial role in the long-term stability of the high power pulsed magnetron sputtering discharge. At peak powers of 1 kW cm^{-2} and pulse duration of $100 \mu\text{s}$, the temperature increase on the surface remains well below the melting point of the target material except at micrometer size protrusions. The concentration of the electric field leading to electro emission, localised heating and thermo-field electron emission from the tips, is a mechanism governing the glow to arc transition, similar to pseudospark discharges. The roughening of Cu cathode surfaces due to massive ion bombardment over longer periods of time, results in an increased probability of arcing. The arcing probability was also found to increase with increasing peak pulse power. For the future development of the high power pulsed sputtering technique it is necessary to consider carefully the choice of target material and process parameters in order to achieve stable discharge conditions over long surface treatments.

4.3. Deposition of CrN Films by Selected PVD

Techniques

Research on CrN PVD thin films has been reported by several groups in the last 20 years [99-102]. Theoretical aspects of CrN thin film deposition [103-105] and its industrial applications have been widely explored [106-111]. CrN is regarded as a suitable material for use in corrosion protection [28, 111], and good adhesion of CrN to steel even at low temperatures makes the deposition process attractive. Some of the drawbacks of CrN films are that they are soft and although the friction coefficient is low ($\mu \sim 0.5$) the wear resistance is average.

The present chapter is concerned with the enhancement of hardness of CrN deposited by continuous dc UBM sputtering by using high substrate bias voltages and high nitrogen partial pressures. Additionally, the investigations explore the applicability of HIPIMS as a PVD source to deposit CrN coatings. A suitable deposition system was developed and the nitride coatings were deposited by HIPIMS for the first time anywhere in the world. The effect of increased ionisation produced in HIPIMS discharges was immediately visible in the dense microstructure and exceptional corrosion and wear resistance of the films.

4.3.1. CrN films deposited by Reactive Unbalanced Magnetron

Sputtering

It has been shown that the application of bias voltages in excess of -200 V and high nitrogen partial pressures can increase the hardness of UBM deposited CrN films [29, 112]. This effect is attributed to the increased dislocation defect density leading to higher stress in the coatings. The efforts described in this chapter were focused on achieving a high hardness of CrN films deposited by UBM. Levels of bias exceeding -120 V during the film growth cause intensive resputtering of the deposited material. Because of its lighter mass, the nitrogen in the coating is preferentially back sputtered and the film composition is strongly affected. It is necessary to find a balance between the bias voltage and nitrogen partial pressure, which would allow high deposition rates, a stable chemical structure and a high hardness of the coating.

In this work, CrN films were grown at high bias voltages by unbalanced magnetron (UBM) sputtering in the Hauzer HTC 1000/ABS machine utilising ABS™ technology. The aim of the experiments was to analyse the effect of high bias voltages

on the mechanical properties and microstructure of the deposited films. Before the actual deposition runs were performed, the discharge and the plasma properties of the reactive UBM sputtering process at different Ar:N₂ gas mixtures were investigated.

It is well known that the flow of reactive gas such as Nitrogen is consumed by the substrates and the sputtering targets. The targets are gradually covered by a nitride layer with a higher secondary electron yield and more importantly a severely reduced sputtering yield in comparison to the metal. The coverage of the target increases with the amount of nitrogen in the chamber until the nitride layer completely covers the area of the target. When this happens the target is said to have reached the point of poisoning which is characterised with a specific nitrogen partial pressure. Sputtering at the point of poisoning occurs at a high rate while coatings with a stoichiometric composition can be deposited. The point of poisoning of the targets was determined by partial pressure measurements. Electrostatic probes were used to determine the plasma density and electron temperature. After plasma characterisation, two coatings were deposited at a bias voltage of -300 V and Argon-Nitrogen gas mixtures and partial pressure ratios of $P_{Ar}:P_{N_2} = 1:1$ and $1:2$ ($Q_{Ar}:Q_{N_2} = 1:3$ and $1:4$). These ratios corresponded to a fully poisoned sputtering regime and a high concentration of excess nitrogen in the chamber volume. The substrates were always etched in a Cr arc discharge plasma using a bias of -1200 V prior to deposition resulting in superior adhesion. The phase composition was analysed by X-Ray Diffraction. Mechanical properties such as hardness, friction coefficient, wear behaviour and roughness of the films were investigated.

Discharge and Plasma properties

The properties of the UBM discharge and the plasma near the substrates were investigated in the range of gas compositions used for coating deposition. Two facing targets at a distance of 1 m operating at 5 kW in constant power mode were used for coating deposition. The partial pressure of N_2 and Ar was measured with a residual gas analyser. While maintaining a constant total pressure of 4×10^{-3} mbar the flow of Nitrogen gas was increased. Figure 4.3.1 shows the Ar and N_2 partial pressures, the total pressure and the partial pressure ratio $P_{Ar}:P_{N_2}$ at different gas flow ratios of Ar: N_2 . The initial increase of nitrogen flow caused only a slow increase in the nitrogen partial pressure (squares) as the entire N_2 was consumed for the formation of a nitride layer on the sputtering cathode surfaces. Increasing the N_2 flow above 40% caused a faster increase in N_2 partial pressure as the targets reached their point of poisoning and additional nitrogen could not be consumed.

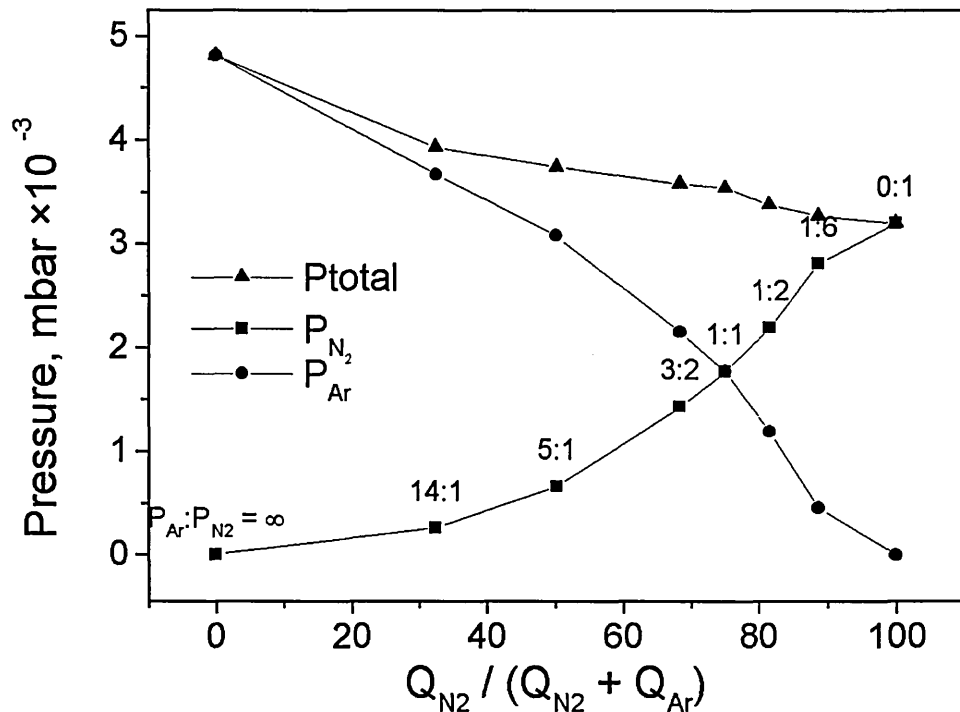


Figure 4.3.1. Influence of nitrogen flow, Q_{N_2} , on the partial pressures of Ar, P_{Ar} , and N_2 , P_{N_2} , and the total pressure, P_{tot} . The resulting partial pressure ratios $P_{Ar}:P_{N_2}$ are shown as labels on the P_{N_2} trace. It was attempted to keep the total pressure constant.

The effect of target poisoning on the properties of the plasma near the substrates was studied by electrostatic probes. Figure 4.3.2 shows the effect of increasing the nitrogen flow on the plasma density and electron temperature (T_e). In pure Ar atmosphere $T_e = 3$ eV. As the nitrogen flow is increased from 50 to 100%, T_e is maintained at an approximately constant value of 2 eV. The plasma density decreased steadily from approximately 2×10^{10} cm⁻³ as the nitrogen flow increased and a drop in density to 1×10^{10} cm⁻³ is observed in pure nitrogen atmosphere.

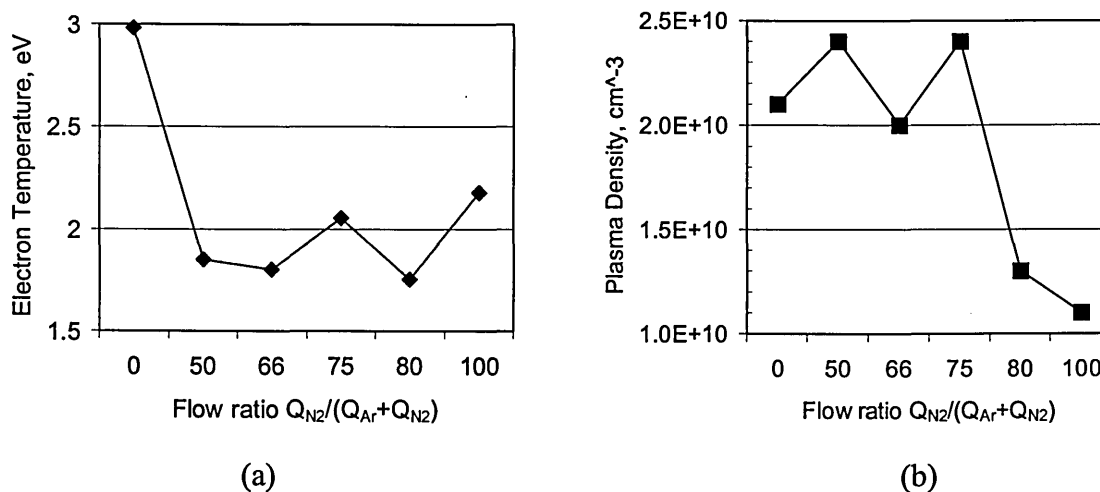


Figure 4.3.2. (a) Electron Temperature, T_e ; and (b) Plasma density at the substrate position for different $Q_{N_2}/(Q_{Ar} + Q_{N_2})$ flow ratios.

The value of the electron temperature is lower than the 6 eV typically measured for the hot electron group in the dense plasma region of the magnetron [163, 75]. However, it is comparable to the average electron energy reported by those authors.

The plasma density values were comparable to those published in the literature [163, 75, 121]. The poisoning of the target due to the increased Nitrogen flow did not influence significantly the plasma density at distances far from the target. The magnetron plasma is known to contain mainly gas ions that are produced in the dense plasma region near the target surface [70]. The threshold of ionisation for N_2 and Ar is similar because of their similar ionisation potentials of 15.58 eV and 15.76 eV respectively. Due to the increased efficiency of ionisation achieved by magnetic field trapping of electrons near the target, the electron impact ionising collision frequency is similar for both the Ar atom and the N_2 molecule despite the large difference in their radii. The fall off in ion density in atmospheres containing high proportion of N_2 may be attributed to an intensified ion-molecule elastic scattering.

In summary, the point of poisoning of the target was reached at Ar:N₂ partial pressure ratios of approximately 14:1. The poisoning of the target reduced both the electron temperature and the plasma density near the substrates.

Film properties

Two CrN coatings were deposited at $U_{bias} = -300$ V at partial pressure ratios $P_{Ar}:P_{N_2} = 1:1$ and $1:2$. All depositions were carried out at 450 °C. The microstructure of the coatings was investigated by XRD analysis. Figure 4.3.3 shows Bragg-Brentano scans for the two coatings. The coatings contained primarily the CrN phase. Cr₂N phase peaks were not measurable. Crystals with [220], [311], [400], and [420] orientation were detected and only a very weak [111] peak was present. The films were strongly textured with a dominating orientation [200]. This orientation has a low packing density and is probably developed due to preferential resputtering of all other orientations under the high-energy (300 eV) ion bombardment during the deposition [29].

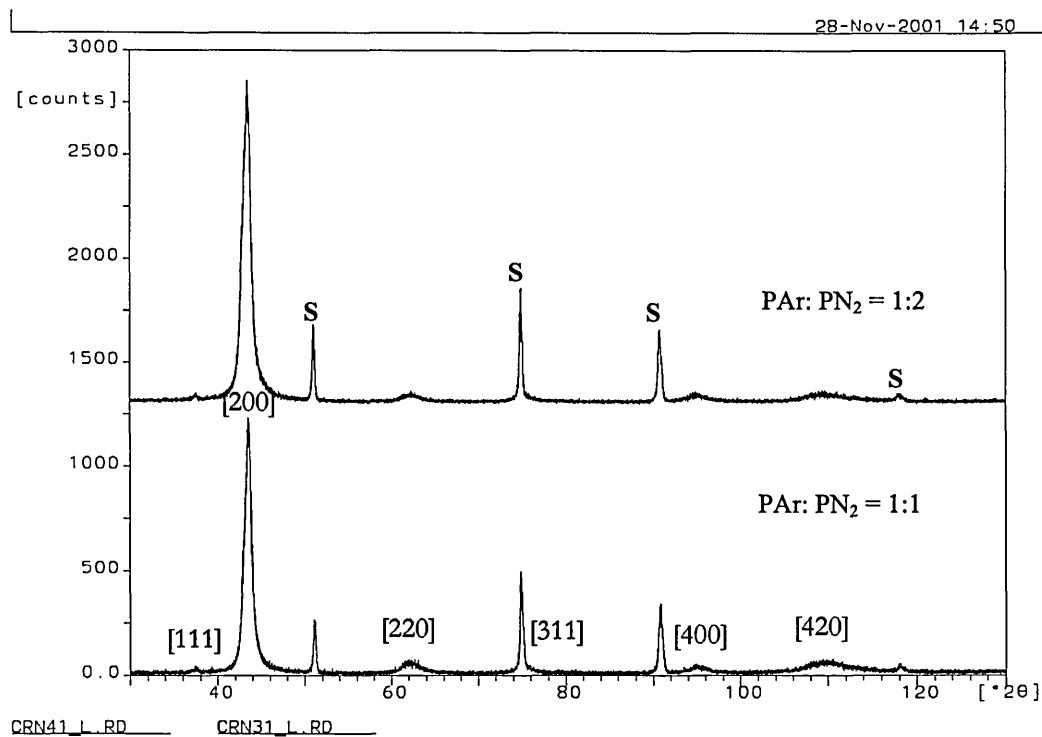


Figure 4.3.3. XRD trace from CrN films deposited in the Hauzer ABS machine with $U_{bias} = -300$ V in mixed Ar+N₂ gas atmosphere with the indicated partial pressure ratios.

The mechanical properties of the coating deposited at $P_{Ar}:P_{N_2} = 1:1$ are summarised in Table 4.3.1. The table gives an indication of the general properties obtained for the films deposited at these extraordinary conditions.

Table 4.3.1. Mechanical properties of the CrN film deposited at $P_{Ar}:P_{N_2} = 1:1$ by the ABS technology

Partial pressure ratio $P_{Ar}:P_{N_2}$	1:1	
Substrate	high speed steel	
Thickness, μm	2	
Knoop Hardness $HK_{0.025}$	1914 \pm 200	
Scratch Critical Load, N	80	
Friction coefficient	0.3	
Roughness	Ra, μm	0.028
	Rt, μm	0.9

The Knoop hardness values measured on a HSS substrate is comparable to the $HK_{0.025} = 2200$ typically reported in the literature [30]. This indicates that the application of high bias voltages in itself and the high nitrogen partial pressure are not sufficient to increase the hardness of the coatings. It is necessary to optimise the deposition parameters further including, for example, increasing the nitrogen gas partial pressure, which could increase the stress additionally due to lattice expansion. It can be speculated also that the change in hardness is due to the measured decrease in plasma density and resulting decrease in ion-to-neutral ratio.

The mechanical properties of the coating do not generally deviate from the results published in the literature. The adhesion to the substrates reaching critical load values of 80 N indicates an effective etching process. The low friction coefficients show a high coating integrity and wear mechanism involving the generation of rather fine wear debris mainly from oxide origin.

It is interesting to note that the roughness of the sample, Ra, was typically in the range 0.03 μm , while Rt, the difference between the highest peak and lowest trough, was 1-2 μm , almost four times the roughness. This corresponds to a smooth coating with a large number of growth defects originating from metal droplets.

As already discussed in the Literature Review, droplets embedded in PVD coatings have a detrimental effect on the mechanical properties and microstructural integrity of coatings. HIPIMS is a promising PVD technique because of three important features. HIPIMS

- a) produces high plasma densities and high ion-to-neutral ratios that allow to control the deposition process to produce coatings with dense microstructure and smooth surface [26]
- b) produces multiply charged metal ions that can be used for implantation pretreatment of substrates prior to coating deposition to enhance the adhesion of hard coatings [23, 25, 26]
- c) eliminates droplets

The following section demonstrates how these advantages can be realised in practice.

4.3.2. CrN films deposited by Reactive High Power Pulsed Magnetron Sputtering (HIPIMS)

The analysis of plasma composition and deposition flux of the HIPIMS process presented in Chapter 4.2 indicated that the method could be used successfully for thin film deposition. The large proportion of highly charged metal ions found both in the plasma and the deposition flux allows the mobility of the condensing species to be flexibly controlled to grow films with dense microstructure. The metal ions could also be used, as outlined in Chapter 4.1 describing the ABS technology, to improve the adhesion of the films by etching and metal ion implantation in the substrate prior to deposition. The combination of a highly ionised deposition flux and droplet free plasma generation makes HIPIMS potentially a valuable tool for coating deposition in corrosion, tribological, high temperature, and oxidation applications.

This chapter presents results from the trials of HIPIMS in two general directions. The first direction was to test the feasibility of HIPIMS as a metal ion source for the etching and implantation pre-treatment of substrates. The second direction was to investigate the properties and microstructure of CrN films deposited in a reactive gas atmosphere by HIPIMS.

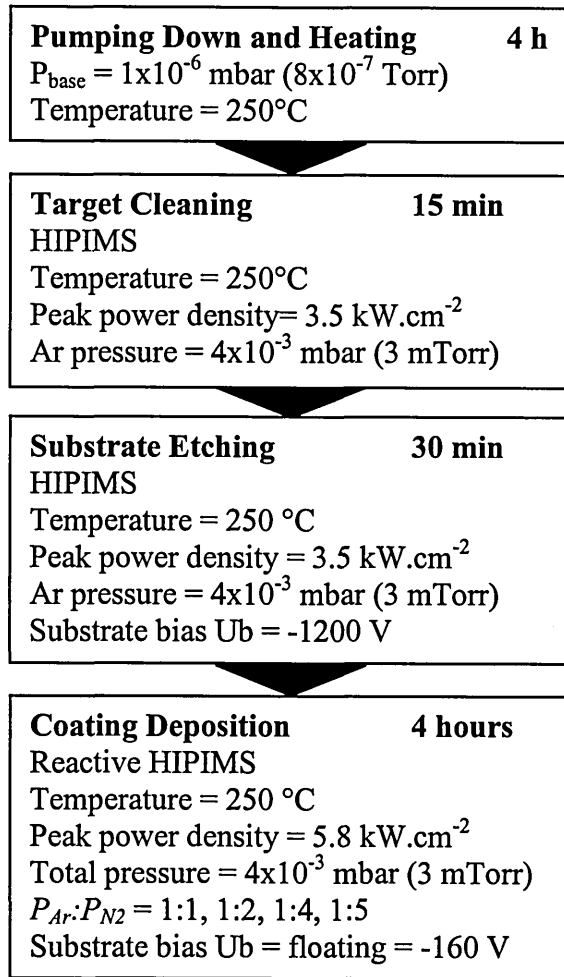


Figure 4.3.4. Deposition sequence

Experimental details of the deposition process

The coating depositions were carried out in a dedicated chamber described in Chapter 3.1 using a two-inch magnetron at a throw distance of 6.5 cm. The deposition sequence consisted of the four steps outlined in Figure 4.3.4. During the first step, the vacuum chamber was evacuated and the substrate was outgassed by radiation heating. During the second step the Cr target was sputter cleaned for 15 minutes by HIPIMS in an Ar atmosphere. A shutter in front of the target prevented any deposition on the substrates. The HIPIMS source was then operated for 30 minutes in inert Ar gas atmosphere at a pressure of $4 \cdot 10^{-3}$ mbar (3 mTorr) (much higher than the $6 \cdot 10^{-4}$ mbar (0.06 Pa) typically used in arc etching in the ABS process - see Chapter 4.2). A high bias of - 1200 V was applied to the substrates to achieve surface sputter cleaning and shallow ion implantation. During the fourth step CrN films were grown by operating the HIPIMS source in an Ar:N₂ mixture at a pressure of $4 \cdot 10^{-3}$ mbar (3 mTorr). The deposition time was 4 hours. The deposition temperature was monitored in situ and was maintained at 250 °C. No bias was applied to the substrates during these initial

deposition trials, however the floating potential established by the interaction of the substrates with the plasma had a peak value of -160 V.

Coating-substrate interface. Adhesion to high speed steel

The properties of the interfacial region influence strongly the adhesion between the coating and the substrate. The quality of the interface is determined by the chemical and physical conditions of the substrate surface. As outlined in Section 4.1.3.4, a substrate surface free of residual oxides and other contaminants is crucial for obtaining a clean interface and therefore strong adhesion. Additionally, metal ion implantation into steel substrates has been shown to promote localised epitaxy influencing the coating growth thus dramatically enhancing the adhesion (see Chapters 4.1 and 2). In many practical deposition processes, substrate sputter-cleaning and metal ion implantation are performed simultaneously by immersing the substrate in a plasma [6, 164]. High substrate bias voltages are used in order to amplify the effect of implantation over sputtering. The etching rate and the metal ion implantation depth are crucial parameters determining the efficiency of the etching process. The following results will describe the effect of the HIPIMS plasma source employed for ion etching on these parameters.

The etching rate was determined by step height measurements on high speed steel (HSS) samples that were masked with TiO_2 powder, biased to -1200 V, and immersed in a HIPIMS plasma. The source was operated in an inert Ar gas atmosphere and, as shown in Chapter 4.2, the plasma contained highly charged Cr metal ions and high density of Ar ions. After a treatment of 1 hour, step height measurements showed that a 300 nm thick layer of substrate material was removed.

In order to determine the range and quantity of implanted metal ions the chemical composition across the interface was determined by Scanning Transmission Electron Microscopy (STEM) - Energy Dispersive Spectroscopy (EDS) analysis of transmission electron microscope cross sections (XTEM). An XTEM micrograph of the analysed area is shown in Figure 4.3.5.

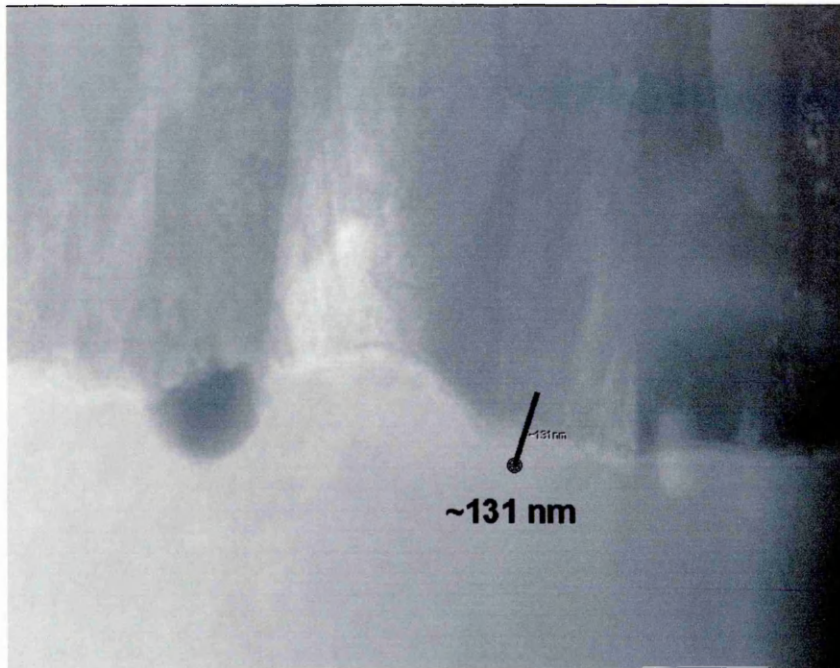


Figure 4.3.5. XTEM micrograph of the coating-substrate produced by HIPIMS. The line indicates the position and length of the area analysed by STEM-EDS

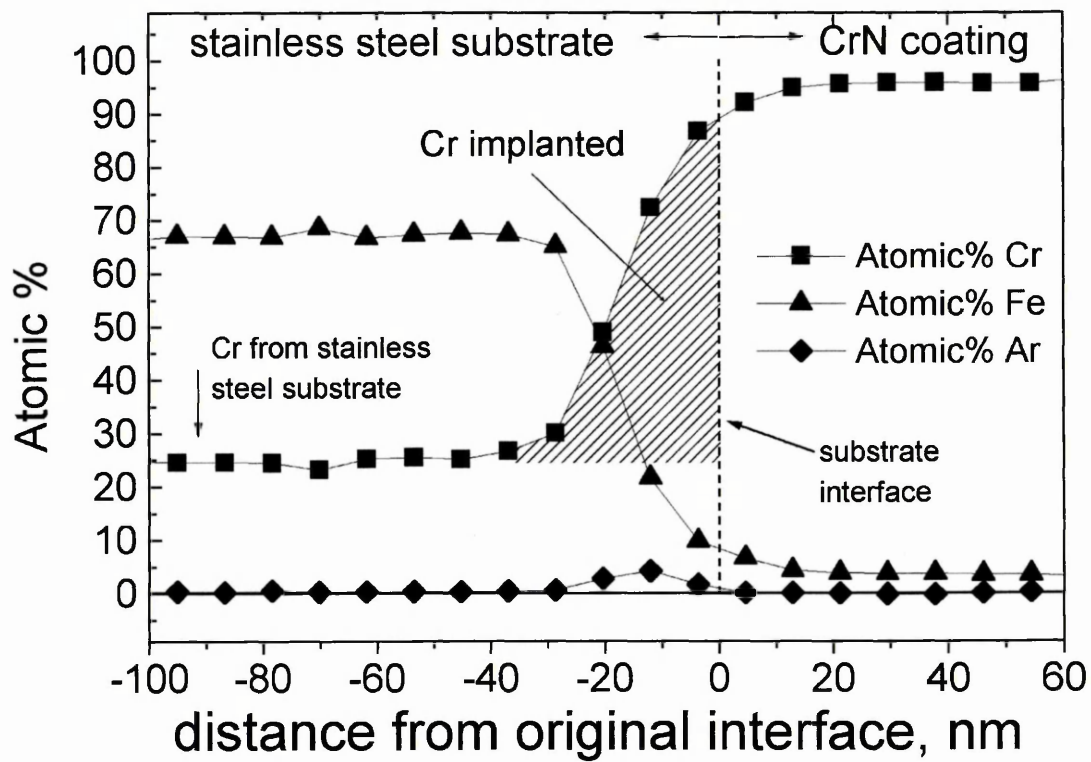


Figure 4.3.6. Chemical composition of the coating to substrate interface produced by HIPIMS. Data obtained by STEM-EDS point analysis. Ni signal is omitted.

The chemical composition of the interface as a function of distance from the interface is shown in Figure 4.3.6. The x-axis shows the distance from what was probably the original substrate surface which was sputtered and implanted during the pretreatment stage. The y-axis shows the atomic ratio of one element relative to the sum of all detected elements: C, Fe, Ar, and Ni (not shown). The STEM-EDS technique does not allow detection of nitrogen due to its low atomic mass, that is why the composition of the coating is given as 100% Cr. The interface was clean and did not contain any other chemical elements except for those from substrate and coating. There was no significant layer of pure Cr deposited after the etching process.

Excess Cr was found in the stainless steel substrates up to depths in the range 10 - 40 nm from the original interface (marked as 0). The measured Cr content shown is a result of a combination of contributions from the thin film, consisting of Cr and N (not shown), and implantation or diffusion of Cr into the substrate due to the pretreatment process. At the present moment the two contributions cannot be clearly separated. In arc etching treatments however, an implantation depth of typically 30 nm has been measured [17]. The content of Ar implanted or trapped in the interface reached values less than 5 at.% which is comparable to an etching performed with the arc discharge. The evaluation of the adhesion of coatings deposited on HSS substrates after etching employing the HIPIMS ion source, showed a scratch test critical load value of $L_C = 85$ N. The failure mode was adhesive, as can be seen from the scratch track in Figure 4.3.7. Critical loads of 65 N have been measured previously for CrN deposited by the ABS technology using Cr steered-arc etching, while values in the range 40 N are typical when Ar ion etching is used [165].

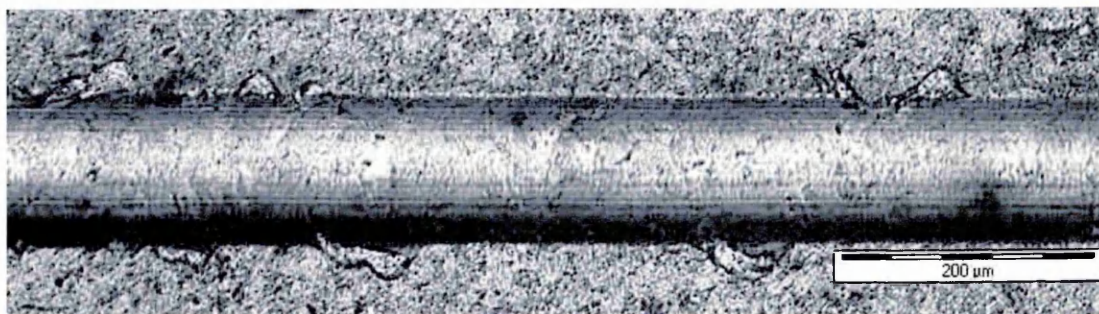


Figure 4.3.7. *Scratch test scar of CrN deposited on HSS.*

Most significantly, there were no droplets observed in the XTEM micrographs neither in the interface nor in the coating.

It can be speculated that metal ion implantation to depths of approximately 30 nm together with effective etching leads to a strong diffusion bonding between the substrate and the coating, could promote local epitaxial growth thus results in a superior adhesion. The high scratch critical loads confirm that a high quality interface has been produced using HIPIMS as a metal ion plasma source.

CrN coating deposition by HIPIMS

Following the substrate pretreatment, CrN coatings were grown at a temperature of 250 °C in a mixed Ar-N₂ gas atmosphere with partial pressure ratios P_{Ar}:P_{N₂} of 1:1, 1:2, 1:4 and 1:5. The deposition rate, measured by a quartz crystal microbalance (QCM) in this range of gas compositions, is shown in Figure 4.3.8. The measurement at the ratio 1:4 was confirmed by step height measurements on a Si substrate masked with TiO₂ powder. The value was 0.459 ± 0.009 µm/hour. At the high Nitrogen content end, the deposition rate was in the range of 0.5 µm/hour at 6.5 cm from the target. For P_{Ar}:P_{N₂} ratios lower than 1:2 the deposition rate increased dramatically indicating that, for the HIPIMS source, the point of poisoning of the target was reached between the ratios 1:1 and 1:2.

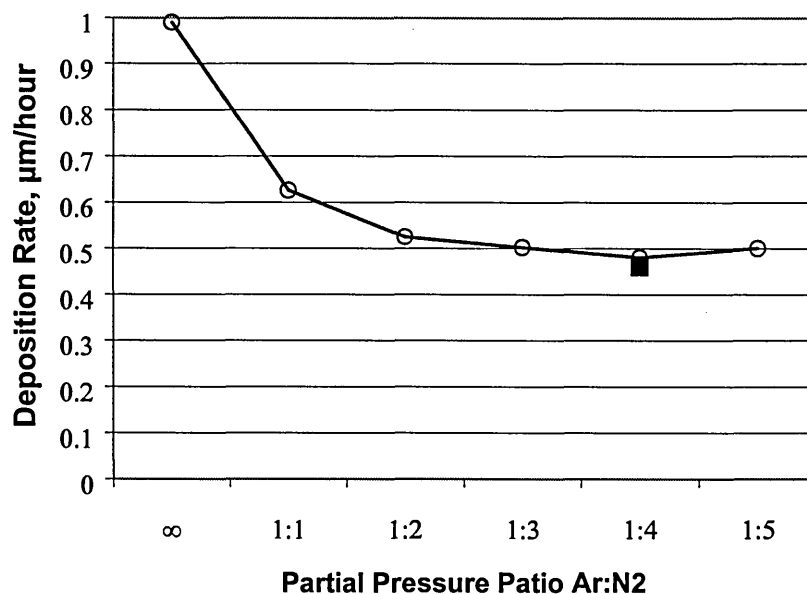


Figure 4.3.8. Deposition rate produced measured in HIPIMS operated in different Ar-N₂ gas mixtures at a constant pressure P_{tot} = 0.4 Pa (3 mTorr). Measurements carried out by QCM are marked with open circles. The full square represents a step height measurement.

CrN coating microstructure

Smooth surface CrN films were deposited by reactive HIPIMS. Dramatically different surface morphology was achieved when CrN was deposited purely by HIPIMS compared to deposition by the ABS™ technology. Optical and secondary electron microscopy (SEM) micrographs of the coating deposited by ABS are shown in Figure 4.3.9 a) and c). A smooth overall coating surface is observed, but there is an appreciable concentration of growth defects originating from droplets produced during the arc pre-treatment phase.

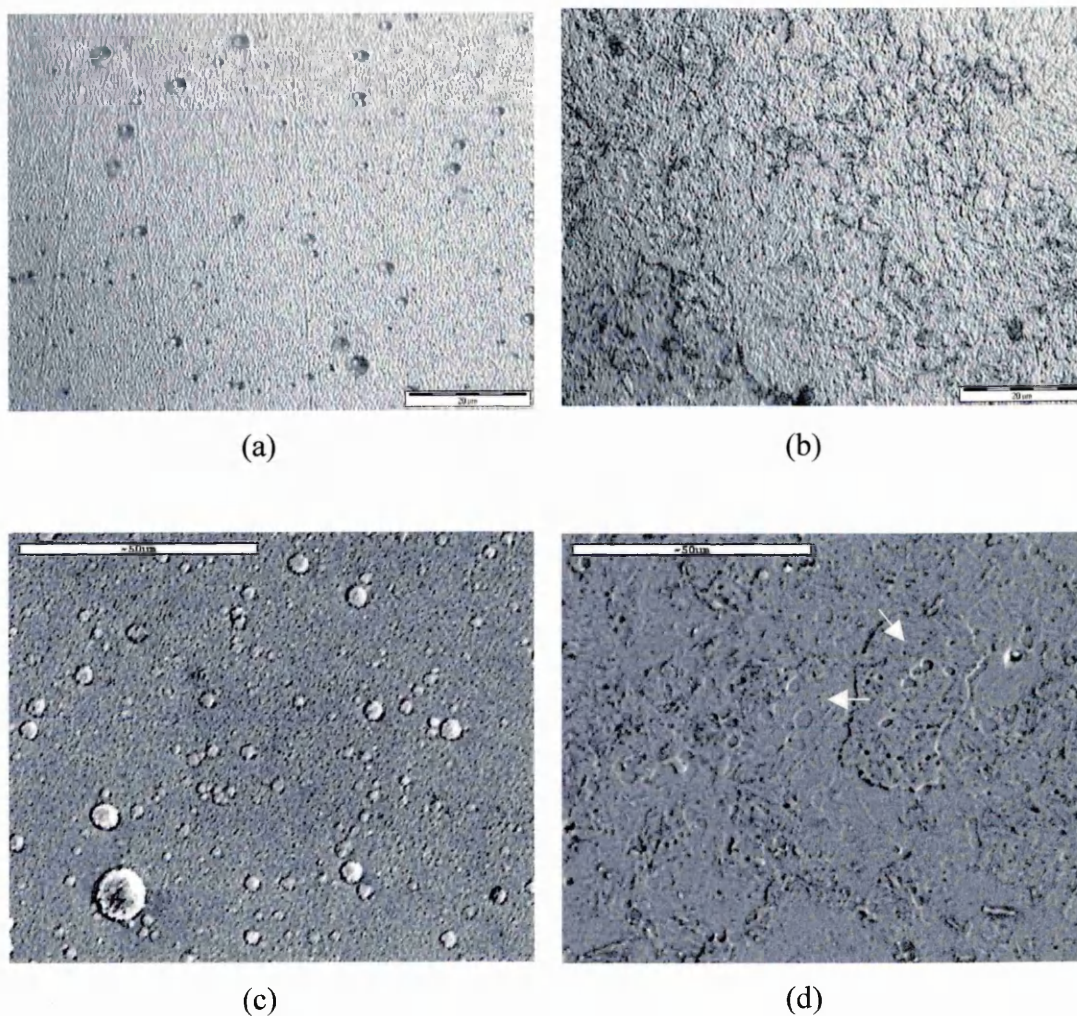


Figure 4.3.9. Micrographs of CrN coating surfaces: (a) optical micrograph of CrN deposited by ABS technology (b) optical micrograph of CrN deposited by HIPIMS, (c) SEM micrograph of CrN deposited by ABS technology and (d) SEM micrograph of CrN deposited by HIPIMS

By contrast, Figure 4.3.9 b) and d) show the optical and SEM micrographs of the HIPIMS CrN coating surface. Large-scale growth defects were not observed. The

surface contains round protrusions with diameter approximately 5 μm marked with white arrows in Figure 4.3.9 d). These protrusions are present in the high speed steel substrate itself after polishing. These features have been enhanced additionally during the etching step.

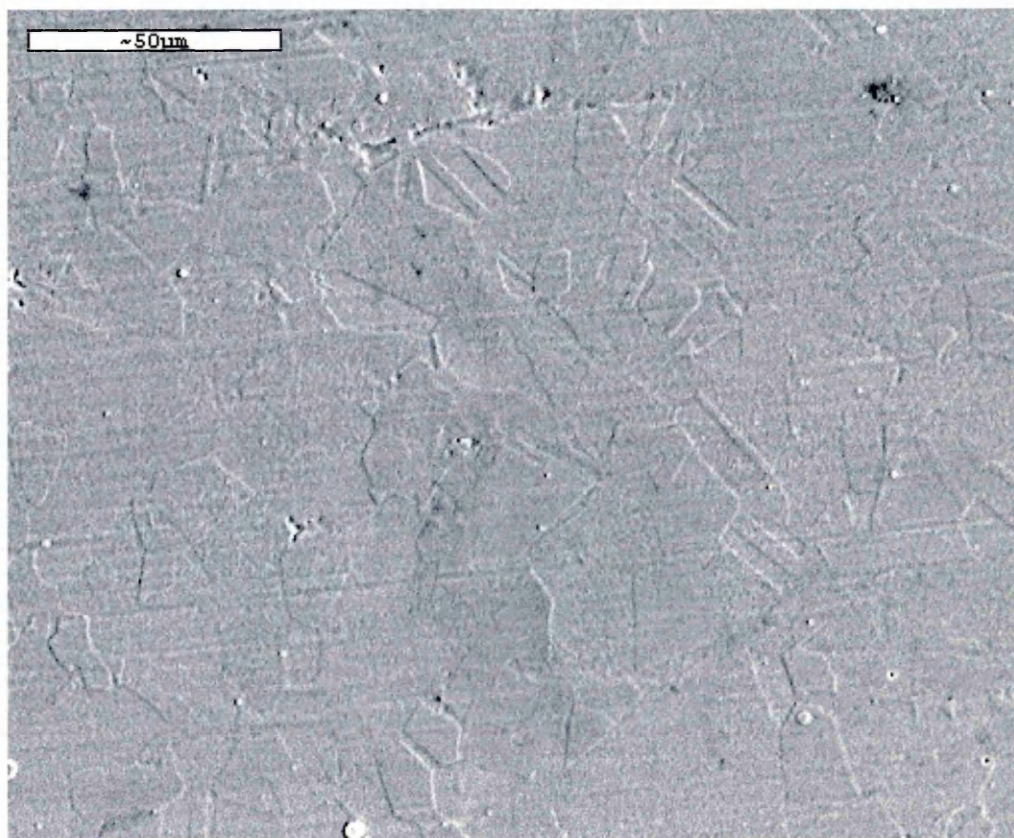


Figure 4.3.10. SEM micrograph of a CrN coating deposited by HIPIMS on 304 austenitic stainless steel.

Figure 4.3.10 shows the surface of HIPIMS CrN films deposited on stainless steel substrates observed by SEM. Protrusions or large scale defects are not observed. The surface of the coating contains large flat areas spanning a few tens of micrometres with angled boundaries, closely resembling the austenitic grain structure of the substrate. TEM observations (see figures 4.3.12-14) showed that the column width of the coating itself was two orders of magnitude smaller than the features on the surface. The difference in height between the grains is probably established during the etching step prior to deposition when the lattice orientation influences the sputtering yield.

The surface features were also studied by atomic force microscopy (AFM). Figure 4.3.11 (a) shows a three dimensional reconstruction of the surface of the coating. Large flat areas and steps are observed. This image correlates well with the SEM image of the surface shown in Figure 4.3.11 (b).

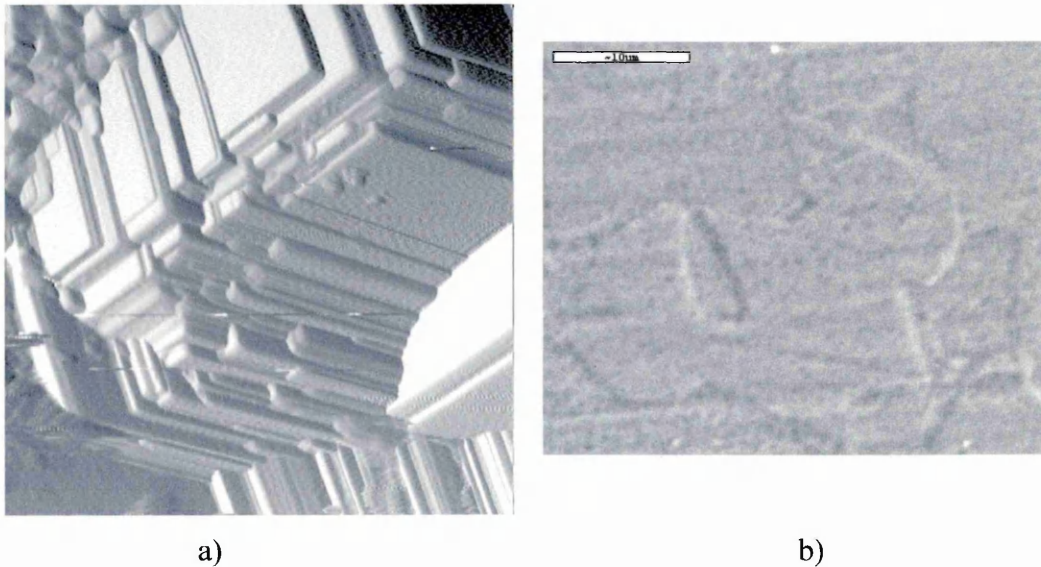


Figure 4.3.11. The CrN coating surface viewed by (a) AFM (b) SEM. The coating conforms well to the structure of the steel grains.

The roughness $R_a = 0.035$ was comparable to that measured for the ABS deposited coating in Table 4.3.1, but R_t , the difference between the highest peak and lowest trough, was much lower reaching a value of $0.5 \mu\text{m}$ compared to $1\text{-}2 \mu\text{m}$ for ABS deposited CrN.

The microstructure of the film was also observed in cross sectional views in a transmission electron microscope (XTEM). Figure 4.3.12 shows an XTEM micrograph of the top part of the coating deposited at $P_{Ar}:P_{N_2} = 1:4$. The structure is made of clearly identifiable columns, which terminated with flat tops (c.f. magnetron sputtered films with sharp 'teeth'). Flat columns are typically formed when the crystals grow at specific crystallographic orientations (texture), but also when the condensing species have a high mobility on the surface or intensive resputtering of the coating during growth is present.

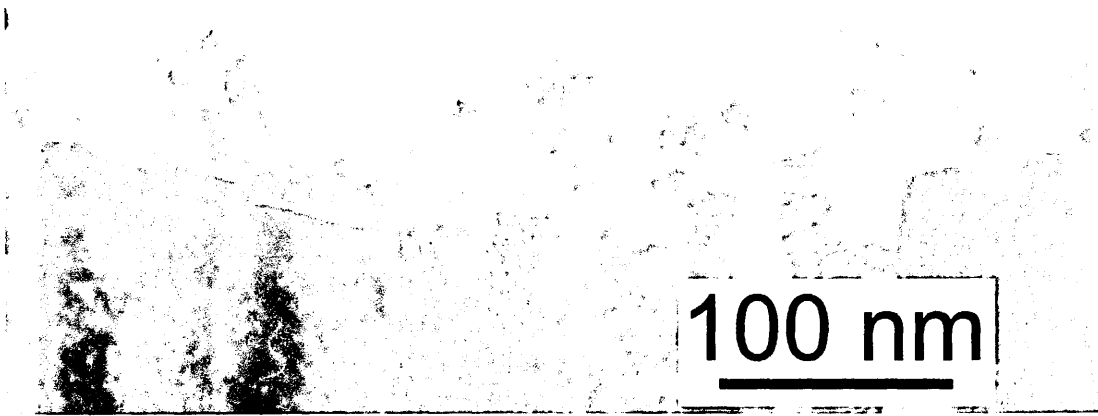


Figure 4.3.12. TEM cross section of a CrN film produced by HIPIMS CrN. The film is columnar and the columns are terminated with flat tops.

Further indication for the high mobility of the condensing flux can be derived from the XTEM view of the overall coating shown in Figure 4.3.13. In the interface region, it can be seen that the grains immediately adjacent to the substrate have a large base of more than 100 nm in size. This is indicative of high adatom mobility during the initial nucleation of the films.



Figure 4.3.13. XTEM micrograph showing the overall structure of HIPIMS CrN.

The high adatom mobility also helps to form a dense microstructure of the films. Figure 4.3.14 a) shows a XTEM micrograph of an intermediate region of the film where several grain boundaries meet. No voids were observed in the coating.

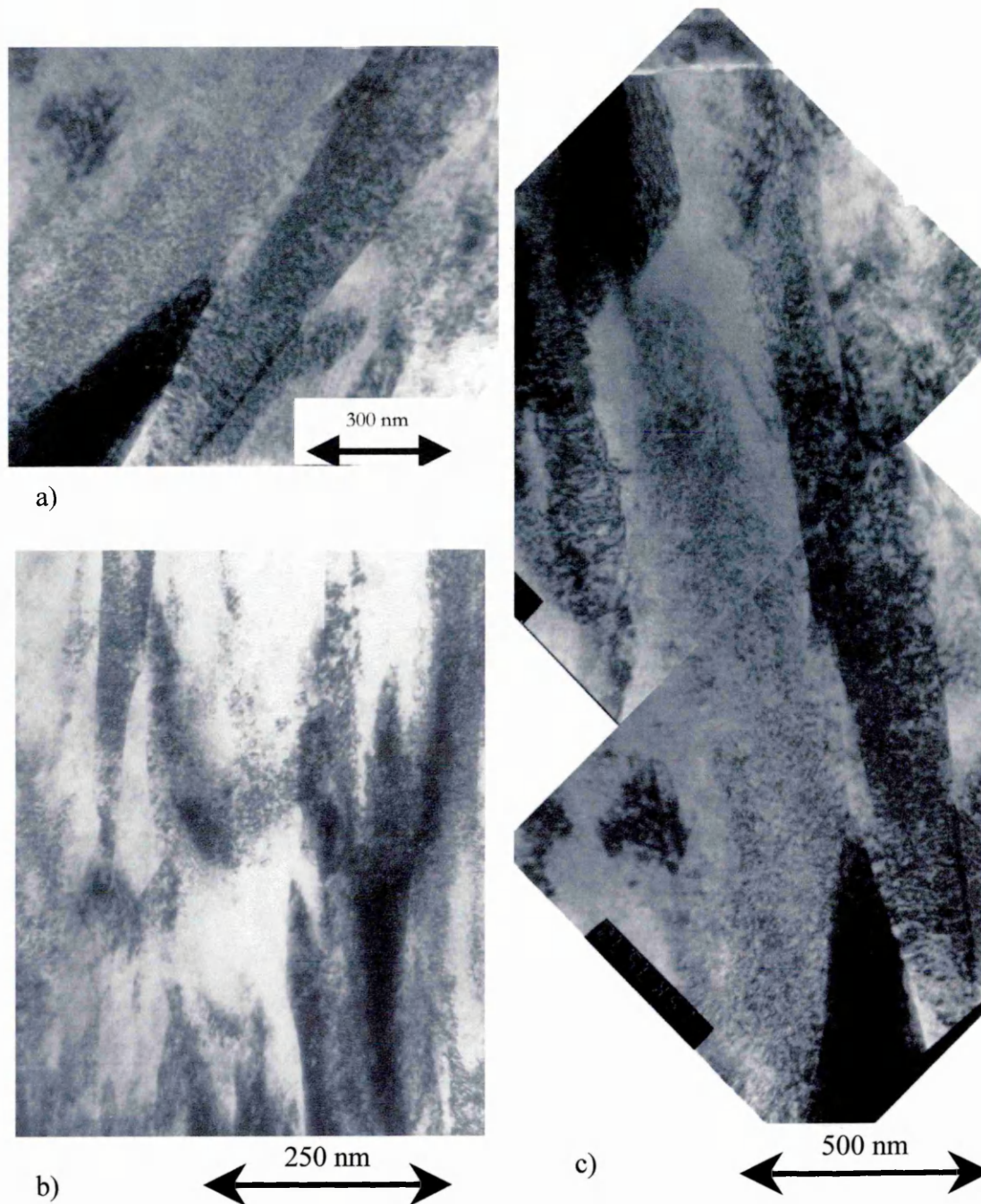


Figure 4.3.14. XTEM micrographs of a HIPIMS CrN film. (a) Void free grain boundaries (b) Grains are formed and extinguished far from the initial nucleation at the interface. (c) Strain and dislocation contrast is observed in the TEM image.

In all Figures 4.3.14, the columns appear 'speckled'. Such a fine scale variation in contrast in the TEM image is usually attributed to strains within the columns or dislocation defects in the film crystal structure. Similar contrast/speckles can be seen throughout the film, as shown in Figure 4.3.13. The observation of speckles has been made by Petrov et al [166] for magnetron sputtered films when the substrate bias voltage exceeded -80 V.

Another feature of the HIPIMS CrN film shown in Figure 4.3.14 b) is that the growth of some grains is extinguished as new grains start forming. This process is known as renucleation and is favoured when the growing film contains a high density of lattice defects [166]. An adatom arriving at a defect can have a very high binding energy and form a stable new nucleation site.

The high density of dislocation defects and the small column size, which are clearly visible in the XTEM micrographs, are typical features of a high energetic deposition show that the condensing flux arrives at the surface with a relatively high energy. Nevertheless the deposition was carried out without applying an ion accelerating bias to the substrate; i.e. the substrates were at floating potential. The origin of the highly energetic ions may be explained in terms of the plasma properties. Figure 4.3.15 shows how the plasma density and potential vary within the plasma sheath around an object at floating potential.

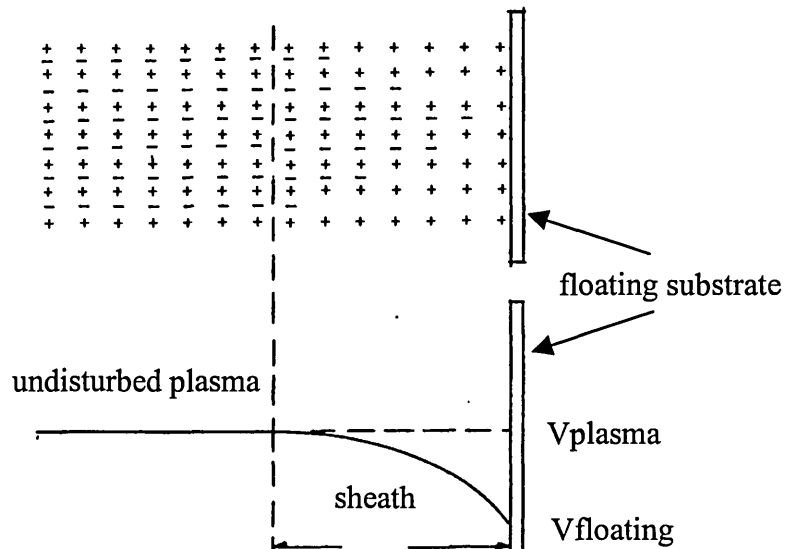


Figure 4.15. Plasma sheath near a floating substrate.

When ions from the plasma enter the substrate sheath, they are accelerated by a field created by the difference between the plasma potential and the floating (substrate) potential. The energy to which the ions are accelerated is then equal to $E_{ions} = e \cdot (V_{plasma} - V_{floating})$. The plasma potential in typical magnetron discharges is established within a few volts from ground, indicating that the ions would be accelerated to an energy approximately equal to the floating potential. Due to complications with time resolved electrostatic probe measurements the plasma potential and electron temperature were not evaluated for the HIPIMS plasma, but it was possible to measure the floating potential. As the discharge plasma developed within the power pulse, a floating potential developed on the substrates. The peak in floating potential matched the peak in target current and reached -160 V at maximum. Assuming a plasma potential of 0 V, the energy gain due to acceleration of ions in the sheath is of the order of 160 eV. The bombardment of ions with such energy can initiate low rate sputtering in the majority of metals. This energy is sufficient to induce also ion irradiation damage in the growing layers [166].

In summary, the growth conditions of the CrN coatings deposited by HIPIMS can be characterised by a high density ion flux and high adatom mobility which promote columnar growth with flat column tops and a near equiaxed grain structure. The coating structure is dense without voids and large scale growth defects. The deposited films are being bombarded by high energy ions thus increasing the dislocation defects in the coatings. Similar flat column tops and dislocation densities have been reported in the literature when nitride films were grown with bias voltages between -100 V and -200 V. [167]

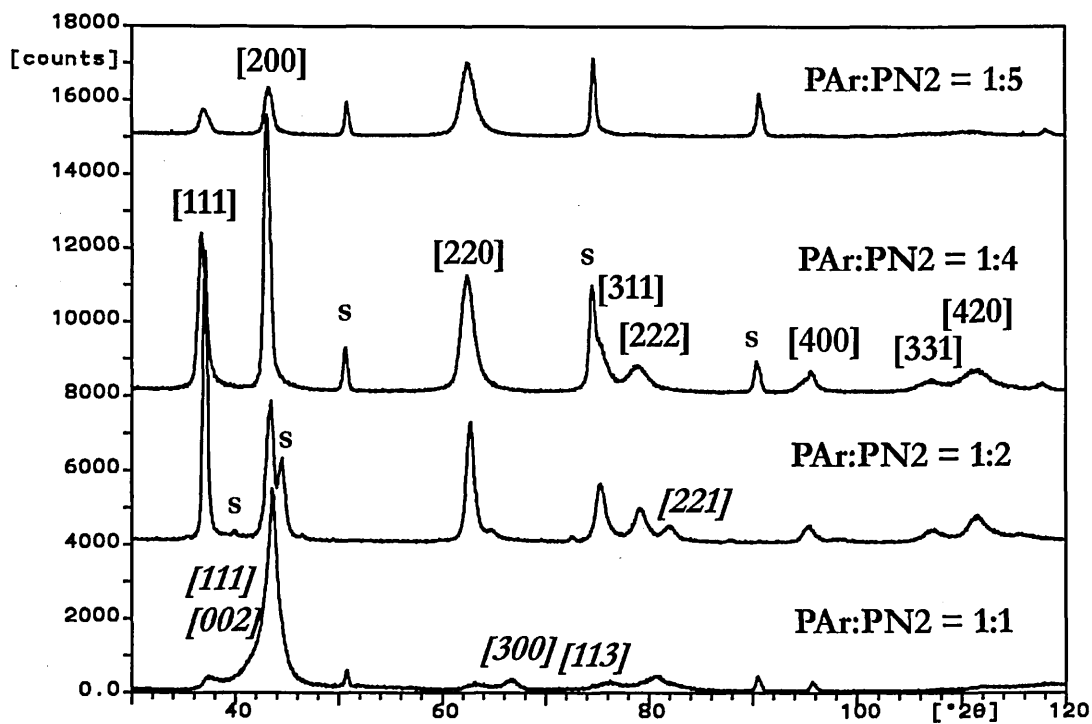


Figure 4.3.16. Glancing angle XRD scans (10° incidence) showing the phase composition of HIPIMS CrN films deposited at different Ar:N₂ partial pressure ratios. Peaks of the Cr₂N phase are marked in italics.

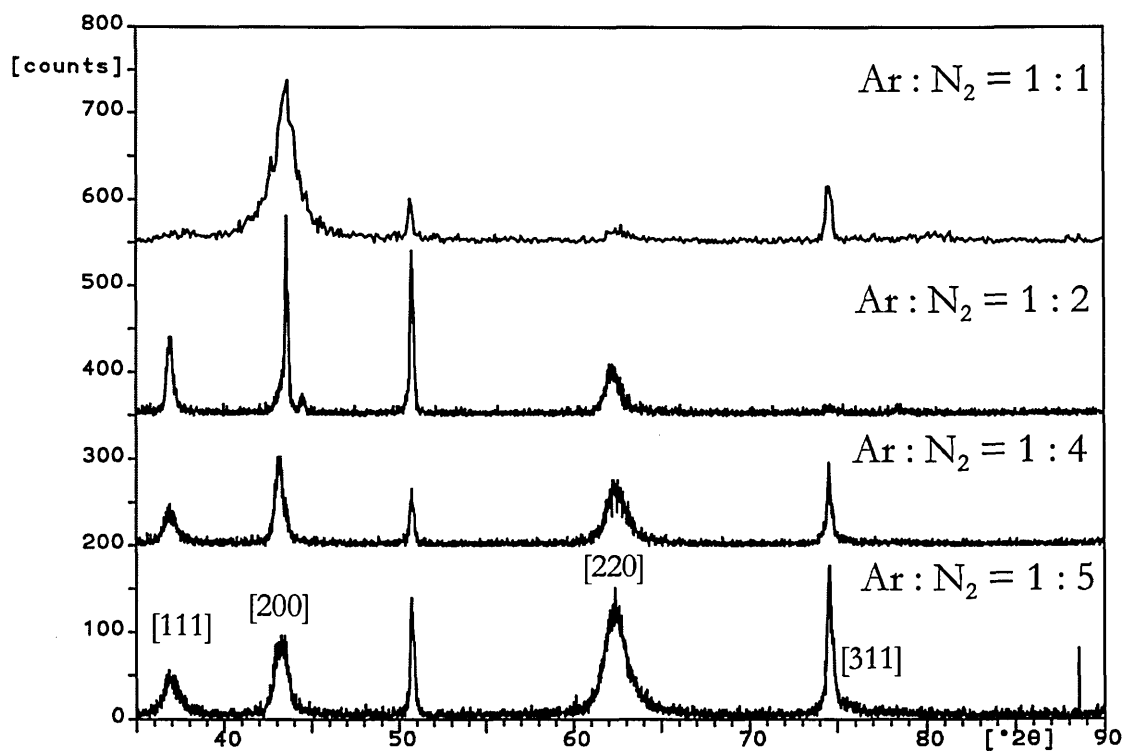


Figure 4.3.17. Bragg-Brentano XRD scans showing the microstructure of CrN films deposited at different Nitrogen partial pressures by Reactive HIPIMS.

The average microstructure was determined using X-Ray Diffraction. Glancing angle XRD θ - 2θ scans were used to analyse the phase composition. Scans in Bragg-Brentano geometry were used to estimate the preferred orientation of the films. Figure 4.3.16 shows GA-XRD spectra at glancing incidence of 10° for four films deposited at different Ar:N₂ partial pressure ratios $P_{Ar}:P_{N_2}$. The films deposited at $P_{Ar}:P_{N_2} = 1:5$ exhibit practically a pure CrN phase. As the nitrogen pressure is decreased, Cr₂N peaks intensify, and at $P_{Ar}:P_{N_2} = 1:1$ the overlapping of Cr₂N and CrN phase peaks is very strong. Figure 4.3.17 shows XRD scans in the Bragg-Brentano geometry. The high nitrogen pressure films are randomly oriented, while for $P_{Ar}:P_{N_2} = 1:1$ the trace exhibits a strong CrN [200] and Cr₂N [111] preferred orientation.

The residual stress, hardness and friction coefficient are summarised in Table 4.3.2.

Table 4.3.2. Residual stress and selected mechanical properties of HIPIMS deposited CrN films.

Partial pressure ratio $P_{Ar}:P_{N_2}$	1:1	1:2	1:4	1:5	Ref
HK _{0.025}		2887 ± 245	2633 ± 47		
Plastic Hardness, Hp, GPa		23.57	21.56		
Elastic modulus, E, GPa		277	268	250 (assumed)	
Residual stress, GPa	- (4.15Å)	-2.55 (4.19Å)	-3.4 (4.21Å)	-2.99 (4.20Å)	4.14 Å
Scratch Test Critical Load, L _C , N			85		
Friction coefficient against Al ₂ O ₃		0.4	0.45		
Wear rate, m ³ N ⁻¹ m ⁻¹		2.3×10 ⁻¹⁶	4.076×10 ⁻¹⁶		
Roughness	Ra, μm		0.035		
	Rt, μm		0.5		

The hardness of the films was in the range of 2700 Knoop. The average residual stress was determined by glancing-angle XRD measurements. The stress for the 1:1 coating could not be evaluated because of the strong texture and overlapping of the Cr₂N and CrN peaks. The residual stress varies with gas composition, is compressive for all films and has a value in the range 2.5 to 3.5 GPa. The microhardness and stress

values shown in Table 1 agree well with results on magnetron sputtered CrN deposited at high bias voltages and nitrogen partial pressures where, in special cases, hardness values reaching $HK_{0.025} = 3000$ were reported [29, 112]. In comparison to other deposition techniques, the residual stress value is higher than typically observed in magnetron sputtered CrN coatings where it can be in the range from 0.2 GPa [28] to -4 GPa [29] but is much lower than the 6 GPa values typical of filtered arc deposition [168]. However, the texture of the HIPIMS films bears similarity to arc deposited CrN at bias voltages of -100 V [169].

The results from pin-on-disk tests of the coatings showed a remarkably low sliding wear coefficients. Figure 4.3.18 shows a comparison of the HIPIMS single layer CrN coating with electroplated hard Cr, conventional UBM sputter deposited CrN, arc evaporated CrN, and high pressure UBM high hardness CrN.

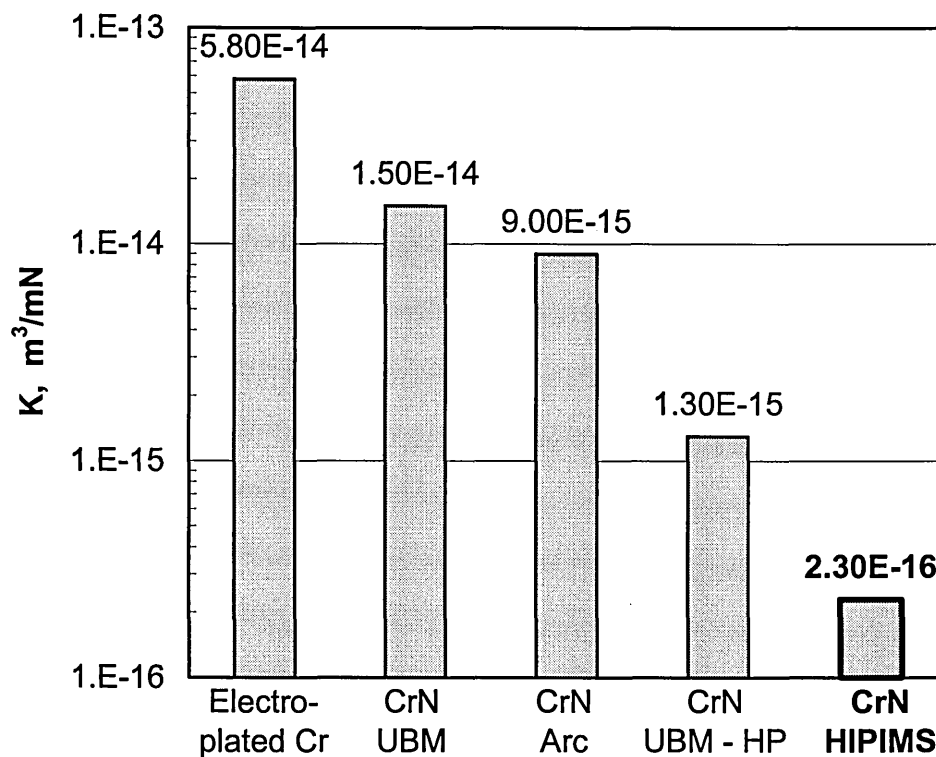


Figure 4.3.18. Comparison of the sliding wear coefficient, K , of CrN deposited by HIPIMS to electroplated hard chrome and CrN deposited by other PVD methods [170].

In columnar single layer coatings, the wear mechanism is based on the bending of the columns due to frictional forces and microwelding occurring at asperities [14]. As the columns bend, existing cracks between them are enhanced and parts reaching up to 70 nm in height are detached from the top of the columns. The debris generated in this process contributes further to the wear as it acts as an abrasive third body.

As shown by the XTEM micrographs, the HIPIMS deposited CrN coatings also exhibit a columnar microstructure. However, the microstructure is characterised also with a high density and relatively large column size compared to UBM or arc deposited coatings [112].

It can be speculated that both these features can improve the wear resistance of the coatings. The high density of the HIPIMS coatings signifies that the columns are strongly bound together. The quasi equiaxed grain morphology and renucleation evident in the microstructure represent discontinuities in the material properties and allow cracks to be deflected parallel to the surface thus diminishing the production of debris and improving the wear resistance of CrN coatings deposited by HIPIMS. Furthermore, bending of the columns due to tangential forces during the wear process is strongly reduced due to the large size and greater toughness of the columns.

The corrosion protection properties of the HIPIMS CrN thin film deposited at $P_{Ar}:P_{N_2} = 1:4$ were evaluated in potentiodynamic aqueous corrosion tests. The polarisation curve of CrN coatings deposited by HIPIMS on SS substrates and tested in potentiodynamic corrosion tests is shown in Figure 4.3.19. It can be seen that the large rise in potential from ~ 200 to 470 mV leads to a small rise in current from 2×10^{-7} to 1×10^{-6} Acm⁻² (passivation current), indicating that the corrosion is passivated in this region. At potentials higher than $+470$ mV (pitting potential), the current rises dramatically as the corrosion process evolves at a large number of pits.

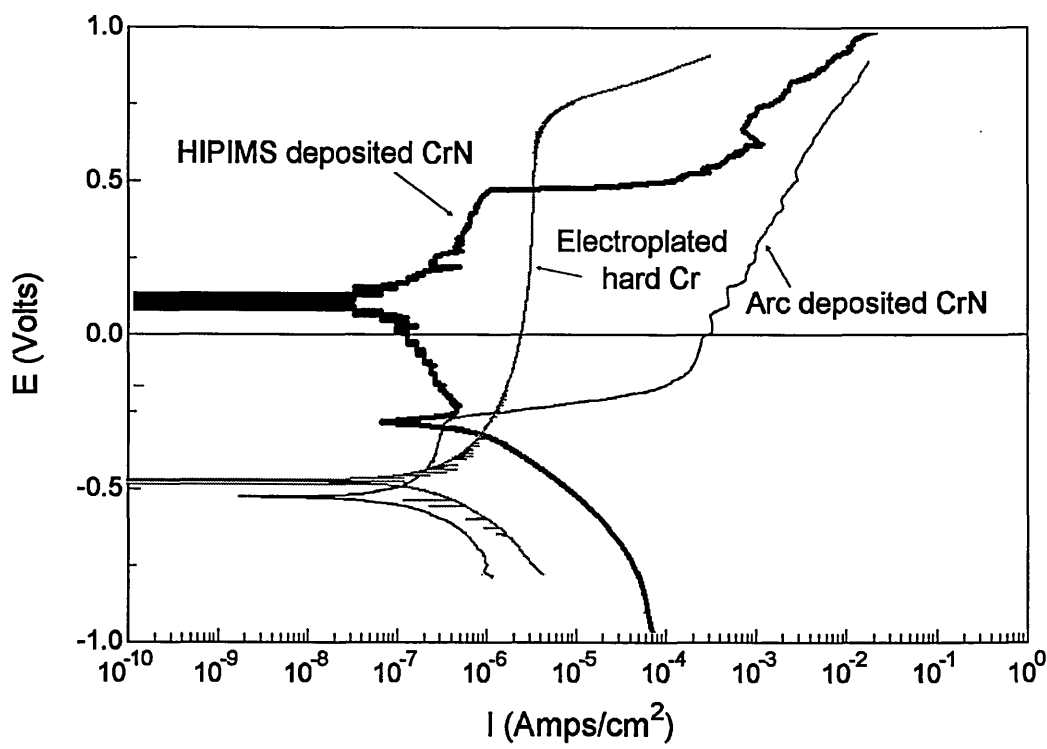


Figure 4.3.19. Potentiodynamic polarisation curve of monolithic CrN deposited by the HIPIMS method. The behaviour of electroplated hard Cr and arc deposited CrN is shown for comparison.

In comparison, 3 μm thick cathodic arc deposited CrN films proved to be clearly inferior. In the case of 25 μm thick electroplated hard Cr we observe higher corrosion currents, but the pitting potential is twice as high as the HIPIMS coating, obviously due to the increased thickness of the electroplated coating.

Corrosion tests give a clear indication of the number of voids and the overall density of PVD films. Nitrides and oxides of the transition metals are known to be chemically inert. The main mechanism for the corrosion of nitride coated components is the direct access of corrosion media to the substrate through coating defects [171]. Direct access is established easily in PVD thin films because of their columnar structure allowing some intercolumnar cracks or intragranular voids to extend from the surface of the coating down to the substrate. A different kind of defect is observed in non-filtered arc deposited coatings where droplets produced in the metal vapour source can induce growth irregularities and consequently voids. Nevertheless, the coatings produced by arc evaporation are characterised by high density in the non-disturbed regions and enhanced corrosion protection because the highly ionised and mobile deposition flux characteristic of the arc discharge is able in some cases to close even the large-scale growth defects caused by droplets.

The corrosion protection properties of HIPIMS CrN films can be compared to those measured in corrosion tests of arc deposited corrosion resistant films. As shown in Chapter 4.2 and the previous paragraphs of this chapter, the condensing flux in HIPIMS comprises at least 30 % metal ions. Due to the high floating potentials a large proportion of adatoms is highly mobile and the overall microstructure is highly dense. Although the renucleation process described above increases the number of column boundaries present in the film, no voids have been observed in the XTEM micrographs. The high density of the film can explain the excellent protection of stainless steel against aqueous corrosion.

Summary

Plasma diagnostics and microstructural studies identify the high power pulsed magnetron sputtering method (HIPIMS) as an extremely promising PVD technique suitable for both substrate pretreatment and coating deposition.

High energy Ar/Cr ion irradiation prior to coating leads to a metal ion implantation profile at the substrate-coating interface similar to the ABS technique. Subsequently deposited CrN films were found to have an excellent adhesion reaching scratch critical load values of 85 N on HSS substrates. CrN deposited in the high density plasma environment of the HIPIMS discharge was columnar with a dense microstructure. No droplets or other large scale growth defects were observed in TEM cross sections. The films were relatively hard and had superior corrosion and wear resistant properties, reaching the quality of nanoscale multilayer/superlattice coatings [172, 173] and superior to high hardness UBM deposited CrN and hard chrome.

4.4. Unbalanced Magnetron Sputtering Glow Discharge with Enhanced Ionisation by Radio Frequency (RF) Coil

As discussed in the Literature review (Chapter 2) and shown experimentally in Chapter 4.1 and Chapter 4.3 metal ion implantation in steel substrates prior to deposition enhances the adhesion of hard coatings. The ABS technology incorporates an arc discharge to produce metal ions and realise this pretreatment. However, a major drawback of arc discharges is the production of droplets causing growth defects in the coating and compromising its mechanical behaviour. One of the best alternative sources to the arc has been developed by Rossnagel *et al.* [19] who proposed a method based on magnetron sputtering which allows 70% of the metal flux to be ionised and no droplets to be formed. The method utilises an *in vacuo* radio frequency powered coil (RF coil) positioned concentrically around the planar magnetron sputtering target. When RF power is applied to the coil the ion and excited species density increases significantly. The principle of operation of this kind of discharge is well understood. The radio frequency power driving the coil is transmitted to the plasma sheath by inductive coupling, similar to the operation of a transformer [20]. Currents are induced near the plasma sheath edge and serve to increase the electron energy and consequently the excitation and ionisation probability [52]. The metal ionisation efficiency of the inductively coupled magnetron sputtering (ICPMS) discharge is enhanced significantly as the atoms spend longer times near the coil. The dwell time of sputtered species can be increased by positioning the coil far from the target, where, after many collisions, the initial energy of the sputtered atoms is significantly reduced. Alternatively, increasing the pressure could slow down the diffusion and could increase the probability of Penning ionisation by collision of gas and metal atoms. Maximum coil efficiency is achieved at pressures typically of 3 Pa (3×10^{-2} mbar) where 70% ionisation of metal flux has been measured [19]. However, the obvious disadvantage of using high pressures is the drastically reduced deposition rate.

This chapter presents results from plasma diagnostics of an RF coil amplified magnetron sputtering discharge. Initially experimental studies were conducted at the Materia Nova Laboratory, of the Universite de Mons-Hainaut, Mons, Belgium. The plasma composition was investigated with optical emission spectroscopy (OES) and mass spectroscopy (MS). Ion energy distribution functions (IEDFs) were measured by

energy resolved mass spectroscopy (EMS). Based on the experience acquired in Materia Nova, an RF coil was designed, manufactured, and installed in the industrially sized Hauzer HTC 1000/ABS deposition machine at Sheffield Hallam University. Preliminary investigations of the discharge parameters, plasma composition and density were carried out in order to estimate the stability and efficiency of the industrially sized RF coil.

4.4.1. Typical Plasma Composition and Ion Energy in the RF Coil Amplified Magnetron Discharge

The typical plasma parameters of the RF coil amplified magnetron discharge were investigated at the Materia Nova Laboratory, Mons, Belgium in a laboratory sized magnetron and RF coil setup. Ti targets were sputtered in an Ar gas atmosphere. Experimental details are described in Section 3.4.

Analysis by OES confirmed an increased metal ion fraction as compared to the magnetron discharge. A typical optical spectrum is shown in Figure 4.4.1. The dominant emission is from Ti and Ar neutral species, however an enhanced proportion of singly ionised Ti ions is visible. Ar ion emission was not detected.

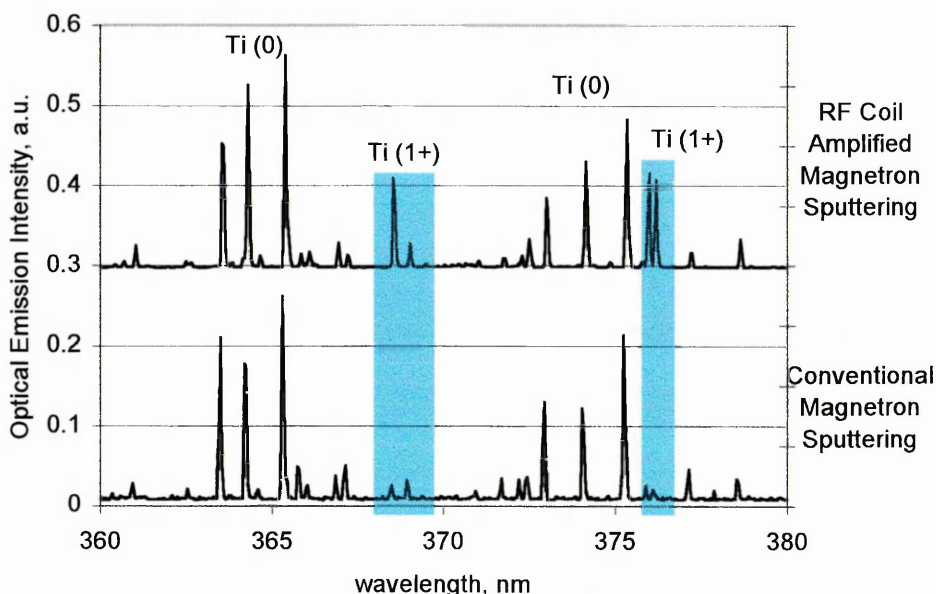


Figure 4.4.1. Typical OES spectra of an inductively coupled RF amplified magnetron discharge and conventional sputtering discharge. Ti ion lines are shaded. Conventional sputtering discharge with DC power = 200 W at Ar pressure 30 mTorr. RF coil discharge in the same conditions and RF power = 500 W.

The plasma composition was additionally analysed with an energy resolved mass spectrometer described in Chapter 3.5.5. The measurements were performed without additional ionisation in the mass spectrometer in order to investigate only the ion composition of the plasma. Figure 4.4.2 shows a typical mass spectrum. Ar^{1+} ions are clearly the dominant species but well-defined peaks of Ti^{1+} and Ar^{2+} ions are also visible.

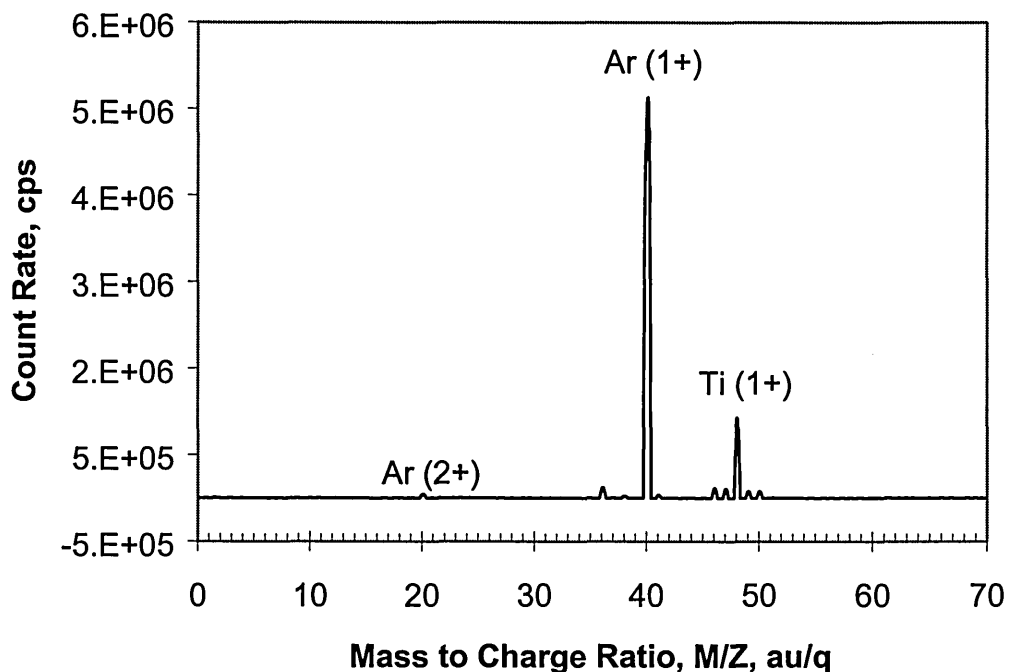


Figure 4.4.2. Typical mass spectrum of an inductively coupled RF amplified magnetron discharge. RF power 250 W, DC power 200 W, Ar pressure 30 mTorr. The small peaks on the sides of the Ti^{1+} are from naturally occurring isotopes of Ti.

The energy spectrum of the ions in the plasma was studied by energy resolved mass spectrometry. The ions in the discharge acquired energies in the range of 40 to 80 eV - some two orders of magnitude higher than conventional magnetrons. Figure 4.4.3 shows that both ion species - Ar and Ti had similar energy distribution functions.

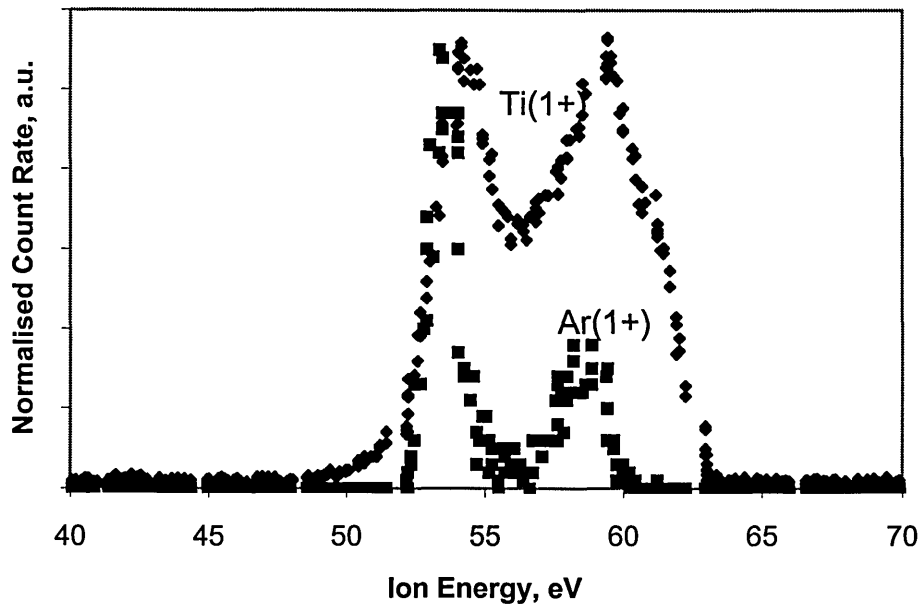


Figure 4.4.3. Typical ion energy distribution function of Ar and Ti ions in an inductively coupled RF amplified magnetron discharge conditions as in Figure 4.4.2 - RF power 250 W, DC power 200 W, Ar pressure 30 mTorr.

The high ion energies are associated with the radio frequency plasma sheath. The high mobility of electrons allows them to follow the RF oscillations in the electric field. In comparison the ions are several orders of magnitude heavier and are not influenced by the oscillations. The combination of fast oscillating electrons and still ions results in a plasma sheath with a high potential drop which accelerates ions in the bulk plasma to the high energies that are experimentally observed [52]. Both Ti and Ar ions are accelerated by the same dominant mechanism and therefore exhibit similar IEDF. It is interesting to note that the energy distribution function was double peaked. This distribution was observed routinely when the coil was operated on its own or in conjunction with the magnetron. At the present time, this behaviour is not understood. Double peaked distributions in RF coil discharges have been reported by other researchers when using RF coil in conjunction with RF sputtering [174]. It is important to note that late in the experiments it was found that the power applied to the magnetron was actually pulsed (frequency of 100 kHz, 50% duty cycle). The IEDF exhibited two peaks when pulsing was used and one peak when continuous mode was used. However, subsequently repeated OES measurements in continuous mode showed that there was a negligible difference between pulsed and continuous magnetron operation in terms of the plasma composition and the effect of RF power and gas pressure on it (private communication with the team in Mons Ref. [113]).

4.4.2. Influence of Power Dissipated in the RF Coil on Ion Density and Energy

The power dissipated in the RF Coil had a significant influence on the discharge parameters, the plasma composition and ion energy distribution functions (IEDF). In operation, the root mean square (rms) current in the coil was in the range 4.6 - 7.2 A and the typical rms voltage in the range 120 - 150 V as measured with an impedance probe. The typical impedance of the coil with the plasma on and minimised reflected power was $Z = 6.4 + j20 \Omega$. The values were influenced by the RF power as well as the degree of impedance matching between the RF power supply and the RF coil as indicated by the standing wave ratio (SWR) measured with a SWR meter.

Figure 4.4.4 shows the effect of RF power on the magnetron current at different operating pressures. As the RF power was increased, the plasma ionisation increased causing the target current also to rise. Because the target was operated in constant power mode the increase in target current induced a decrease in voltage from 200 to 150 V shown in Figure 4.4.5.

The effect of gas pressure on the discharge parameters is also visible in Figure 4.4.4. For a given RF power, the target current increases with increasing pressure. This indicates that a higher plasma density is produced. Since the RF coil power is the same, the increase in plasma density can be attributed to the more efficient inductive coupling of the coil and the plasma and the decreased mean free path of electron impact ionisation.

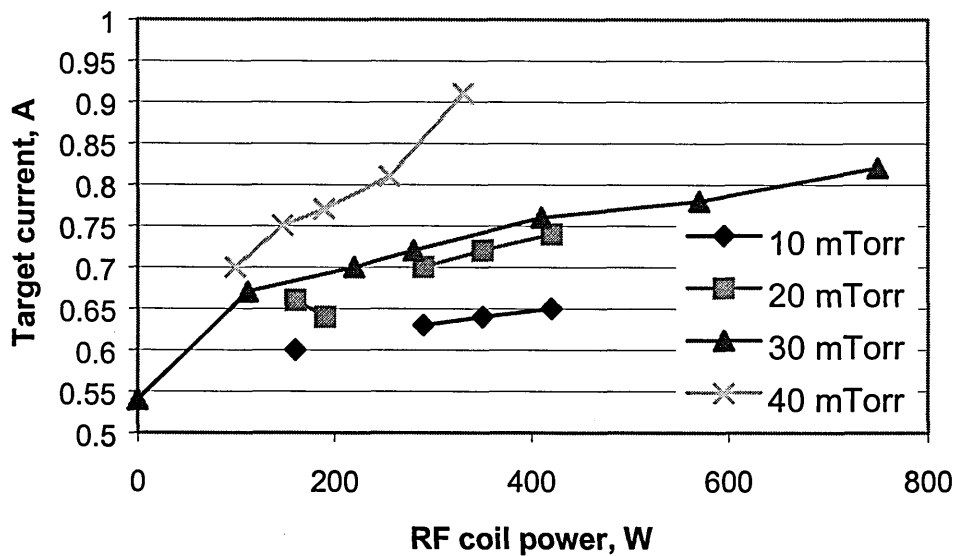


Figure 4.4.4. Magnetron target current increases with increasing RF coil power.

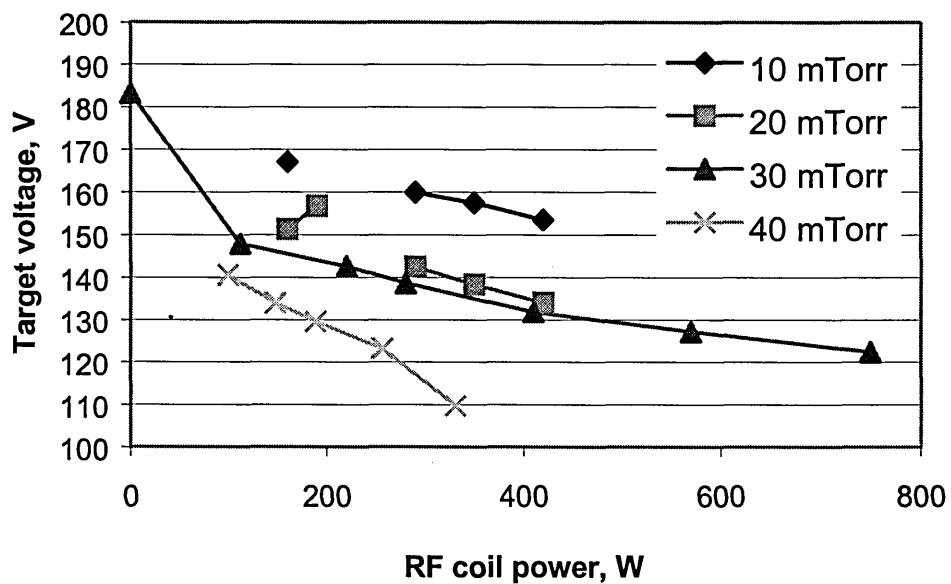


Figure 4.4.5. Magnetron target voltage decreases with increasing RF coil power

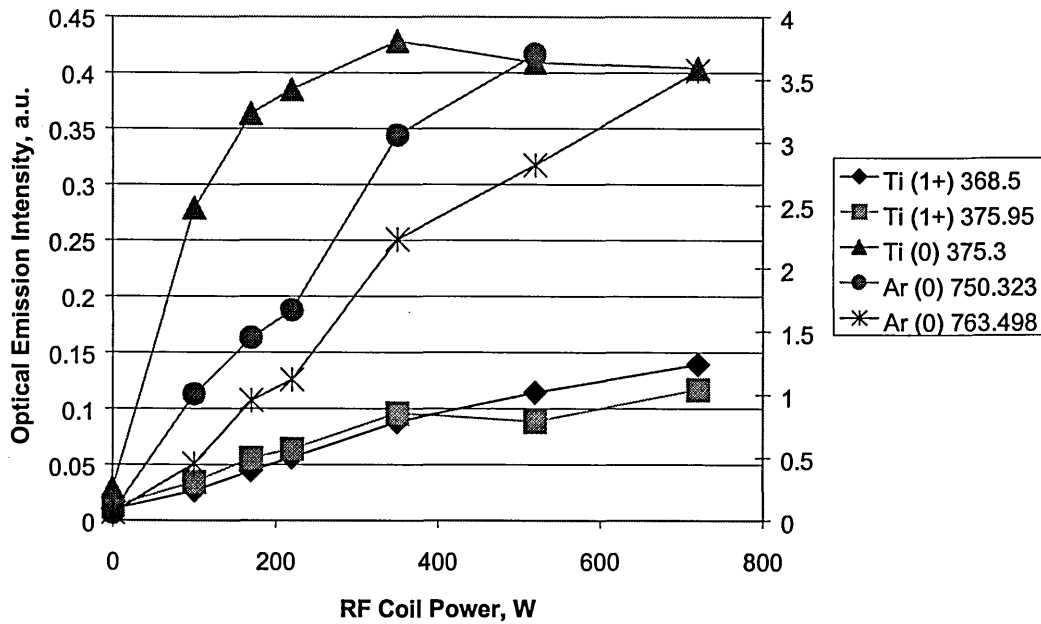


Figure 4.4.6. Optical emission signals as a function of RF Coil Power. 100 W DC, 10 mTorr.

The effect of RF power on the plasma composition was analysed by OES. Figure 4.4.6 shows the variation in intensity of ionic and neutral Ar and Ti species. It can be seen that Ti ion intensity increases monotonically with RF power. A similar behaviour is observed for the Ar neutral emission. The intensity of Ti neutral emission however saturated between 200 and 400 W RF power.

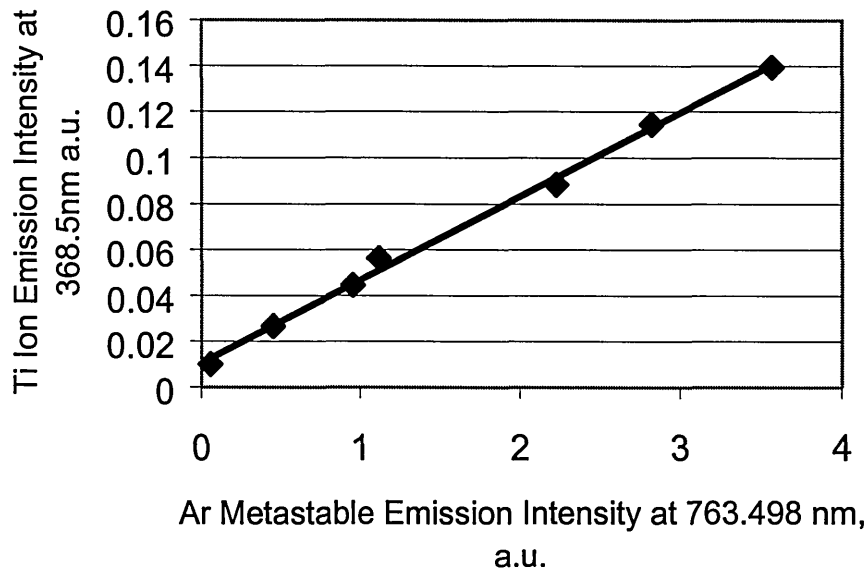
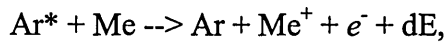


Figure 4.4.7. Dependence of Ti ion emission on Ar* metastable emission.

Figure 4.4.7 shows the emission intensity of Ti^+ ions versus Ar^* metastables line emission at 763.498 nm. The direct proportionality of the emission line intensities indicates a strong relation between the Ti ion production and the Ar^* metastable density. The Ar emission line that was investigated is produced by electrons decaying to a metastable state with energy 11.55 eV. By definition, a transition from a metastable state to a ground state is disallowed by the selection rules (see Section 3.5.1). Thus, metastable states are characterised with a long lifetime, and, in the case of Ar, with a remarkably high energy. Upon collision with metal atoms, for example, a Penning ionisation reaction can occur, such as:



where Ar^* is an Argon atom in a metastable state, Me is a metal atom, e^- is an electron, and dE is an energy defect. In the case of $Ar^* + Ti$, $dE = + 4.73$ eV. The energy dE is usually shared between the colliding species, increasing their kinetic energy, however this increase is small in comparison to the average energy observed in IEDF measurements. The collisions Ar^*+Ar have a much higher cross section but Penning ionisation is less likely to occur because $dE = -4$ eV < 0.

According to Hopwood et al [81], the Penning ionisation process is the dominant path for sputtered metal ion production at high pressures. As the power is increased Ar^* metastable states are more populated and the probability of the Penning process is increased. Consequently, the population of the sputtered Ti neutrals is depleted as more atoms undergo ionisation in the plasma [113]. This is supported by the saturation in Ti^0 emission intensity at higher powers shown in Figure 4.4.6.

The ion energy distribution function was investigated as a function of RF power. Figure 4.4.8 shows that there are two peaks in the energy distribution. The higher energy peak appeared in the range 75 - 80 eV depending on the RF power. The lower energy peak shifted from 56 eV at 100 W RF power to 67 eV at 700 W, representing a 10% shift.

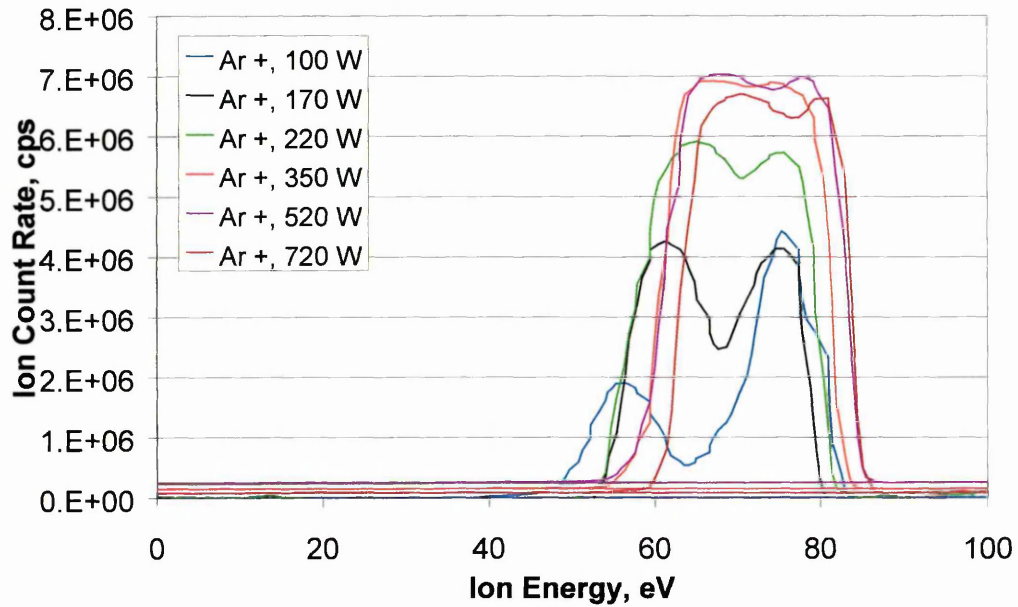


Figure 4.4.8. Ion Energy Distribution for Ar Ions at Varying RF Coil Power at DC power 100 W, and Ar pressure of 10 mTorr

4.4.3. Influence of Ar pressure on the RF Coil Discharge

The pressure of Ar gas in the chamber had a strong influence on the Ar IEDF. Figure 4.4.9 shows the IEDF for Ar ions at different Ar gas pressures. At a constant RF power of 700 W, the mean energy shifted from 50 eV at 40 mTorr to 80 eV at 10 mTorr. The shift represents approximately 50% of the average ion energy. The drop in ion energy with increasing pressure is attributed to the increased frequency of ion-atom collisions and hence accelerated thermalisation of the ions. The separation between the two peaks also increased with increasing pressure.

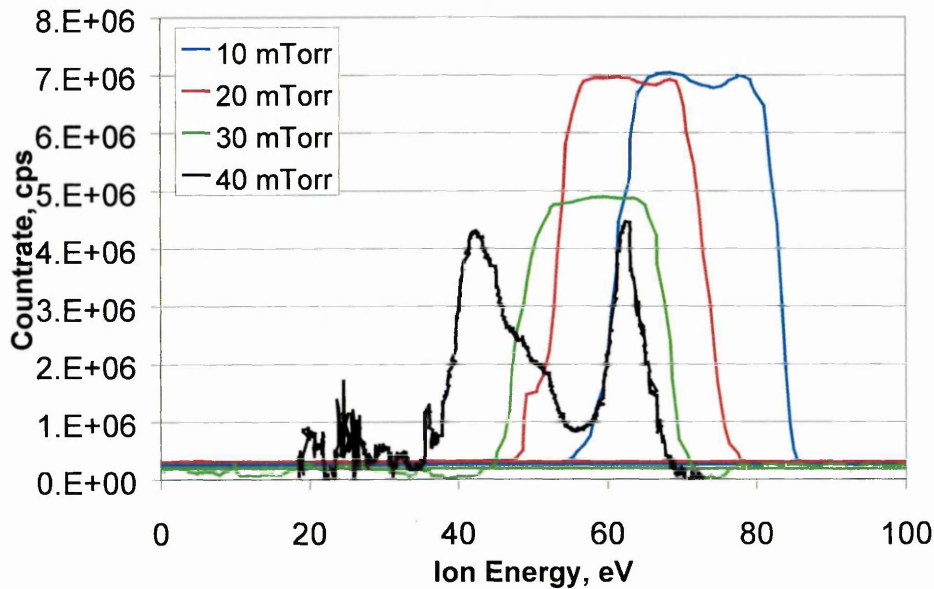


Figure 4.4.9. Dependence of the ion energy distribution function on the Ar pressure.

The double peaked distribution was observed also in a discharge where the RF coil was the only plasma source. Figure 4.4.10 shows that the shift for both peaks in this case was similar from 80 to 55 eV and 90 eV to 65 eV respectively. Further investigations are necessary in order to clarify the origin of the two energy peaks.

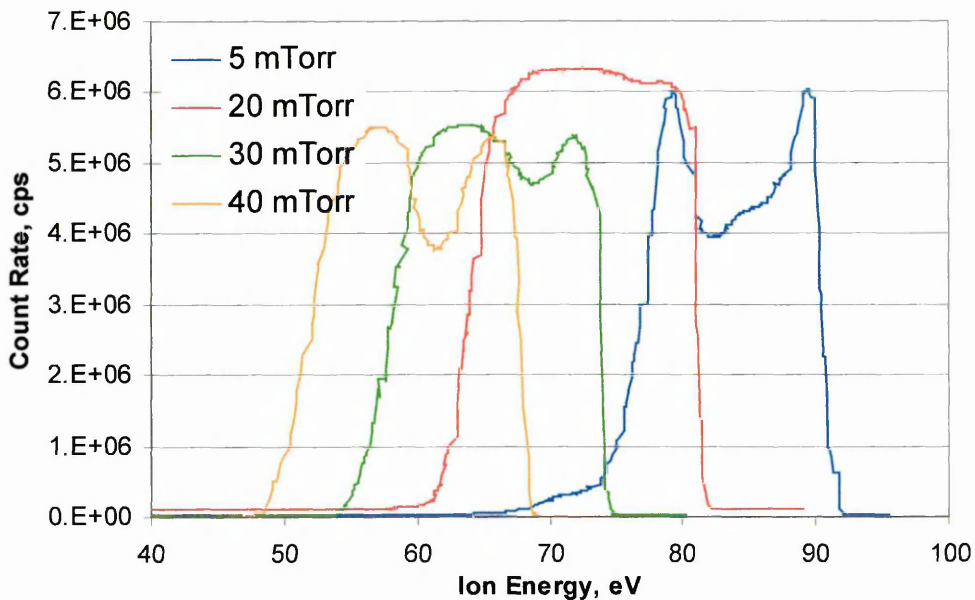


Figure 4.4.10. Ion energy distribution function of Ar^+ measured when the RF coil operated as a sole plasma generator

4.4.4. Implementation of the RF Powered Coil in the Hauzer HTC 1000/ABS™ Coating Deposition Machine and Influence of RF Power and Pressure on the Ionisation and Plasma Composition

A large RF coil was constructed and installed in the industrially sized Hauzer HTC 1000/ABS™ coating deposition machine. Figure 4.4.11 shows an overview of the RF coil as installed in the deposition machine. The positioning of the coil retained full functionality of the machine, including performing magnetron sputtering and arc evaporation, operating the target shutters, changing targets, applying substrate bias, heating and rotation. The coil consisted of one rectangular loop of copper tubing (outside diameter 6mm) with dimensions 620×220 mm which was positioned at a distance of 4 cm from the surface of the target. A two-pin water-cooled feedthrough (Caburn-MDC Ref. MCT-C-2-K40) was attached to the K40 flange on the top in the middle of the chamber door replacing the gas inlet feedthrough. The feedthrough and coil were connected with Swagelok connectors and the overall construction was supported inside the chamber with two isolated holders placed above and below the target. Figure 4.4.13 shows a photograph of the lower supporting holder. The outside two pins of the feedthrough were connected to a coaxial connector UG-560/U as shown in the photograph in Figure 4.4.12. The feedthrough was completely encased in a grounded aluminium box that served as a shield preventing the emission of RF radiation to the environment. Cooling water pipes from the cooling circulation flow of the deposition machine were connected to the feedthrough to avoid overheating of the RF coil during operation. The coil was powered with a Plasma Technologies Inc. RF power supply HS2500 (maximum power 2500 W) through a direct connection without an external matching box.

Important considerations for the design of the coil were the geometrical factors enabling installation in the machine and optimised efficiency for the given geometry. This set up also allows the coil to be placed close to the target where sputtered atoms have high energies and a short dwell time. A single loop was used in order to minimise the impedance of the coil and maximise the currents induced in the plasma. One end of the coil was grounded in order to avoid self-biasing to large voltages, which is known to induce sputtering of the coil and contaminating the deposition flux.

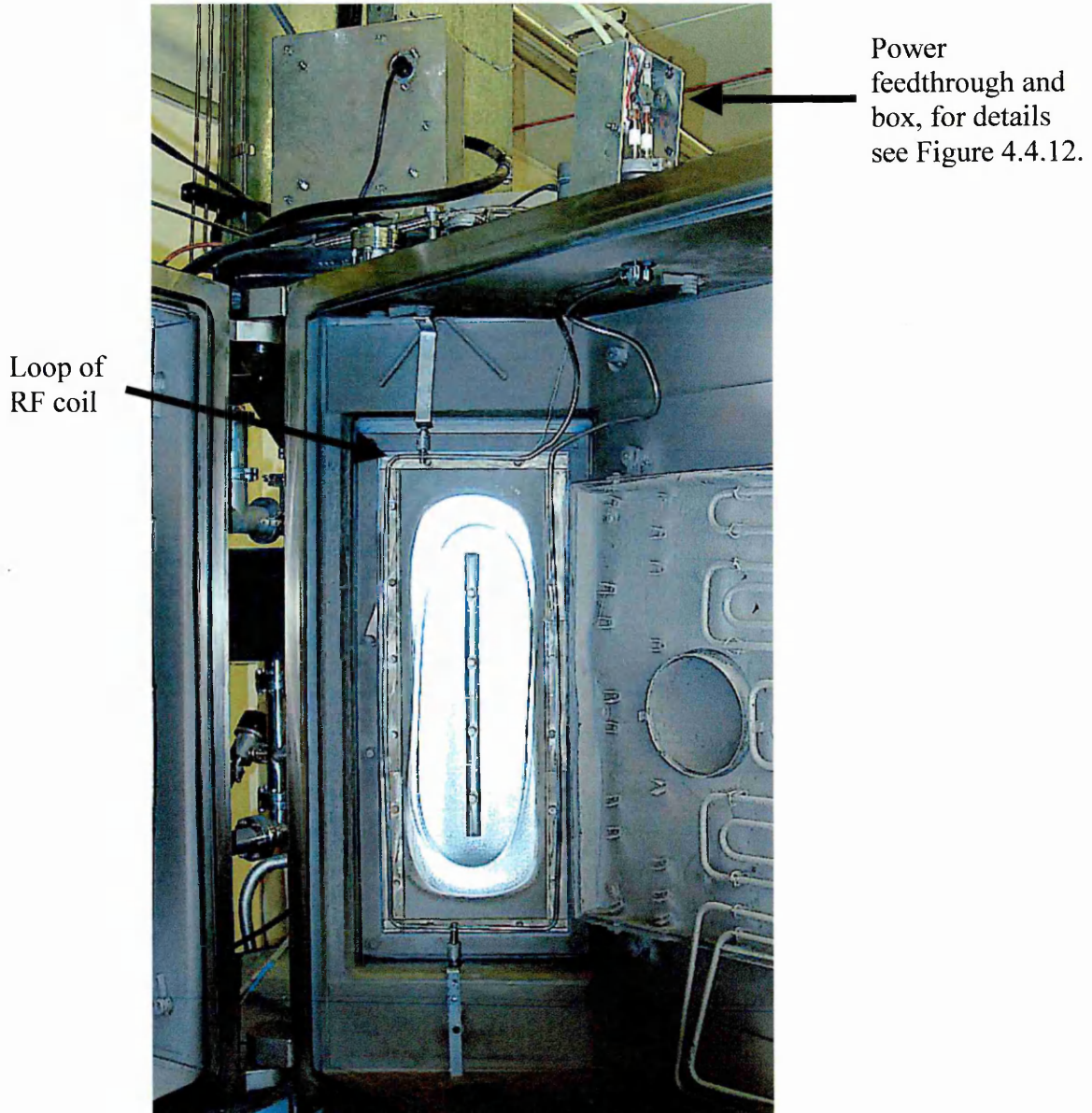


Figure 4.4.11. Overall appearance of the water cooled RF coil and feedthrough installed in the Hauzer HTC 1000/ABSTTM coating machine



Figure 4.4.12. Water cooled 2-pin power feedthrough with coaxial connector and one half of the screening aluminium box.

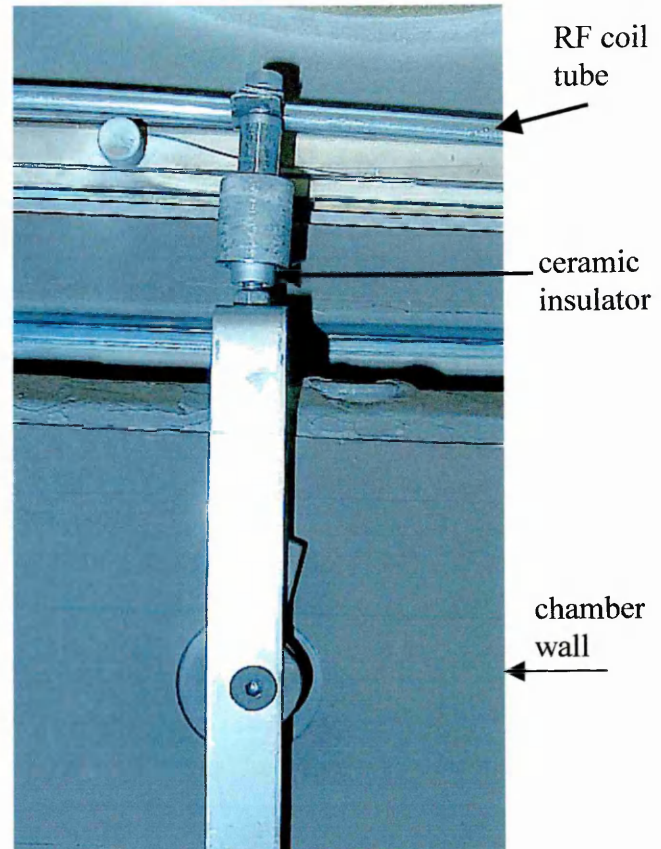


Figure 4.4.13. Lower insulated support of the RF coil in the chamber

The coil was tested in operation in conjunction with a magnetron discharge as well as on its own. The effects of pressure, power dissipated in the coil, and power dissipated in the magnetron were studied by monitoring the magnetron discharge current and voltage, forward and reflected RF power, ion current density and optical emission from the plasma.

The primary purpose in designing the RF coil was to increase the degree of ionisation of the metal flux generated in the magnetron sputtering process. The simultaneous operation of a DC powered magnetron and an RF coil can induce harmful currents in the DC power supply. An inductor was connected to the DC power supply in series with the magnetron serving as a high frequency filter. Due to the current carrying capabilities of the inductor, the maximum power on the magnetrons was

limited to 4 kW. In order to judge the ionisation capability of the RF coil alone, the unbalancing coils were not turned on and two adjacent magnetron cathodes were operated at a constant low power of 0.5 kW.

A series of experiments were carried out whereby the power on one magnetron cathode and the RF coil was varied. As the power on the RF coil was increased the voltage on the magnetron cathode decreased, while a high current was drawn to maintain a constant power. The optical emission from the plasma increased both in the vicinity of the coil and the overall volume of the chamber. The emission from neutral Cr and Ar atoms dominated the optical spectrum of the plasma in all ranges of RF power. However, as shown on Figure 4.4.14, the increase in RF power caused the emission intensity of the observed species to increase ten-fold indicating an enhanced excitation and ionisation of the plasma.

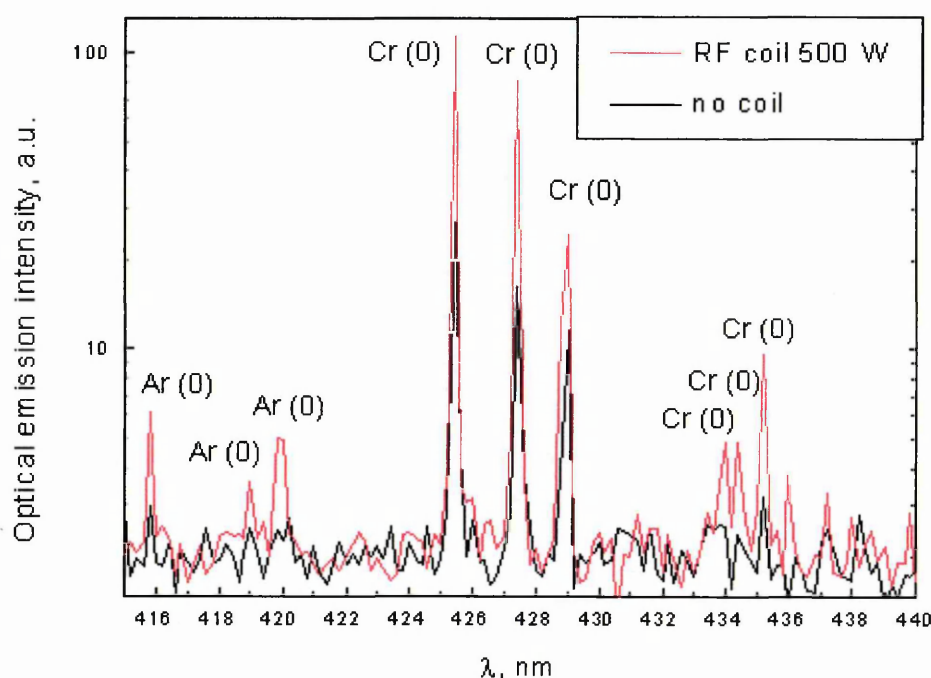


Figure 4.4.14. Comparison of the Optical Emission of RF coil enhanced and conventional magnetron sputtering

At the position of the substrates no emission from higher ionised Cr charge states or Ar ions were detected, but the transition probabilities for these species are very low and their lines could be indistinguishable from the background noise. Figure 4.4.15 shows the ion saturation current density (J_s) measured with a flat probe positioned at a distance of 20 cm from the magnetron. J_s increased monotonically from 0.06 mA.cm⁻² at 0 W RF to 0.27 mA.cm⁻² at 1500 W RF. (see).

The increase in optical emission signal and plasma density for a constant sputtering power and gas pressure indicates that the RF coil served successfully to increase the ionisation density of the magnetron plasma and the excitation probability of the species. It can be estimated that the ion to neutral ratio was increased by 5 times compared to conventional DC magnetron sputtering.

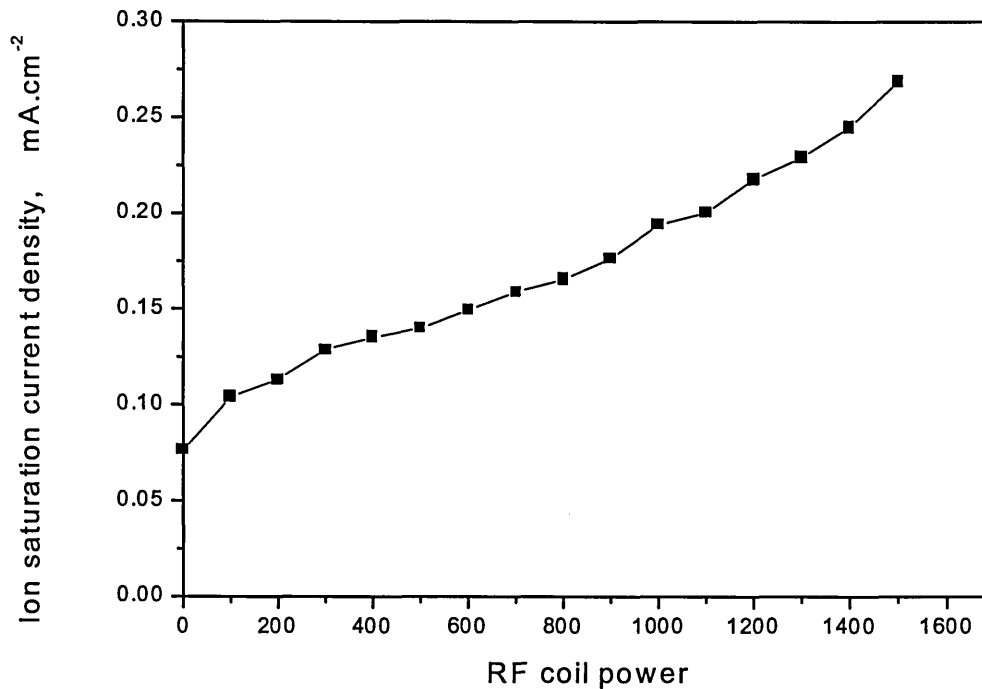


Figure 4.4.15. Ion saturation current density as a function of applied RF power.

Reports in the literature suggest that the increase of magnetron sputtering power could lead to cooling down of the plasma and decreasing the efficiency of the RF coil. In order to verify the extent of this effect in the present set-up, the increase of ion saturation current due to magnetron power was compared for two different powers of the RF coil - 0 W and 500 W. Figure 4.4.16 shows variations in the power applied on the magnetron target did not influence the plasma density produced by the RF coil.

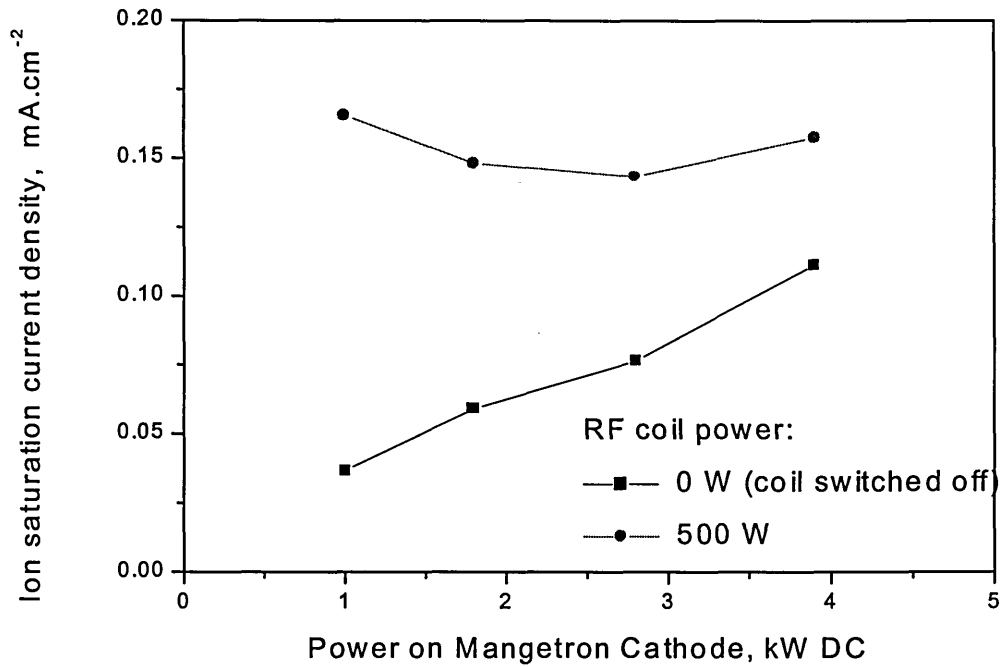


Figure 4.4.16. Comparison of the ion saturation current density in RF enhanced and conventional magnetron sputtering

This could mean that, similar to unbalanced sputtering, the ionisation could be controlled independently of the sputtering rate by the power applied to the coil thus giving a possibility to vary the ion to neutral ratio in a wide range.

The production of plasma using the RF coil without additional ionisation from a magnetron discharge was possible in a wide range of gas pressures. In Ar atmosphere, the minimum required pressure for igniting a discharge was approximately 4×10^{-3} mbar. The minimum operation pressure was 2.7×10^{-4} mbar. The increase in pressure from 2.7×10^{-4} mbar to 9.9×10^{-3} mbar did not influence significantly the ion saturation current density as shown in Figure 4.4.17.

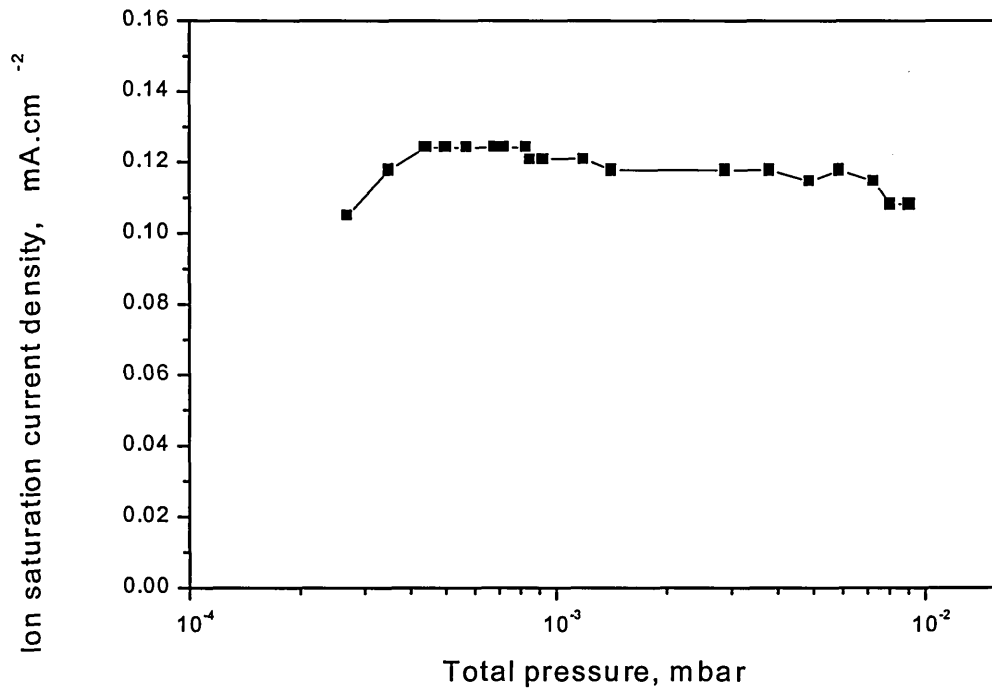


Figure 4.4.17. Ion saturation current density as a function of Ar gas pressure. RF power = 500 W

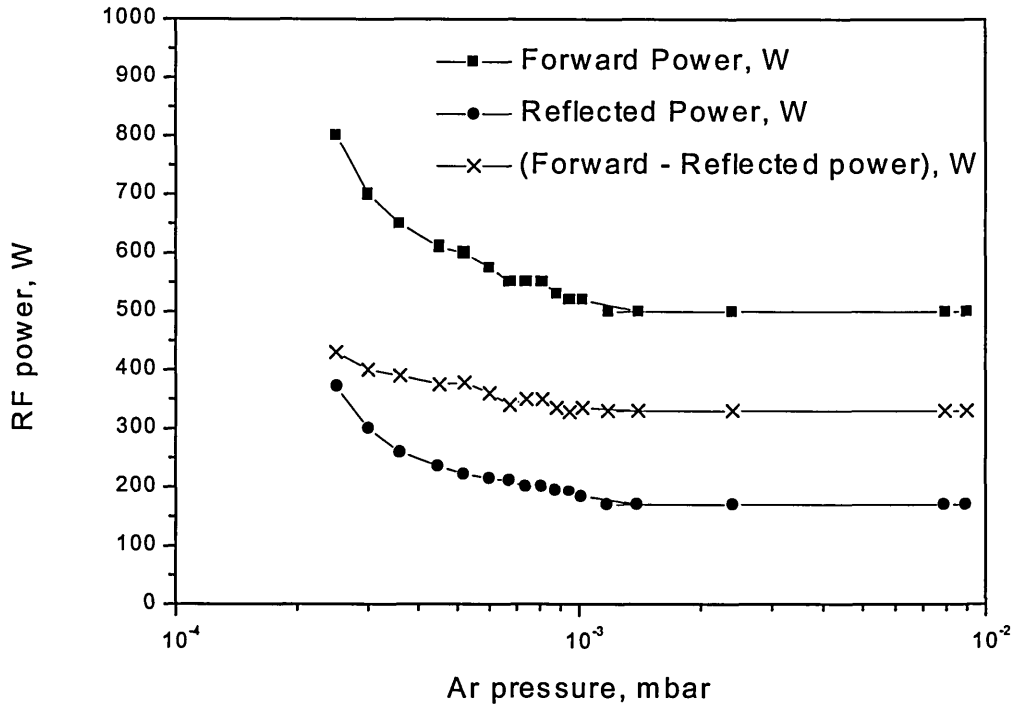


Figure 4.4.18. Forward, reflected and effective rf power delivered to the coil as a function of Ar gas pressure

Figure 4.4.18 shows that at pressures below approximately 1×10^{-3} mbar, more forward power was required to sustain the same difference of (Forward power – Reflected power) and the efficiency of the coil deteriorated. This problem could be due to the increase in mismatch between the output impedance of the power supply and the impedance of the plasma and might be solved with an additional matching box. However, the ionisation efficiency of the RF coil could be maintained over a wide range of pressures. The operation of the RF coil as the sole plasma source in the vacuum chamber can be utilised in several applications. Ar etching using the RF coil can be performed with enhanced ion flux compared to glow discharge plasmas. The RF coil could also replace the magnetron as the plasma source in low pressure (8×10^{-3} mbar) plasma nitriding [175] and avoid contamination of the substrates with sputtered metal and the poisoning of targets even in 100% N_2 atmosphere. Finally, high pressure CVD processes can be realised with highly reactive gases such as HMDSO by employing the RF coil for ionisation.

5. Conclusions

The conclusions of the thesis can be summarised in categories as follows:

Arc discharge pretreatment:

Sample pretreatment in arc plasma environment is an essential requirement for enhancing adhesion of hard coatings to steel substrates in current ABS processes. The influence of the pretreatment is strongly dependent on the plasma chemistry. Plasma diagnostic studies presented in this thesis gave evidence of important particle interactions in arc plasmas that can influence the plasma chemistry and plasma-surface interactions (see Chapter 4.1):

- The predominant interactions of arc discharge plasmas with gas are gas ionisation, charge exchange and scattering by elastic collisions.
- Charge exchange reactions are responsible for reducing the mean charge state of Nb in an Ar atmosphere from 3 in pure vacuum to 2 at a pressure of 0.01 Pa and for Cr in an Ar atmosphere from 2.1 in pure vacuum to 1.6 at a pressure of 0.01 Pa. These results show that highly charged ions can only be transported to the substrates under conditions of low gas pressures.
- Increased gas pressure contributes to a higher plasma density and ion bombardment at the substrate position. This phenomenon can be used for efficient etching of substrates.

Based on these findings, a novel two-stage substrate pretreatment based on an arc discharge has been developed allowing an increased adhesion and enhanced metal implantation in the substrate surface (see Chapter 4.1). The first stage is conducted at elevated gas pressures (0.1 Pa) ensuring high rates (>10 nm/min, three-fold rotation) of substrate etching. The second stage is carried out in pure vacuum to ensure highest mean charge states of metal ions and to maximise the implantation depth of the metal ions into the substrate. The coatings deposited after the two-stage pretreatment exhibit an enhanced metal ion implantation zone with depth of penetration in the substrates of 30 nm (compared to 15 nm in conventional etching). An enhanced adhesion on the substrates was achieved with scratch test critical loads of 85 N (compared to 65 N in conventional pretreatment).

The novel two-stage pretreatment is now exploited on a commercial production basis by Bodycote/SHU Coatings Ltd.

High power (im)pulsed magnetron sputtering (HIPIMS)

The deposition of high density coatings with good adhesion and the elimination of droplet-induced growth defects are highly desirable for a variety of applications. Plasma diagnostic studies of a novel HIPIMS discharge (Chapter 4.2) showed that it can be implemented as a powerful PVD tool that can meet these demands due to the exceptional properties of the generated particle flux:

- High power (im)pulsed magnetron sputtering (HIPIMS) discharges in Ar atmosphere with peak power density of 3000 Wcm^{-2} contain ionised sputtered metal with charge state up to $2+$ for Cr and Ti that can be used for efficient low energy ion implantation in steel substrates and consequently to enhance coating adhesion.
- Increasing HIPIMS power in the range $30 - 3000 \text{ Wcm}^{-2}$ increases the ion-to-neutral ratio by a factor of 10 and the deposition rate by a factor of 6. The increased ion to neutral ratio is a crucial requirement for the deposition of high density coatings.
- HIPIMS of Cr is a stable process capable of maintaining arc free operation over interrupted periods of time with a total operation times in excess of 200 hours on a single target.
- HIPIMS of a number of materials including Ti, Cu, Ta, and C has been performed successfully although long term tests have not been carried out.

Chromium Nitride coating deposition by HIPIMS

Tests utilising HIPIMS as a PVD technique were carried out for the first time with nitride coating depositions. The resulting coating properties, microstructure and wear and corrosion protection capabilities provided hard evidence of the wide possibilities provided by HIPIMS (Chapter 4.3).

A special deposition sequence was used whereby the substrates were pretreated in a HIPIMS plasma environment in order to enhance the adhesion. Subsequently, a chromium nitride coating was deposited in the highly ionised environment of HIPIMS.

- Substrate pretreatment with highly energetic ion bombardment (-1200 V bias) in a HIPIMS discharge environment produces high rates of etching ($>10 \text{ nm/min}$) and a metal ion implantation zone of depth in the range $5 - 20 \text{ nm}$ in the substrate, which enhances the adhesion of $2 \mu\text{m}$ thick CrN films on high speed steel substrates to scratch test critical loads of as much as 85 N , compared to $40-60 \text{ N}$ in pure Ar ion etching.

- Chromium nitride coatings deposited by HIPIMS in an Ar/N₂ atmosphere exhibit a dense columnar structure typical of deposition at high ion-to-neutral ratios. The coatings perform exceptionally well in sliding wear with wear coefficients of $2.3 \times 10^{-16} \text{ m}^2\text{N}^{-1}$ that are superior to hard chrome, arc-deposited CrN, and UBM deposited CrN. The HIPIMS deposited 2 μm thick dense coatings protected stainless steel substrates in wet corrosion tests with low passivation current $< 1 \times 10^{-16} \text{ Acm}^{-2}$, comparable to 20 μm thick hard chrome and far superior to arc deposited CrN. A Knoop hardness in the range $\text{HK}_{0.025} = 2800$ was achieved at high nitrogen partial pressures.
- Exceptionally smooth surfaces are observed in CrN films grown by HIPIMS due to the absence of macroparticles or large-scale growth defects.

Radio Frequency Powered Coil

The quest of this thesis to develop a PVD source providing a high ion-to-neutral ratio and eliminate droplets was started with investigations of a discharge produced by a combination of a radio frequency powered coil and an unbalanced magnetron. This method developed originally by Rosnagel et al [19] produces 70 % metal ionisation, however efficient operation requires extremely high pressures that are invariably linked with low deposition rates. Nevertheless, the investigations showed that the RF coil could be scaled up and used successfully in several applications. The important conclusions of this part of the work can be summarised as follows:

- A radio frequency powered coil was designed, installed and operated successfully in an industrially sized PVD coating unit as described in Chapter 4.4. Efficient ionisation and excitation was produced by the RF coil in the complete chamber volume. Potential uses of this technique are envisaged in plasma nitriding applications.
- No highly charged metal ions were found in radio frequency coil amplified magnetron sputtering discharges.

Building of necessary plasma diagnostic tools

Optical emission spectroscopy and electrostatic probe plasma diagnostic equipment and techniques were developed largely in house (Sections 3.5.1 to 3.5.4). These methods served as a basis for the entire work presented in this thesis. These techniques were used extensively for the first time for investigations of plasmas in the industrially sized Hauzer HTC 1000/ABS coating machine and contributed to a better understanding of the plasma properties and coating deposition process parameters (Chapter 4.1). During the tests at Linköping University, the OES and probe equipment was transported to Sweden and utilised to obtain highly accurate measurements of time resolved plasma chemistry (Chapter 4.2).

Future work

The investigations contained in the present thesis have opened several questions that will probably need to be answered in the future.

In particular, the field of high power pulsed magnetron sputtering (HIPIMS) requires further plasma diagnostics and modelling experiments in order to investigate the mechanisms for plasma production. The applicability of the method to a variety of sputtering target materials and reactive gas mixtures and operation under those conditions over extended periods of time is still an uncharted territory. The industrial upscaling of the technique is another direction, which needs more consideration before the full potential of HIPIMS can be exploited.

HIPIMS gives the possibility to explore the effect of highly ionised deposition flux on the mechanical properties and microstructure of thin films without the complications caused by droplet induced growth defects.

In the field of RF coil enhanced unbalanced magnetron sputtering, the generation of two energy groups of ions is an interesting phenomenon requiring more investigations over the cause and its effects on thin films.

6. References

- 1 W.D. Munz, *J. Vac. Sci. Technol. A*, 4(6), (1986), 2717
- 2 I.J. Smith, I. Wadsworth, L.A. Donohue, J.S. Brooks, W.D. Munz, *Vide Science, Technique et Applications*, 284, (1997), 141
- 3 B. Window, N. Savvides, *J. Vac. Sci. Technol. A*, 4, (1986), 196
- 4 S. Kadlec, J. Musil, United States Patent, 5,234,560
- 5 D.G. Teer, United States Patent, 5,556,519
- 6 W.D. Munz, D. Schulze, F.J.M. Hauzer, *Surf. Coat. Technol.*, 50(2), (1992), 169, A new method for hard coatings: ABS (arc bond sputtering)
- 7 P.J. Kelly, R.D. Arnell, *J. Vac. Sci. Technol.*, A16(5), (1998), 2858
- 8 U. Helmersson, S. Todorova, S.A. Barnett, J.E. Sundgren, L.C. Markert, J.E. Greene, *J. Appl. Phys.*, 62(2), (1987), 481
- 9 G. Hakansson, L. Hultman, J.E. Sundgren, J.E. Greene, W.D. Munz, *Surf. Coat. Technol.*, 48(1), (1991), 51
- 10 C. Schonjahn, L.A. Donohue, D.B. Lewis, W.D. Munz, R.D. Twesten, I. Petrov, *J. Vac. Sci. Technol. A*, 18(4), (2000) 1718
- 11 S. Creasey, D.B. Lewis, I.J. Smith, W.D. Muenz, *Surf. Coat. Technol.*, 97(1-3), (1997), 163
- 12 W.D. Munz, D.B. Lewis, S. Creasey, T. Hurkmans, T. Trinh, W. v-Ijzendorf, *Vacuum*, 46(4), (1995), 323
- 13 I. Petrov, P. Losbichler; D. Bergstrom, JE Greene, W.-D. Münz, T. Hurkmans, T. Trinh, *Thin Solid Films*, 302(1-2), (1997), 179
- 14 Q. Luo, W.M. Rainforth, W.D. Munz, *Wear*, 225-229 (1), (1999), 74
- 15 M.I. Lembke, D.B. Lewis, W.D. Munz, *Surf. Coat. Technol.*, 125(1-3), (2000), 263
- 16 C. Schonjahn, H. Paritong. W.D. Munz, R.D. Twesten, I. Petrov, *J. Vac. Sci. Technol. A*, 19(4), (2001), 1392
- 17 C. Schönjahn; A.P. Ehiasarian; D.B. Lewis; R. New; W.-D. Münz; R.D. Twesten; I. Petrov, *J Vac Sci Technol*, A19(4), 1415, 2001
- 18 C. Bergman, *Surf. Coat. Technol.*, 36, (1988), 243-255
- 19 S.M. Rossnagel, J. Hopwood, *J. Vac. Sci. Technol.*, B12(1), (1994), 449
- 20 R.B. Piejak, V.A. Godyak, B.M. Alexandrovich, *Plasma Sources Sci. Technol.*, 1, (1992), 179

- 21 V. Kouznetsov, K. Macak, J.M. Schneider, U. Helmersson, I. Petrov, *Surf. Coat. Technol.*, 122(2-3), (1999), 290
- 22 V. Kouznetsov, U.S. Patent No. 6,296,742
- 23 A.P. Ehasarian, W.-D. Munz, L. Hultman, U. Helmersson, V. Kouznetsov, *Vacuum*, 65, (2002), 147
- 24 K.M. Macak, A. Ehasarian, W.D. Munz, Z. Khan, U. Helmersson, An analysis of breakdown mechanisms of high power pulsed magnetron sputtering, Proceedings of 13th International Colloquium on Plasma Processes, Antibes - Juan-les Pins, France, 2001
- 25 W.-D. Münz, A.P. Ehasarian, P.Eh. Hovsepian, German and European patent application No. 101 24 749.4
- 26 A.P. Ehasarian, W.-D. Munz, L. Hultman, U. Helmersson, I. Petrov, paper presented at ICMCTF 2002, San Diego, USA, accepted for publication in *Surf. Coat. Technol.*
- 27 D.V. Mozgrin, I.K. Fetisov, G.V. Khodachenko, *Plasma Physics Reports*, 21(5), (1995), 400 Translated from: *Fizika Plazmy*, 21(5), (1995), 422
- 28 B. Navinšek, P. Panjan, A. Cvelbar, *Surf. Coat. Technol.*, 64-65, (1995), 155
- 29 X.-M. He, N. Baker, B.A. Kehler, K.C. Walter, M. Nastasi, *J. Vac. Sci. Technol.*, A 18(1), (2000), 30
- 30 T. Hurkmans, D.B. Lewis, J.S. Brooks, W.-D. Münz, *Surf. Coat. Technol.*, 86-87, (1996), 192
- 31 W.R. Grove, *Phil. Mag.*, 5, (1853), 203
- 32 B.A. Movchan, A.V. Demchishin, *Fiz. Metal. Metalloved.*, 28 (4), (1969), 653
- 33 J.A. Thornton, *J. Vac. Sci. Technol.*, 11, (1974), 666
- 34 D.M. Mattox, G.J. Kominiak, *J. Vac. Sci. Technol.*, 9(1), (1972), 528
- 35 R. Messier, A.P. Giri, R.A. Roy, *J. Vac. Sci. Technol.*, A2(2), (1984), 500
- 36 G. Hakanson, J.-E. Sundgren, D. McIntyre, J.E. Greene, W.-D. Münz, *Thin Solid Films*, 153, 55
- 37 K.-H. Müller, *Phys. Rev. B*, 35, (1987), 7906
- 38 H. Ljungkrantz, L. Hultman, J.-E. Sundgren, L. Karlsson, *J. Appl. Phys.*, 78 (2), (1995), 832
- 39 I. Petrov, L. Hultman, U. Helmersson, J.-E. Sundgren, J.E. Greene, *Thin Solid Films*, 169(2), (1989), 299
- 40 L. Hultman, S.A. Barnett, J.-E. Sundgren, J.E. Greene, *J Cryst. Growth*, 92(3-4), (1988), 639

- 41 F.L. Williams, R.D. Jacobson, J.R. McNeil, G.J. Exarhos, J.J. McNally, *J. Vac. Sci. Technol.*, 6(3), (1988), 2020
- 42 J.C. Maxwell-Garnett, *Phil. Trans. R. Soc. London*, 203, (1904), 385
- 43 W.D. Westwood, *J. Vac. Sci. Technol.*, 15, (1978), 1
- 44 K.M. Shih, D.B. Dove, *J. Vac. Sci. Technol.*, A12(2), (1993), 321
- 45 Ed. R. Behrisch, K. Klaus Wittmaack, *Sputtering by particle bombardment*, Berlin. Springer. 1981-91
- 46 Hubler in ASM handbook Vol.5. Surface engineering. prepared under the direction of the American Society for Metals. Handbook Committee Materials Park, Ohio, ASM International, 1994
- 47 O.R. Monteiro, Wang Zhi, I.G. Brown, *Diamond for Electronic Applications. Symposium. Mater. Res. Soc.*, Pittsburgh, PA, USA; 1996; xii+477 pp. p.139-44
- 48 I.G. Brown, B. Feinberg, J.E. Galvin, *J Appl Phys*, 63 (1), (1988), 4889
- 49 I.G. Brown, A. Anders, S. Anders, M.R. Dickinson, R.A. MacGill, E.M. Oks, *Surf. Coat. Technol.*, 84, (1996), 550
- 50 A. Anders, S. Anders, B. Jüttner, H. Lück, *IEEE Trans Plas Sci*, 24 (1), (1996), 69
- 51 A. Anders, *Phys. Rev. E.*, 24, (1991), 969
- 52 M.A. Lieberman, A.J. Lichtenberg, *Principles of Plasma Discharges and Materials Processing*, New York, John Wiley & Sons, Inc., 1994, p. 79
- 53 A. Anders, G.Yu. Yushkov, *J. Appl. Phys.*, 91(8), (2002), 4824
- 54 J.M. Schneider, A. Anders, G.Yu. Yushkov, *Appl. Phys. Lett.*, 78(2), 2001, 150
- 55 P.J. Martin, D.R. McKenzie, R.P. Netterfield, P. Swift, S.W. Filipczuk, K.H.Müller, C.G. Pacey, B. James, *Thin Solid Films*, 153, (1987), 91-102
- 56 V.M Lunev, V.D. Ovcharenko, V.M. Khoroshikh, *Sov. Phys. Tech. Phys.*, 22(7), (1977), 855
- 57 V.M Lunev, V.G. Padalka, V.M. Khoroshikh, *Sov. Phys. Tech. Phys.*, 22(7), (1977), 858
- 58 J.E. Daalder, *J. Phys. D*, 8, (1975), 130
- 59 G.Y. Yushkov, A. Anders, *IEEE Trans. Plas. Sci.*, 26 (2), (1998), 220
- 60 J.B. Hasted, *Physics of Atomic Collisions*, 2nd ed., London, Butterworths, 621
- 61 B.H. Bransden, M.R.C. McDowell, *Charge Exchange and the Theory of Ion-Atom Collisions*, Clarendon Press, Oxford, 1992, p. 128
- 62 G. Praburam, J. Goree, *J. Vac. Sci. Technol. A*, 12(6), (1994), 3137

- 63 H.W. Wang, M.M. Stack, S.B. Lyon, P. Hovsepian, W.-D. Munz, *Surf. Coat. Technol.*, 135, (2000), 82
- 64 S. Ramalingam, Apparatus for Driving the Arc in a Cathodic Arc Coater, U.S. Pat. 6009829, (2000)
- 65 A.A. Plyutto, V.N. Ryzhkov, A.T. Kapin, *Sov. Phys. JETP*, 20, (1965), 328
- 66 R.L. Boxman, D. Sanders, P.J. Martin, Ed. Handbook of Vacuum Arc Science and Technology, New Jersey, Noyes Data Corp., 1995
- 67 I.I. Aksenov, V.A. Belous, V.G. Padalka, V.M. Khoroshikh, *Sov. J. Plasma Phys.*, 4, (1978), 425
- 68 D.A. Karpov, *Surf. Coat. Technol.*, 96, (1997), 22 and references therein
- 69 B.S. Danilin, V.K. S'rchin, Magnetron Sputtering Systems, Radio i Svyaz', (1982), Moscow, in Russian
- 70 I. Petrov, A. Myers, J.E. Greene, J.R. Abelson, *J. Vac. Sci. Technol.*, A 12(5), (1994), 2846
- 71 S.M. Rossnagel, H.R. Kaufman, *J. Vac. Sci. Technol. A*, 6(2), (1988), 223
- 72 S.M. Rossnagel, *J. Vac. Sci. Technol.*, A6(3, pt.2), (1988), 1821-1826
- 73 M. Misina, J. Musil, *Surf. Coat. Technol.*, 74-75, (1995), 450
- 74 R. Pintaske, Th. Welzel, M. Schaller, N. Kahl, J. Hahn, F. Richter, *Surf. Coat. Technol.*, 99, (1998), 266
- 75 T.E. Sheridan, M.J. Goeckner, J. Goree, *J. Vac. Sci. Technol.*, A9(3), (1991), 688
- 76 T.E. Sheridan, M.J. Goeckner, J. Goree, *J. Vac. Sci. Technol.*, A8(3), (1990), 1623
- 77 S. Kadlec, J. Musil, W.-D. Munz, G. Hakanson, J.-E. Sundgren, *Surf. Coat. Technol.*, 39/40, (1989), 487
- 78 I. Ivanov, P. Kazansky, L. Hultman, I. Petrov, J.-E. Sundgren, *J. Vac. Sci. Technol. A*, 12 (2), (1994), 314
- 79 P.J. Kelly, R.D. Arnell, *Surf. Coat. Technol.*, 108-109, (1998), 317
- 80 A. Leyendecker, G. Erkens, S. Esser, H.-G. Fuss, B. Hermeler, R. Wenke, United States Patent No. 6,352,627 B2
- 81 J. Hopwood, F. Qian, *J. Appl. Phys.*, 78(2), (1995), 758
- 82 J.M. Schneider, W.D. Sproul, A. Matthews, *Surf. Coat. Technol.*, 98, (1998), 1473
- 83 H. Backer, paper presented at PPST 2002, Melbourne, FL, U.S.A.

- 84 C.C. Muratore, J.J. Moore, J.A. Rees, paper presented at ICMCTF 2002, San Diego, U.S.A.
- 85 J.W. Bradley, H. Backer, P.J. Kelly, R.D. Arnell, *Surf. Coat. Technol.*, 135, (2001), 221
- 86 J. Alami, J.T. Gudmundsson, A.P. Ehiasarian, W.-D. Münz, U. Helmersson, paper presented at ICMCTF 2002, San Diego, U.S.A.
- 87 S. Jager, B. Szyszka, J. Szczyrbowski, G. Brauer, *Surf. Coat. Technol.*, 98, (1998), 1304
- 88 J. Christiansen, C. Schultheiss, *Z. Phys.*, A290, (1979), 35
- 89 K. Frank et al., *IEEE Trans. Plasma Sci.*, 16, (1988), 317
- 90 W. Hartman, V. Dominic, G.F. Kirkman, M.A. Gundersen, *J. Appl. Phys.*, 65(11), (1989), 4388
- 91 A. Anders, S. Anders, M. A. Gundersen, *J. Appl. Phys.* 76, 1595-1502 (1994).
- 92 G.A. Mesyats, D.I. Proskurovsky, Pulsed Electrical Discharge in Vacuum, Springer-Verlag Berlin, 1989
- 93 W. Hartmann, G. Lins, *IEEE Trans. Plasma Sci.*, 21, (1993), 506
- 94 V. Puchkarev, *IEEE Trans. Plasma Sci.*, 21, (1993), 725
- 95 A. Martsinovski, *IEEE XVIIth Int. Symp.on Discharges and Elec. Insulation in Vacuum*, 1018
- 96 V.I. Volosov, I.N. Churkin, *Surf. Coat. Technol.*, 96, (1997), 75
- 97 I.K. Fetisov, A.A. Filippov, G.V. Khodachenko, D.V. Mozgrin, A.A. Pisarev, *Vacuum*, 53, (1999), 133
- 98 K. Macak, V. Kouznetsov, J.M. Schneider, U. Helmersson, I. Petrov, *J. Vac. Sci. Technol.*, A 18(4), pt.1-2, (2000), 1533-1537
- 99 A. Aubert, R. Gillet, A. Gaucher, J.P. Terrat, *Thin Solid Films*, 108(2), (1983), 165
- 100 O. Knotek, W. Bosch, M. Atzor, W.-D. Munz, D. Hoffmann, J. Goebel, *High Temperatures - High Pressures*, 18(4), (1986), 435
- 101 W.D. Munz, J. Gobel, *Surface Engineering*, 3(1), (1987), 47
- 102 O. Knotek, R. Elsing, M. Atzor, H.G. Prengel, *Wear*, 133(1), (1989), 189 The influence of the composition and coating parameters of PVD Ti-Al-V(C,N) films on abrasive and adhesive wear of coated cemented carbides
- 103 C. Gautier, J. Machet, *Thin Solid Films*, 295, (1997), 43
- 104 A. Ehrlich, M. Kühn, F. Richter, W. Hoyer, *Surf. Coat. Technol.*, 76-77, (1995), 280

- 105 C. Rebholz, H. Ziegele, A. Leyland, A. Matthews, *Surf. Coat. Technol.*, 115, (1999), 222
- 106 B. Bhushan, B.K. Gupta, Handbook of Tribology, McGraw-Hill, New York, 1991
- 107 O. Knotek, W. Bosch, M. Atzor, W.-D. Münz, D. Hoffman, J. Goebel, *High Temp. - High Press.*, 18 (1986)
- 108 G. Berg, C. Friedrich, E. Broszeit, C. Berger, *Surf. Coat. Technol.*, 86-87, (1996), 184
- 109 B. Navinšek, P. Panjan, I. Milošev, *Surf. Coat. Technol.*, 97, (1997), 182
- 110 G.J. van-der-Kolk, T. Hurkmans, C. Strondl, W. Fleischer, *Vide Science, Technique et Applications*, 56 (295), (2000), 38
- 111 O. Knotek, F. Löffler, G. Krämer, *Surf. Coat. Technol.*, 54-55 (1992), 241
- 112 A.P.A. Hurkmans, PhD thesis, Sheffield-Hallam University, Sheffield, UK, 2002
- 113 C. Nouvellon, S. Konstantinidis, J.P. Dauchot, M. Wautelet, P.Y. Jouan , A. Ricard , M. Hecq, to be published in *J. Appl. Phys.*
- 114 I.Brown, J.Galvin, R.MacGill, R.Wright, *Rev.Sci.Instrum.*, 58 (9), (1987), 1589
- 115 Wutz, Adam, Walcher, Theory and Practice of vacuum technology, Friedr. Vieweg & Sohn, Braunschweig/Wiesbaden, 1989
- 116 R. Eisberg, R. Resnick, Quantum physics of atoms, molecules, solids, nuclei, and particles, New York. Chichester. Wiley, (1985)
- 117 R.W.P. McWhirter, in Ed. R.H. Huddleston, S.L. Leonard, Plasma Diagnostic Techniques, New York, Academic Press, 1965
- 118 C.E. Moore - Atomic energy levels : as derived from the analyses of optical spectra. - Vol.1, 2, 3, Washington : U.S.G.P.O., 1949
- 119 NIST atomic spectra database: <http://physics.nist.gov/ASD>
- 120 C. Palmer, Diffraction Grating Handbook, Richardson Grating Laboratory, New York, 2000, p.52
- 121 B. Chapman, Glow Discharge Processes Sputtering and Plasma Etching, John Wiley&Sons, Inc., 1980, p. 109
- 122 F.Chen, Introduction to Plasma Physics, Plenum Press, 1974
- 123 Ed. Lochte-Holtgreven, Plasma Diagnostics, North-Holland Publishing Company, Amsterdam, 1968
- 124 I.Petrov, I.Ivanov, V.Orlinov, J.Kourtev, *Contrib.Plasma Phys.*, Vol. 30, 1990, pp.223-231

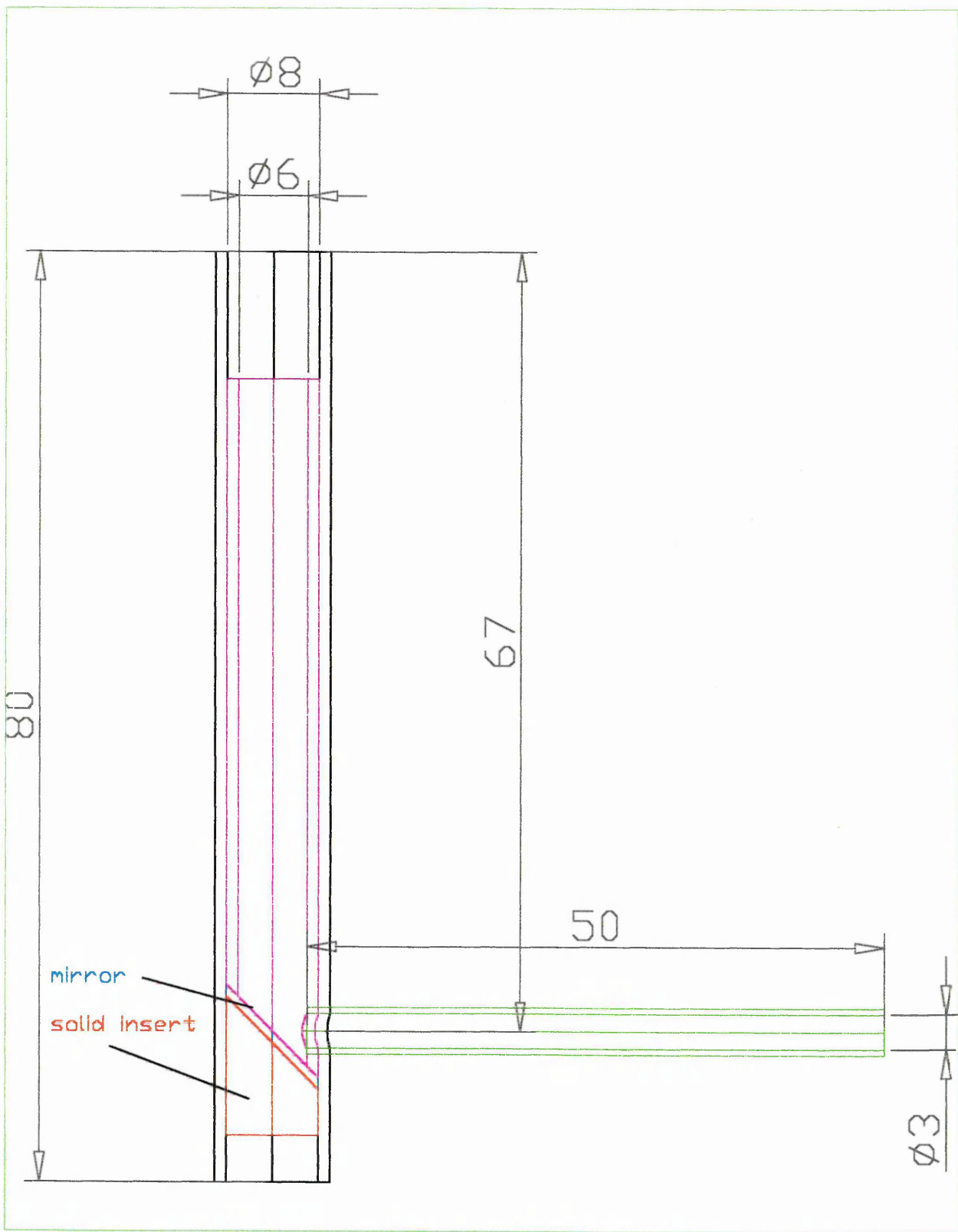
- 125 P.Špatenka, I.Leipner, J.Vlcek, J.Musil - *Plasma Sources Sci. Technol.*, vol.6, 1997, pp.46-52
- 126 J.Vlcek, P.Špatenka, J.Musil, L.Forejt, *Surf.Coat.Technol.*, Vol.98, 1998, pp.1557-1564
- 127 J.D.Swift, M.J.R.Schwar, *Electrical Probes for Plasma Diagnostics*, London, Iliffe Books Ltd., 1970
- 128 R.M.Clements, *J.Vac.Sci.Technol.*, Vol.15, No.2, 1978, pp.193-198
- 129 I.Petrov, V.Orlinov, I.Ivanov, J.Kourtev, *Contrib.Plasma Phys.*, Vol. 28, 1988, pp.157-167
- 130 J.E.Allen, *Plasma Sources Sci.Technol.*, Vol.4, 1995, pp.234-241
- 131 J.Sasaki, I.Brown, *J.Appl.Phys.*, Vol.66, No.11, 1989, pp.5198-5203
- 132 A.Pljutto, V.Ryzhkov, A.Kapin, *Zh.E.T.F.*, vol.47, No.2, 1964, pp.494-507
- 133 F.F. Chen, Chapter 4 in Ed. R. Huddleston, S. Leonard, *Plasma Diagnostic Techniques*, New York, Academic Press, 1965
- 134 J. Vyskocil, HVM Plasma Ltd., Prague, Czech Republic, private communication
- 135 J.B.A. England, *Techniques in Nuclear Structure Physics*, MacMillan Press, 1974, Chapter 2
- 136 B.D. Cullity, *Elements of X-Ray Diffraction*, Addison-Wesley Publishing Company Inc., 1978, Reading, USA
- 137 D. Geist, A. Perry, J. Treglio, V. Valvoda, D. Rafaja, *Advances in X-ray Analysis*, 38, (1995), 47
- 138 D.B. Williams, C.B. Carter, *Transmission Electron Microscopy*, Plenum Press, New York, 1996, Chapter 9
- 139 *Instruction Manual for Micro Hardness Testing Machine Model: MVK-H1/H2/H3*, Mitutoyo Corporation
- 140 H.E. Boyer, *Hardness Testing*, ASM International, (1987), Ohio, USA
- 141 A. Anders, G. Yu. Yushkov, *Appl. Phys. Lett.*, 80 (14), (2002), 2457
- 142 I. Demidenko, N.S. Lomino, V.D. Ovcharenko, V.G. Padalka, G.N. Polyakova, *Sov. Phys., Tech., Phys.*, vol. 29, (1984), pp.895
- 143 C. Schonjahn, D.B. Lewis, W.D. Munz, I. Petrov, *Surface Engineering*, 16(2), (2000), 176
- 144 M.K. Puchert, C.A. Davis, D.R. McKenzie, B.W. James, *J Vac Sci Technol A*, 10 (6), (1992), 3493-3498

- 145 V.N. Zhitomirsky, U. Kinrot, B. Alterkop, R.L. Boxman, S. Goldsmith, *Surf. Coat. Technol.*, vol. 86-87, (1996), 263-270
- 146 H.S. Maciel, J.E. Allen, *J. Plasma Physics*, 42(2), (1989), 321-352
- 147 V.E. Golant, A.P. Zhilinsky, I.E. Sakharov, S.C. Brown, *Fundamentals of Plasma Physics*, John Wiley & Sons, New York, 1980, p.51
- 148 N.R. Daly, R.E. Powell, *Proc. Phys. Soc.*, 89, (1966), 281
- 149 D.C.S. Allison, A. Dalgarno, *Proc. Phys. Soc.*, 85, (1965), 845
- 150 A.G. Nikolaev, E.M. Oks, G.Yu. Yushkov, *Zh. Tekh. Phys.*, 1998, 68(9), 24
- 151 P. Spadtke, H. Emig, B.H. Wolf, E. Oks, *Review of Scientific Instruments*, 65(10), (1994), 3113
- 152 B.-J. Kim, Y.-C. Kim, J.-J. Lee, *Surf. Coat. Technol.*, 114, (1999), 85-89
- 153 W.-D. Münz, G. Nayal, I.J. Smith, *VDI Berichte NR. 155*, 2000
- 154 S.M. Rosnagel, H.R. Kaufman, *J. Vac. Sci. Technol.*, A6(2), (1988),:223-229
- 155 M. Kühn, R. Pintaske, F. Richter, *IEEE Trans in Plasma Sci*, 25(4), 694, 1997
- 156 A.A. Voevodin, J.G. Jones, J.S. Zabinski, L. Hultman, Plasma characterisation during laser ablation of graphite in nitrogen for the growth of fullerene-like CN_x films, submitted to *J Appl Phys*, 2002.
- 157 J. Alami, D. Music, U. Helmersson, unpublished results
- 158 M. List, U. Krausse, T. Wünsche, *Proceedings 44rd Annual Technical Conference of the Society of Vacuum Coaters*, 2000, Philadelphia, USA, p. 246
- 159 M.A. Lutz, *IEEE Transactions in Plasma Science* 2,1-10 (1974)
- 160 A. Anders, *A Formulary for Plasma Physics*, Akademie-Verlag Berlin 1990
- 161 E. Hantzsche, *Beitraege aus der Plasma Physik* 22, 325 (1982).
- 162 A. Rizk, S.K. Habib, and N.S. Rizk, *Journal of Materials Science* 24, 2408-14 (1989).
- 163 P. Špatenka, J. Vlcek, J. Blazek, *Vacuum*, 55, (1999), 165
- 164 A. Andres, S. Anders, I.G. Brown, K.M. Yu, *Nucl. Inst. Meth. Phys. Res.*, B102, (1995), 132
- 165 W.-D. Münz; C. Schönjahn; H. Paritong; I.J. Smith, *Vide*, 297(3/4); 205, 2000
- 166 I. Petrov, L. Hultman, U. Helmersson, J.-E. Sundgren, J.E. Greene, *Thin Solid Films*, 169(2), (1989), 299
- 167 P.E. Hovsepiyan, D.B. Lewis, W.D. Munz, S.B. Lyon, M. Tomlinson, Combined cathodic arc/unbalanced magnetron grown CrN/NbN superlattice coatings for corrosion resistant applications, *Surf. Coat. Technol.*, 120-121, (1999), 535

- 168 A.C. Vlasveld, S.G. Harris, E.D. Doyle, D.B. Lewis, W.D. Münz, Characterisation and performance of partially filtered arc TiAlN coatings, *Surf. Coat. Technol.*, 149(2-3), (2002), 217
- 169 M. Oden, C.Ericsson, G. Hakansson, H. Ljungkrantz, *Surf Coat Technol*, 114 (1999) 39
- 170 Th. Schönfuss, Placement Semester Report, Surface Engineering Research Group, Materials Research Institute, Sheffield Hallam University, 2000
- 171 H.W. Wang, M.M. Stack, S.B. Lyon, P. Hovsepian, W.-D. Münz, *Surf. Coat. Technol.*, 126, (2000), 279
- 172 W.-D. Münz, D.B. Lewis, P.E. Hovsepian, C. Schönjahn, A. Ehiasarian, I.J. Smith, *Surf Eng*, 17(1), 15, 2001
- 173 P.Eh. Hovsepian, W.-D. Münz, invited paper presented at 45th Ann Tech Conf SVC, 2002
- 174 E. Kusano, N. Kashiwagi, T. Kobayashi, H. Nanto, A. Kinbara, *Surf. Coat. Technol.*, 108-109, (1998), 177
- 175 G. Nayal, A.P. Ehiasarian, K.M. Macak. R. New, W.-D. Münz, Low Pressure plasma nitriding, paper presented at eMRS, Strasbourg, (2000)

Appendix A:

OES Probe Mirror Assembly



A

B

C

D

E

F

Itemref	Quantity	Title/Name, designation, material, dimension etc			Article No./Reference	
Designed by A.Ehiasarian	Checked by	Approved by - date	File name OESprobeheads	Date 8/2/2002	Scale 2:1	
SERG, SHU, UK			OES Probe Mirror Assembly			
			x		Edition 1	Sheet 1/1

1

4

Appendix B:

Articles Published in Well- Refereed Journals

Optimization of *in situ* substrate surface treatment in a cathodic arc plasma: A study by TEM and plasma diagnostics

C. Schönjahn,^{a)} A. P. Ehiasarian, D. B. Lewis, R. New, and W.-D. Münz
Materials Research Institute, Sheffield Hallam University, Sheffield S11WB, United Kingdom

R. D. Twesten and I. Petrov
Fredrick Seitz Materials Research Laboratory and the Materials Science Department, University of Illinois, Urbana, Illinois 61801

(Received 25 September 2000; accepted 27 December 2000)

Cr ions generated by a steered cathodic arc discharge are utilized to control and enhance the adhesion properties of 3.5 μm thick $\text{Ti}_x\text{Al}_{(1-x)}\text{N}$ based coatings deposited on high speed steel substrates. A two-step etching procedure (negative substrate bias, $U_S=1200$ V) is suggested, operating the arc discharge initially in an Ar atmosphere ($p_{\text{Ar}}=0.09$ Pa, 6.75×10^{-4} Torr) to achieve predominantly metal removing effects (etching rate: 9 nm min^{-1}) with a mixture of Ar and Cr ions. In the second stage at residual gas pressure level ($p_{\text{Ar}}\leq 0.006$ Pa, 4.5×10^{-5} Torr, etching rate: 4 nm min^{-1}) pure Cr ion irradiation leads to a Cr penetration as deep as 20 nm with a Cr accumulation of approximately 37 at % at the interface substrate/coating. This procedure promotes localized epitaxial growth of $\text{Ti}_x\text{Al}_{(1-x)}\text{N}$ and enhances critical load values up to 85 ± 5 N. © 2001 American Vacuum Society. [DOI: 10.1116/1.1349726]

I. INTRODUCTION

It is well-known that the coating/substrate interface plays a key role with respect to the functionality of coated parts.¹⁻³ In particular, dry high speed machining of hard die steels [up to a Rockwell hardness (HRC) 65] demands especially high interface strength of the coated system. It has been shown earlier³ that the microstructure and microchemistry of the interface region of 3.5 μm $\text{Ti}_x\text{Al}_{(1-x)}\text{N}$ based coatings deposited on high speed steel (HSS) and cemented carbide is directly correlated to tool life in dry high speed milling. Utilizing the combined steered arc/unbalanced magnetron deposition method⁴ best results were obtained for Cr ion bombardment where the metal ions are extracted from a steered cathodic arc discharge using Cr as the target material and Ar to stabilize the discharge ($p_{\text{Ar}}=0.06$ Pa, 4.5×10^{-4} Torr). The substrates were negatively biased at $U_S=1200$ V, which leads to localized epitaxial growth of the coating. The exposure to ion bombardment lasted for 20 min.^{3,5} This long exposure time was used to ensure a clean surface. However, particularly for small tools and parts this long etching time may lead to local substrate overheating depending on the tool geometry causing detrimental softening effects. In addition, the number of droplets deposited on the substrate during ion bombardment increases with the etching time, thus leading to growth defects, when, e.g., $\text{Ti}_x\text{Al}_{(1-x)}\text{N}$ is deposited on top of the droplet by magnetron sputtering.⁶ Growth defects locally reduce the oxidation resistance of the coated substrate⁷ and also increase the surface roughness of the coating.⁸ Therefore a minimization of the exposure time is desirable. Finally, a reduction of the overall process time will reduce production costs and target life is prolonged.

This article describes a modified and improved sputter cleaning process with reduced exposure times. The modified

etching procedure consists of two steps: first the steered arc discharge is carried out over a period of 8 min in the environment of a relatively high partial pressure of Ar (0.09 Pa, 6.75×10^{-4} Torr) allowing a high substrate etching rate. Second, the Ar pressure is reduced to base pressure level (0.006 Pa, 4.5×10^{-5} Torr) promoting enhanced ion implantation (2 min) resulting in a total etching time of 10 min. Previous experiments with Ti ions have shown that the etching procedure is indeed more aggressive when taking place at a low gas pressure level, respectively,⁹ leading also to a deeper penetration depth of the incorporated Ti atoms.¹⁰

II. EXPERIMENT

Experiments were carried out in an industrially sized HTC 1000 ABS (arc bond sputtering) coater (Hauzer Techno Coating Europe B.V., Venlo, NL)⁴ with four ABS cathodes capable of running either in steered arc or in unbalanced magnetron mode. Two turbomolecular pumps (2200 l/s^{-1} each) provide a base pressure of 0.006 Pa. The total pressure was measured by a highly accurate viscosity pressure gauge (Leybold Viscovac VM212). The arc spot was steered by a combination of permanent magnets positioned behind the target and electromagnetic coils disposed concentrically around the cathode.

Three different substrate materials were used to meet the requirements of various analytical techniques comprising plan view transmission electron microscopy (TEM) imaging, energy dispersive x-ray (EDX) analysis performed on cross-sectional TEM (XTEM) samples in a scanning transmission electron microscope (STEM), and critical load (L_C) measurements to assess adhesion. All substrates (low carbon steel sheets for TEM, austenitic stainless steel for x-ray diffraction (XRD), and high speed steel for critical load measurements) were polished to $R_a=0.05$ μm using 1 μm diamond paste in the final step. They were wet cleaned in an

^{a)}Electronic mail: c.schonjahn@shu.ac.uk

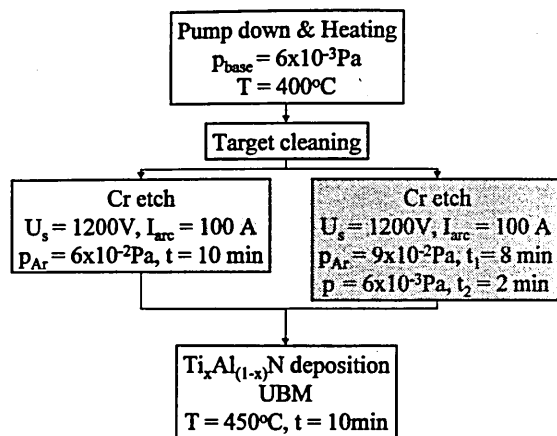


Fig. 1. Process sequence of the one-step and two-step etching procedures.

automatic ten stage industrial cleaning line (UCM, St. Mar- arethen, CH) containing a range of aqueous based alkali etergents and deionized water. Drying was performed by acum radiant heating before loading to the deposition hamber. Prior to sputter cleaning and coating, the chamber as evacuated to a base pressure of 0.006 Pa and heated to) °C. One Cr target was used as the cathodic arc source $I_A = 100$ A) for all etching experiments. Ion etching param- eters were varied as summarized in Fig. 1. The target power n the two TiAl targets used was 8 kW each and the negative ias voltage was 75 V during reactive unbalanced magnetron uttering of $Ti_xAl_{(1-x)}N$ in an Ar/N_2 atmosphere (0.35 Pa, .6 mTorr). The deposition time was 10 min giving a coating 'ckness of ~ 100 nm.

Coating adhesion was assessed by critical load scratch sts performed on industrially proven coatings consisting f an approximately 300 nm $Ti_{0.46}Al_{0.54}N$ base layer, eposited on HSS substrates under conditions as described ove. Subsequently, an approximately 3.2 μm thick $_{0.44}Al_{0.53}Cr_{0.03}Y_{0.02}N$ coating was deposited.¹¹ A CSEM VETEST scratch instrument was used to measure L_C . e L_C value was registered when first adhesive failure oc- curred as observed by reflected light microscopy.

XTEM samples were prepared by mechanical polishing d subsequent Ar ion beam milling. The elemental compo- sition of the interface was analyzed by energy dispersive -ray analysis performed in a vacuum generator HB.501 TEM, equipped with a field emission gun, using a probe e of ~ 1 nm. Under the applied conditions a resolution of .7 nm was achieved. TEM imaging was performed in a hilips CM20. Plan view samples were prepared by dissolv- g the low carbon steel substrate in H_2SO_4 . The remaining) nm $Ti_xAl_{(1-x)}N$ film was placed on a copper mesh. lancing angle XRD measurements were carried out using a hilips PW 1710 automated diffractometer using $Cu K\alpha$ ra- tion. During the experiments an incidence angle of 0.5° as employed to determine the residual stress in $i_xAl_{(1-x)}N$ coating and in the substrate itself. The metal moval rate was measured on steps after etching masked stenitic stainless steel substrates. For step height determi- tion a UBM laser profilometer was employed.

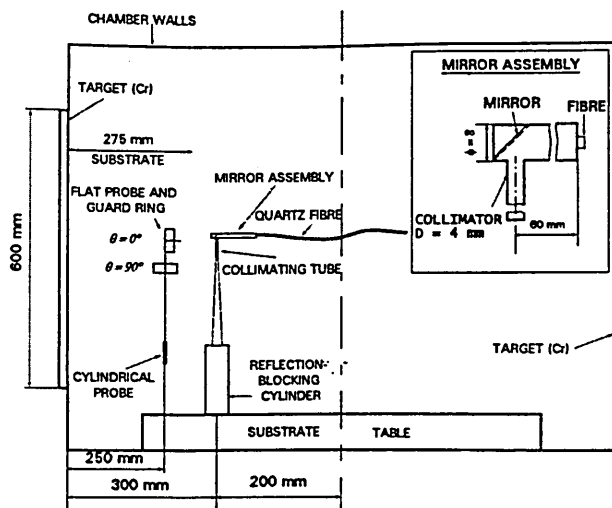


Fig. 2. Vertical cross section of the vacuum chamber with Langmuir probe positions and OES sampling volume. The inset shows a detailed view of the mirror assembly.

The plasma diagnostics was performed by electrostatic (Langmuir) probes and optical emission spectroscopy (OES). A flat Langmuir probe with a disk diameter of 20 mm and a concentric guard ring was used for measuring the ion saturation current. The disk and the guard ring were kept at the same potential and the current to the disk was measured. A cylindrical Langmuir probe consisting of a 100 μm diameter and 10 mm length tungsten wire was used to estimate the electron temperature. Both probes were mounted at a distance of 25 cm from the cathode. While keeping the same distance, the collecting plane of the flat probe could be directed in two orientations with respect to the cathode plane, namely parallel (angle between planes $\theta = 0^\circ$) and perpendicular ($\theta = 90^\circ$). The comparison of the probe current in both orientations enabled the qualitative assessment of the directionality of the ion flux produced by the steered arc discharge. The experimental setup is schematically shown in Fig. 2.

A Jobin Yvon Triax320 spectrometer was furnished with a 300 nm blaze grating (1200 grooves/nm) and photomultiplier tube (PMT) with a resolution of 0.12 nm. For *in situ* plasma observation a quartz fiber bundle was positioned inside the chamber and coupled through a quartz window to a second fiber bundle connected to the spectrometer. The setup allowed a spectral range of 200–850 nm. In order to avoid coating the fiber a mirror assembly was used. A collimator tube, 4 mm $\phi \times 60$ mm, was attached to the mirror assembly to sample a defined conical volume of the plasma. In order to minimize interference from scattered light the collimating tube was directed towards a larger tube 20 mm in diameter and 200 mm in length. This auxiliary tube was blocked at one end and mounted at the opposite side of the chamber. The sampled volume was 20 cm long and situated 30 cm from the cathode with a symmetry axis parallel to the target surface (Fig. 2).

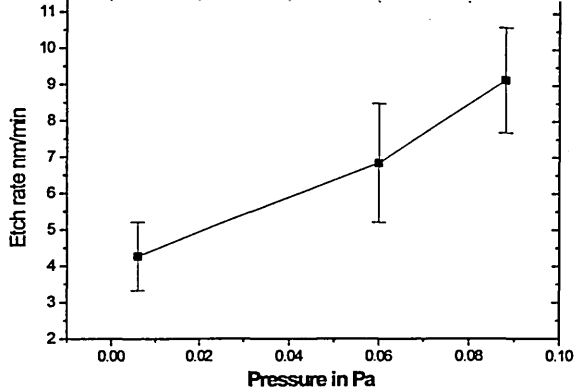


FIG. 3. Etch rate variation with Ar pressure determined from step height measurements.

III. RESULTS AND DISCUSSION

A. Substrate etching rate and plasma diagnostic measurements during Cr arc discharges

In order to further optimize the Cr-arc etching procedures which were found to provide enhanced $Ti_xAl_{(1-x)}N$ coating adhesion on steel substrates in Refs. 3 and 5, we performed etching rate R_{etch} measurements in combination with plasma diagnostic measurements at different Ar pressures p_{Ar} during the arc discharge. Figure 3 shows the variation of the substrate etch rate as a function of p_{Ar} at a constant arc current on the Cr target of 100 A. The etch rate increased from 4.2 to 9.1 nm/min (by $\sim 115\%$) as the pressure increased from 0.006 Pa to 0.09 Pa.

Plasma probe measurements indicate that the increase in etching rates at higher gas pressures correlates with the increase in the ion saturation currents at the substrates indicating higher plasma density values. Figure 4 shows the ion saturation currents measured at a probe voltage of -150 V with the flat and cylindrical probe in the two probe orientations given in Fig. 2. The flat probe values in both orientations increase by $<50\%$ as the pressure is increased from 0.006 Pa to 0.1 Pa (7.5×10^{-4} Torr) and remain nearly constant at higher pressures. In pure metal discharge (at 0.006 Pa with no intentionally introduced gas in the cham-

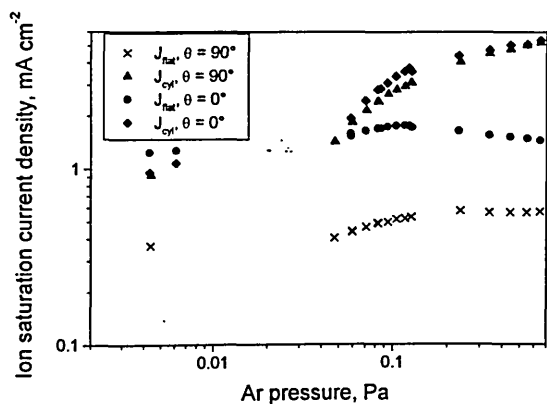


FIG. 4. Ion saturation current densities measured by a flat Langmuir probe for positions $\theta=0^\circ$ (●) and $\theta=90^\circ$ (x) and cylindrical probe (◆,▲).

ber) the metal vapor flux is highly directional and a fraction of the electrons is lost in the ionization process when scattered away from the metal plume. As the Ar pressure is increased the gas fills uniformly the chamber volume thus reducing these losses which results in more effective utilization of the thermal electrons in the ionization processes.^{12,13} This effect of increased plasma density around the substrate saturates for pressures above 0.1 Pa for the conditions of our experiment.

The measured increase in the ion current values (by $<50\%$) in the pressure range <0.1 Pa, however, accounts for less than half of the increase in the etch rate over the same pressure interval. The further enhancement of R_{etch} with p_{Ar} can be ascribed to an additional glow discharge, maintained at the substrate surface by the bias voltage of -1200 V, accelerating the electrons ejected in a secondary ion-electron emission by ions impinging on the substrate surface. The current density associated with this discharge would be an increasing function of the gas pressure.¹⁴ Such a discharge can be observed visually as a uniform glow around the biased substrates with an intensity which increases with p_{Ar} .

The data in Fig. 4 show that the currents with the flat probe facing the cathode, $\theta=0^\circ$, are larger than the currents with $\theta=90^\circ$ by a factor of >3 . When the probe plane is parallel to the cathode plane it collects both ions arriving directly from the cathode spot (line of sight effect) and randomized ions which have undergone a number of collisions. In the case of the perpendicular probe plane ($\theta=90^\circ$), only randomized ions are collected.¹⁵ Particularly at low pressures substantial differences in the current densities collected in the two different orientations were observed (Fig. 4) indicating a highly anisotropic ion velocity distribution in the plasma. However, the dependencies tend to converge for both orientations with increasing $p_{Ar} > 0.1$ Pa due to gas scattering. This effect is more pronounced for the cylindrical probe where the measured ion current density increases rapidly with pressure and has overall higher values. In view of the practical applications the latter means that, for samples with complex geometries, sharper edges and protruding parts will be etched at higher rates. To minimize such distortions in the sample shape it is desirable to keep the gas pressure <0.1 Pa and to reduce the overall etching time.

The ion flux originating from the cathode spot is highly ionized and contains multiply charged metal ions, in the Cr arc an average charge of up to 2^+ with up to threefold multiply charged ions have been reported.¹⁶ We were able to detect optical emission signals from Cr neutrals and Cr ions with charges 1^+ and 2^+ within the spectral range of 200–850 nm of the spectrometer used. An example of a spectrum collected at an Ar pressure of 0.06 Pa is presented in Fig. 5. When the metal vapor coming from the spot enters the anodic region of the arc discharge, the Cr ions collide with Ar atoms. These collisions are the main reason for Cr neutralization since the process of direct recombination of electrons with metal ions in two-body collisions does not conserve energy and momentum and is therefore unlikely.¹⁷ The ion-atom collection leads to a charge exchange process of the

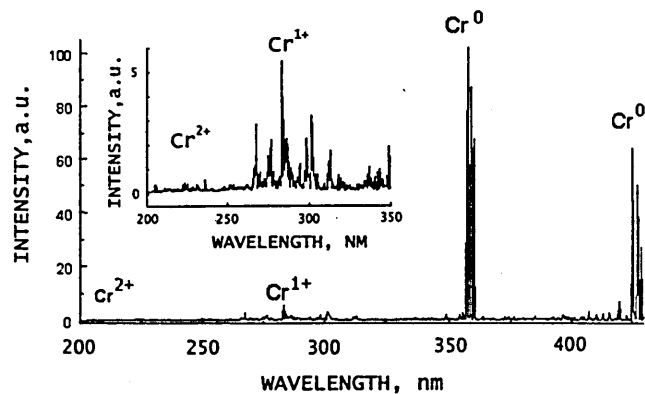


Fig. 5. Typical emission spectrum of the arc spot of a Cr arc. Cr^{2+} , Cr^{1+} , and Cr neutral species are detected. The neutral emission is from electron transitions to the ground state that have a high probability of decay. The fine lines are generated by transitions to metastable states and have a smaller probability of decay.

pe: $\text{Cr}^{(n)+} + \text{Ar} \rightarrow \text{Cr}^{(n-1)+} + \text{Ar}^+$ whereby the mean charge state can alter.¹⁸⁻²⁰ The Q values for this reaction are 0.73 and -8.95 eV for $n=2$ and 1, respectively. While the case $n=2$ is energetically favorable, for $n=1$ the threshold energy of 20.6 eV as calculated using the method given in Ref. 7 is such that charge exchange with Cr^{1+} is only possible if some of the ion kinetic energy is transferred to internal energy. The probability of charge exchange depends on the Ar pressure. Figure 6 shows in relative values the optical emission measurements of Cr^0 , Cr^{1+} , and Cr^{2+} received from a Cr arc discharge as a function of p_{Ar} . As the Ar pressure is increased the concentration of Cr^{1+} and Cr^{2+} ions decreases continuously. Particularly in the case of twofold charged Cr the intensity drops to half of its value when the Ar pressure is raised from 0.01 Pa to 0.1 Pa. The overall ion current densities increase, however, which indicate that this increase is largely due to Ar ions.

In summary, increasing the Ar pressure during Cr arc discharges of constant current leads to enhanced etching rates as a result of an increase in the plasma density around the substrate, randomization of the ion fluxes generated in the cathode spot, and ignition of an additional glow discharge on the negatively biased substrates. The concentration of Cr ion

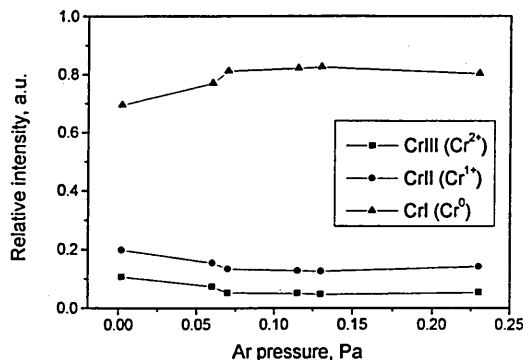


Fig. 6. Variation of the emission from neutral, singly ionized, and doubly ionized chromium with Ar pressure. Intensities are plotted relative to the overall intensity of the three lines.

species, as revealed by optical spectroscopy, falls thus the increase in the ion densities is primarily due to ionization of argon atoms by thermal electrons. Using this information we designed and investigated the two-step etching process presented in Fig. 1. During the high-pressure (0.09 Pa) etching step, which is with longer duration (8 min), we used ion irradiation with a significant component of Ar ions to clean the substrate at a high rate and effectively remove surface oxides and carbides. During the shorter (2 min) second step we used Cr arc with no intentionally introduced gases seeking to maximize the effects of metal ion implantation while preserving the crystallographic order of the substrate grains and thus allowing localized epitaxial growth during subsequent film deposition. The total time is reduced in half compared to the procedure developed in Refs. 3 and 5 in which Cr-arc etch at $p_{\text{Ar}}=0.06$ Pa for 20 min was used. As presented in Fig. 1 we also investigated the latter process with the etching time reduced to 10 min.

B. Relation between interface microstructure, composition, residual stress, and adhesion

As shown previously a clean substrate surface together with a well-preserved crystal structure at the substrate surface is crucial to promote local epitaxial growth and to achieve beneficial preconditions for excellent adhesion.^{3,5} A combined/mixed Cr^+ and Ar^+ ion bombardment of the substrate surface lasting over a period of 20 min has been shown to be sufficient to satisfy both demands mentioned above. In those experiments the substrate material removal rate was estimated to be approximately 7 nm/min leading to a total etching depth of approximately 140 nm ($p_{\text{Ar}}=0.06$ Pa). In both procedures studied here the etching period has been reduced to only 10 min. The total etched depth in the present experiments was determined to be approximately 70 and 80 nm (two-step etch procedure), respectively. Although the total removal of substrate material is reduced to approximately 80 nm the substrate surface is obviously clean enough to provide conditions for local epitaxial growth of $\text{Ti}_x\text{Al}_{(1-x)}\text{N}$ on α -Fe. A definite indication of localized epitaxial growth of the $\text{Ti}_x\text{Al}_{(1-x)}\text{N}$ coating on the ferritic low carbon steel substrate is observed from plan view TEM imaging. This can be concluded from dark field (DF) images of a 100 nm $\text{Ti}_x\text{Al}_{(1-x)}\text{N}$ film (steel substrate was dissolved) as given in Fig. 7(a). The low magnification for that DF image was chosen in order to illustrate that the large film grains are brightly illuminated at the same time. The latter fact is proof that the grains have the same crystallographic orientation. Regions of identical crystallographic orientation extend over several micrometers, exhibiting sharp grain boundaries between adjacent $\text{Ti}_x\text{Al}_{(1-x)}\text{N}$ grains. That these boundaries are correlated to grain boundaries of the underlying steel substrate was previously shown by cross-sectional TEM for the case of 20 min Cr ion bombardment at $p_{\text{Ar}}=0.06$ Pa,⁵ indicating typical coating grain sizes of several micrometers. In the absence of local epitaxial growth of $\text{Ti}_x\text{Al}_{(1-x)}\text{N}$ on the substrate grains

identified. However, high compressive stresses were found in the 100 nm thin coatings grown after both sputter-cleaning processes. The interface with the lower Cr incorporation exhibited a higher compressive residual stress in the coating (-8.3 GPa) in comparison to the case when pure Cr ion bombardment was involved (-6.8 GPa). It is interesting to note that the average residual stress in a $3.5 \mu\text{m}$ thick $\text{Ti}_x\text{Al}_{(1-x)}\text{N}$ coating was 3 GPa, independent of the two etching procedures applied.

The lower stress gradient found in the two stage etching process might explain the significant differences in the critical load values L_C obtained for both interfaces. Indeed the critical load values for samples processed in the two-step etching mode showing the enhanced Cr incorporation ranged $L_C=85\pm 5N$ as compared to samples prepared after the one-step etching procedure ($L_C=63\pm 3N$). Although the high stress values found in the 100 nm thin $\text{Ti}_x\text{Al}_{(1-x)}\text{N}$ coating adjacent to the interface could be attributed to grain size effects when competitive growth is involved (Hall-etch), it is believed that epitaxial stresses are more likely to explain the observed effects. The higher Cr content found at the steel surface resulting from the two stage sputter cleaning procedure could therefore be responsible for an increase of the lattice parameter of the substrate which should reduce the mismatch between steel and $\text{Ti}_x\text{Al}_{(1-x)}\text{N}$ coating therefore leading to a lower epitaxial stress component and a flatter stress gradient at the interface. Similar observations were made for plasma nitriding the surfaces.^{21,22}

IV. CONCLUSION

It was found that the etching rates of negatively biased (1200 V) steel substrates more than doubled with the introduction of argon gas to pressures 0.09 Pa at constant arc current using a steered arc on a Cr target. Plasma probe measurements indicate that the ion current density on negatively biased substrates increases significantly with the increase of the argon pressure which is attributed to more efficient volume ionization processes in the presence of gas atmosphere and to the ignition of an auxiliary glow discharge at the substrate surface which is sustained by ionization by electrons generated as a result of secondary ion-electron emission and accelerated in the substrate sheath to energies corresponding to the full value of the bias voltage. Optical emission spectroscopy revealed a decrease in the concentration of metal ions with p_{Ar} , as a result of charge exchange processes, thus the increase in the ion current densities and correspondingly in the etching rates is due to argon ions. Based on these results we designed a two-stage sputter-cleaning procedure with reduced overall duration that involves a high-rate etch in the presence of Ar and an ion implantation step in pure Cr discharge. The modified sputter

cleaning procedure provides substantial improvement of the adhesion conditions of the $\text{Ti}_x\text{Al}_{(1-x)}\text{N}$ coatings thus making the PVD process more robust. This improvement may be mainly attributed to the microchemistry in the interface transition zone controlled by the incorporation of Cr into the steel matrix. Critical load measurements confirm an increase of L_C from typically $63\pm 3N$ to $85\pm 5N$. Stress measurements in the interface region suggest a flatter stress gradient in case of enhanced Cr content.

ACKNOWLEDGMENTS

The content of this article is part of the Ph.D. research projects of C. Schönjahn and A. P. Ehiasarian presently being carried out at Sheffield-Hallam University, Sheffield, United Kingdom. This research was further supported by the U.S. Department of Energy, Division of Materials Science, under Grant No. DEFG02-96-ER45439. We also appreciate the use of the Center for Microanalysis of Materials at the University of Illinois, which is supported by the U.S. Department of Energy under Grant No. DEFG02-96-ER45439.

¹S.-J. Bull, Surf. Coat. Technol. 50, 25 (1991).

²J. Musil, J. Vyskocil, and S. Kadlec, Phys. Thin Films 17, 79 (1993).

³C. Schönjahn, D. B. Lewis, W.-D. Münz, and I. Petrov, Surf. Eng. 16, 176 (2000).

⁴W.-D. Münz, F. J. M. Hauzer, D. Schulze, and B. Buil, Surf. Coat. Technol. 49, 161 (1991).

⁵C. Schönjahn, L. A. Donohue, D. B. Lewis, W.-D. Münz, R. D. Twesten, and I. Petrov, J. Vac. Sci. Technol. A 18, 1718 (2000).

⁶I. Petrov, P. Losbichler, D. Bergstrom, J. E. Greene, W.-D. Münz, T. Hurkmans, and T. Trinh, Thin Solid Films 302, 179 (1997).

⁷M. I. Lembke, D. B. Lewis, and W.-D. Münz, Surf. Coat. Technol. 125, 263 (2000).

⁸W.-D. Münz, I. J. Smith, D. B. Lewis, and S. Creasey, Vacuum 48, 473 (1997).

⁹J. S. Brooks, J. L. Davidson, S. D. Forder, W.-D. Münz, and M. Larsson, Thin Solid Films 308-309, 351 (1997).

¹⁰G. Håkansson, L. Hultman, J.-E. Sundgren, J. E. Greene, and W.-D. Münz, Surf. Coat. Technol. 48, 51 (1991).

¹¹W.-D. Münz and I. J. Smith, 42nd Annual Conference Soc. Vac. Coatings, Chicago, 1999 (unpublished), pp. 350-356.

¹²M. K. Puchert, C. A. Davis, D. R. McKenzie, and B. W. James, J. Vac. Sci. Technol. A 10, 3493 (1992).

¹³V. N. Zhitomirsky, U. Kinrot, B. Alterkop, R. L. Boxman, and S. Goldsmith, Surf. Coat. Technol. 86-87, 263 (1996).

¹⁴A. von Engel, *Ionized Gases* (Oxford University, New York, 1965).

¹⁵H. S. Maciel and J. E. Allen, J. Plasma Phys. 42, 321 (1989).

¹⁶T. G. Brown, B. Feinberg, and J. E. Galvin, J. Appl. Phys. 63, 4889 (1988).

¹⁷C. Bergman, Surf. Coat. Technol. 36, 243 (1988).

¹⁸P. J. Martin, D. R. McKenzie, R. P. Netterfield, P. Swift, S. W. Filipczuk, K. H. Müller, C. G. Pacey, and B. James, Thin Solid Films 153, 91 (1987).

¹⁹I. Demidenko, N. S. Lomino, V. D. Ovcharenko, V. G. Padalka, and G. N. Polyakova, Sov. Phys. Tech. Phys. 29, 895 (1984).

²⁰M. Kühn, R. Pintaske, and F. Richter, IEEE Trans. Plasma Sci. 25, 694 (1992).

²¹B.-J. Kim, Y.-C. Kim, and J.-J. Lee, Surf. Coat. Technol. 114, 85 (1999).

²²W.-D. Münz, G. Nayal, and I. J. Smith, VDI-Ber. 155, 228 (2000).



PERGAMON

Vacuum 65 (2002) 147–154

VACUUM
SURFACE ENGINEERING, SURFACE INSTRUMENTATION
& VACUUM TECHNOLOGY

www.elsevier.com/locate/vacuum

Influence of high power densities on the composition of pulsed magnetron plasmas

A.P. Ehiasarian^{a,*}, R. New^a, W.-D. Münz^a, L. Hultman^b, U. Helmersson^b,
V. Kouznetsov^c

^a Materials Research Institute, Sheffield Hallam University, Howard Street, Sheffield S1 1WB, UK

^b Thin Film Physics Division, Department of Physics, Linköping University, SE-581 83 Linköping, Sweden

^c Chemfilt R&D AB, Kumla Gårdsvägen 28, SE-145 63 Norsborg, Sweden

Received 15 October 2001; accepted 5 November 2001

Abstract

The application of high power pulses with peak voltage of -2 kV and peak power density of 3 kW cm⁻² to magnetron plasma sources is a new development in sputtering technology. The high power is applied to ordinary magnetron cathodes in pulses with short duration of typically some tens of microseconds in order to avoid a glow-to-arc transition. High plasma densities are obtained which have been predicted to initiate self-sputtering. This study concerns Cr and Ti cathodes and presents evidence of multiply charged metal ions as well as of Ar ions in the dense plasma region of the high power pulsed magnetron discharge and a substantially increased metal ion production compared to continuous magnetron sputtering. The average degree of ionisation of the Cr metal deposition flux generated in the plasma source was 30% at a distance of 50 cm. Deposition rates were maintained comparable to conventional magnetron sputtering due to the low pressure of operation of the pulsed discharge—typically 0.4 Pa (3 mTorr) of Ar pressure was used.

Observations of the current–voltage characteristics of the discharge confirmed two modes of operation of the plasma source representing conventional pulsed sputtering at low powers (0.2 kW cm⁻²) and pulsed self-sputtering at higher powers (3 kW cm⁻²). The optical emission from the various species in the plasma showed an increase in metal ion-to-neutral ratio with increasing power. The time evolution within a pulse of the optical emission from Ar⁰, Cr⁰, Cr¹⁺, and Cr²⁺ showed that at low powers Cr and Ar excitation develops simultaneously. However, at higher powers a distinct transition from Ar to Cr plasma within the duration of the pulse was observed. The time evolution of the discharge at higher powers is discussed. © 2002 Elsevier Science Ltd. All rights reserved.

Keywords: Pulsed magnetron sputtering; Time evolution; Ionised sputtering; Highly charged metal ions; High density plasma; Ionised metal plasma

1. Introduction

Magnetron sputtering is a well-established physical vapour deposition technique. It is used

to deposit metallic as well as compound thin films for a wide range of applications. In most cases, it is beneficial to produce dense, defect-free coatings, which often requires low-energy ion bombardment of the condensing film surface to increase the mobility of adatoms [1–3] to achieve void free thin films. To obtain considerable ion bombardment a

*Corresponding author. Fax: +44-114-221-3053.

E-mail address: a.ehiasarian@shu.ac.uk (A.P. Ehiasarian).

sufficient ion-to-neutral ratio in the condensing flux needs to be achieved. Conventional magnetron plasma sources produce mainly sputtering gas ions [4] reaching a typical charge carrier density of 10^9 cm^{-3} . Arc evaporators easily reach densities of 10^{18} cm^{-3} producing highly ionised metal ion fluxes, however, their main disadvantage is that they produce a droplet of the target material, which deteriorates the quality of deposited coatings. Several attempts have been made to enhance the plasma density in the vicinity of the substrates using sputtering techniques. An effective method, suggested by Window et al. [5], was to unbalance the magnetic field, thus guiding the Ar plasma far away from the magnetron. In the work of Rosnagel and Hopwood [6], an additional ionisation source comprising an inductively coupled radio frequency (RF) antenna was introduced in the magnetron discharge producing increased plasma density as well as ionisation of the sputtered metal flux. Recently, Kouznetsov et al. [7] reported a modified operational mode of the conventional magnetron utilising high power density pulsed magnetron sputtering (HIPIMS). Due to a high plasma density, they reported that the metal ion-to-neutral ratio in the deposition flux reached as much as 70% in the case of Cu.

The present paper reports on the transition between conventional pulsed magnetron sputtering to HIPIMS as the power dissipated in the discharge is increased. Cr and Ti cathodes were used as model systems. The discharge parameters are compared to conventional magnetron sputtering. High peak plasma densities of the order of 10^{13} cm^{-3} containing multiply ionised metal species as observed by optical emission spectroscopy (OES). The effect of power on the temporal evolution of the plasma composition is discussed.

2. Experimental

The experiments concentrated on characterising the pulsed magnetron plasma, by measuring current–voltage characteristics, carrying out optical emission and probe diagnostics and determining the metal ion-to-neutral ratio in the deposition

flux using a biasing/deposition technique. The chamber, power supply characteristics and discharge current and voltage measurements were as described previously [8]; however, a target with a diameter of 50 mm was used.

The plasma composition was analysed by OES utilising a Jobin Yvonne Triax 320 scanning monochromator with resolution 0.12 nm and a grating groove density of 1200 grooves/mm. Time evolution of the OES signals was studied using the same monochromator, with the output of its photo-multiplier tube (PMT) connected to ground via a 100 k Ω resistor. The voltage across the resistor was proportional to the current signal in the PMT and was monitored using a Tektronix 520 digitising oscilloscope with a 10 M Ω probe, triggering on the target voltage signal. In order to obtain the temporal evolution of a certain emission line, the monochromator was set to transmit the wavelength of interest and the voltage across the resistor was recorded with time. The optical emission was collected in vacuo by an optical fibre bundle equipped with a collimating tube ($\phi = 4 \text{ mm}$, $l = 50 \text{ mm}$) positioned at a distance of 1 cm parallel to the target surface. The complete optical set-up was sensitive to emission in the wavelength range 200–950 nm. Macak et al. [8] were first to report a study of the plasma composition and temporal evolution of the HIPIMS using OES. Similar measurements presented in this work go beyond previous investigations in terms of an enhanced spectral range, covering the ultraviolet region, an improved resolution reducing the signal-to-noise ratio and a vastly superior sensitivity of PMT over charge coupled device detectors.

Ion saturation current measurements were performed with a flat probe with a diameter of 2 cm equipped with a guard ring and positioned 3.5 cm from the target surface. The deposition rate was measured using a quartz crystal microbalance situated at a distance of 6.5 cm from the target surface. The metal ion-to-neutral ratio in the deposition flux was calculated by depositing for a known time on a positively biased and a floating metal plate located 50 cm from the target. The difference in mass between the plates was measured and the metal ion and neutral flux were

determined for a medium peak power density of 1.5 kW cm^{-2} .

3. Results and discussion

3.1. $I-U$ characteristic at $p=\text{const}$

It is well documented that conventional magnetron $I-U$ characteristics follow a power law $I = kU^n$. The exponent n is typically in the range 5–15 [9] reaching low values when the discharge operates at very low pressures or is confined by a weak magnetic field. Fig. 1 shows the $I-U$ characteristics of a magnetron discharge operated on a typical industrially sized rectangular cathode and the high power density pulsed magnetron discharge of the present work operated on a cylindrical cathode, 50 mm diameter. Both discharges were operated at a pressure of 0.4 Pa (3 mTorr). The exponent calculated from the slope of the relation for the conventional magnetron is 8, which is well within the defined range. The pulsed discharge exhibits two slopes depending on the target current. At low currents ($< 600 \text{ mA cm}^{-2}$),

the exponent is approximately 7 indicating normal magnetron operation. At higher currents, the exponent changes to 1, in a mode of operation in which the increase of discharge voltage to very high values of 1.6 kV is not accompanied by a large increase in the discharge current. One possible explanation of this mode of operation is that the secondary electrons accelerated in the sheath to 1.6 keV cannot be trapped by the magnetic field and the probability of ionising collisions per electron is decreased. Nevertheless, as shown in Fig. 2, at the higher powers the plasma density at a distance of 3.5 cm from the target increases faster than at low powers. The peak density calculated from the ion saturation current and assuming low ion energy was estimated to be 10^{13} cm^{-3} at a target power density of 3 kW cm^{-2} . The reasons for the steeper increase of saturation current at higher powers are not fully understood. It is possible to attribute it to the escape of the plasma from the target due to poor electric and magnetic field confinement at high target voltages.

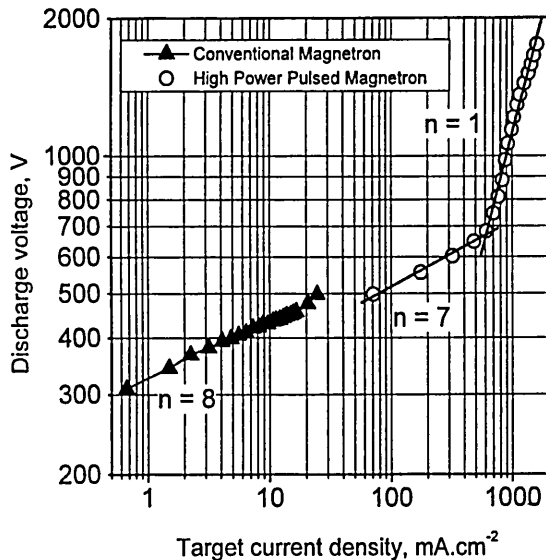


Fig. 1. $I-U$ characteristics of the pulsed discharge. The exponent n of the power law $I = kU^n$ is indicated. Cr sputtering in Ar atmosphere at a pressure of 0.4 Pa (3 mTorr).

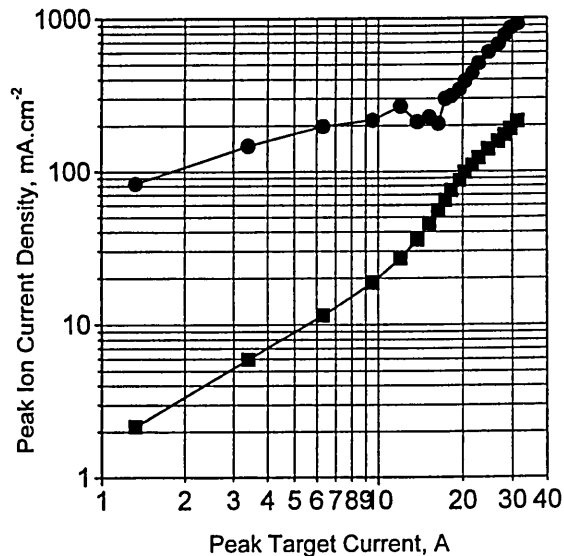


Fig. 2. Ion saturation current at a distance of 3.5 cm with the probe facing the target (circles) and with the probe perpendicular to the target surface (squares). The flat probe was biased to -150 V . Maximum plasma densities derived from the current densities are in the range 10^{13} cm^{-3} .

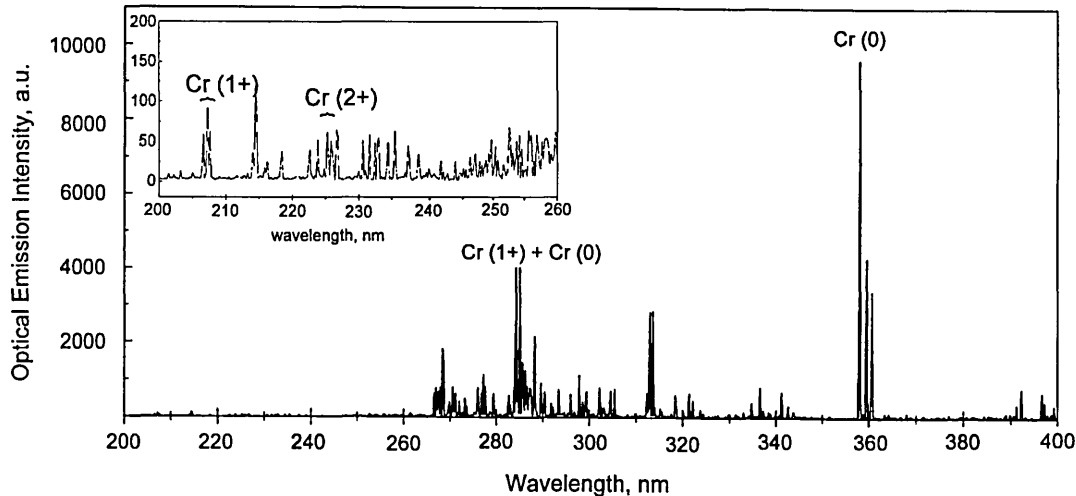


Fig. 3. Optical emission spectrum of high power pulsed sputtering of Cr in an argon atmosphere. Peak target power = 3000 W cm^{-2} , $P_{\text{Ar}} = 0.4 \text{ Pa}$ (3 mTorr), 1 cm from target. Two-fold and one-fold ionised Cr was observed in the dense plasma region of the magnetron.

3.2. Detection and study of metal ions in the plasma at high target currents

It is well known that the probability of ionisation of species depends on their dwell time in the plasma and the energy of ionising species. In typical magnetrons, the plasma comprises mainly residual gas ions [4]. Electrons confined in an ExB drift loop in the magnetron collide with the almost stationary gas atoms and the ionisation probability per electron is quite high. On the other hand, sputtered metal atoms leave the target surface with relatively high energies, typically a few eV, traversing the dense plasma region in a few microseconds. In typical magnetron discharges, the plasma density is such that the traverse time is too short for ionising collisions to occur and only a negligible proportion of metal ions is created. In the high power pulsed discharge, although the sputtering voltage can be at least two times higher, the sputtered atoms leave the target with the same energy of a few eV. However, they cannot penetrate the dense highly energetic electron cloud formed in the sheath due to the high discharge power without collisions and the probability of ionisation of the pulse-sputtered flux is high. The maximum tangential magnetic field of the magnetron ($\sim 500 \text{ G}$) is not sufficient to magnetise the

ionised metal and it readily escapes from the dense plasma region and reaches long distances where deposition samples can be placed. On the other hand, a portion of the metal ions is accelerated back to the target surface, giving rise to self-sputtering and decreasing the sputtering rate due to the low self-sputtering yield. Preliminary results show a clear trend between self-sputtering yield and deposition rate [10]. In the present work, the deposition flux at a distance of 50 cm from a Cr target surface was found to contain 30% metal ions for peak target power of 1.5 kW cm^{-2} .

OES studies confirm an enhanced proportion of ions of both sputtered species and residual gas in the HIPIMS discharge. The plasma composition during sputtering of Cr and Ti was investigated using OES. The spectrum during Cr sputtering at a peak power of 3 kW cm^{-2} is shown in Fig. 3. One- and two-fold ionised metal species were detected in the dense plasma region of the magnetron.

Up to two-fold ionised metal ions were found also in a Ti pulsed discharge. The optical emission spectra in Fig. 4 show three kinds of magnetron sputtering discharges. Pulsed magnetron sputtering plasma was realised with peak power 1.5 kW cm^{-2} and average power 300 W. A conventional magnetron was operated at an average power of 300 W. A magnetron with enhanced

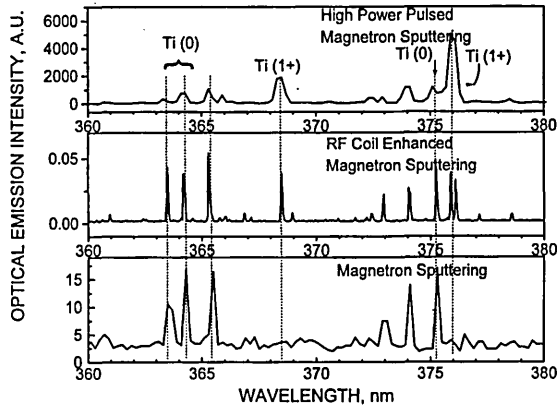


Fig. 4. Optical emission spectra of plasmas produced by discharges in a conventional DC magnetron (bottom), a RF coil enhanced magnetron (middle) and high power pulsed magnetron.

ionisation by RF coil.¹ The Ti ion to neutral spectral line ratio is negligible in the conventional magnetron sputtering, and increases from 0.9 in the RF coil enhanced discharge to 5 in the pulsed discharge. The numbers quoted above are regarded only as a qualitative comparison of the degree of ionisation in the three methods of sputtering.

The above evidence for significant ionisation is further supported by the dense, smooth films generated in subsequent coating runs which will be described in detail elsewhere [12]. The films had an excellent adhesion due to the pre-treatment of the substrates by metal ion containing HIPIMS plasma bombardment under a bias of -1200 V.

3.3. Plasma density and composition as a function of peak target current

As can be seen from Fig. 2, the peak density of the magnetron plasma increased monotonically by approximately two orders of magnitude as the peak target current increased by a factor of 30. It is interesting to note that when high powers are dissipated in the discharge, the discharge voltage increases simultaneously with the current with an

¹The discharge was operated with DC magnetron power of 300 W, RF coil power of 450 W, and $P_{Ar}=4$ Pa (30 mTorr). The experimental details are described in Ref. [11].

exponent close to 1 (see Fig. 1). The increased discharge voltage is probably responsible for increasing, for example, the hot electron temperature, which, combined with the increased plasma density, is a pre-requisite for an improved ionisation efficiency of the sputtered Cr atoms.

OES measurements of the Cr^{2+} line at 232.03 nm, Cr^{1+} line at 205.55 nm and the Cr^0 line at 399.11 nm were carried out in order to investigate the degree of ionisation of the sputtered metal flux. These particular emission lines have been chosen because they are formed by transitions for which the upper level energies are similar: 5.4, 6.0 and 5.66 eV for Cr^{2+} , Cr^{1+} , and Cr^0 , respectively. Assuming a Corona model for the plasma [13], the line emission intensity ratio can be used as a qualitative measure of the density ratio of the species because of the similarity in their excitation energies. It should be noted that, since only Cr neutrals are sputtered from the target all Cr ions are created in the discharge by a process of electron impact ionisation, which depends strongly on the electron temperature. The intensity ratio of such optical emission lines depends directly on the density of the species and is influenced indirectly

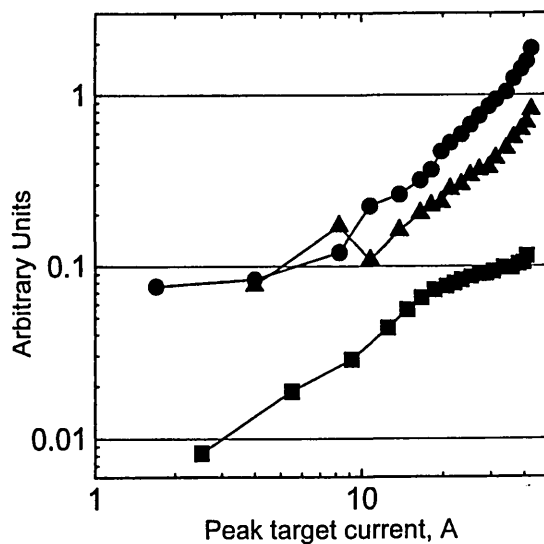


Fig. 5. Ion-to-neutral ratio vs. peak target current for Cr from optical emission line intensities $I(\text{Cr}^{2+})/I(\text{Cr}^0)$ (triangles) and $I(\text{Cr}^{1+})/I(\text{Cr}^0)$ (circles). Also shown is the ratio of the ion current density and deposition rate (squares).

by changes in electron temperature. The ratio of the spectral line intensities of Cr^{2+} and Cr^0 indicated in Fig. 5 with triangles shows an increasing ionisation with target current. Two other diagnostic results that indicate an increased ion-to-neutral ratio are also shown in Fig. 5, namely the spectral line intensity ratio $I(\text{Cr}^{1+})/I(\text{Cr}^0)$ recorded during early conditioning runs. The ratio of saturation current to deposition rate is also given as a qualitative measure of the ion-to-neutral arrival rate.

3.4. Time evolution of the plasma composition

The temporal evolution of the plasma was found to be strongly influenced by the power of the discharge pulse. Fig. 6a shows a typical temporal evolution of a pulsed magnetron discharge at relatively low power. The target current and the optical emission from Ar and Cr neutrals occur almost simultaneously. This kind of relationship is routinely observed in the widely used pulsed magnetron discharges operating at lower powers

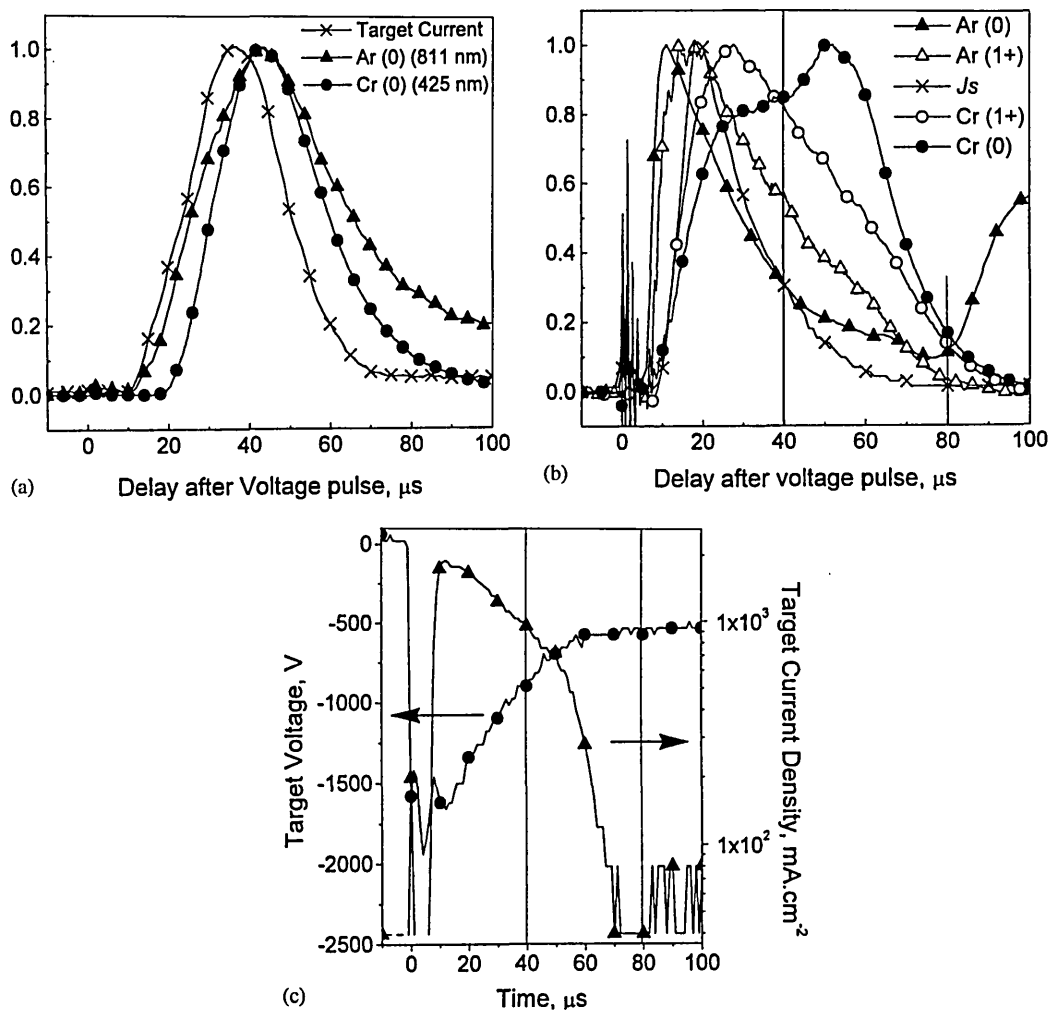


Fig. 6. Typical temporal evolution of the plasma. (a) OES and target current at low power (peak target voltage = -500 V), (b) OES and ion saturation current J_s at high power, (c) target voltage and current at high power (the apparent fluctuations in the current signal after $80\mu\text{s}$ are principally caused by digitisation noise). The species shown are: Cr^0 (399 nm), Cr^{1+} (232 nm), Ar^0 (811 nm), Ar^{1+} (440 nm).

than presented here [14]. However, when the peak power density is increased to a few kW cm^{-2} the temporal evolution of the discharge plasma is quite different as is illustrated in Fig. 6b. The OES maxima appear in a clearly differentiated sequence beginning with Ar neutral and ending in Cr neutral. Such a separation in time between the optical emission of Ar and Ti neutral lines at high powers was first reported by Macak et al. [8]. The plasma model proposed by them assumed that the plasma developed from being Ar dominated to metal ion dominated due to the gas rarefaction effects discussed by Rossnagel et al. [15]. The separation for high powers is also confirmed for Cr in the present work.

In detail, the evolution of the optical emission signals shown in Fig. 6b can be separated into three stages as follows. A high power and high plasma density discharge is produced during the first stage, from 0 to 40 μs . The first emission is observed from Ar atoms, present in the background gas when vacuum breakdown occurs. As Ar is ionised the plasma density and target current increase, and Ar^{1+} emission is developed. With a delay of a few microseconds after the Ar lines, the Cr^0 emission lines are detected. After a further 3 μs emission from Cr ion lines is detected, indicating that the sputtered Cr flux is being ionised in the high density plasma. The Cr^{1+} lines peak at approximately 30 μs , approximately 10 μs after the ion saturation current J_s has reached its maximum value. The rapid fall in Ar emission at this time may indicate that the Ar pressure is being locally reduced by the momentum transfer from sputtered Cr atoms [15,9]. The Cr ion emissions fall over the next 40 μs .

At 40 μs the discharge voltage and current have fallen to levels which indicate the start of a second stage. At this time the voltage is approximately -750 V and the discharge is leaving the high power regime as shown in Fig. 1 and entering a regime of normal magnetron operation with a high target current. During this phase the Cr^0 emission is stronger and the Cr^{1+} emission is weaker than in the high power stage, and the target current shown in Fig. 6c starts to drop quickly for a small decrease in voltage as is typical of a normal magnetron discharge. The magnetic confinement

field in these circumstances is very efficient and works in favour of decreasing the rate of decay of the plasma density peak at 20 μs .

The final stage of the discharge occurs at about 80 μs when a typical magnetron glow discharge is initiated with voltage of -500 V and current density some tens of mA cm^{-2} . The subsequent emission from Ar neutral probably indicates the return of the discharge voltage and current to typical magnetron levels and the restoration of the Ar pressure, respectively.

4. Conclusions

High power pulsed magnetron sputtering with peak powers of 3 kW cm^{-2} were used to produce magnetron glow discharges with very high plasma densities. By optical emission, doubly and singly charged metal ions were detected in the dense plasma region for both Cr and Ti targets. The degree of ionisation of the sputtered flux that was measured for the Cr reached a value of 30%. The plasma conditions were strongly influenced by the peak power applied to the target as seen from $I-U$ characteristic and temporal evolution of the composition of the discharge and a threshold current when the discharge switched from typical magnetron sputtering to ionised sputtering was observed.

Acknowledgements

The work presented in this paper was carried out with the financial support of EPSRC Grant Ref: GR/R32420/01, The Swedish Foundation for Strategic Research Program on Low Temperature Thin Film Synthesis and The Swedish Research Council.

References

- [1] Petrov I, Hultman L, Sundgren JE, Greene JE. *J Vac Sci Technol A* 1992;10(2):265–72.
- [2] Hultman L, Helmersson U, Barnett SA, Sundgren JE, Greene JE. *J Appl Phys* 1987;61(2):552–5.

- [3] Helmersson U, Hentzell HTG, Hultman L, Hibbs MK, Sundgren JE. *AIP Conf Proc* 1986;149:79–94.
- [4] Petrov I, Myers A, Greene JE, Abelson JR. *J Vac Sci Technol A* 1994;12(5):2846–54.
- [5] Window B, Sharples F, Savvides N. *J Vac Sci Technol A* 1985;3(6):2368–72.
- [6] Rossnagel SM, Hopwood J. *J Vac Sci Technol* 1994;B 12(1):449–53.
- [7] Kouznetsov V, Macak K, Schneider JM, Helmersson U, Petrov I. *Surf Coat Technol* 1999;122(2–3):290–3.
- [8] Macak K, Kouznetsov V, Schneider JM, Helmersson U, Petrov I. *J Vac Sci Technol A (Parts 1 and 2)* 2000;18(40):1533–7.
- [9] Rossnagel SM, Kaufman HR. *J Vac Sci Technol A* 1988;6(2):223–9.
- [10] Alami J, Music D, Helmersson U, unpublished results.
- [11] Nouvellon C, Konstantinidis S, Dauchot JP, Wautelet M, Jouan PY, Ricard A, Hecq M. *J Appl Phys*, in press.
- [12] Ehasarian AP, et al. manuscript in preparation.
- [13] McWhirter RWP. In: Huddleston RG, Leonard SL, editors. *Plasma diagnostic techniques*. New York: Academic Press, 1965. p. 208.
- [14] List M, Krausse U, Wünsche T. Paper presented at the 43rd Annual Technical Conference of the Society of Vacuum Coaters, April 2000, Philadelphia, USA.
- [15] Rossnagel SM. *J Vac Sci Technol A (Part 2)* 1988; 6(3):1821–6.



High power pulsed magnetron sputtered CrN_x films

A.P. Ehiasarian^{a,*}, W.-D. Münz^a, L. Hultman^b, U. Helmersson^b, I. Petrov^c

^aMaterials Research Institute, Sheffield-Hallam University, Howard St., Sheffield, S1 1WB, UK

^bDepartment of Physics and Measurement Technology (IFM), Linköping University, S-581 83, Linköping, Sweden

^cFrederick Seitz Materials Research Laboratory, University of Illinois, 104 S. Goodwin Avenue, Urbana, IL 61801, USA

Abstract

Microstructure and macroscopic properties of droplet free CrN films deposited by the recently developed high power pulsed magnetron sputtering (HIPIMS) technique are presented. Magnetron glow discharges with peak power densities reaching 3000 W cm⁻² were used to sputter Cr targets in both inert and reactive gas atmospheres. The flux arriving at the substrates consisted of neutrals and ions (approx. 70/30) of the sputtered metal and working gas atoms (Ar) with significantly elevated degree of ionization compared to conventional magnetron sputtering. The high-speed steel and stainless steel substrates were metal ion etched using a bias voltage of -1200 V prior to the deposition of CrN films. The film-to-substrate interfaces, observed by scanning transmission electron microscope cross-sections, were clean and contained no phases besides the film and substrate ones or recrystallized regions. CrN films were grown by reactive HIPIMS at floating potential reaching -160 V. Initial nucleation grains were large compared to conventional magnetron sputtered films, indicating a high adatom mobility in the present case. The films exhibited polycrystalline columnar growth morphology with evidence of renucleation. No intercolumnar voids were observed and the corrosion behavior of the film was superior to arc deposited CrN_x. A high density of lattice defects was observed throughout the films due to the high floating potential. A residual compressive stress of 3 GPa and a hardness value of HK_{0.025} = 2600 were measured. A low friction coefficient of 0.4 and low wear rates against Al₂O₃ in these films are explained by the absence of droplets and voids known to contribute to extensive debris generation.

© 2002 Published by Elsevier Science B.V.

Keywords: Pulsed magnetron sputtering; Chromium nitride; Ion implantation; Ion bombardment

1. Introduction

High density, corrosion- and wear-resistant physical vapor deposition (PVD) hard coatings with excellent adhesion to steel are in high demand for a wide range of applications in the metal forming, plastic molding, machining, automotive, petrochemical, food industries and as decorative applications. Existing PVD techniques such as magnetron sputtering and arc evaporation suffer from porous microstructure, due to low ionization in the former or from defects generated by macroparticles in the latter case. A number of theoretical and experimental works have indicated an enhanced densification of growing films when high ion-to-neutral ratios are present in the plasma and the deposition flux [1-3]. An appropriate

control of the energy of ion bombardment during deposition allows the microstructure density and surface roughness to be tailored to specific wear or corrosion intensive applications. Important to the performance of coatings, especially in demanding metal cutting applications, is the adhesion to the substrates [4]. Metal ion implantation prior to coating deposition on steel substrates has been shown to promote localized epitaxial growth and improve the adhesion of even highly stressed superhard nanoscale, compositionally modulated coating systems [5,6].

The high power pulsed magnetron sputtering (HIP-IMS) discharge [7] is a newly developed PVD technique, which allows high plasma density and ionized metal particles [7,8] to be produced at low pressures and without macroparticle generation. This paper describes a deposition process performed entirely by HIPIMS where the substrates are initially etched ($U_{\text{bias}} =$

*Corresponding author. Tel.: +44-114-221-3046; fax: +44-114-221-3053.

E-mail address: a.ehiasarian@shu.ac.uk (A.P. Ehiasarian).

74
75
76
77
78
79
80
-1200 V) in a metal/gas plasma and subsequently coated with a 2- μm -thick CrN thin film. The optical emission spectroscopy (OES) and flat electrostatic probe plasma diagnostic techniques were used to characterize the etching and deposition conditions. The coating microstructure and mechanical properties were correlated with the results from the plasma characterization.

81 2. Experimental set-up

82 The experimental work was carried out in three stages. Firstly, the plasma conditions in HIPIMS were evaluated in both inert and reactive gas atmospheres. Secondly, a set of CrN thin films were deposited on high speed steel (HSS) and stainless steel (SS) substrates by reactive HIPIMS at different Ar/N₂ partial pressure ratios $P_{\text{Ar}}/P_{\text{N}_2}$. Finally, the microstructure and mechanical properties of the thin films were investigated.

90 The depositions and plasma diagnostic experiments were performed in a turbomolecular pumped (1380 l/s) vacuum chamber with a base pressure lower than 10⁻⁵ Pa (10⁻⁷ torr). A circular magnetron with target diameter of 50 mm (2 inch) was used in all experiments. The ion flux densities at a distance of 3.5 cm from the target were measured with a flat electrostatic probe. Optical emission signals stemming from a region located 1 cm in front of the magnetron target surface were collected through a collimator and quartz fiber assembly [9], and analyzed by a Jobin Yvon Triax 320 spectrometer. The complete system was sensitive to a wavelength range of 200–900 nm.

103 For the CrN coating depositions, a stationary heated substrate holder equipped with a thermocouple was installed at a distance of 6.5 cm from the magnetron target surface.

107 The sequence of the coating process is shown schematically in Fig. 1. In the pretreatment stage, the substrates were biased to -1200 V, and the HIPIMS discharge was operated with peak power of 2.6 kW cm⁻² in pure Ar atmosphere at a pressure of 0.4 Pa (3 mtorr) for 30 min. Finally, the coatings were deposited for a duration of 4 h without biasing (floating bias) at a temperature 250 °C. All coatings were deposited at a constant total pressure of 0.4 Pa in mixed Ar and N₂ atmosphere.

117 The microstructure of the coatings was analyzed by cross-sectional transmission electron microscopy (X-TEM) using a 200 kV Philips CM20 instrument. The chemical composition at the coating-substrate interface was evaluated using scanning TEM-energy dispersive spectroscopy (STEM-EDS) analysis in a Hitachi HB.501 microscope with a beam diameter of 3 nm.

124 Phase analysis of the coatings was performed by X-ray diffraction (XRD) in the Bragg–Brentano geometry. Glancing angle XRD (GA-XRD) was used for residual stress determination. The microhardness was measured

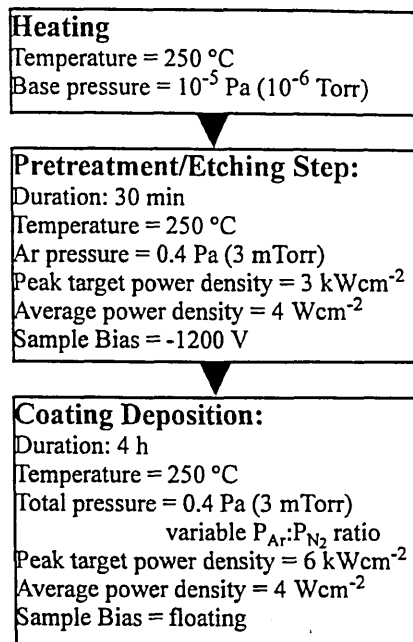


Fig. 1. Coating deposition sequence.

12 with a Mitutoyo HVK-G1 hardness tester using a Knoop indenter and a load of 25 g. The sliding friction and wear coefficients were measured using a CSEM pin-on-disk tester with a 6 mm Al₂O₃ ball under a load of 5 N, sliding distance of 24 km and linear velocity of 10 cm/s. Critical loads, L_C , were measured in a CSEM scratch tester with a diamond tip of radius 200 μm to evaluate the adhesion. The corrosion resistance of the coating deposited on a SS substrate polished to $R_a = 0.05 \mu\text{m}$ was evaluated in potentiodynamic polarization tests in a 3% NaCl solution using an EG&G 263A Potentiostat.

14 3. Results and discussions

14 3.1. HIPIMS discharge

14 The HIPIMS discharge was operated with a duty cycle of 1% and pulse repetition frequency of 50 Hz. HIPIMS of Cr in an Ar atmosphere with peak power density of 3 kW cm⁻² was performed while the average power was limited to 400 W. Non-localized HIPIMS discharge currents were maintained for more than 100 h of operation without arcing. Discharge voltages as high as -1.9 kV were measured while the discharge current densities in these conditions reached peak values of 2.2 A cm⁻². The addition of N₂ gas into the chamber caused the discharge current density to increase to 3.6 A cm⁻² for a constant voltage of -1.9 kV and a total pressure of 0.4 Pa.

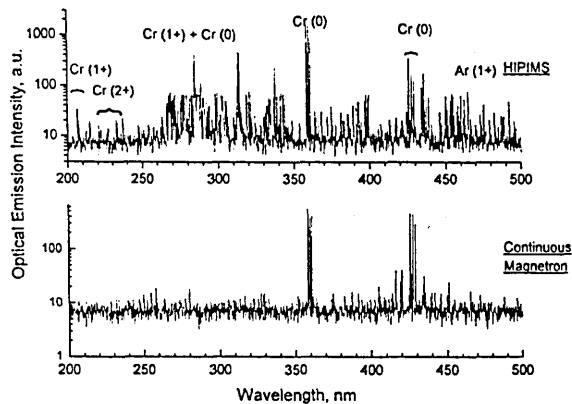


Fig. 2. OES spectra, comparing the plasma composition in HIPIMS and conventional magnetron sputtering of Cr in Ar atmosphere at the same average power.

3.2. Plasma conditions during the substrate pretreatment

During the substrate pretreatment stage, the HIPIMS source was operated in a pure Ar atmosphere at a pressure of 0.4 Pa. The plasma density produced in these conditions was estimated to be of the order of 10^{13} cm^{-3} [8,7].

Fig. 2 shows a typical OES spectrum of HIPIMS of Cr in Ar at an average power of 300 W (15 W cm^{-2}). Emission lines from excited Cr(0), but also many from metal ions charged up to 2+, are clearly seen. It has been shown previously that the lifetime of these metal ions extends over practically the complete discharge duration [8]. OES investigations of HIPIMS, which are not presented here, have confirmed the presence of multiply charged metal ions when sputtering Ti and Ta. In comparison, the emission spectrum of a continuous magnetron, operated at a similar average power and gas pressure, contained mostly neutral metal and gas lines (see Fig. 2). A metal ionization degree of 30% was estimated for HIPIMS of Cr by a weight gain method [7], sampling the deposition flux at a distance of 50 cm from the target.

These high ionization levels of metals are uncommon in magnetrons where the proportion of secondary ions produced by the sputtering process itself is negligible. However, it can be speculated that the sputtered species can undergo ionizing collisions while traversing the relatively large high voltage cathode sheath and the dense plasma formed near the target in HIPIMS.

3.3. Plasma conditions during coating deposition (reactive HIPIMS)

The effect of reactive gas on the HIPIMS discharge parameters and plasma composition was investigated in order to clarify the conditions under which the coating

growth developed. The plasma composition was observed by OES. Carbon was chosen as target material because of its low sputtering yield and therefore low emission intensity in the plasma. Thus, one could expect to avoid the overlapping of emission lines from the N_2 gas plasma with that of eventual Cr.

Fig. 3 shows a typical spectrum of HIPIMS of carbon in N_2 atmosphere exhibiting excited but also singly ionized $\text{N}_2(1+)$ (391.4 nm), the intensity of the latter peak being two times higher than that of $\text{N}_2(0)$ (337.1 nm). In the case of continuous magnetron discharge the $\text{N}_2(1+)$ and $\text{N}_2(0)$ peaks reach similar intensities. The vibrational temperature of the N_2 molecule in the HIPIMS discharge was evaluated according to the procedure outlined in Pintaske et al. [10]. The resulting value of 7000 K as calculated in this study, is higher than values reported in the literature for r.f. magnetron sputtering discharges (6000 K) [10], arc discharges (4000–6000 K) [11] and d.c. magnetron sputtering discharges (3000 K) [10]. This suggests that the nitrogen molecules in the HIPIMS plasma are strongly activated and reactive which could lead to target poisoning at a relatively low N_2 partial pressures and enhanced N incorporation at the substrate side. An interesting effect, which has also been observed in laser ablation [12] of C in N_2 atmosphere, is the detection of emission from CN molecules in the HIPIMS plasma.

During the actual CrN deposition processes a floating potential with a peak value of -160 V was established on the substrates. This value was variable within the duration of the pulse, following closely the ion saturation current over the entire pulse length. The peak floating potential varied within $\pm 20 \text{ V}$ from process to process. The reasons for the high value and the observed variation are not fully understood, however, assuming a value of the plasma potential near ground, it can be speculated

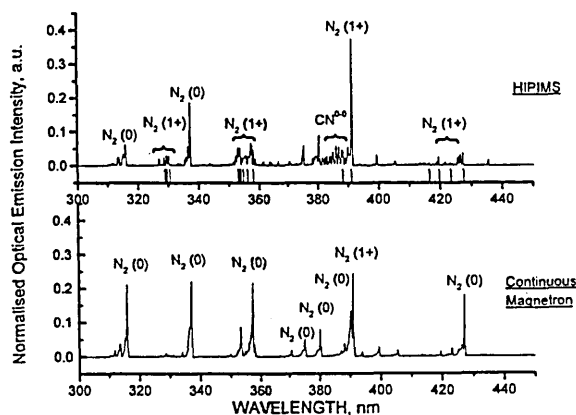


Fig. 3. Optical emission spectrum of carbon sputtering in HIPIMS and conventional magnetrons. Reference heads of bands of N_2^+ (FNS) are marked in the HIPIMS spectrum.

189

190

191

192

193

194

195

196

197

198

199

200

201

202

203

204

205

206

207

208

209

210

211

212

213

214

215

216

217

218

219

220

221

222

223

224

14

175

176

177

178

179

180

181

182

183

184

185

186

187

188

15

16

17

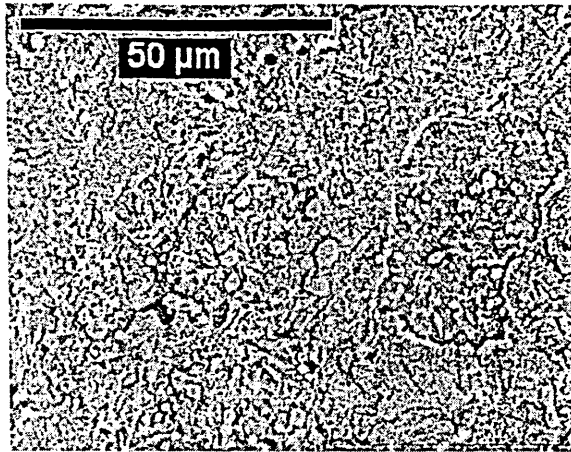


Fig. 4. SEM micrograph of CrN film deposited on HSS after pretreatment by HIPIMS.

that ions arriving at the substrate gain an energy of the order of more than 100 eV in the substrate sheath. The microstructure of the resulting coatings observed by XTEM shown in the following sections confirms a highly energetic ion bombardment during growth.

3.4. Substrate pretreatment

A substrate pretreatment was carried out prior to the deposition of coatings for all samples (see Fig. 1). The substrates were biased to a voltage of -1200 V. The HIPIMS source was operated in pure Ar atmosphere at a pressure of 0.4 Pa. As shown by the plasma investigations, under these conditions high-density plasma containing highly charged metal ions is produced. Fig. 4 shows an SEM micrograph of the surface of a $2\text{-}\mu\text{m}$ -thick CrN layer deposited on a HSS substrate. As a result of the highly efficient etching during pretreatment, the martensitic granular structure of the substrate is clearly recognizable. The circular flat-topped carbide inclusions are especially clearly seen. No growth defects (droplet defects) can be observed on the film surface or in XTEM (see further sections) views of the coatings.

Fig. 5 shows the spatially resolved composition of the interface determined by XTEM-EDS analysis. It can be seen that Cr is implanted in the stainless steel substrates. The interface is characterized also with an incorporation of 4 at.% of Ar, which is a typical value for gas/metal ion etching reported in the literature [6]. CrN coatings with thickness of $2\text{ }\mu\text{m}$ deposited on HSS substrates and pretreated with a HIPIMS etching had a scratch test critical load of 85 N.

The high metal ion concentration found in the bombardment flux could be the cause for the Cr implantation/diffusion profile observed in the interface and the high L_C values measured for the HIPIMS-deposited CrN

films. Similar high adhesion, but also implantation profiles for Cr, have been found when steel substrates were bombarded with high energy metal ions (1200 eV) stemming from a cathodic arc discharge (ABS technology). Again, substantial metal ion implantation effects were observed in conjunction with efficient cleaning of the substrates. This process was shown to promote local epitaxial growth thus significantly enhancing the adhesion with values of L_C up to 90 N [4,6].

In many PVD processes, inert Ar is used to clean the substrate surface. Besides its inefficient etching rate of oxides, the incorporation of a high concentration of Ar gas in the interface is disadvantageous. Consequently, the critical load values in scratch tests are rather low, typically $L_C=40$ N [5].

3.5. Coating microstructure and mechanical properties

Fig. 6 shows a TEM cross-section of the CrN film deposited at $P_{Ar}/P_{N_2}=1:4$. The coating grains near the substrate have a wide base indicating high adatom mobility during the initial nucleation stages of film formation. The subsequent growth adjacent to the interface is competitive with no observable porosity. Further on, the film assumes a well defined densely packed columnar structure with low surface roughness. The intercolumnar porosity is low and observed primarily in the upper part of the coating. It is interesting to note that the grains contain an appreciable amount of lattice defects visible by the speckled contrast produced in the TEM image. Additionally, some columns can be observed forming on top of existing columns due to a renucleation mechanism. Both these features as well as the high density of the coating microstructure show that all stages of the coating growth occur under conditions of energetic and highly ionized deposition flux, thus

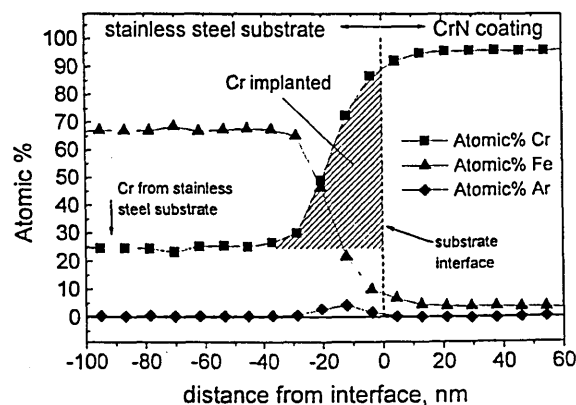


Fig. 5. STEM-EDS analysis of the chemical composition at the coating-substrate interface after pretreatment and CrN coating deposition by HIPIMS.

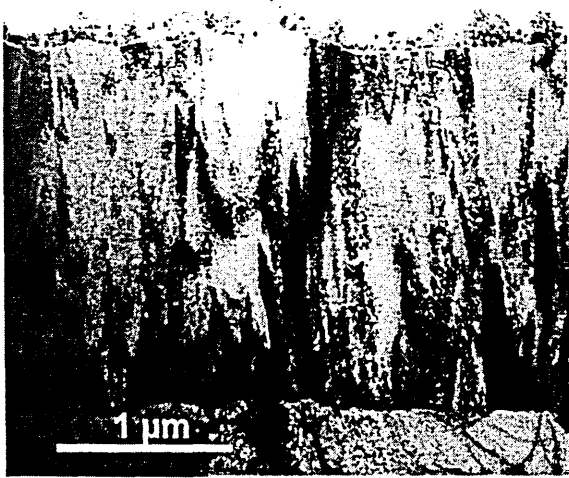


Fig. 6. Cross-sectional TEM view of CrN coating deposited by HIPIMS at $P_{Ar}/P_{N_2} = 1:4$.

confirming the findings of the plasma diagnostic investigations.

The microstructural integrity of PVD films is best tested under corrosion conditions, and structural defects in the coating such as porosity or incorporated macroparticles allow the substrate material to be severely attacked. Fig. 7 shows the polarization curve of a CrN coating deposited by HIPIMS, CrN deposited by arc evaporation and electroplated hard Cr on SS substrates. The passivation current of HIPIMS CrN is 1×10^{-6} A cm^{-2} and the pitting potential is +480 V. In comparison, PVD 3- μm -thick cathodic arc deposited CrN showed to be clearly inferior. In case of 25- μm -thick electroplated hard Cr we observe higher corrosion currents, but the pitting potential is two times higher than the HIPIMS coating, obviously due to the increased thickness of the former.

The crystalline microstructure of four samples deposited at $P_{Ar}/P_{N_2} = 1:1, 1:2, 1:4$ and $1:5$ is shown in the Bragg-Brentano XRD scans in Fig. 8. It can be seen that as the nitrogen partial pressure increases, the films

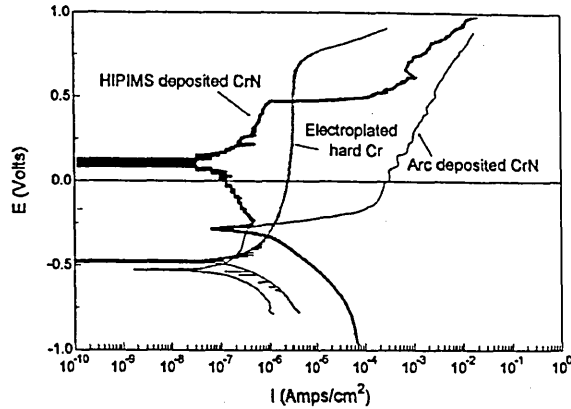


Fig. 7. Polarization curve plots comparing CrN coatings deposited by HIPIMS, arc evaporation and electroplating.

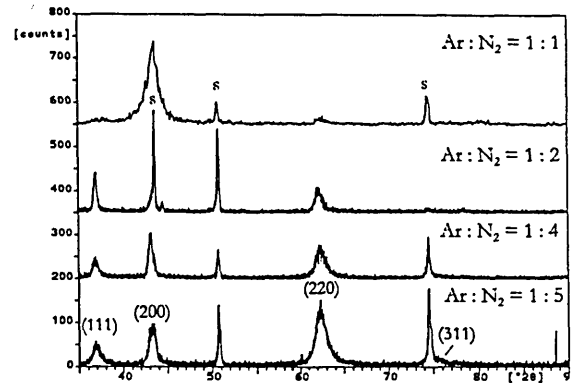


Fig. 8. XRD analysis of CrN coatings deposited at different Ar/N_2 partial pressure ratios by HIPIMS.

become more randomly textured and the preferred orientation shifts to $\langle 220 \rangle$. The dominant peaks are those of the CrN phase, however, diffraction peaks of the Cr_2N phase could also be observed in GA-XRD traces (not shown) in the samples with $P_{Ar}/P_{N_2} = 1:1$ and $1:2$. Table 1 summarizes the residual stress and some mechanical properties of the coatings. Precise calculation

Table 1
Residual stress and mechanical properties of CrN coatings deposited by HIPIMS in Ar/N_2 atmosphere

Partial pressure ratio P_{Ar}/P_{N_2}	1:1	1:2	1:4	1:5	Substrate
HK _{0.025}	—	2887 ± 245	2633 ± 47	—	HSS
Residual stress (GPa)	—	-2.55	-3.4	-2.99	SS
Lattice parameter (Å)	4.15	4.19	4.21	4.20	SS
Friction coeff. against Al ₂ O ₃	—	0.4	0.45	—	HSS
Wear rate ($m^3 N^{-1} m^{-1}$)	—	7.6×10^{-17}	2.3×10^{-16}	—	HSS

of the stress in the film deposited at $P_{Ar}/P_{N_2} = 1:1$ was not possible due to its strong texture.

The microhardness and stress values agree well with results on magnetron sputtered CrN deposited at high bias voltages and nitrogen partial pressures where, in special cases, hardness values reaching $HK_{0.025} 3000$ were reported [13,14]. However, the texture of the HIPIMS films bears more similarity to arc deposited CrN at bias voltages of -100 V [15].

The high hardness, high density microstructure and low surface roughness of the HIPIMS deposited coatings can provide for resistance to cracking under tensile loads. The sliding wear coefficients ($2.3 \times 10^{-16} \text{ m}^3/\text{Nm}$) measured in pin-on-disk tests for these films are low compared to high hardness CrN (1.3×10^{-15}), arc deposited CrN ($9 \times 10^{-15} \text{ m}^3/\text{Nm}$), and electroplated hard Cr ($5.8 \times 10^{-14} \text{ m}^3/\text{Nm}$) [16].

4. Conclusions

Plasma diagnostics and microstructural studies identify the high power pulsed magnetron sputtering method (HIPIMS) as an extremely promising PVD technique suitable for both substrate pretreatment and coating deposition.

Plasma diagnostic studies of the HIPIMS discharge revealed that in inert gas atmosphere a high density plasma is created containing even multiply charged sputtered metal ions only known from the cathodic arc discharge [17]. In reactive mode, a high degree of excitation and ionization of the nitrogen gas in HIPIMS was observed. High energy Ar/Cr ion irradiation prior to coating leads to a metal ion implantation profile at the substrate-coating interface similar to the ABS technique. Subsequently, deposited CrN films were found to have an excellent adhesion reaching scratch critical load values of 85 N. CrN deposited in the high density plasma environment of the HIPIMS discharge was columnar with a dense microstructure. No droplets or other macroscopic growth defects were observed in TEM cross-sections. The films were clearly harder than con-

ventional PVD CrN (UBM, cathodic arc) and had superior corrosion and wear resistant properties, reaching the quality of nanoscale multilayer/superlattice coatings [16,18].

References

- [1] J.E. Greene, S.A. Barnett, *J. Vac. Sci. Technol.* 21 (2) (1982) 285.
- [2] I. Petrov, L. Hultman, U. Helmersson, J.E. Sundgren, J.E. Greene, *Thin Solid Films* 169 (2) (1989) 299.
- [3] L. Hultman, W.-D. Münz, J. Musil, S. Kadlec, I. Petrov, J.E. Greene, *J. Vac. Sci. Technol. A* 9 (3) (1991) 434.
- [4] C. Schönjahn, L.A. Donohue, D.B. Lewis, W.-D. Münz, R.D. Twesten, I. Petrov, *J. Vac. Sci. Technol. A* 18 (4) (2000) 1718.
- [5] W.-D. Münz, C. Schönjahn, H. Paritong, I.J. Smith, *Vide* 297 (3/4) (2000) 205.
- [6] C. Schönjahn, A.P. Ehiasarian, D.B. Lewis, R. New, W.-D. Münz, R.D. Twesten, I. Petrov, *J. Vac. Sci. Technol. A* 19 (4) (2001) 1415.
- [7] V. Kouznetsov, K. Macak, J.M. Schneider, U. Helmersson, I. Petrov, *Surf. Coating Technol.* 122 (2-3) (1999) 290.
- [8] A.P. Ehiasarian, R. New, W.-D. Münz, L. Hultman, U. Helmersson, V. Kouznetsov, *Vacuum* 65 (2002) 147.
- [9] A.P. Ehiasarian, K.A. Macak, C. Schönjahn, R. New, W.-D. Münz, *Proceedings of the 44th Annual Technical Conference SVC, 2001*, p. 382.
- [10] R. Pintaske, T.h. Welzel, M. Schaller, N. Kahl, J. Hahn, F. Richter, *Surf. Coating Technol.* 99 (1998) 66.
- [11] M. Kühn, R. Pintaske, F. Richter, *IEEE Trans. Plasma Sci.* 25 (4) (1997) 694.
- [12] A.A. Voevodin, J.G. Jones, J.S. Zabinski, L. Hultman, Plasma characterisation during laser ablation of graphite in nitrogen for the growth of fullerene-like CN_x films, *J. Appl. Phys.* (submitted).
- [13] X. He, N. Baker, B. Kehler, K. Walter, M. Nastasi, Y. Nakamura, *J. Vac. Sci. Technol. A* 18 (1) (2000) 30.
- [14] A.P.A. Hurkmans, Ph.D. Thesis, Sheffield-Hallam University, Sheffield, UK, 2002.
- [15] M. Oden, C. Ericsson, G. Hakansson, H. Ljungkrantz, *Surf. Coating Technol.* 114 (1999) 39.
- [16] W.-D. Münz, D.B. Lewis, P.E. Hovsepian, C. Schönjahn, A. Ehiasarian, I.J. Smith, *Surf. Eng.* 17 (1) (2001) 15.
- [17] I.G. Brown, B. Feinberg, J.E. Galvin, *J. Appl. Phys.* 63 (1) (1988) 4889.
- [18] P.Eh. Hovsepian, W.-D. Münz, Invited Paper to be Presented at 45th Annual Technical Conference SVC, 2002.

36

36

36

36

36

36

36

36

36

36

37

37

37

37

37

37

37

37

37

37

38

38

38

38

38

38

38

38

38

39

39

39

39

39

39

39

39

39

40

40

40

40

40

40